Materials Horizons: From Nature to Nanomaterials

Pankaj Sharma
Gagan Kumar Bhargava
Sumit Bhardwaj
Indu Sharma *Editors*

Engineered Ferrites and Their Applications

Springer

Materials Horizons: From Nature to Nanomaterials

Series Editor

Vijay Kumar Thakur, School of Aerospace, Transport and Manufacturing, Cranfield University, Cranfield, UK

Materials are an indispensable part of human civilization since the inception of life on earth. With the passage of time, innumerable new materials have been explored as well as developed and the search for new innovative materials continues briskly. Keeping in mind the immense perspectives of various classes of materials, this series aims at providing a comprehensive collection of works across the breadth of materials research at cutting-edge interface of materials science with physics, chemistry, biology and engineering.

This series covers a galaxy of materials ranging from natural materials to nanomaterials. Some of the topics include but not limited to: biological materials, biomimetic materials, ceramics, composites, coatings, functional materials, glasses, inorganic materials, inorganic-organic hybrids, metals, membranes, magnetic materials, manufacturing of materials, nanomaterials, organic materials and pigments to name a few. The series provides most timely and comprehensive information on advanced synthesis, processing, characterization, manufacturing and applications in a broad range of interdisciplinary fields in science, engineering and technology.

This series accepts both authored and edited works, including textbooks, monographs, reference works, and professional books. The books in this series will provide a deep insight into the state-of-art of Materials Horizons and serve students, academic, government and industrial scientists involved in all aspects of materials research.

Review Process

The proposal for each volume is reviewed by the following:

1. Responsible (in-house) editor
2. One external subject expert
3. One of the editorial board members.

The chapters in each volume are individually reviewed single blind by expert reviewers and the volume editor.

Pankaj Sharma · Gagan Kumar Bhargava ·
Sumit Bhardwaj · Indu Sharma
Editors

Engineered Ferrites and Their Applications

Springer

Editors
Pankaj Sharma
Applied Science Department
National Institute of Technical Teachers Training and Research
Chandigarh, India

Sumit Bhardwaj
Department of Physics
Chandigarh University
Mohali, Punjab, India

Gagan Kumar Bhargava
Department of Physics
Chandigarh University
Mohali, Punjab, India

Indu Sharma
Department of Physics
Career Point University
Hamirpur, Himachal Pradesh, India

ISSN 2524-5384 ISSN 2524-5392 (electronic)
Materials Horizons: From Nature to Nanomaterials
ISBN 978-981-99-2582-7 ISBN 978-981-99-2583-4 (eBook)
https://doi.org/10.1007/978-981-99-2583-4

This Springer imprint is published by the registered company Springer Nature Singapore Pte Ltd.
The registered company address is: 152 Beach Road, #21-01/04 Gateway East, Singapore 189721, Singapore

Preface

Ferrites have been a subject of extensive research for over a century, with their unique magnetic and electrical properties making them a promising material for a wide range of applications. In recent years, the development of engineered ferrites has opened up new avenues for their use in various industries, from electronics to biomedical engineering.

This book, *Engineered Ferrites and Their Applications*, presents a comprehensive overview of the latest research on these fascinating materials, including their synthesis, characterization, and applications. The book covers a broad range of topics, from the fundamental properties of ferrites to their use in advanced technological applications. Chapter 1 of the book, "Basic Physics and Chemistry of Ferrites," covers the basics of ferrites, including their crystal structures, and their magnetic properties. This part provides an in-depth understanding of the principles governing the behaviour of ferrites and serves as a foundation for the subsequent chapters. Chapter 2 of the book, "Tuning of Structural, Electrical and Magnetic Properties of Ferrites," delves into the engineering of ferrites, discussing topics such as doping, size and shape control, and magnetic anisotropy. This part provides a comprehensive overview of the techniques used to tailor the properties of ferrites to suit various applications. Chapter 3 of the book, "Advances in the Processing of Ferrite Nanoparticles," presents the latest developments in the synthesis and processing of ferrite nanoparticles. This part covers topics such as the synthesis of monodisperse nanoparticles, the use of template-assisted methods, and the role of surfactants in controlling particle size and shape. The subsequent chapters of the book present various applications of ferrites. Chapter 4 "Ferrite Nanoparticles for Water Decontamination Applications" discusses the use of ferrite nanoparticles for water treatment, while Chap. 5 "Ferrite Nanoparticles for Hyperthermia Treatment Application" focuses on their use in cancer therapy. Chapter 6 "Ferrite Nanoparticles for Telecommunication Application" presents the use of ferrite nanoparticles in microwave devices, and Chap. 7 "Role of Ferrite Materials in Renewable Energy Harvesting" discusses the use of ferrite for different type of energy harvesting sources along with multi-ferrite material used in developing

their components. Chapter 8 "Ferrite Nanocomposites for EMI Shielding Applications" covers their use in electromagnetic interference shielding, and Chap. 9 "Ferrite Nanoparticles for Sensing Applications" presents their use in sensing applications. Chapter 10 "Ferrite Nanoparticles for Energy Storage Applications" discusses their use in energy storage, while Chap. 11 "Ferrite Nanoparticles for Antimicrobial Applications" covers their use in antimicrobial applications. Finally, Chap. 12 "Ferrite Nanoparticles for Corrosion Protection Applications" discusses their use in corrosion protection, and last chapter "Biomedical Applications of Ferrites" discusses the various biomedical applications of ferrites.

This book is intended for researchers, scientists, and engineers who are interested in the latest developments in the field of engineered ferrites. It provides a comprehensive overview of the current state of research in this exciting area and offers insights into the future directions of this rapidly evolving field.

We would like to express our sincere gratitude to all the contributors for their invaluable contributions to this book. We hope that this volume will serve as a useful resource for researchers and engineers working in this field and inspire new ideas and innovations in the use of ferrites for a wide range of applications.

Chandigarh, India — Pankaj Sharma
Mohali, India — Gagan Kumar Bhargava
Mohali, India — Sumit Bhardwaj
Hamirpur, India — Indu Sharma

Contents

About the Editors

Dr. Pankaj Sharma is presently working as a professor at Applied Sciences Department, National Institute of Technical Teachers Training and Research, Chandigarh, India. He pursued his M.Phil. degree in Physics from Himachal Pradesh University, India, and Ph.D. in Physics from Jaypee University of Information Technology, Waknaghat, India. He is an experimentalist by inclination, and his research interests include the development of materials in 0D, 1D, and 2D for various optoelectronic, thermoelectric, and biomedical applications. Few materials of recent interest include ferrites, chalcogenides, polymers, and dilute magnetic semiconductors. He has published more than 130 research articles in SCI/Scopus indexed journals. He has published 8 book chapters and 4 review papers. He has contributed more than 50 articles in various conferences. He has executed 2 government-sponsored projects. He has successfully supervised 5 research scholars to earn their Ph.D. degree. He is a senior member of IEEE and a founder member and the joint secretary of Materials Research Society of India—Himachal Pradesh Chapter, India. He is also serving as a member of editorial board of two international journals and a reviewer for many Web of Science indexed journals.

Dr. Gagan Kumar Bhargava is currently working as a professor at the Department of Physics, Chandigarh University, India. He obtained his Ph.D. degree in Physics from Himachal Pradesh University, India. His current research interests are synthesis of nanomaterials for antenna, EMI shielding, electromagnet, and biomedical applications. He has more than 14 years of teaching and research experience. He has published more than 50 research papers in different peer-reviewed international journals and 6 book chapters. He has guided 2 Ph.D. scholars, 1 M.Phil., and 12 M.Sc. dissertations. He was the former editorial board member of American Journal of Nanosciences and acted as an editor for American Institute of Physics Conference Proceedings in 2018 for AMDFA-2018.

Dr. Sumit Bhardwaj obtained his M.Tech. degree in Metallurgical and Materials Engineering from Thapar University, India, and Ph.D. degree in Materials Science and Engineering from National Institute of Technology (NIT), Hamirpur, India. His current research interests are in the field of ferrite, multiferroic, and composite materials. He has more than 12 years of research and teaching experience. Before joining Chandigarh University, he worked at Punjab Engineering College (Deemed to be University), Chandigarh, India. He has published more than 23 research papers in different peer-reviewed international journals and 3 book chapters and also edited 1 book. He has supervised two M.Tech. dissertations, and currently, he is supervising three Ph.D. students.

Dr. Indu Sharma is currently working as an associate professor at Department of Physics, Career Point University, India. She obtained her Ph.D. in Physics from National Institute of Technology (NIT), Hamirpur, India, and has more than 15 years of research experience. She has published more than 20 research papers in different peer-reviewed international journals and 5 book chapters. She has guided 1 Ph.D., 3 M.Phil., and 30 M.Sc. dissertations.

Chapter 1
Basic Physics and Chemistry of Ferrites

Shubhpreet Kaur, Akhil Sharma, and Neha Thakur

1 Introduction of Ferrites

The creation of modem technology resulted in the extensive use of magnetic materials. For more than 50 years, ferrites, ceramic ferromagnetic materials, have indeed been regarded as extremely significant electronic materials. "Ferrites" are magnetoceramic materials that are mostly made of ferric oxide (Fe_2O_3) and a few other divalent metal oxides. The first to prepare Fe_3O_4 was Hilpert [1]. It is believed that antiquated people were aware of magnetite's magnetic and that it was employed as a mariner's navigator in China over two thousand years ago. Magnetite is a true ferrite and is a naturally occurring mineral with the chemical formula Fe_3O_4. However, it was not until the beginning of the twentieth century that the first effort to synthesize ferrites was performed. About 60 years ago, ferrites actually began to be commercialized.

2 Classification of Ferrites

Ferrites can be classified by two ways: one depending upon the crystal structure and other according to the magnetic field. Based upon the crystal structure and magnetic properties [2], the ferrites are categorized as shown in Fig. 1. There are four subclasses under the crystal structure category, which are spinal ferrite, hexagonal ferrite, garnet

S. Kaur (✉) · A. Sharma
Multifunctional Materials Laboratory, Department of Physics, Guru Nanak Dev University, Amritsar, Punjab 143005, India
e-mail: shubhpreetphy.rsh@gndu.ac.in

N. Thakur
Research and Development Laboratory, Department of Physics, Career Point University, Hamirpur, Himachal Pradesh 176041, India

P. Sharma et al. (eds.), *Engineered Ferrites and Their Applications*, Materials Horizons: From Nature to Nanomaterials, https://doi.org/10.1007/978-981-99-2583-4_1

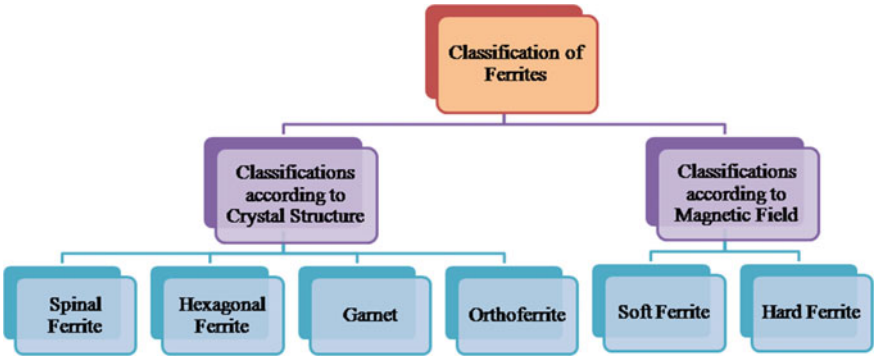

Fig. 1 Classification of ferrites [2]

ferrite, and ortho-ferrite. Furthermore, spinal ferrites and hexagonal ferrites are sub-categorized into several components. On the other hand, relying on the magnetic field, there are only two categories in which all the ferrites come, i.e., soft and hard ferrites. Hard ferrites are highly magnetic than soft ferrites. According to this class, the hexagonal ferrites with various types comprise the hard ferrites, whereas spinel ferrites come under soft ferrite. On the other hand, garnet and ortho-ferrites have minimum magnetic character; hence, they do not lie under this classification. Therefore, it is much convenient to study this ferrite with the help of later class, i.e., classification according to magnetic field.

3 Hard Ferrite

Hard ferrites are basically naturally occurring and have permanent magnetic properties for example loadstone (magnetite, Fe_3O_4). These have high coercivity as shown in Fig. 2; therefore, they are inconvenient to demagnetize and are utilized in order to make applications-based instruments such as magnets of refrigerator, loudspeakers, and electric motors. Hexagonal-structured hard ferrites are used as microwave devices and permanent magnets. In 1952, van Oosterhout and colleagues at the Philips Research Laboratories (Eindhoven, the Netherlands) made the very first announcement of hexagonal ferrites as permanent magnetic materials [3, 4]. They were inspired on Snoek's earlier work on magnetic oxides, which was also done at Philips [5]. These substances belong to the class of ternary or quaternary iron oxides, which form a hexagonal lattice with a very long c-dimension (23.03–84.11) [6, 7].

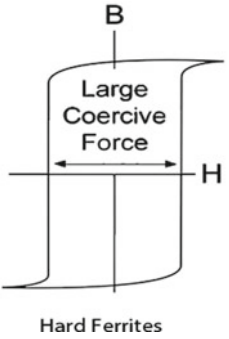

Fig. 2 Hard ferrite [7]

3.1 Hexagonal Ferrites

The hexagonal ferrites are majorly categorized into five classes in the view of their crystal structure and chemical formulae as given in Table 1 [8]. The arrangement of the basic stacking blocks S [$BaFe_2O_4$], R [$BaFe_6O_{11}]^{2-}$, and T [$Ba_2Fe_8O_{14}$] [9] describes the crystal structures of these hexaferrites as shown in Fig. 3.

Table 1 Different types of hexaferrites

Ferrite	Chemical formula
M-type hexaferrites	$BaMeFe_{12}O_{19}$
W-type hexaferrites	$BaMe_2Fe_{16}O_{27}$
Y-type hexaferrites	$Ba_2Me_2Fe_{12}O_{22}$
Z-type hexaferrites	$Ba_3Me_2Fe_{24}O_{41}$
U-type hexaferrites	$Ba_4Me_2Fe_{36}O_{60}$

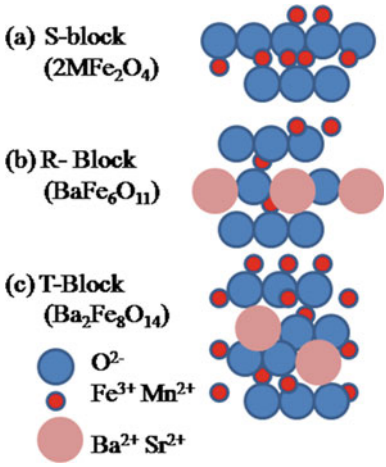

Fig. 3 Stacking sequence of S, R, and T bricks [9] (*Source* Created in VESTA software)

S block

The S block comprises two spinel units, i.e., [$Ba_2Fe_4O_8$] which is same as the S2 unit as shown in Fig. 3. Each S block comprises of four O atoms in two layers with three metal ions beneath each layer. The cation is covered by six O anions in the octahedral sites, and also there are two tetrahedral locations where four O anions are covering the positive ions.

R block

The R block basically composes from the hexagonally three layers containing four O atoms each. However, one of the O atoms present in the middle layer is substituted by an equivalent Ba atom to formulate $BaFe_6O_{11}$. The one barium atom in this stack forms asymmetry among several cation sites, which in turn produce five octahedral sites. Also, the Ba atom pushes the tetrahedral sites into octahedral one. This type of unique positioning is only found in the R block having five-coordinate trigonal bipyramidal locations where the cation is enclosed in with the help of five O anions.

T block

Similarly, the T block is built up of four O layers, where a Ba atom substitutes an oxygen atom in the two central layers, to make the unit formula $Ba_2Fe_8O_{14}$. There are two big Ba atoms in adjacent layers facing each other, and these Ba ions cause the displacement of cations in opposing directions. This decreases the five-coordinate trigonal bipyramidal locations to four-coordinate tetrahedral sites, giving birth to six octahedral and two tetrahedral sites.

These S, R, and T blocks combine in different sequence to give various types of hexagonal ferrites known as hexaferrites.

3.1.1 Classification of Hexaferrite

M-type hexaferrite

The overlapping of hexagonally and cubically packed layers by combination of S and R blocks each gives M-type hexaferrite. The mirror plane which is the basal plane contains a barium atom. Above and below the R block, there are two S blocks showing 180° rotation along the c-axis of one another. Therefore, to continue the structure, a mirror R (R*) block is needed as shown in Fig. 4, and hence, the unit cell requires two M units forming SRS*R* stacking, where * is the 180° rotation of the block around the c-axis [10–13]. The lattice parameters are $a = 0.59$ nm and $b = 2.32$ nm.

W-type Hexaferrite

The combination of one R block and two S blocks results in W-type hexaferrite. In this case, each R block has two S blocks above and below followed by a mirror plane in it. The two W units combine to give SSRS*S*R* [10, 14]. The structure of W-type hexaferrite is shown in Fig. 5.

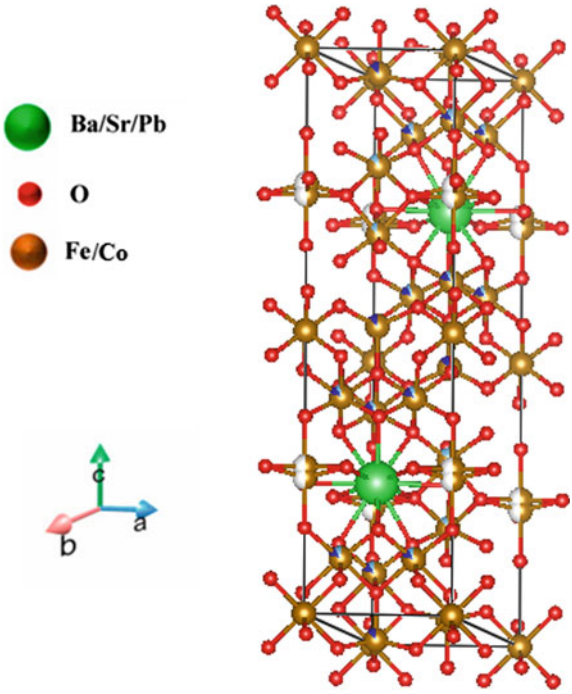

Fig. 4 Perspective layouts of the M-type hexaferrite [18] (*Source* Created in VESTA software)

Y-type hexaferrite

Single S and single T block combines in six layers and gives Y-type structure, and the unit cell is from R3m space group and comprises three of these units having c lattice parameters value 43.56 Å [15]. This results in the unit cell formula being just 3 (ST) as shown in Fig. 6.

Z-type hexaferrite

One Y and one M unit combines to give one molecular unit of Z-type hexaferrite, and hence, with a mirror plane in the R block, it is made up of ST + SR. Hence, to form a single Z-type unit cell, two molecular units are required for ferrite with stacking sequence STSRS*T*S*R* [16] as shown in Fig. 7.

U-type hexaferrite

The structure of U-type hexaferrite comprises Z + M-type hexaferrite or 2 M + Y, which creates the block stacking structure SRS*R*S*T [17] as shown in Fig. 8.

The longest unit cell and perhaps most complicated structure of all hexaferrites with complicated magnetoplumbite are found in U-type hexaferrites [20–24]. Due to their greatest intrinsic magneto-crystalline anisotropy (MCA) and maximum intricacy, U-type hexaferrites have demonstrated greater microwave absorption over a broad frequency range.

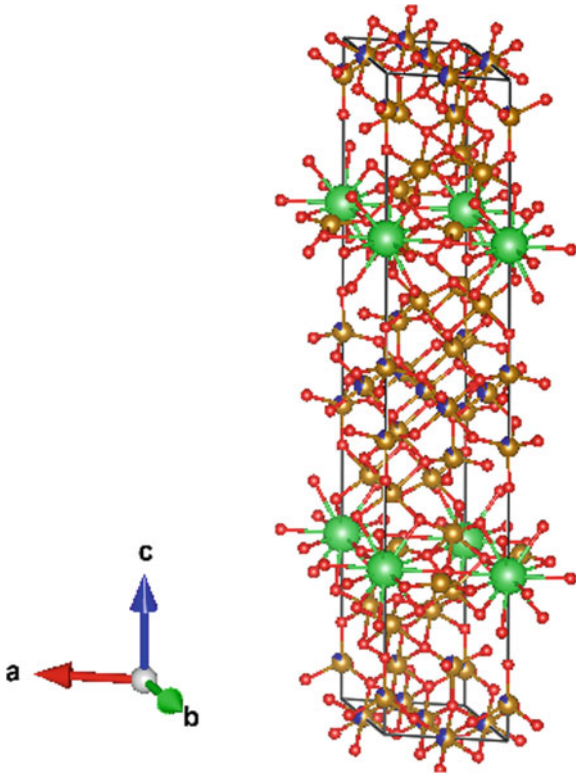

Fig. 5 Perspective of W-type hexaferrite [19] (*Source* Created in VESTA software)

4 Soft Ferrites

On the other hand, magnetically soft ferrites are usually man-made or manufactured artificially. They are temporarily magnetic with different sizes and shapes. These ferrites have weak coercivity as shown in Fig. 9; hence, they can easily modify their magnetization and behave as conductors in magnetic fields. Soft ferrites are generally spinel and garnets and are crucial for high-frequency application. Soft ferrites were first identified in 1946 by J. L. Snoek at Philips Research in the Netherlands [25]. Due to the intriguing magnetic and electrical characteristics, such as strong saturation magnetization, large squareness ratio, huge magneto-crystalline anisotropy, and poor coercivity [7, 26], Spinel ferrites are known as soft ferrites.

4.1 Spinel Ferrite

The cubic structure with the empirical formula AB_2O_4—where A stands for a divalent cation and B for a trivalent cation—is referred to as a spinel [27]. The full structural

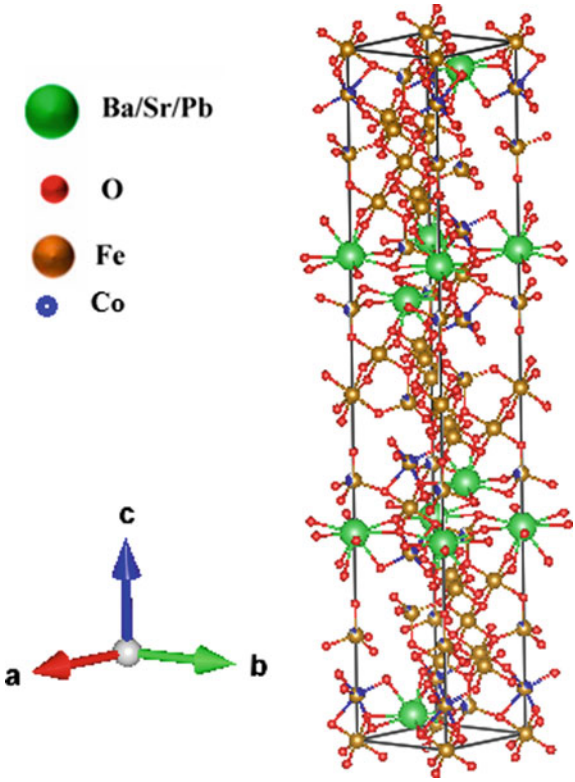

Fig. 6 Y-type hexaferrite with stacking representation [15] (*Source* Created in VESTA software)

formula of spinel ferrites is AFe_2O_4, which can be regarded as densely compacted cubic structures with ironclad, (Fe^{3+}) as a trivalent cation. Fe, Ni, Zn, Co, Mn, Mg, Cu, Cd, or mixtures of these metals are examples of divalent cations (A). Due to the structural resemblance between these ferrites and the naturally occurring mineral spinel, $MgAl_2O_4$, they were given the term ferrites. These cubic ferrites, also known as ferro-spinels, are semiconducting by nature [28, 29]. Spinel ferrite MFe_2O_4 has eight formula units per cubic unit cell which ultimately count as 56 ions [27, 30]. A face-centered cubic structure is formed by massive O_2- ions as given in Fig. 10, tiny divalent metal cations filling the spaces between larger ones [31, 32] with space group $Fd_{3m}O_k^7$ (227) [29, 33–35]. The spinel unit cell maintains its electrical neutrality overall.

4.1.1 **Classification of Spinel ferrite:** The spinel ferrites could be roughly divided into two groups dependent on how the two cationic areas' divalent metal ions and trivalent ferric ions are arranged [36–38].

Normal Spinel Ferrite: According to the formula $[M^{2+}]_A[Fe^{3+}]_BO_2$, A and B locations exhibit opposite spin directions, these spinel ferrites contain 16 trivalent ferric cations at all 16 B-sites and eight divalent metal cations at all eight A locations

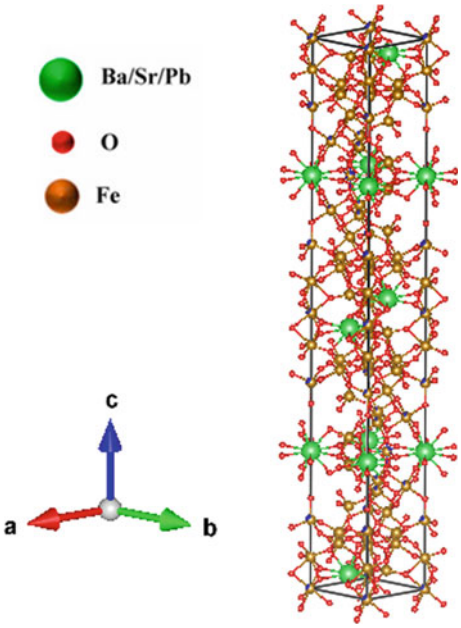

Fig. 7 Structure of Z-type hexaferrite [16] (*Source* Created in VESTA software)

(Fig. 11). In this case, M^{2+} ions act as network formers, whereas Fe^{3+} ions act as network modifiers. Some examples of typical spinel ferrites include $ZnFe_2O_4$ and $CdFe_2O_4$.

Inverse Spinel Ferrite: According to the formula $[Fe^{3+}]_A[M^{2+}Fe^{3+}]_BO_2{}^{4-}$, these spinel ferrites include 16 ferric cations at eight A-sites and the remaining eight B-sites, together with eight metal cations at eight of the possible 16 B-sites (Fig. 12). In this case, Fe^{3+} ions function as both network makers and network modifiers. Inverse spinel ferrites include Fe_3O_4, $CoFe_2O_4$, $NiFe_2O_4$ [39], and Ni-Zn ferrites [40–42].

5 Magnetic Properties of Ferrites

It is clear from the above sections that U-type hexaferrites have highly complex structure. In the absence of an external magnetic field, the average magnetic moment of a ferro- or ferrimagnetic material is oriented in the crystallographic axis where the free energy F reaches its lowest amount. The easy axis, often known as the favorable magnetization direction, is in this direction. As a result, a portion of the overall free energy—known as the magneto-crystalline free energy or the magnetic anisotropy—depends on the magnetization direction relative to the various crystallographic directions. In ferrite materials, due to the spin orbit resonance which encourages the aligning of the magnetic moment along a specific crystallographic axis, magnetic crystalline anisotropy develops. This developed anisotropy depends

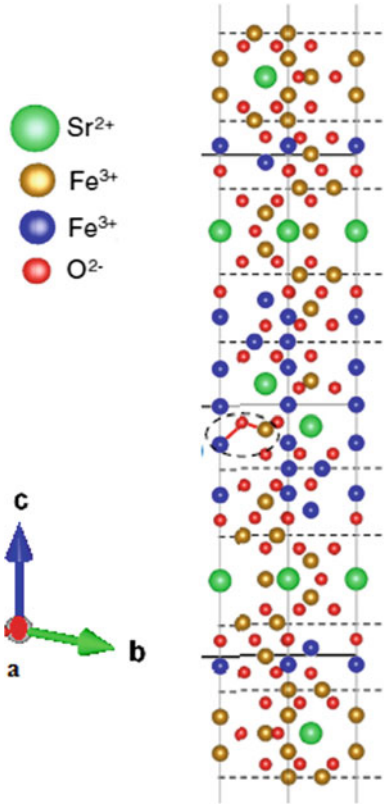

Fig. 8 Structure of U-type hexaferrite [17] (*Source* Created in VESTA software)

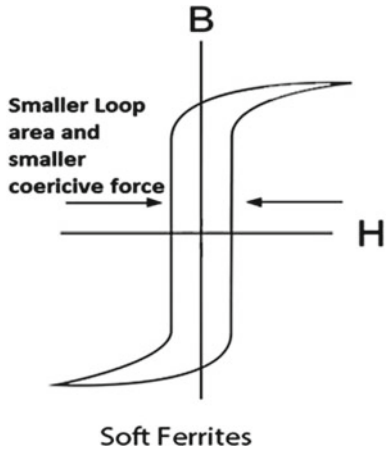

Fig. 9 Soft ferrite [7]

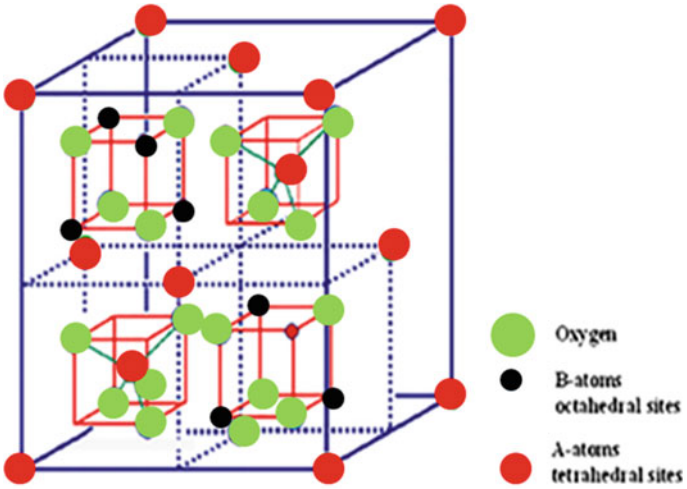

Fig. 10 Spinel ferrite cell structure [36] (*Source* Created in VESTA software)

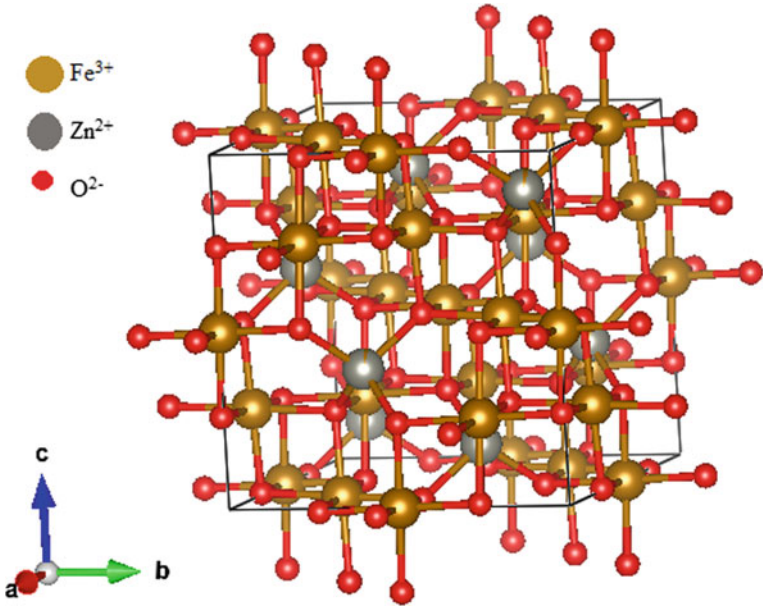

Fig. 11 Normal spinel ferrite's unit cell structure [38] (*Source* Created in VESTA software)

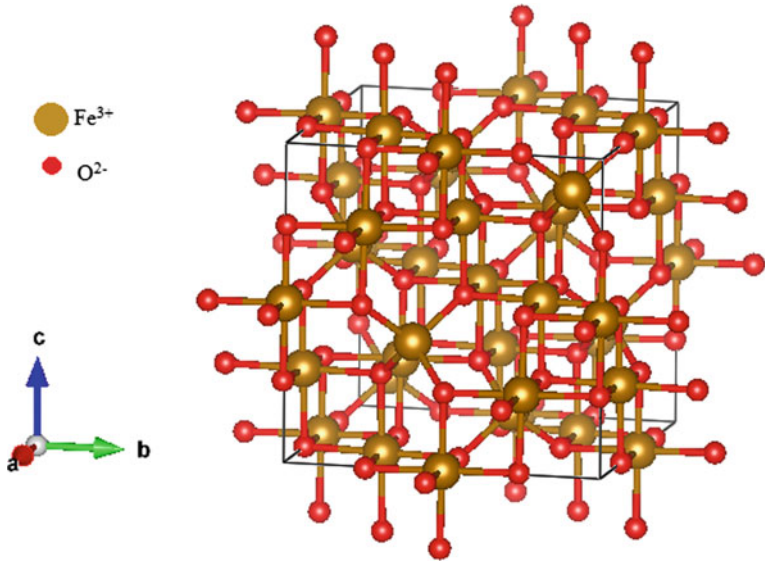

Fig. 12 Inverse spinel ferrite's unit cell structure [38] (*Source* Created in VESTA software)

upon the doping as base elements, therefore varies from material to material. Here, it is worth noting that the U-type hexaferrite materials have highly complex structure as well as magnetic anisotropy.

6 Basic Applications Based upon the Properties

Ferrites basically are really crucial owing to its various technological applications such as in magnetoelectric and microwave gadgets, and permanent magnets [43].

The spectrum of applications for magnetic materials expands as their magnetic, mechanical, electrical, and thermal properties increase. Figure 13 illustrates the basic applications of magnetic materials. Other applications include driving engines, igniters, ventilation systems, speed indicators, and existing power stations in electric drive trains; sensors, routers, and converters in electro-technology; magnetrons, couplings, and zero friction bearings in aviation and space technology; speakers and motors for home appliances. In medicine, there are clocks, ear buds, and magnetic locks; and magnetic prosthetics, cancer cell artificial organs, nuclear magnetic resonance equipment, and separators, and audiovisual analogue devices in manufacturing [44–48].

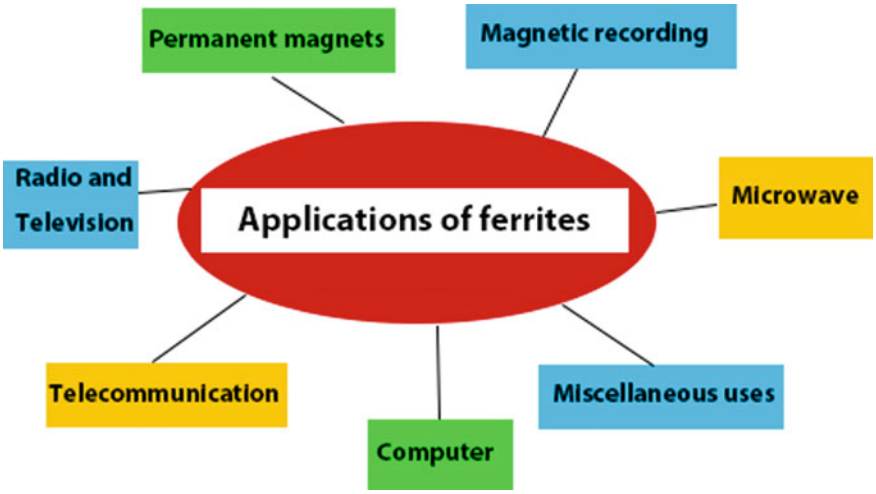

Fig. 13 Applications of ferrites

7 Conclusion

The term "magnetic materials" refers to a broad category of materials with a variety of uses. Electricity is produced, distributed, and, for the most part, used in appliances by the usage of magnetic materials. They are employed to store data on computer disks as well as audio and video tapes. They are applied in a variety of medical applications where they are attached to or implanted into the body, including body scanners. Magnetic materials are used in devices including PCs, CD players, televisions, gaming consoles, and loudspeakers in the home entertainment market. Upgraded magnetic materials and technologies are required for efficient electricity generation and usage. Electric vehicles that emit no emissions will rely on powerful motors made of cutting-edge magnetic materials. The telecommunications sector is always pursuing quicker data transmission and device miniaturization, both of which call for the creation of enhanced magnetic materials. Equipments that were once thought to be stationary are now able to be changed anywhere. A world without magnetic material is hard to fathom, and they are playing a bigger role in the advancement of contemporary society.

Acknowledgements One of the authors wants to acknowledge the Multifunctional Laboratory, Department of Physics, Guru Nanak Dev University, for providing opportunity to do the research on magnetic materials and their properties.

References

1. Hilpert S (1909) Correspondence as to structure and origin in magnetic properties of ferrite and iron oxide. Ber Dtsch Chem Ges 42:2248–2261
2. Jadhav VV, Mane RS, Shinde PV (2020) Basics of ferrites: structures and properties. In: Bismuth-Ferrite-based electrochemical supercapacitors. SpringerBriefs in Materials. Springer, Cham
3. Went JJ, Rathenau GW, Gorter EW, van Oosterhout G (1952) Ferroxdure, a class of new permanent magnet materials. Philips Tech Rev 13
4. Went JJ, Rathenau GW, Gorter EW, Van Oosterhout GW (1952) Hexagonal iron-oxide compounds as permanent-magnet materials [15]. Phys Rev 86:424–425. https://doi.org/10.1103/PhysRev.86.424.2
5. Snoek JL (1947) New developments in ferromagnetic materials: with introductory chapters on the statics and the dynamics of ferromagnetism, vol. 19
6. Pullar RC (2012) Hexagonal ferrites: A review of the synthesis, properties and applications of hexaferrite ceramics. Prog Mater Sci 57:1191–1334. https://doi.org/10.1016/j.pmatsci.2012.04.001
7. Srivastava R, Yadav BC (2012) Ferrite materials: introduction, synthesis techniques, and applications as sensors. Int J Green Nanotechnol Biomed 4:141–154. https://doi.org/10.1080/19430892.2012.676918
8. Kohan JA, Eckart DW (1971) SCIE NCE 172:519–525
9. Kamishima K, Mashiko T, Kakizaki K et al (2015) Synthesis and magnetic characterization of Sr-based Ni2X-type hexaferrite. AIP Adv 5. https://doi.org/10.1063/1.4934792
10. Mali A, Ataie A (2005) Structural characterization of nano-crystalline BaFe12O 19 powders synthesized by sol-gel combustion route. Scr Mater 53:1065–1070. https://doi.org/10.1016/j.scriptamat.2005.06.037
11. Sugimoto S, Haga K, Kagotani T, Inomata K (2005) Microwave absorption properties of Ba M-type ferrite prepared by a modified coprecipitation method. J Magn Magn Mater 290–291: PA:1188–1191. https://doi.org/10.1016/j.jmmm.2004.11.381
12. Fu YP, Lin CH (2005) Fe/Sr ratio effect on magnetic properties of strontium ferrite powders synthesized by microwave-induced combustion process. J Alloys Compd 386:222–227. https://doi.org/10.1016/j.jallcom.2004.04.148
13. Qiu J, Zhang Q, Gu M, Shen H (2005) Effect of aluminum substitution on microwave absorption properties of barium hexaferrite. J Appl Phys 98. https://doi.org/10.1063/1.2135412
14. Xu G, Ma H, Zhong M et al (2006) Influence of pH on characteristics of BaFe12O19 powder prepared by sol-gel auto-combustion. J Magn Magn Mater 301:383–388. https://doi.org/10.1016/j.jmmm.2005.07.014
15. Chen J, Wang Z, Cheng Z et al (2022) Investigation on the structural, magnetic, and dielectric properties of Ni2+–Zr4+ co-doped Y-type hexaferrite Ba2Ni2Fe12O22. J Mater Sci Mater Electron 33:16889–16898. https://doi.org/10.1007/s10854-022-08568-0
16. Nakamura T, Hankui E (2003) Control of high-frequency permeability in polycrystalline (Ba, Co)-Z-type hexagonal ferrite. J Magn Magn Mater 257:158–164. https://doi.org/10.1016/S0304-8853(02)00114-2
17. Malhi PS, Singh A, Singh M et al (2021) Enhanced magneto-dielectric response in La-doped Co2U hexaferrite. J Adv Dielectr 11
18. Mathews SA, Babu DR (2021) Analysis of the role of M-type hexaferrite-based materials in electromagnetic interference shielding. Curr Appl Phys 29:39–53. https://doi.org/10.1016/j.cap.2021.06.001
19. Ahmad M, Aen F, Islam MU et al (2011) Structural, physical, magnetic and electrical properties of La-substituted W-type hexagonal ferrites. Ceram Int 37:3691–3696. https://doi.org/10.1016/j.ceramint.2011.06.031
20. Pullar RC, Bhattacharya AK (2001) The synthesis and characterisation of Co2X (Ba2Co2Fe28O46) and Co2U (Ba4Co2Fe36O60) ferrite fibres, manufactured from a sol-gel process. J Mater Sci 36:4805–4812. https://doi.org/10.1023/A:1017947625940

21. Lisjak D, McGuiness P, Drofenik M (2006) Thermal instability of Co-substituted barium hexaferrites with U-type structure. J Mater Res 21:420–427. https://doi.org/10.1557/jmr.2006.0048
22. Lisjak D, Drofenik M (2003) Synthesis and characterization of Zn2U (Ba4Zn2Fe36O60) hexaferrite powder. J Appl Phys 93:8011–8013. https://doi.org/10.1063/1.1540159
23. Lisjak D, Makovec D, Drofenik M (2004) Formation of U-type hexaferrites. J Mater Res 19:2462–2470. https://doi.org/10.1557/JMR.2004.0317
24. Lisjak D, Drofenik M (2004) The thermal stability range and magnetic properties of U-type hexaferrites. J Magn Magn Mater 272–276:2003–2005. https://doi.org/10.1016/j.jmmm.2003.12.879
25. Snoek JL (2008) Scanning our past from the Netherlands: early investigations on ferrite magnetic materials. Proc IEEE 96:900–904. https://doi.org/10.1109/JPROC.2008.917767
26. Heiba ZK, Mohamed MB, Hamdeh HH, Ahmed MA (2015) Structural analysis and cations distribution of nanocrystalline Ni1-xZnxFe1.7Ga0.3O4. J Alloys Compd 618:755–760. https://doi.org/10.1016/j.jallcom.2014.08.241
27. Atiq S, Majeed M, Ahmad A et al (2017) Synthesis and investigation of structural, morphological, magnetic, dielectric and impedance spectroscopic characteristics of Ni-Zn ferrite nanoparticles. Ceram Int 43:2486–2494. https://doi.org/10.1016/j.ceramint.2016.11.046
28. Ditta A, Khan MA, Junaid M et al (2017) Structural, magnetic and spectral properties of Gd and Dy co-doped dielectrically modified Co-Ni (Ni0.4Co0.6Fe2O4) ferrites. Phys B Condens Matter 507:27–34. https://doi.org/10.1016/j.physb.2016.11.030
29. Jalaiah K, Vijaya Babu K (2017) Structural, magnetic and electrical properties of nickel doped Mn-Zn spinel ferrite synthesized by sol-gel method. J Magn Magn Mater 423:275–280. https://doi.org/10.1016/j.jmmm.2016.09.114
30. Vijaya Kumar K, Chandra Shekhar Reddy A, Ravinder D (2003) High-frequency dielectric behaviour of erbium substituted Ni-Zn ferrites. J Magn Magn Mater 263:121–126. https://doi.org/10.1016/S0304-8853(02)01544-5
31. Ali R, Khan MA, Manzoor A et al (2017) Investigation of structural and magnetic properties of Zr-Co doped nickel ferrite nanomaterials. J Magn Magn Mater 429:142–147. https://doi.org/10.1016/j.jmmm.2017.01.007
32. Wahba AM, Bakr Mohamed M (2015) Structural and magnetic characterization and cation distribution of nanocrystalline CoxFe3-xO4 ferrites. J Magn Magn Mater 378:246–252. https://doi.org/10.1016/j.jmmm.2014.10.164
33. Xie JL, Han M, Chen L et al (2007) Microwave-absorbing properties of NiCoZn spinel ferrites. J Magn Magn Mater 314:37–42. https://doi.org/10.1016/j.jmmm.2007.02.124
34. Dosoudil -Vladimír Olah R, (2001) Complex permeability spectra of Manganese-Zinc ferrite and its composite. J Electr Eng 52:24–29
35. Praveena K, Sadhana K, Bharadwaj S, Murthy SR (2010) Development of nanocrystalline Mn-Zn ferrites for forward type DC-DC converter for switching mode power supplies. Mater Res Innov 14:56–61. https://doi.org/10.1179/143307510X12599329343727
36. Issa B, Obaidat IM, Albiss BA, Haik Y (2013) Magnetic nanoparticles: surface effects and properties related to biomedicine applications. Int J Mol Sci 14:21266–21305. https://doi.org/10.3390/ijms141121266
37. Pardavi-Horvath M (2000) Microwave applications of soft ferrites. J Magn Magn Mater 215:171–183. https://doi.org/10.1016/S0304-8853(00)00106-2
38. Sonia, Kumari H, Suman S et al (2023) Spinel ferrites/metal oxide nanocomposites for waste water treatment. Appl Phys A
39. Patange SM, Shirsath SE, Jadhav SS, Jadhav KM (2012) Cation distribution study of nanocrystalline NiFe 2-xCr xO 4 ferrite by XRD, magnetization and Mössbauer spectroscopy. Phys Status Solidi Appl Mater Sci 209:347–352. https://doi.org/10.1002/pssa.201127232
40. Özgür Ü, Alivov Y, Morkoç H (2009) Microwave ferrites, part 1: Fundamental properties
41. Ünal B, Baykal A (2014) Effect of Zn substitution on electrical properties of nanocrystalline cobalt ferrite. J Supercond Nov Magn 27:469–479. https://doi.org/10.1007/s10948-013-2285-2

42. Wang Y, Wu X, Zhang W, Chen W (2016) Synthesis and electromagnetic properties of La-doped Ni-Zn ferrites. J Magn Magn Mater 398:90–95. https://doi.org/10.1016/j.jmmm.2015.09.044
43. Sugimoto M (1999) The past, present, and future of ferrites. J Am Ceram Soc 82:269–280. https://doi.org/10.1111/j.1551-2916.1999.tb20058.x
44. Soiński M, Magnetic materials in engineering
45. McHenry ME, Willard MA, Laughlin DE (1999) Amorphous and nanocrystalline materials for applications as soft magnets
46. Dobrzański LA, Drak M, Ziebowicz B (2007) New possibilities of composite materials application-Materials of specific magnetic properties. J Mater Process Technol 191:352–355. https://doi.org/10.1016/j.jmatprotec.2007.03.029
47. Jiles DC (2003) Recent advances and future directions in magnetic materials. Acta Mater 51:5907–5939. https://doi.org/10.1016/j.actamat.2003.08.011
48. M. Leonowicz (1998) Nanocrystalline magnetic materials

Chapter 2
Tuning of Structural, Electrical and Magnetic Properties of Ferrites

S. Bharadwaj and Y. Kalyana Lakshmi

Abbreviations

FWHM	Full width half maxima
N	Avogadro's number
O_h (B-site)	Octahedral site
T_h (A-Site)	Tetrahedral site
XRD	X-ray diffraction
T_C	Curie temperature
M_w	Molecular weight
M_s	Saturation magnetization
H_c	Coercivity
M_r	Remanence
FCC	Face-centered cubic structure
μ_B	Magnetic moment
ε'	Dielectric constant
ε''	Dielectric loss

S. Bharadwaj (✉)
Department of Physics, GITAM School of Science, GITAM (Deemed to Be University), Hyderabad, Telangana, India
e-mail: ba626k@gmail.com; bsomayaj@gitam.edu

Y. Kalyana Lakshmi
Department of Physics, University College of Science, Osmania University, Hyderabad, Telangana, India
e-mail: yklou@osmania.ac.in

P. Sharma et al. (eds.), *Engineered Ferrites and Their Applications*, Materials Horizons: From Nature to Nanomaterials, https://doi.org/10.1007/978-981-99-2583-4_2

1 Introduction

Ferrites are ferrimagnetic materials and possess high resistivity and exhibit superior dielectric and magnetic properties. Spinel ferrites are special subclass of ferrite family which possesses low eddy current, low dielectric losses and high Curie temperature (T_C) that can be operated under high-frequency range. The basic formula of ferrite is $X.Fe_2O_4$ where 'X' can be divalent or monovalent or trivalent ion, which balances according to the stoichiometry. Among spinel ferrites, soft ferrites are popular due to low coercivity and magnetic losses. Magnetic and electrical properties depend on processing steps such as synthesis and sintering temperatures, where the nature of dopant also plays dominant role in grain growth, refining the microstructure of the ferrite.

Although several thousands of papers were published in the field of ferrites, as reviewing all of them is not possible in current scope of chapter due to limited constraints of the proposed chapter, and hence, few ferrite's compositions were selected based on the commonality showing magnetic, electric and structural variation. Analysis of structural characteristics only limited to XRD and magnetic interpretations are confined to room temperature studies. Observation of electrical properties is discussed with respect to changes in resistivity and activation energies.

2 Structural Properties in Ferrites

XRD studies provide the initial basic information regarding the structure, phase purity and crystallinity of the as-prepared samples. A single phased ferrite possesses spinel and inverse spinel structure exhibiting (*hkl*) peaks at (220), (311), (400), (422), (511) and (440) with corresponding to 2θ of 31.6°, 37°, 44.1°, 55.4°, 59.1° and 65.1°, respectively. Any peaks appearing other than the primary peaks hints the presence of secondary phase. Usually, the secondary phase appears due to the unreacted elements or dissolution during the synthesis procedure. The crystal structure does not change its symmetry with the variation in synthesis, sintering or by doping at X or Fe site with trivalent or divalent ions. Using XRD data, as shown in Fig. 1, several parameters such as crystallite size, strain, lattice parameter (a), bond angle and length, a tentative distribution of iron ions in octahedral (O_h) and tetrahedral (T_h) sites can be determined.

2.1 Determination of Structural Parameters

The confirmation of crystal structure and the structural parameters can be obtained from the Rietveld refinement software such as FullProf, GSAS and MAUD. Most of the researchers prefer FullProf program [1], as it is an open source available for

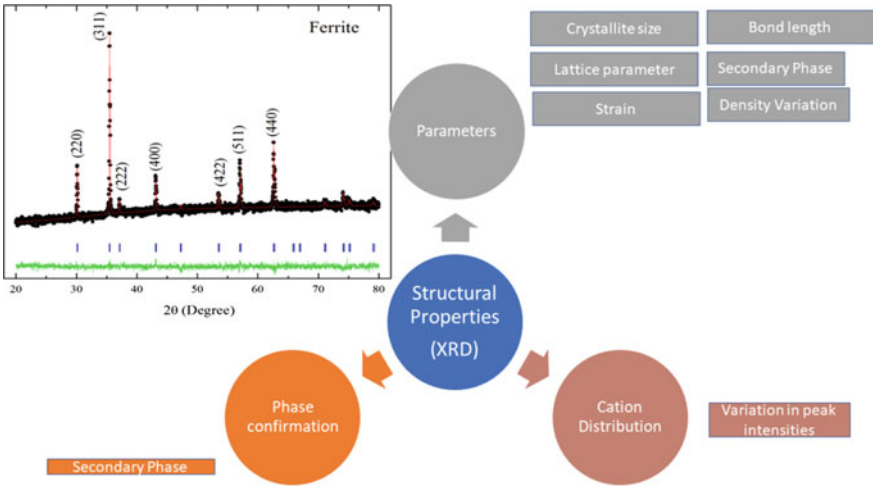

Fig. 1 Identifying structural properties through X-ray diffraction (XRD) in spinel ferrites. Inset is sample ferrite figure with proper indexing and undergone Rietveld refinement

refining the crystal structure of the samples. Goodness of fit (χ^2) value below 2 authenticates the quality of the Rietveld refinement. Using the information about Miller indices (*hkl*) and d-spacing (*d*), the lattice parameter (*a*) can be determined using the relation:

$$[d_{\text{cubic}}]_{\text{spinelferrite}} = \frac{a_{\text{cubic}}}{\sqrt{h^2 + k^2 + l^2}}. \tag{1}$$

The theoretical lattice parameter (a_{th}) could be further estimated using a [2, 3] a relation:

$$a_{\text{th}} = \frac{8}{3\sqrt{3}}\Big[(r_{\text{A}} + R_{\text{O}}) + \sqrt{3}(r_{\text{B}} + R_{\text{O}})\Big], \tag{2}$$

where R_{O} is the radius of the oxygen ion and the ionic radii of r_{A} and r_{B} sub-lattices are calculated using the relation:

$$\begin{aligned} r_{\text{A}} &= \sqrt{3}a_{\text{O}}(u - 0.25) - R_{\text{O}} \\ r_{\text{B}} &= a_{\text{O}}(0.625 - u) - R_{\text{O}}. \end{aligned} \tag{3}$$

2.2 X-ray Density

Obtained XRD data can be further used to calculate X-ray density (d_{xd}). The molecular weight of the compound (M_w), Avogadro's number ($N = 6.023 \times 10^{23}$) and the unit cell volume (V) (a^3) of the prepared sample are substituted to determine the X-ray density (d_{xd}) values, which can be calculated using the well-known relation [4]:

$$d_{\mathrm{xd}} = \left[\frac{8 \times M_{\mathrm{w}}}{N \times a^3}\right]. \tag{4}$$

The calculated values can be compared with the ones found experimentally from the mass (m), radius (r), thickness (h) and volume (V) of the sample using the relation which is as follows

$$d_{\mathrm{exp}} = \frac{m}{V} = \left[\frac{m}{\pi r^2 h}\right]. \tag{5}$$

Using density calculation, the porosity percentage can be calculated from the formula

$$P_{\mathrm{Ferr}}(\%) = \left[1 - \frac{d_{\mathrm{exp}}}{d_{\mathrm{xrd}}}\right] \times 100. \tag{6}$$

The hopping length can be further related to lattice parameter (a) and given as

$$\begin{aligned} L_{\mathrm{A-A}} &= \frac{a_{\mathrm{O}} \times \sqrt{3}}{4} \\ L_{\mathrm{A-B}} &= \frac{a_{\mathrm{O}} \times \sqrt{11}}{8} \\ L_{\mathrm{B-B}} &= \frac{a_{\mathrm{O}}}{2\sqrt{2}}. \end{aligned} \tag{7}$$

Furthermore, the cation distribution at various sites can be estimated from the XRD data by using Bertaut method [4, 5]. Intensities of any two *hkl* planes are considered in this method. Usually, the variations in the peak intensities of *hkl* (220) and (440) are used and also indicate the occupation of cations in tetrahedral and octahedral sites. The equation can be written as

$$\frac{I_{hkl}^{\mathrm{Obse}}}{I_{h'k'l'}^{\mathrm{Obse}}} = \frac{I_{hkl}^{\mathrm{calc}}}{I_{h'k'l'}^{\mathrm{calc}}}. \tag{8}$$

In the above equation, I_{hkl}^{Obse} are the intensities of the observed ones and $I_{h'k'l'}^{\mathrm{cal}}$ are the intensities of the calculated ones for any two considered peaks. For the calculation of the intensities for the chosen plane, Buerger's formula [6] has been adopted which

is as follows:

$$I_{h'k'l'} = |F|^2 \times P \times L_P$$
$$L_{\mathrm{P}} = \frac{1 + \cos^2 \theta}{\sin^2 \theta \cos \theta}. \tag{9}$$

Here, L_{P} is Lorentz polarization factor, 'F' is structure factor, and 'P' is multiplicity factor for any chosen plane. Profile fits show clear variation for different dopant ferrites [7].

2.3 Crystallite Size and Micro-Strain

The synthesis procedure adopted, sintering temperatures, soaking time, different dopant ions, concentration and presence of additives in the ferrite sample influence the crystallite sizes. Gaussian fitting can be used to determine FWHM obtained from XRD data which is then substituted as β in the Debye–Scherrer's formula [8], to determine the average crystallite size (D) of the samples, given by the relation:

$$D = \left[\frac{k \times \lambda}{\beta \times \cos \theta} \right]. \tag{10}$$

where 'k' is the shape factor, varies from material to material, and 'λ' is the wavelength. Generally, k value in spinel ferrite is around $0.8 \sim 0.9$. In addition to crystallite size, structural defects such as stacking faults, inter growths, twin boundaries and dislocations, can be preliminarily estimated using reflections obtained from XRD. These can be understood on the basis of strain (ε) which can be calculated using angle (θ) and β, given by relation:

$$\varepsilon = \left[\frac{\beta_{\mathrm{strain}}}{\tan \theta} \right]. \tag{11}$$

It is clear from Eqs. (10) and (11) that the D varies as $1/\cos\theta$ and ε depends on $1/\tan\theta$.

It is often ostensible that broadening between D and ε is generally summative, contributing to built-in of a Bragg peak. The dependencies of D and ε broadening effects laid to the separation of these effects in the analysis of Williamson and Hall (W–H) [9].

$$\beta_{hkl} = \beta_{\mathrm{strain}} + \beta \tag{12}$$

The W–H formula is also used to determine the crystallite size of a sample

$$\boldsymbol{\beta\cos\theta = \frac{0.89\lambda}{D} + 4\varepsilon\sin\theta} \tag{13}$$

In general, the determination of average crystallite size, the FWHM would be evaluated from prominent peaks. In ferrite compounds, (*hkl*) at (220), (311), (400) and (422) have the intense peaks. If $4\sin\theta$ is considered on *X*-axis and $\beta_{hkl}\cos\theta$ is along *Y*-axis, then the plot gives a straight line. Clearly, Eq. (13) can be used to estimate *D* and ε from the slope and intercept of linear fit. Ferrites with different dopant such as zinc, nickel, copper and cobalt were discussed to obtain the *D* and ε [7], whereas same is used in cobalt distribution in Ni–Zn ferrites [5] as given in Table 1.

The crystal structure of the spinal ferrites is cubic with Fd $\bar{3}$ m space group with $a = b = c = 0.832$–0.850 nm [2]. The synthesis conditions (method of synthesis, sintering temperature or soaking time), the dopant ions and their concentration both at divalent or iron ion site do not vary the crystal structure of the ferrite materials, as observed in Table 1. A change in the intensity, broadness of the peak and shifting of the peak positions are usually observed in the XRD results with the variation in any one of the above effects. For the ferrite samples sintered at lower temperatures, less soaking time and synthesizing the samples using solution-based techniques, a decrease in FWHM and an increase in the broadness of diffraction peaks are noticed and this information primarily confirms the lower crystallite of the samples. The effect of sintering temperature (600–1200 °C) of $Li_{0.5}Fe_{2.5}O_4$ was studied and found that the major diffraction peaks become sharper when particle size increases gradually from 26 to 70 nm with sintering temperature [2]. On the other hand, in the case of cobalt ferrites, an improvement in the density, i.e., from 75 to 95% along with a distinguished variation in the microstructure was reported [21] for different sintering temperatures and soaking time. In addition, a slight shift in the Bragg angles toward lesser angle side was also reported in the case of $CoFe_2O_4$ [21], and $CoFe_{2-x}Al_xO_4$ [13] ferrites with increasing sintering temperatures have a direct impact on the physical properties such as electrical, elastic and magnetic behavior of the ferrites.

As discussed, the dopant ion (divalent or iron site) and chemical composition also influence the structural properties of the ferrite system, which is evident from Table 1. Substitution of larger ions at X site in $X_{1-x}A_xFe_2O_4$ with divalent ion such as Zn^{2+} and Cd^{2+} results in shifting of Bragg's angles toward lower angle side and decreasing the intensity and particle size of the prepared samples [11, 15, 18, 22]. The lattice parameters increase linearly with dopant concentration, and this behavior is in agreement with Vegard's law [23] which also confirms the incorporation of dopant ion into the host lattice and expansion of crystal lattice [11]. Interestingly, a change in the crystal structure from spinal (Fd $\bar{3}$ m) to perovskite $\left(Pm\,\bar{3}\,m\right)$ was reported in Strontium (Sr)-doped cobalt ferrites, and with increasing in its concentration, a secondary phase belonging to CoC_2O_4 and N_2O_3 was observed [24]. Reports on Fe^{3+} site doping with various trivalent ions such as Ce^{3+}[15], Al^{3+} [25], Er^{3+} [18] and La^{3+} [14] in various ferrites also exhibit results almost similar to divalent doping. In some cases, i.e., secondary phases appear in the XRD data, and this could be due

Table 1 Structural factors in ferrites

Type of ferrite	Dopant value (x)	Synthesis methods	Sintering conditions	Lattice parameter (nm)	Crystallite size (nm)	Reference
Lithium ferrite		Ball milling method	800	0.832	27.41	[2]
			1000	0.833	69.58	
			1200	0.834		
$Li_{0.5}$ $Al_xFe_{2.5-x}O_4$	0	Citric gel auto-combustion method	800	0.832	41.67	[10]
	0.1			0.831	41.51	
	0.2			0.831	41.48	
$Ni_{1-x}Zn_xFe_2O_4$	0	Co-precipitation method	–	~ 0.834	16	[11]
	0.1			~ 0.835	18	
$Ni_{1-x}Cd_xFe_2O_4$	0.2	Sol–gel auto-combustion method	800	0.850	46	[12]
	0.4			0.836	48	
$Co_{0.5}Cd_{0.5}$ $Al_xFe_{2-x}O_4$	0	Co-precipitation method	900	0.836	54	[13]
	0.2			0.834	55	
	0.4			0.830	46	
$Mg_{0.5}Cd_{0.25}Cu_{0.25}Fe_{2-x}La_xO_4$	0	Co-precipitation method	850	0.850	26	[14]
	0.0125			0.849	29	
	0.025			0.851	32	
$Cu_{0.5}Cd_{0.25}$ $Co_{0.25}$ $Ce_xFe_{2-x}O_4$	0	Co-precipitation method	850	0.846	–	[15]
	0.0125			0.845	–	
	0.025			0.844		
$Co_{-x}Zn_xFe_2O_4$	0	Co-precipitation method	600	0.835	12	[16]
	0.1			0.837	13	

(continued)

Table 1 (continued)

Type of ferrite	Dopant value (x)	Synthesis methods	Sintering conditions	Lattice parameter (nm)	Crystallite size (nm)	Reference
	0.2			0.837	16	
Co Fe_2O_4	0	Co-precipitation method	–	0.837	16	[17]
$Co_{0.9}Nd_{0.1}Fe_2O_4$	0.1			0.840	17	
$Co_{0.9}Eu_{0.1}Fe_2O_4$	0.1			0.838	21	
$Co_{0.9}Gd_{0.1}Fe_2O_4$	0.1			0.841	22	
$Ni_{0.4}Co_{0.6}Er_xFe_{2-x}O_4$	0	Surface-assisted co-precipitation route	500	0.810	14.8	[18]
	0.015			0.812	14.8	
	0.03			0.795	14.9	
$NiFe_2O_4$	–	Solid-state reaction	1000	0.831	–	[19]
			1100	0.833		
			1150	0.835		
			1200	0.834		
$Co_{1-x}Zn_xFe_2O_4$	0	Combustion reaction method	900	0.837	37	[20]
	0.2			0.839	43	
	0.8			0.842	51	

to either dilution of trivalent ions in the iron ion site or inadequate synthesis steps or evaporation of certain elements during sintering stage.

3 Magnetic Properties in Ferrites

Ferrites are cost-effective magnetic ceramics which can be produced in large scale, providing the lowest magnetic strength and moderate energy with respect to permanent magnets. Ferrites are basically high resistive and show little corrosion under different environmental conditions. Some of these materials are best suited to work under high-temperature conditions, especially above 200 °C with minimum loss. During demagnetization, ferrite is resistive in nature, making them suitable to different motors and electric applications in different shapes or dimension.

Magnetic character of material is obtained from temperature and field-dependent magnetization studies. The hysteresis curve (M–H) reflects whether a sample is soft or hard magnetic material. Apart from the shape of the curve, magnetic properties such as saturation magnetization (M_s), coercivity (H_c) and remanence (M_r) can be assessed, preferable at room temperature. Here are the few listed points the researcher may consider while analyzing the magnetic behavior:

A. Under constant temperature condition, if the hysteresis shows broad leaf with high coercivity, then it is hard magnetic material. On other hand, if the leaf shows thin curve with faster saturation response with lower coercivity, then it is soft magnetic material.
B. Rate of increase of hysteresis curve indicates the domain response and ferromagnetic fraction in the sample. It also indicates whether the sample has superparamagnetic behavior or not.
C. Variation in M_s, M_r, M_r/M_s ratio and H_c for all the investigated samples can be obtained.
D. Make analysis on the basis of synthesis conditions, sintering temperatures and dopant concentration.
E. Other factors (influences are) such as grain size and anisotropic value are also be correlated with changes in M_s and H_c using theoretical equations.
F. Ratio of M_r/M_s indicates the interacting nature of the sample. If the values are less than 0.5, then it is non-interacting nature or else if the value > 0.5, then it is interacting nature [26].
G. To determine the nature of magnetic transition (Curie temperature), magnetization should be measured with varying temperature at constant applied field. At low temperature, magnetic curve slightly differs in path for zero field cooled (ZFC) and field cooled (FC), indicating the nature of crystallinity in the samples.

Variation in magnetic properties depends on the presence of metal ion in O_h–T_h site. The dopant metal ion can be dia/para/ferromagnetic in nature with different individual magnetic moments, ionic radii and its interaction with other metal ions. These exchange interactions among themselves via O^{2-} ions, give rise to magnetic moment

in sub-lattices of O_h–T_h sites and contribute to overall net magnetic moments. The net magnetic moment further depends on order of A–B, A–A and B–B interactions, but mostly attributed to the strongest A–B interaction. Furthermore, this interaction depends on bond angle and bond length. Generally, exchange interaction decreases with increase in bond length, whereas the strongest magnetic interaction is observed for A–B interaction with angle 180°. In general, spinel ferrite comprises octahedral site (B-site) in which metal ion is encircled by six oxygen ions and tetrahedral site (A-site) with four oxygen ions. Spinel ferrite has eight molecules in formula unit with $Fd\bar{3}m$ space group and has FCC. Altogether, there are 64 A-sites and 32 B-sites, combining 96 voids along with oxygen ion (O^{2-}). Among the total available sites, only eight A-site and 16 B-site are occupied by metal ions. Spinel matrix allows the smaller ionic radii cations to relocate from one site to another site. In view of the above, the magnetic properties [27] strongly depend on the nature of dopant in O_h–T_h sites, and equation for spinel ferrite could be written as

$$\left[X_{1-\delta}Fe_{\delta}\right]_{A-site}(X_{\delta}Fe_{2-\delta})_{B-site}O_4, \tag{14}$$

where 'δ' is degree of inversion, which dominates the cation distribution. Depending on the value of δ, the spinel ferrites are classified as normal ($\delta = 0$), inverse ($\delta = 1$) and mixed ($\delta = 0 \leftrightarrow 1$) ferrites. Among popular spinel ferrites, cobalt ferrite is classified as inverse, zinc ferrite as normal and magnesium ferrite as mixed. The preparation of normal and inverse ferrite depends on synthesis and sintering conditions, which is difficult to achieve with given interactions of metals ions. Nature of valency of dopant ions also contributes to occupancy in both sites. In case of trivalent ion dopant, T_h sites are occupied, whereas divalent ion occupies O_h site. For instance, the cobalt ferrite, a well-known inverse spinel ferrite, in which cobalt ion prefers toward octahedral site but literature also suggests that cobalt is also present at tetrahedral site in minor concentration [28], making it a mixed ferrite. Each ion has preference toward one site due to the energies (elastic, electrostatic and crystal field stabilization) and exchange interaction among those sites but also moves toward other site due to polarization effects. Smaller ionic radii elements have tendency to occupy tetrahedral site, resulting in minimum strain. The other factors which effect their distribution also depend on lattice energies, synthesis and sintering conditions which are variable. Overall, roadmap of tuning the magnetic properties can be understood from Fig. 2.

Neel's theory [29] on ferrite magnetism relates to summation of net magnetic moment in these individual sites and difference between O_h and T_h sites, which could be written as

$$M = |(M_B) - (M_A)|. \tag{15}$$

Thus, magnetism in ferrites arises from exchange mechanism among different spins aligned in a particular direction. If the direction of spins or domains is aligned uniformly in octahedral sites, then it can be presumed that sub-lattice results in higher magnetic moment. For any change in spin direction, there is an anti-alignment of

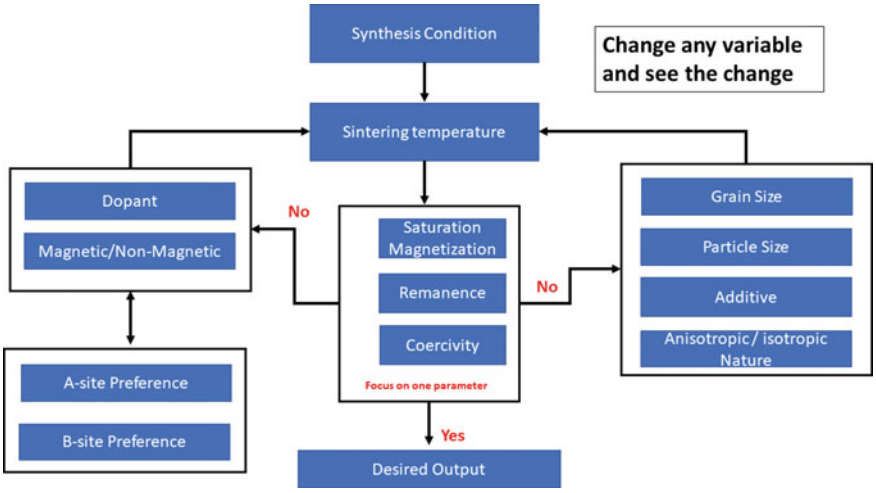

Fig. 2 Flowchart representing the tuning magnetic characters in spinel ferrites

domains, which results in negative exchange interaction, thereby lowering the net magnetic moment. Based on above discussion in terms of equation formed, it can be expressed as

$$\mu_B^{\text{Neel}} = \Big|\big([(x) \times \mu_B]_{1-x} + [(\text{Fe}) \times \mu_B]_y\big)_{\text{B-site}} \uparrow\uparrow - \big([(x) \times \mu_B]_x + [(\text{Fe}) \times \mu_B]_{2-y}\big)_{\text{A-site}} \downarrow\Big|. \tag{16}$$

Thus, occupancy of cation at various sub-lattices is one of the most important factors which decide the net magnetization in ferrites. Many reports show that individual magnetic moment depends on number of unpaired electrons in a dopant ion. Therefore, by choosing an appropriate ion and its concentration, one can tune the magnetic behavior for specific application. In case of zinc ferrite, zinc ion has no free electrons and has $\sim 0\mu_B$, whereas iron ion with Fe^{3+} has $\sim 5\mu_B$ (whereas) and Fe^{2+} has $\sim 4\mu_B$. In the case of zinc ferrite [30], magnetic properties not only depend on particle size but also on distribution of zinc ions. If Zn^{2+} occupies at A-site only, then the ferrite may show lower values. But if it occupies B-site in fraction, then M_s value may increase.

The magnitude of experimental magnetic moment in terms of Bohr magneton can be calculated using relation [31]:

$$\mu_B(\text{exp}) = \left[\frac{M_w \times M_s}{5585}\right], \tag{17}$$

where M_w is molecular weight of the respective ferrite used. The difference between Eq. (16) and Eq. (17) gives rise to value reflecting to canting effects [32, 33].

Magnetization is also dependent on density of the material, and this can be understood on the basis of equation:

$$M_s = \left[\frac{N \times d_{exp}}{M_w}\right]\left(\sum n_B - \sum n_A\right), \tag{18}$$

where is the 'd_{exp}' is the density of the material.

It can be corroborated from Table 2 that the value of M_s changes for different synthesis condition, sintering temperatures and substituted dopants. It has been reported that, as sintering temperature increases, there is increase in M_s values which was observed in the case of lithium ferrite [2] and nickel ferrite [19]. M_s value also differs for cobalt ferrite prepared through combustion method [20] and co-precipitation method [17]. Increase in M_s with sintering temperature has been attributed to grain growth and change in the anisotropy, whereas for synthesis condition, often it is related to change in density or the particle size. Along with preparation technique, other sintering techniques such as microwave sintering [34] could further improve the densification of ferrites resulting in enhanced magnetic properties.

Coercivity (H_c) is an important parameter, and based on its magnitude, it can be characterized as soft or hard magnetic material, which can be applicable in various magnetic applications. Anisotropy is one of the most important factors that contributes to magnetic properties. Coercivity (H_c) relation with anisotropy (K) and saturation magnetization (M_s) is given through the relation [35]:

$$H_c \sim \left[\frac{2K}{\mu_o M_s}\right]. \tag{19}$$

The anisotropy (K) is intern sensitive to grain/particle size and distribution of cations. The inclusion of particle size (d) with anisotropy could be related to equation [36, 37]:

$$K = K_{bu} + \left[\frac{6}{d}\right]K_{sur} \tag{20}$$

with 'K_{bu}' as bulk anisotropy and 'K_{sur}' as surface anisotropy. Here, anisotropy value may be different from magnetocrystalline anisotropy which is cumulative factor of the ions which are present in the system.

Variation in coercivity for lithium ferrite [2] or nickel ferrite [19] is attributed to changes in Ms or K. In case, the decrease of M_s and H_c, it could indicate the lower anisotropic nature of sample. Role of particle or crystallite size could also play determinable value in increasing anisotropic value as suggested using Eq. (19). Element doping in composition will have tendency to occupy B-site, A-site or both. Depending upon the preferential energies, cation distribution in both the sites will vary, influencing net magnetization. It is known that as grain size increases with increase in sintering temperature, it in turn increases the number of domain walls. Due to reordering in domain wall, magnetization and demagnetization effects in

Table 2 Magnetic properties in ferrites

Type of ferrite	Dopant value (x)	Synthesis methods	Sintering conditions (°C)	Saturation magnetization (emu/g) (M_s)	Coercivity (Hc) (Oe/Tesla)	Reference
Lithium ferrite		Ball milling method	800	76.55	38.12	[3]
			1000	79.56	8.41	
			1200	84.86	2.25	
$Li_{0.5}\ Al_xFe_{2.5-x}O_4$	0	Citric gel auto-combustion method	800	~ 52		[10]
	0.1			~ 47		
	0.2			~ 45		
$Ni_{1-x}Zn_xFe_2O_4$	0	Co-precipitation method	–	19	–	[11]
	0.1			22		
$Ni_{1-x}Cd_xFe_2O_4$	0.2	Sol–gel auto-combustion method	800	97	13	[12]
	0.4			94	19	
$Co_{0.5}Cd_{0.5}\ Al_xFe_{2-x}O_4$	0	Co-precipitation method	900	56	1288 Oe	[13]
	0.2			–	–	
	0.4			31	349	
$Mg_{0.5}Cd_{0.25}Cu_{0.25}Fe_{2-x}La_xO_4$	0	Co-precipitation method	850	19	793 Oe	[14]
	0.0125			19	780 Oe	
	0.025			22	768 Oe	
$Cu_{0.5}Cd_{0.25}\ Co_{0.25}\ Ce_xFe_{2-x}O_4$	0	Co-precipitation method	850	29	675	[15]
	0.0125			36	653	
	0.025			44	529	
$Co\ Fe_2O_4$	0	Co-precipitation method	–	61	440	[17]

(continued)

Table 2 (continued)

Type of ferrite	Dopant value (x)	Synthesis methods	Sintering conditions (°C)	Saturation magnetization (emu/g) (M_s)	Coercivity (Hc) (Oe/Tesla)	Reference
$Co_{0.9}Nd_{0.1}Fe_2O_4$	0.1			45	336	
$Co_{0.9}Eu_{0.1}Fe_2O_4$	0.1			51	383	
$Co_{0.9}Gd_{0.1}Fe_2O_4$	0.1			57	416	
$Ni_{0.4}Co_{0.6}Er_xFe_{2-x}O_4$	0	Surface-assisted co-precipitation route	500	35	160	[18]
	0.015			41	400	
	0.03			45	200	
$NiFe_2O_4$	–	Solid-state reaction	1000	42	76	[19]
			1100	44.3	41.4	
			1150	45.5	6.2	
			1200	46.5	5.02	
$Co_{1-x}Zn_xFe_2O_4$	0	Combustion reaction method	900	56	500	[20]
	0.2			47	250	
	0.8			2	–	

sample require less energy, decreasing the coercivity. Nature of dopant influences the sintering temperature, coercivity, saturation magnetization and grain size. When aluminum [10] is substituted in lower concentration at $x = 0.1$, the M_s value decreases drastically, whereas when the concentration increases to $x = 0.2$, M_s value decreases by small value. Same phenomenon is observed for cadmium [12] and zinc [11]. As zinc is diamagnetic, high concentration of zinc in cobalt ferrite [20] could decrease magnetization immensely. Rare-earth metals should be doped in lower concentration due to higher ionic radii. Generally, rare-earth metals are doped in iron ion as to compactable ionic radii and should occupy B-site or octahedral sites. These are rare-earth magnetic moment varied from 0 to 10 μ_B and are costly but show interesting characteristics. Different rare-earth metals doping in cobalt ferrite [17] clearly shows variation for M_s and H_c, clearly indicating role of anisotropy. Lanthanum (L_a) doped in complex Mg–Cd–Cu ferrite [14] shows no changes, whereas erbium (E_r) in Ni–Co ferrite [18] shows systematic increase in M_s values. Hence, it can be said the magnetic properties of spinel ferrites depend mainly on crystal structure, domains, grain size, particle size, density and electronic structure of individual atoms. In addition to these factors, distance and angle between adjacent atoms along with the magnitude of magnetic moments play determinantal role in moderating magnetic properties.

4 Electrical Properties in Ferrites

Ferrites have important role in design and development of materials, especially in electromagnetic interference (EMI) detection device. Ferrites are often used as beads, chokes and inductors, but these functionalities deviate at higher frequency. In addition to EMI, extension of ferrites to microwave devices, transformers and biomedical applications marks them as an important material.

Presence of ferrite core enables suppression of unwanted signal and purging the noise, generated via electromagnetic interference. Mere presence of ferrite acts as inductor in toroid shape providing impedance on the basis of Faraday's law. As ferrite is having moderate to high resistance, providing high impedance at lower frequencies and as the frequency increases, capacitive nature of ferrite drops and only resistive is present. In addition, the ferrites also dissipate lot of heat which is being absorbed at different frequencies. Although the operating temperature range of ferrite is very high, the aspects of Curie temperature (T_c) have to be taken care while designing the application. Hence, resistance is a vital parameter in characterizing the transport properties which gives important information on tailoring a material based on specific applications. Transport properties provide insight about localized and hopping mechanism of charge carriers, etc.

Electrical resistance in ferrites can be measured as described below:

1. The temperature-dependent resistance is measured either using two probes or preferably four-probe method with a highly sensitive nano/pico-ammeter and voltmeter. The data will be collected by measuring the current with temperature

by maintaining a constant voltage across the ferrite sample. Here, the magnitude of resistance indicates the intrinsic nature of the ferrite and depends on several factors such as composition, sintering condition, synthesis methods, porosity, grain size and grain boundary as similar to magnetic and structural properties.

2. The resistivity can be calculated using the formula

$$\rho = \left[\frac{R \times A}{L}\right] \Omega.\text{m}, \tag{21}$$

where 'A' is equivalent to area of the sample and 'L' is the measured thickness of the sample. Here, radius and thickness of the sample play a vital role in determining the resistivity of the sample, and hence, proper care should be taken while measuring them.

3. The resistivity (ρ) or conductivity (σ) behavior with temperature can be analyzed using Arrhenius relation [38]:

$$\rho = \rho_0 \exp^{(E_a / K_B T)} \tag{22}$$

$$\sigma = \sigma_o e^{\left[-\frac{E_a}{K_B T}\right]}. \tag{23}$$

'E_a' is the activation energy, 'K_B' is the Boltzmann constant, ρ is the resistivity (or σ conductivity), and ρ_o (σ_o) is the resistivity (conductivity) value at 0 K. Temperature-dependent resistivity shows a trend of exponential decrease in resistivity with increase in temperature, confirming the semiconducting nature. As the temperature increases, a kink is observed in graph at ferromagnetic to paramagnetic behavior, indicating T_c in ferrites.

Under the influence of temperature conditions, the ability of electron to jump or move from one site to another site improves its mobility and lowering their resistivity. Therefore, while understanding the concept of electrical properties, one has to keep in mind about lattice deformation, activation energies and energy gap of different dopants substituted in the ferrite compound (stoichiometric formula). In addition to this, higher sintering temperature promotes densification and reduction in porosity, improving conductivity and lowering the activation energy. It can be said that ordered sample possesses higher resistive nature when compared to disordered sample. Thus, synthesis and sintering conditions also play vital role in determining the nature of the sample and acquire tuning to its optimum efficiency, and these factors are summarized in Fig. 3.

With measurement of resistivity, one can calculate the number of charge carriers and mobility in any semiconducting material. Furthermore, the activation energy (E_a) is obtained from the slope of T^{-1} versus lnρ plots. The variation of activation energy occurs due to different dopants substitution at various sites, hopping of charge carriers and the energy gap between conduction-valence bands. Value of E_a in ferromagnetic is less than paramagnetic region, which reflects the spin ordering behavior in material

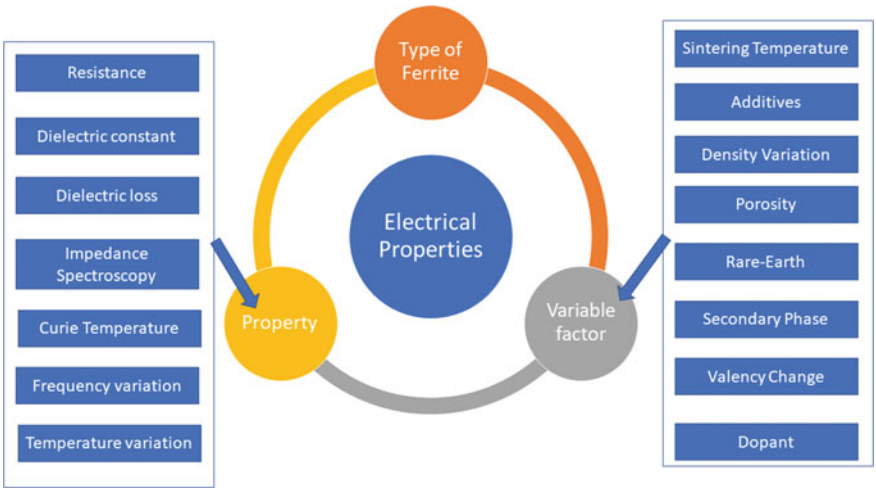

Fig. 3 Tuning electrical properties in spinel ferrites

and also a change in band gap. The temperature variation in most of the ferrites is systematic, and generally carrier concentration is mostly unaffected in different temperature zones.

In ferrites, the electrical properties depend on the localized charge carriers which are surrounded by different oxygen ions at octa-tetrahedral sub-lattices. Hence, stoichiometric value of oxygen plays vital role and free electrons are mostly bonded to their respective positions. Different models related to electrical resistivity were discussed [39], but mostly discussed are the hopping mechanism of electron in different localized states, polaron and thermally activated mechanism. Depending on the type of ferrite, the bonding of electron in the localized states varies, which further vary the magnitude of resistance or resistivity. Furthermore, the presence of ferrous or ferric ions in octa-tetrahedral sites also determines the value of resistivity. Under thermal agitated or applied frequency conditions, the electrons can move within or among the sites of octa-tetrahedral sites, which results in a change in energy state. A change in energy state results in type of charge carriers. In case of mixed ferrites, the two transition regions in resistivity versus temperature plots clearly point to n-type with excess of cations and p-type behavior with deficient ions. In mixed ferrites, it is known that dopant X and dopant Fe occupy both octa-tetrahedral sites in different stoichiometric ratios which further depend on synthesis and sintering conditions. Multiple dopants could further hinder the movement of electrons due to difference in their energy levels and thus increasing the resistivity values. The concept of Verwey mechanism [12] allows us to understand the hopping mechanism with different lengths between octa-octa, octa-tetra and tetra-tetrahedral sites [40]. With the presence of iron ion and other dopant in particular site, the hopping mechanism of electrons among similar states could result in formation of 2+ states or 3+ states among the states which are randomly distributed in crystallographic sites and

could be written as

$$\begin{aligned} Fe^{2+} &\rightleftarrows Fe^{3+} + e^{-} \\ D^{2+} &\rightleftarrows D^{3+} + e^{-}. \end{aligned} \tag{24}$$

In the view of the above, it has been that as sintering temperature increases, resistance decreases in case of nickel ferrite [19]. The activation energy increases initially and then decreases in case of lithium ferrite [2]. But in case of nickel ferrite [19], activation energy decreases with increase in sintering temperature, clearly suggesting the role of dopant at B-site. On comparison of nickel [19] and lithium ferrite [2], nickel may occupy A- and B-site depending on concentration, but in case of lithium ferrite, lithium prefers B-site. As sintering temperature increases, there is possibility of evaporation of lithium, which induces the transformation of $Fe^{3+} \rightarrow Fe^{2+}$ causing a change in bond length in sub-lattices. A–B bond length is greater than B–B, A–A, and among them A–A hopping does not take place. Activation energy or resistance depends on ability of the mobility of charge carriers instead of carrier concentration. Most of the charge carrier accumulates near grain boundaries, which further depends on grain size, which in turn depends on sintering temperature. Depending on the nature of dopant, resistance varies which could be observed from Ni–Zn ferrite [11]. Doping rare-earth metals result in increase in resistance as observed from Table 3. Higher concentration of cesium (Ce) resulted in decrease in resistivity [15], and same is observed for Erbium (Er) [18] and lanthanum (La) [27] substitution in ferrite matrix.

Since ferrites have high resistance, they also exhibit good dielectric constant and low dielectric loss as function of temperature and frequency, making them suitable material till date. Dielectric value gives fundamental information of a material under applied field (E). As availability of free electrons is less, they exhibit high resistances under the application of applied field, and polarization (P) of charges occurs. These charges may accumulate in intra–inter-grain or grain boundaries, contributing to dielectric constant (ε'). From application point of view, ferrite operating under high applied electric field should retain the dielectric nature, even when field is reversed. If a material is unable to withstand at a particular frequency, then value at that field is called dielectric loss (ε''). Hence, it is often desirable to measure resistance and dielectric nature of material at different temperature and frequency ranges. Although, the resistance can be measured at room temperature by applying direct current (D.C), it can be also measured at alternating frequency. Dielectric constant and dielectric loss measured at different frequency ranges could also be referred as impedance spectroscopy. Impedance spectroscopy studies include capacitance and inductor reactance along with resistance of sample. The aspects of dielectric nature and impedance spectroscopy could not be covered in present context of the chapter.

Table 3 Basic electrical properties in ferrites

Basic compound	Dopant (x)	Synthesis method	Sintering Condition (°C)	Resistivity (Ω cm)/Conductivity (μS/cm)	Activation Energy (eV)	Curie Temperature (T_C)	Reference
$Li_{0.5}Fe_{2.5}O_4$	–	Ball milling	800	–	0.83	–	[2]
			1000		0.86		
			1200		0.71		
$Ni_{1-x}Zn_xFe_2O_4$	0	Co-precipitation method		10 μS/cm			[11]
	0.1			26 μS/cm			
$Ni_{1-x}Cd_xFe_2O_4$		Sol–gel auto-combustion method	800		0.38	860	[12]
					0.21	797	
$Co_{0.5}Cd_{0.5}$ $Al_xFe_{2-x}O_4$	0	Co-precipitation method	900		0.928	598	[13]
	0.2				0.792	583	
	0.4				0.789	548	
$Mg_{0.5}Cd_{0.25}Cu_{0.25}Fe_{2-x}La_xO_4$	0	Co-precipitation method	850	2.67×10^4	0.005		[14]
	0.012			8.94×10^3	0.0165		
	0.025			7.95×10^4	0.004		
$Cu_{0.5}Cd_{0.25}$ $Co_{0.25}$ $Ce_xFe_{2-x}O_4$	0	Co-precipitation method	850	9.9×10^7	0.40	373	[15]
	0.0125			9.7×10^7	0.15	373	
	0.025			5.2×10^7	0.30	373	
$Ni_{0.4}Co_{0.6}Er_xFe_{2-x}O_4$	0	Surface-assisted co-precipitation route	500	6.20×10^7	–	–	[18]
	0.015			1.93×10^7			
	0.03			1.36×10^7			

(continued)

Table 3 (continued)

Basic compound	Dopant (x)	Synthesis method	Sintering Condition (°C)	Resistivity (Ω cm)/Conductivity (μS/cm)	Activation Energy (eV)	Curie Temperature (T_C)	Reference
$NiFe_2O_4$	–	Solid-state reaction	1000	2.43×10^6	0.52		[19]
			1100	1.32×10^6	0.39		
			1150	0.58×10^6	0.35		
			1200	0.3×10^6	0.28		

5 Conclusion

The main objective of tuning magnetic and electrical properties in ferrites is to enhance the properties pertaining specific application. Selection of dopant ions, suitable synthesis techniques, sintering conditions and presence of additives play a vital role in improving the properties of ferrites. Due to the above condition, particle/grain size, phase formation and distribution of cations at different sites also contribute to the properties. Hence, all the above factors have to be taken into consideration in optimizing the performance of ferrite for wider applications.

References

1. Rodríguez-Carvajal J (2001) Fullprof. CEA/Saclay, France
2. Mazen SA, Abu-Elsaad NI (2015) Structural, magnetic and electrical properties of the lithium ferrite obtained by ball milling and heat treatment. Appl Nanosci 5:105–114. https://doi.org/10.1007/s13204-014-0297-2
3. Mazen SA, Abdallah MH, Sabrah BA, Hashem HAM (1992) The effect of titanium on some physical properties of CuFe2O4. Phys Status Solidi (A) Appl Mater Sci 134:263–271. https://doi.org/10.1002/pssa.2211340123
4. Weil L, Bertaut F, Bochirol L (1950) Propriétésmagnétiques et structure de la phase quadratique du ferrite de cuivre. J Phys Radium 11:208–212. https://doi.org/10.1051/jphysrad:01950001105020800
5. Chintala JPK, Bharadwaj S, Varma MC, Choudary GSVRK (2022) Impact of cobalt substitution on cation distribution and elastic properties of Ni–Zn ferrite investigated by X-ray diffraction, infrared spectroscopy, and Mössbauer spectral analysis. J Phys Chem Solids 160:110298. https://doi.org/10.1016/j.jpcs.2021.110298
6. Buerger MJ (1960) Crystal structure analysis. Wiley, New York
7. Vara Prasad BBVS, Ramesh KV, Srinivas A (2017) Structural and magnetic studies of nanocrystalline ferrites MFe2O4 (M= Zn, Ni, Cu, and Co) synthesized via citrate gel autocombustion method. J Supercond Nov Magn 30:3523–3535. https://doi.org/10.1007/s10948-017-4153-y
8. Cullity BD (1956) Elements of X-ray diffraction. Addison-Wesley Publishing
9. Williamson GK, Hall WH (1953) X-ray line broadening from filed aluminium and wolfram. Acta Mater 1:22–31. https://doi.org/10.1016/0001-6160(53)90006-6
10. Dar MA, Batoo KM, Verma V, Siddiqui WA, Kotnala RK (2010) Synthesis and characterization of nano-sized pure and Al-doped lithium ferrite having high value of dielectric constant. J Alloys Compd 493(1–2):553–560. https://doi.org/10.1016/j.jallcom.2009.12.154
11. Anu K, Hemalatha J (2022) Synthesis and analysis of structural, compositional, morphological, magnetic, electrical and surface charge properties of Zn-doped nickel ferrite nanoparticles. Ceram Int 48:3417–3425. https://doi.org/10.1016/j.ceramint.2021.10.118
12. Devmunde BH, Raut AV, Birajdar SD, Shukla SJ, Shengule DR, Jadhav KM (2016) Structural, electrical, dielectric, and magnetic properties of Cd2. J Nanoparticle Res. https://doi.org/10.1155/2016/4709687
13. Zaki HM, Al-Heniti SH, Aljwiher MM (2020) Synthesis, structural, magnetic and dielectric studies of aluminum substituted cobalt-copper ferrite. Phys B Condens Matter 597:412382 (2020). https://doi.org/10.1016/j.physb.2020.412382
14. Arshad MI, Hasan MS, Rehman AU, Akhtar M, Amin N, Mahmood K, Ali A, Trakoolwilaiwan T, Thanh NTK (2022) Structural, optical, electrical, dielectric, molecular vibrational and

magnetic properties of La3+ doped Mg–Cd–Cu ferrites prepared by Co-precipitation technique. Ceram Int 48(10):14246–14260. https://doi.org/10.1016/j.ceramint.2022.01.313
15. K.Hussain, N.Amin, M.I. Arshad, Evaluation of structural, optical, dielectric, electrical, and magnetic properties of Ce3+ doped Cu0.5Cd0.25Co0.25Fe2-xO4 spinel nano-ferrites. *Ceram. Int. 47*, 3401–3410 (2021). https://doi.org/10.1016/j.ceramint.2020.09.185
16. Gul HI, Abbasi AZ, Amin F, Anis-ur-Rehman M, Maqsood A (2007) Structural, magnetic and electrical properties of Co {sub 1-}{sub x} Zn {sub x} Fe {sub 2} O {sub 4} synthesized by co-precipitation method. J Magn Magn Mater 311. https://doi.org/10.1016/j.jmmm.2006.08.005
17. Amiri S, Shokrollahi H (2013) Magnetic and structural properties of RE doped Co-ferrite (REåNd, Eu, and Gd) nano-particles synthesized by co-precipitation. J Magn Magn Mater 345:18–23. https://doi.org/10.1016/j.jmmm.2013.05.030
18. Warsi MF, Iftikhar A, Yousuf MA, Sarwar MI, Yousaf S, Haider S, Aboud MFA, Shakir I, Zulfiqar S (2020) Erbium substituted nickel–cobalt spinel ferrite nanoparticles: Tailoring the structural, magnetic and electrical parameters. Ceram Int 46:24194–24203. https://doi.org/10.1016/j.ceramint.2020.06.199
19. Zabotto FL, Gualdi AJ, Eiras JA, Oliveira AJAD, Garcia D (2012) Influence of the sintering temperature on the magnetic and electric properties of NiFe2O4 ferrites. Mater Res 15:428–433. https://doi.org/10.1590/S1516-14392012005000043
20. Fonseca SGC, Neiva LS, Bonifácio MAR, Santos PRCD, Silva UC, Oliveira JBLD (2018) Tunable magnetic and electrical properties of cobalt and zinc ferrites CO 1-x Zn x Fe 2 O 4 synthesized by combustion route. Mater Res 21. https://doi.org/10.1590/1980-5373-MR-2017-0861
21. Albalah MA, Alsabah YA, Mustafa DE (2020) Characteristics of co-precipitation synthesized cobalt nanoferrites and their potential in industrial wastewater treatment. SN Appl Sci 2:1–9. https://doi.org/10.1007/s42452-020-2586-6
22. Anu K, Hemalatha J (2019) Magnetic and electrical conductivity studies of zinc doped cobalt ferrite nanofluids. J Mol Liq 284:445–453. https://doi.org/10.1016/j.molliq.2019.04.018
23. Vegard L (1921) Diekonstitution der mischkristalle und die raumfüllung der atome. Z Phys 5:17–26. https://doi.org/10.1007/BF01349680
24. Mir A, Qadeer M, Waqas R, Khan SN (2020) Study of morphological, optical and microwave properties of strontium-doped cobalt ferrites. J Electron Mater 49:4801–4808. https://doi.org/10.1007/s11664-020-08212-9
25. Rahman MM, Hasan N, Hoque MA, Hossen MB, Arifuzzaman M (2022) Structural, dielectric, and electrical transport properties of Al3+ substituted nanocrystalline Ni-Cu spinel ferrites prepared through the sol-gel route. Results Phys 105610. https://doi.org/10.1016/j.rinp.2022.105610
26. Muthuselvam IP, Bhowmik RN (2010) Mechanical alloyed Ho3+ doping in CoFe2O4 spinel ferrite and understanding of magnetic nanodomains. J Magn Magn Mater 322:767–776. https://doi.org/10.1016/j.jmmm.2009.10.057
27. Mane RS, Jadhav V (eds) (2020) Spinel ferrite nanostructures for energy storage devices. Elsevier. https://doi.org/10.1016/B978-0-12-819237-5.00003-1
28. Rao KS, Kumar AM, Varma MC, Choudary GSVRK, Rao KH (2009) Cation distribution of titanium substituted cobalt ferrites. J Alloys Compd 488:L6–L9. https://doi.org/10.1016/j.jallcom.2009.08.086
29. Néel L (1984) Magnetic properties of ferrites: ferrimagnetism and antiferromagnetism. Phys Chem Earth Sci 31:18. https://hal.archives-ouvertes.fr/hal-03070529/document
30. Chinnasamy CN, Narayanasamy A, Ponpandian N, Chattopadhyay K, Guerault H, Greneche JH (2000) Magnetic properties of nanostructured ferrimagnetic zinc ferrite. J Condens Matter Phys 12:7795. https://doi.org/10.1088/0953-8984/12/35/314
31. Bhukal S, Namgyal T, Mor S, Bansal S, Singhal S (2012) Structural, electrical, optical and magnetic properties of chromium substituted Co–Zn nanoferrites Co0. 6Zn0. 4CrxFe2− xO4 ($0 \leqslant x \leqslant 1.0$) prepared via sol–gel auto-combustion method. J Mol Struct 1012:162–167. https://doi.org/10.1016/j.molstruc.2011.12.019

32. Smart JS (1955) The Néel theory of ferrimagnetism. Am J Phys 23:356–370. https://doi.org/10.1119/1.1934006
33. Varma MC, Bharadwaj S, Babu KV (2019) Observation of anomalous site occupancy in Ni-Co-Cu-Cr ferrite system synthesized by sol-gel method. Physica B Condens 556:175–182. https://doi.org/10.1016/j.physb.2018.12.002
34. Bharadwaj S, Ramesh T, Murthy SR (2013) Fabrication of microinductor using Nanocrystalline NiCuZn ferrites. J Electroceramics 31:81–87. https://doi.org/10.1007/s10832-013-9799-7
35. Aharoni A (2000) Introduction to the theory of ferromagnetism, vol 109. Clarendon Press
36. Shirsath SE, Liu X, Yasukawa Y, Li S, Morisako A (2016) Switching of magnetic easy-axis using crystal orientation for large perpendicular coercivity in CoFe2O4 thin film. Sci Rep 6:1–11. https://doi.org/10.1038/srep30074
37. Limaye MV, Singh SB, Date SK, Kothari D, Reddy VR, Gupta A, Sathe V, Choudhary RJ, Kulkarni SK (2009) High coercivity of oleic acid capped CoFe2O4 nanoparticles at room temperature. J Phys Chem B 113:9070–9076. https://doi.org/10.1021/jp810975v
38. Smith J, Wijn HPJ (1959) Ferrites. Wiley Inc, New York, p 229
39. Viswanathan B, Murthy VRK (eds) (1990) Ferrite materials: science and technology. Springer Verlag, pp 26–27
40. Barkule RS, Kurmude DV, Raut AV, Waghule NN, Jadhav KM, Shengule DR (2014) Structural and electrical conductivity studies in nickel ferrite nano-particles. Solid State Phenom 209:177–181. https://doi.org/10.4028/www.scientific.net/SSP.209.177

Chapter 3
Advances in the Processing of Ferrite Nanoparticles

Ankush Thakur and Sunanda Sharda

1 Introduction

Since the discovery of ferrites by Philips in 1950s have attracted the intention for the applications of recording media, permanent magnets, plasto ferrites, drug delivery agent, biomedical, sensors, wastewater treatment, medical diagnosis, biocompatible magnetic nanoparticles for cancer treatment, high-frequency devices, electromagnetic wave absorbers, and microwave devices because of high magnetization, coercivity, large magnetocrystalline anisotropy, and corrosion resistivity. Ferrites have high positive susceptibility value that becomes the useful characteristic for their operation in high-frequency power supplies [1–3]. The magnetic and thermal stability helps the data storage industry for the fabrication of hard drive, secure digital card, and disk. Electronic industry also fruited from the ferrites in designing of antennas, microwave devices, and inductor core owing to temperature varied coercivity. Soft/hard magnetic characteristics of ferrites have attracted the interest of manufacturers as a permanent magnet. Tunable alteration in electromagnetic properties makes them suitable for high-frequency device and microwave absorbing materials [4]. With rise in industry, atmospheric pollution became the challenging task for scientific community as well as the safety in industry and environmental sectors became the key factor to tackle the problem in better way. The responsible behavior of ferrites in respect to their properties when it comes in contact with an analyte concentration makes them suitable for gas-sensing technology. Abd-Elkader et al. [5] have deliberated that the gas-sensing efficiency of ferrites is observed from their microstructural properties and further these properties are dependent upon synthesis route. The low-cost designing along with high stability, faster response, and recovery

A. Thakur (✉)
Department of Physics, Lovely Professional University, Phagwara, India
e-mail: ankush9888@gmail.com

S. Sharda
Department of Physics, Faculty of Sciences, SGT University, Gurugram, Haryana, India

P. Sharma et al. (eds.), *Engineered Ferrites and Their Applications*, Materials Horizons: From Nature to Nanomaterials, https://doi.org/10.1007/978-981-99-2583-4_3

time makes them sensitive for variety of gases. There are six types of hexaferrite such as $SrFe_{12}O_{19}$ (M-type), $SrMe_2Fe_{16}O_{27}$ (W-type), $SrMe_2Fe_{12}O_{22}$ (Y-type), $Sr_2Me_2Fe_{28}O_{46}$ (X-type), $Sr_2Me_2Fe_{24}O_{41}$ (Z-type), and $Sr_4Co_2Fe_{36}O_{60}$ (U-type). M-type hexaferrite has paramount benefits over the other. In M-type hexaferrite, most of the research was carried out on Sr, Ba, and Pb because of their excellent chemical, mechanical, and thermal stabilities. In M-type hexaferrite, Fe^{3+} ions are distributed over five different crystallographic sites, viz. three octahedral (12 k, 2a, $4f_2$), one tetrahedral ($4f_1$), and one trigonal bipyramidal (2b). The parallel (12 k, 2a, $4f_2$) and anti-parallel ($4f_1$, $4f_2$) crystallographic sites are coupled with O^{2-} anions to obtain ferrimagnetic order and super-exchange interaction between Fe^{3+}–O^{2-}–Fe^{3+}. The magnetic characteristics of ferrite can be easily tuned by substituting the cations on iron sites. Most of the research work has been carried out to improve intrinsic magnetic characteristic by substituting the cations at Sr^{2+}, Ba^{2+}, Pb^{2+} ions, and/or Fe^{3+} ions in host lattice with La^{3+}, Gd^{3+}, Sm^{3+}, Ce^{3+}, Al^{3+}, Nd^{3+}, Ho^{3+}, Co^{2+}, Ni^{2+}, Cu^{2+}, Zn^{2+}, and Ti^{4+}, etc. The substitution of metal ions or rare earth elements in host lattice plays a vital role to produce optimal properties because of their solubility [6–9]. Generally, magnetite and hematite were appeared as main secondary phases, and even the mixture of stoichiometric compound leads the formation of intermediate phases that is why the knowledge of the desired methodology leads the industry to gain advantage of wide range. Moreover, the substitution of smaller or larger ionic radii in host creates discrepancy in lattice which leads in the alteration of properties. Narang et al. [10] have highlighted that high resistivity, high stability, and high microwave magnetic loss make ferrite as a suitable candidate for the preparation of microwave absorbing materials. Thus, it is an effective way to tune electrical, dielectric, morphological, and magnetic properties after incorporating dopant ions in desired crystallographic sites by using different method of synthesis. Tremendous efforts have been made to enhance their electrical, dielectric, and magnetic capabilities for futuristic demands in electrical, electronic, and medical by using different synthesis route. Crystallographic sites are sole responsible for the improvement of structural, morphological, electrical, dielectric, and magnetic properties ferrites and that help in the development of advanced ultrafine nanoparticles. Various processing techniques have been proposed, viz. solid-state reaction, sol–gel method, co-precipitation method, hydrothermal method, solvothermal method, citrate precursor method, reverse micelle method, sonochemical method, aerosol spray pyrolysis method, auto-combustion method, green synthesis for the preparation of ferrites to make co-relation between substitution, and their effect on structural, morphological, electrical, dielectric, and magnetic properties. In this chapter, efforts have been made to explore the different methodology and preparation technique for the formation of ultrafine nanoparticles.

2 Synthesis Methods

2.1 Solid-State Reaction

Solid-state reaction is a synthesis technique where the starting materials are taken, mixed together, and then heated at a controlled temperature. Heating is required to increase the reaction rate or sometimes even to initiate the reaction. It is a conventional and most used synthesis method to fabricate nanoparticles. High-temperature superconductors were first prepared via this method. This method is also known as 'shake and bake' or 'heat and beat method'. Zhou et al. [11] have prepared indium-doped hexaferrite ceramics using solid-state reaction method. M-type indium-doped strontium hexaferrites have been prepared with the help of $SrCO_3$ (99.99%), In_2O_3 (99.99%), and Fe_2O_3 (99.99%). The desired amounts of starting materials were well ball-milled. The mixed amount of mixture was sintered for 6 h at 1100 °C in air medium (Fig. 1). Thereafter, pallet of dimension 8 mm in diameter and thickness of 1 mm was prepared by using hydraulic press and finally sintered at 1200 °C (air) for 10 h. The reaction for the synthesis of polycrystalline $SrIn_xFe_{12-x}O_{19}$ (x = 0, 1.8, 2.4 and 3.0) is stated below:

$$SrCO_3 + \left(6 - \frac{1}{2}x\right)Fe_2O_3 + \left(\frac{1}{2}x\right)In_2O_3 \rightarrow SrFe_{12-x}In_xO_{19} + CO_2 \uparrow .$$

The substitution of indium ions in host lattice was not an easy way because the diamagnetic ions affect the super-exchange interactions that amend the magnetic and dielectric characteristics significantly of M-type hexaferrites. The incorporation of indium ions in lattice causes increase in structural parameters, decrease in dielectric characteristics (dielectric constant and dielectric loss) with frequency, and magnetic properties decrease (saturation magnetization and coercivity) with the indium concentration. The discrepancy in ionic radii may be the responsible for increase in lattice parameters, i.e., indium (0.80 Å, CN 6) and Fe^{3+} ion (0.64 Å, CN 6). Vinnik et al. [12] have reported $Ba_{1-x}Pb_xFe_{12}O_{19}$ ($x = 0.23$–0.80) hexaferrites by using stoichiometric ratios of starting materials such as iron oxides (Fe_2O_3), lead oxides (PbO), and barium carbonate ($BaCO_3$). The high purity materials are purchased from Ural Plant of Chemicals, Russia. Author uses resistive furnace and platinum crucible for the preparation of single crystal growth. Huang et al. [13] have synthesized $Ba_{0.5}Ca_{0.5}Fe_{12-2x}Mg_xTi_xO$ ($0.0 \leq x \leq 0.5$) with the help of $BaCO_3$, $CaCO_3$, Fe_2O_3, MgO, and TiO_2. The analytical grade reagents are used in stoichiometric ratio and then mixed by using ball milling for 4 h under 300 rpm in deionized water. Ball to powder weight ratio was kept at 15:1. Then, obtained mixtures were dried in oven at 140 °C and finally calcined in muffle furnace at 1250 °C (3 h, air). Pulverized was done with the help of vibrating mill to produce fine powder.

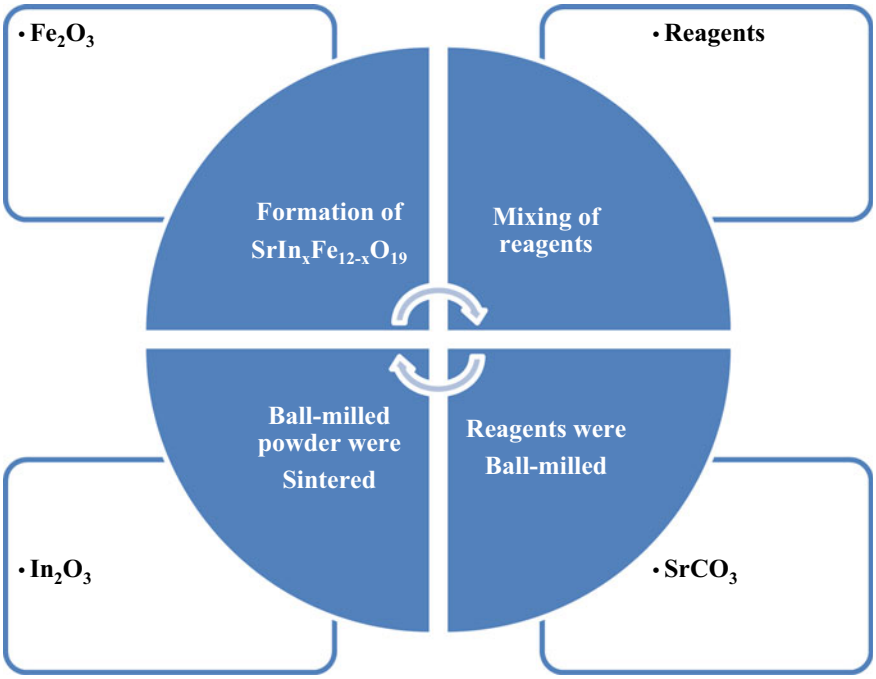

Fig. 1 Basic steps for the preparation of hexaferrite from solid-state method

2.2 Sol–gel Method

Sol–gel method is a bottom-up wet chemical technique for the preparation of glassy and ceramic materials. A sol is a liquid state of colloidal solution, whereas gel is a solid or semisolid state of colloidal solution. This technique is capable of producing high-quality nanoparticles at industrial scale, highly homogeneous, and pure composites. Moreover, it is a low-temperature, simple, and effective synthesis technique. In order to investigate the magnetic characteristics of Co and Ti substituted strontium hexaferrite, sol–gel method has been employed by Zhang et al. [14] for the preparation of ferrites. Strontium acetate hemihydrates, cobalt (II) acetate tetrahydrate, titanium tetrabutanolate, and iron (III) nitrate nonahydrate were used as raw materials in stoichiometric amount. The regents were dissolved in 12 ml ethylene glycol without any purification. The solution mixing was done with magnetic stirrer, and glacial acetic acid has been added in mixture to form viscous brown sol. Further, sol was subjected for drying process in oven at 80 °C for 1–2 days. Calcination at 400 °C for 3 h has been carried out after drying process. Obtained powder was subjected for grinding and sintering process at 900 °C (24 h in air). For the desired characterization, sintered powder was pressed to form pellet with the help of hydraulic machine and finally sintered at 1200 °C (24 h in air). Chokprasombat et al. [15] have analyzed the prepared $BaFe_{12-x}Bi_xO_{19}$ samples ($x = 0.1$ and 0.5) and $Ba_{1-x}Fe_{12-x}Bi_xCu_xO_{19}$ ($x =$

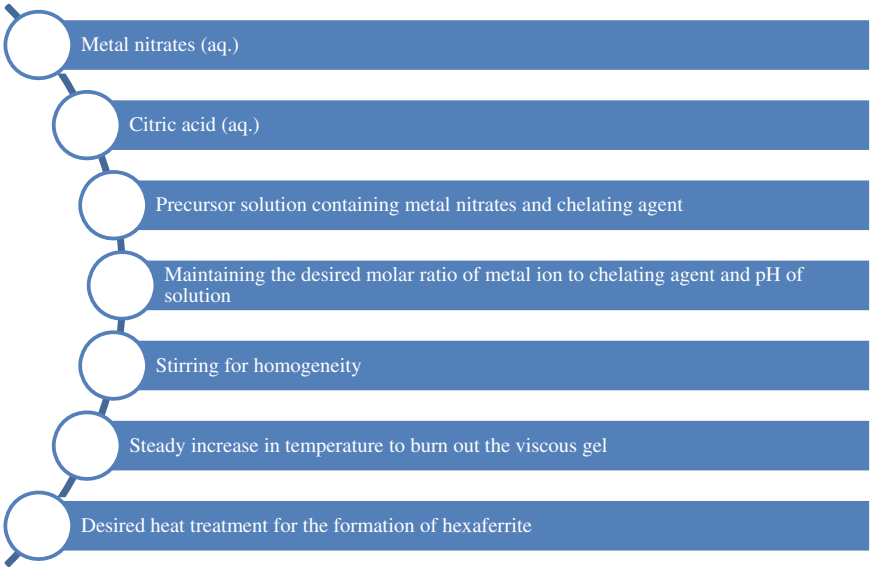

Fig. 2 Basic steps for the preparation of hexaferrite from sol–gel method

0.1, 0.2, and 0.3) by using ($Bi(NO_3)_3{\cdot}5H_2O$), ($Cu(NO_3)_2{\cdot}3H_2O$), ($Fe(NO_3)_3{\cdot}9H_2O$), ($Ba(NO_3)_3$), NH_4OH solution (25%), and citric acid. The starting reagents were dissolved in deionized water (30 ml). The solution of citric acid (1.441 g) was prepared and then mixed to prepare precursor solution. The citric acid is generally used as fuel. The pH of bath was maintained at 7 with the help of ammonium hydroxide solution. Then, solution was heated at 90 °C for 230 min till the formation of viscous gel from solution, (Fig. 2). Thereafter, viscous gel was heat treated at 150 °C for 190 min to obtain precursor powder followed by combustion process. Finally, brown-colored powder was grounded and subjected for subsequent heat treatment in a muffle furnace at 450 °C for 2 h and at 1050 °C for 3 h (4.5 °C/min).

2.3 Co-Precipitation Method

Co-precipitation method is generally used for the synthesis of magnetic nanoparticles. In this method, a homogeneous solution of metal chlorides or nitrates (dissolved in appropriate molar ratios) is obtained. A base is added drop wise in the solution for obtaining the precipitates. The co-precipitated powder is then washed, dried, and sintered to obtain the required M-type ferrites. Ashraf et al. [16] investigated M-type magnetic barium hexaferrites by co-precipitation technique. Barium nitrate dihydrate ($Ba(NO_3)_2.2H_2O$), iron (III) chloride ($FeCl_3.6H_2O$), and $CuCl_2.2H_2O$ were dissolved in stoichiometric amounts in deionized water under constant stirring at

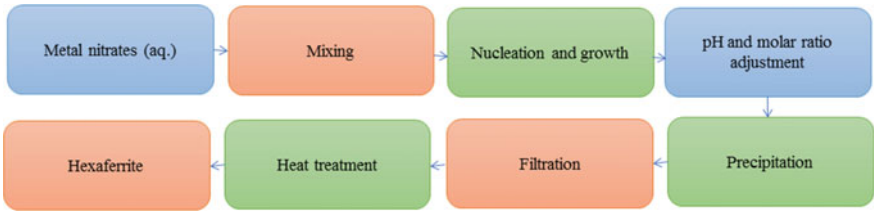

Fig. 3 Basic steps for the preparation of hexaferrite from co-precipitation method

70 °C. A separate solution of concentrated HNO_3 and $Gd(NO_3)_3$ was prepared and slowly poured in the desired solution. NaOH was added for pH control into the solution which was vigorously stirred for attaining homogeneity. The obtained suspensions were filtered, washed, and then dried at 150 °C. Vadivelan et al. [17] have examined nickel-doped barium ferrite by using co-precipitation method. As purchased, nitric acid and metal barium nitrate, ferric nitrate, and nickel nitrate were used and mixed in deionized water. Then, aqueous solution was mixed with ammonium hydroxide and nitric acid for the preparation of precursor solution. The filtration technique was used to obtain precipitate. The precipitates are washed several times with the help of deionized water. The precipitates are dried at 80 °C (6 h) and then subjected for sintering process, i.e., obtained product gets sintered at 950 °C (6 h) to obtain nickel-doped barium ferrite compound, (Fig. 3).

Hu et al. [18] have prepared $BaFe_{12}O_{19}$ nano-powder by using co-precipitation method. The chlorides were used to prepare precursor solution. The ferric chloride ($FeCl_3 \cdot 6H_2O$), barium chloride ($BaCl_2 \cdot 2H_2O$), and sodium hydroxide (NaOH) were used as starting materials. Solution of mixture having molar ratio 8 of Fe^{3+}/Ba^{2+} ions was co-precipitated with the addition of NaOH. The precursor solution was stirred at 200 rpm for different durations (3, 4, and 5 h). The pH of the bath was attained at 9. The distilled water was used to wash obtained co-precipitated samples and was dried at 50 °C for 12 h. Finally, dried samples were heat treated at different temperatures such as 700, 800, 900, 1000, and 1100 °C for 2 h in static air atmosphere at a rate of 20 °C/min.

2.4 Hydrothermal Method

Hydrothermal method is a versatile technique for the preparation of advanced nanoparticles and requires autoclave apparatus to provide high temperature and pressure during reaction. The terminology was originated from earth science because it involves the high temperature and pressure during preparation. In the hydrothermal synthesis of ferrites, an aqueous solution of salts is prepared to which NaOH/KOH is added drop wise. NaOH or KOH plays an important role in the co-precipitation of aqueous solution of metal nitrates. This solution is stirred for obtaining homogeneity

and then put in autoclave. The autoclave is put in the oven at a temperature of 150–290 °C to give heat treatment to the solution. The obtained precipitates are filtered, washed, and dried in an oven. Jing et al. [19] have conducted an experiment for the preparation of strontium hexaferrite by using analytical reagents of metal nitrates, viz. iron nitrate nonahydrate, strontium nitrate, and sodium hydroxide as starting materials with the help of hydrothermal technique. The metal nitrate solution was prepared and mixed with alkaline solution with the help of magnetic stirrer at room temperature. Then, after mixing, solution gets converted into slurry and can be transferred on reaction kettle with agitating device for heat treatment at 220 °C for 2 h. The initial pressure was maintained to 1.5 MPa by supplying the high purity nitrogen gas into the closed system. Thereafter, particles get separated and washed with deionized water and ethanol for several times and dried at 80 °C to obtain hexaferrite. Tang et al. [20] have accessed the impact of strontium hexaferrite nanoparticles synthesized by using hydrothermal route. The metal nitrates, viz. ($Fe(NO_3)_3.9H_2O$), ($Sr(NO_3)_2$), (NaOH), (HCl), ($C_{18}H_{34}O_2$), ethylene glycol, acetone, and ethanol, were used as starting materials. The analytical reagents were used as purchase, and experiment was performed in a Teflon-lined stainless steel autoclaves (200 mL) vessel. Fe^{3+}/Sr^{2+} ions molar ratio was kept at 3:1 and mixed with mixture of ethylene glycol/deionized water. $[OH^-]/[NO^-_3]$ was kept at 16, and NaOH solution was added in metal ions solution. The mixture was subjected for continuous stirring until the formation of precipitation of hydroxide precursors. Then, precursor was heat treated for half an hour at 80 °C and poured into a Teflon-lined stainless steel autoclave (200 mL) for 24 h. The obtained product was washed with deionized water. Diluted acetic acid (aq.) was used to wash the obtained product and to dissolve excess amount of strontium. Again, particles were washed with deionized water and ethanol several times. Centrifugation was done to collect the desired product and subjected for drying process at 100 °C in ambient air.

2.5 Solvothermal Method

In solvothermal method, metal precursors are dissolved in a solvent. The solvent used may be aqueous or non-aqueous. The reaction mixture is then kept in an autoclave (for achieving high temperature and pressure) placed in an oven for the crystal growth. The vapor pressure of the solvent increases the boiling point of the solvent. The crystals obtained are then washed and dried. Solvothermal method has various advantages over other methods like precise control on size, shape, and crystalline phases (Shaikh et al. [21]). The physical features can be controlled by altering the synthesis conditions like the precursors, solvent, reaction temperature, and reaction time. Shafiu et al. [22] have studied the prepared strontium hexaferrite by using solvothermal method without calcination with the help of chlorides in which $SrCl_2.2H_2O$ and $FeCl_3.6H_2O$ are dissolved in 15 ml of distilled water by keeping the molar ratio of 1/8. 30 ml of Teflon-lined stainless steel autoclaves used for continuous stirring after the addition of NaOH and kept in oven for different temperature (170, 180, 190, 200,

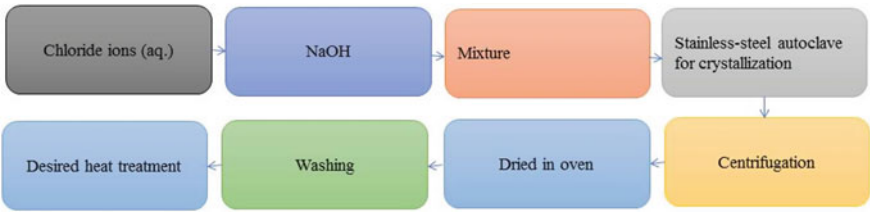

Fig. 4 Basic steps for the preparation of hexaferrite from solvothermal method

210, and 220 °C) for 18 h. Finally, prepared ultrafine particles are extracted with the help of magnet and dried at 60 °C for 4 h after washing with distilled water, alcohol, and acetic acid for several times (Fig. 4). Zheng et al. [23] have prepared La-substituted barium ferrite by using solvothermal method to analyze magnetic properties. P123 ($EO_{20}PO_{70}EO_{20}$) was used to prepare product in which triblock copolymer was dissolved in 30 mL of ethylene glycol. Iron (III) nitrate barium nitrate and lanthanum nitrate were mixed in molar ratio of 1:10 for (Ba + La)/Fe. Thereafter, NaOH was added to the prepared solution under continuous stirring for 6 h. Crystallization was carried out in stainless steel autoclave. The temperature of autoclave was maintained at 230 °C for 24 h. Thereafter, precipitate was obtained through centrifugation and washed with distilled water. Now drying was carried out at temperature 50 °C before calcination at 950 °C for 6 h followed by pre-calcination at 400 °C for 4 h.

2.6 Citrate Precursor Method

Ferrites can be synthesized via citrate precursor method (also known as Pechini method) at low temperatures. In the citrate precursor method, the precursor nitrates are dissolved in deionized water using a magnetic stirrer. Citric acid is slowly added to this precursor mixture as fuel. Ammonia solution is used to control the pH of the reaction mixture. The solution is continuously stirred at around 60–100 °C until a viscous gel is formed. This viscous gel is then dried in an oven to obtain the material in powder form. Thakur et al. [24] have conducted studies on the synthesis of M-type hexagonal strontium ferrites using citrate precursor method. Strontium nitrate, holmium nitrate pentahydrate, and iron nitrate were taken as precursors. The mole ratio of citric acid to metal ions was kept to be 1.5: 1. The reaction mixture was stirred at 70–80 °C. A viscous brown gel was obtained which was dried at 100 °C for 2 days to finally get the precursor powder. Satyapal et al. [25] have estimated the impact of prepared $BaFe_{12-x}Nd_xO_{19}$ magnetic nanoparticles with varying neodymium concentration at a low-temperature range, 200 °C. High purity grade $Ba(NO_3)_2$ and $Nd(NO_3)_3$ and $Fe(NO_3)_3$ were used for synthesis. Citric acid was used for chelation, and the stoichiometric ratio of citric acid to metal was kept to be 1:3. The mixture containing stoichiometric nitrates, dissolved in deionized water,

was stirred continuously till a gel was formed. This gel was dried overnight in an oven. A voluminous like ash powder was finally obtained which was grinded to fine powder and was further annealed at 800 °C for 2 h. Kumar et al. [26] have synthesized strontium hexaferrite nanoceramic using citrate precursor sol–gel process. Nitrates of Sr and Fe were dissolved in deionized water in stoichiometric amounts. The salt to citric acid ratio was taken to be 3:1. The pH of the solution was maintained at 7 by adding sodium hydroxide. The reaction mixture was kept on a hot plate at 80 °C till a brown color viscous jelly-like structure was formed. The dried jelly resulted into the formation of lightweight voluminous powder which was annealed at 850 °C for three hours. The chemical reaction taking place during the process is

$$\mathrm{Sr(NO_3)_2 + Fe(NO_3)_3.9H_2O + C_6H_8O_7 + NH_4OH} \rightarrow \mathrm{SrF_{12}O_{19} + NH_4NO_3 + CO_2 + H_2O.}$$

Koga et al. [27] have worked on preparation of doped barium hexaferrite by using citrate precursor method. $Fe(NO_3)_3.9H_2O$ and $Co(NO_3)_2.6H_2O$ were used as starting materials to prepare precursor solution by dissolving in distilled water. NaOH (3 M) solution was added to prepare solution to maintain pH equal to 8. Then, hydroxides were added to citric acid (1 M) solution along with $BaCO_3$ and $Ti(OCH(CH_3)_2)_4$. Then, homogenous solution was prepared after proper mixing at 323 K. In order to increase viscosity, ethylene glycol was added to solution and then mixed solutions were heated at 360 K. Finally, synthesized nanoparticles were sintered in air at 1423 K for 4 h. Jacobo et al. [28] have reported the synthesis, Co-Nd strontium hexaferrite by using $Fe(NO_3)_3.9H_2O$, $SrCO_3$, Nd_2O_3, and $Co(CH_3COO)_2{\cdot}4H_2O$ as starting materials with the help of citrate precursor method. The stoichiometric amount of metal ions was dissolved in nitric acid solution and ammonium hydroxide added to solution to maintain the pH at 7. Then, molar ratio of citric acid to nitric acid was kept in 2:1 to prepare precursor solution and stirred on magnetic stirrer for several hours to obtain dried gel. The dried gel gets ignited and converted from gel as loose magnetic powder (Fig. 5). Then, powder was calcined in air at 1100 °C for 2 h. Urea-assisted citrate precursor methods have been employed to prepare barium hexaferrite by Mudsainiyan et al. [29]. The metal nitrates including $Ba(NO_3)_2$, $Co(NO_3)_2.6H_2O$, $ZrO(NO_3)_2.6H_2O$, and $Fe(NO_3)_3.9H_2O$ were used as starting materials for the synthesis purpose. Then, aqueous solution of metal ions mixed the solution of citric acid in a molar ratio of 1:1.1. Then, urea solution was added to the mixture of metal ions and citric acid. The molar ratio of metal ion:urea was maintained at 1:2. The acidic environment was maintained by adding nitric acid in solution and subjected for evaporation at 80 °C that leads the formation of black color viscous gel. This viscous gel was heated at 120 °C for 1 h to obtain polymeric resin and further heat treated at higher temperature 150 °C for 2 h to remove excess residue. The obtained powder was heat treated at 800 °C for 4 h and finally powder grinded by mortar pestle to produce fine product. The urea as a fuel along the presence of citric acid helps in achieving crystalline phase at lower temperature than other route.

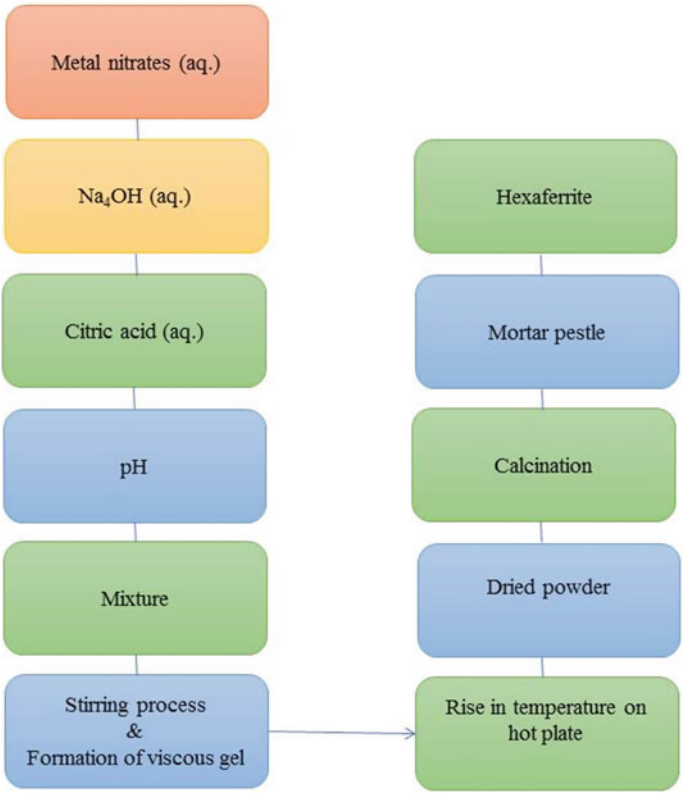

Fig. 5 Basic steps for the preparation of hexaferrite from citrate precursor method

2.7 Reverse Micelle Method

The precursor salt solutions are prepared according to the stoichiometry. The reaction mixture of the salt solutions is prepared by stirring them. For the preparation of micro-emulsion (reverse micelle), a surfactant, co-surfactant, and oil are required. The reverse micelle is added to the reaction mixture, and NaOH is added to it in order to control the pH. The mixture is heated with constant stirring. The obtained precipitates are washed with acetone/ethanol and deionized water to remove the contaminants, excess surfactant, and unreacted metal ions. Nanoparticles are obtained by centrifugation and heating of the washed precipitates. Baig et al. [30] have synthesized La^{3+} ion substituted $MnFe_2O_4$ ferrites by reverse micelle technique. Surfactant triton-100, co-surfactant 1-butanol, and paraffin oil were used for the preparation of reverse micelle. NaOH (1 M) solution was added drop wise to the reaction mixture to maintain the pH at 11. Constant stirring was done for two hours, and then the precipitates were washed with ethanol and deionized water followed by oven drying. Finally, the dried materials were annealed for four hours at 400 °C in vacuum.

2.8 Sonochemical Method

Sonochemical method involves the dissolution of precursors in the deionized water separately which are then mixed together through vigorous stirring at room temperature. The mixture solution is then put in the sonication reactor. The intense ultrasonic waves can drive the oxidation, reduction decomposition, hydrolysis, and dissolution reactions. The precipitates thus obtained are dried in an oven to obtain the final product. Sapkota et al. [31] have extended note on synthesized cobalt ferrite nanoparticles using sonochemical method. A reaction mixture of precursor's cobalt nitrate and iron acetate was first formed and was then sonicated for two hours. The sonicator was driven at a frequency of 20 kHz and operated at 62% amplitude. Solid brown precipitates were obtained which were separated by sonication and then dried in an oven at 80 °C to get the cobalt ferrite nanoparticles. Palomino et al. [32] have prepared strontium hexaferrite by using sonochemical method in which strontium acetate and iron acetate were used as per following reaction:

$$Sr^{2+} + 12Fe^{2+} + 19H_2O_2 \rightarrow SrFe_{12}O_{19} + 19H_2O.$$

Highly pure reagents are mixed together in 50 ml solution of a diethylene glycol with water in a ratio of diethylene glycol to water (2:1) for 30 min with the help of magnetic stirrer. Ultrasonic homogenizer Q700 sonicator was used for the sonication process in which precursor solution was subjected for different sonication times (10 min to 3 h). The reaction temperature was controlled with the help of water bath and temperature maintained at 25 °C during irradiation. Powder was washed several times after sonication process by forming a suspension in ethanol. Centrifugation was performed three times at rpm of 16,000 for 15 min. Drying process was carried out at 80 °C in air medium. Finally, obtained powder was subjected for annealing process at different temperature 300–900 °C in air. Sivakumar et al. [33] have showed that strontium acetate $(CH_3\text{-}CO_2)_2Sr$ and iron (III) acetylacetonate $(Fe(C_5H_7O_2)_3$ and ammonia solution 30% (NH_4OH) can be used as starting materials for the preparation of hexaferrite. 0.31 g (0.015 M) of strontium acetate and 6.36 g (0.18 M) of iron (III) acetylacetonate were mixed together in 100 ml distilled water with the help of magnetic stirrer for 2 min. The molar ratio of Sr^{2+}:Fe^{3+} was maintained at 1:12. Then, mixture was irradiated with high intensity ultrasonic horn (Fig. 6). Thereafter, 1 ml of NH_4OH solution was added drop wise into the solution to keep pH around eight after 15 min and subjected to ultrasound radiation for 1 h. Now solution was mounted on hot plate to evaporate the water at 80 °C and obtained powder gets dried on hot air for 5 h (at temperature 100 °C). To obtain fine product, samples were subjected to muffle furnace for calcination process at 1100 °C for 3 h (10 °C/min).

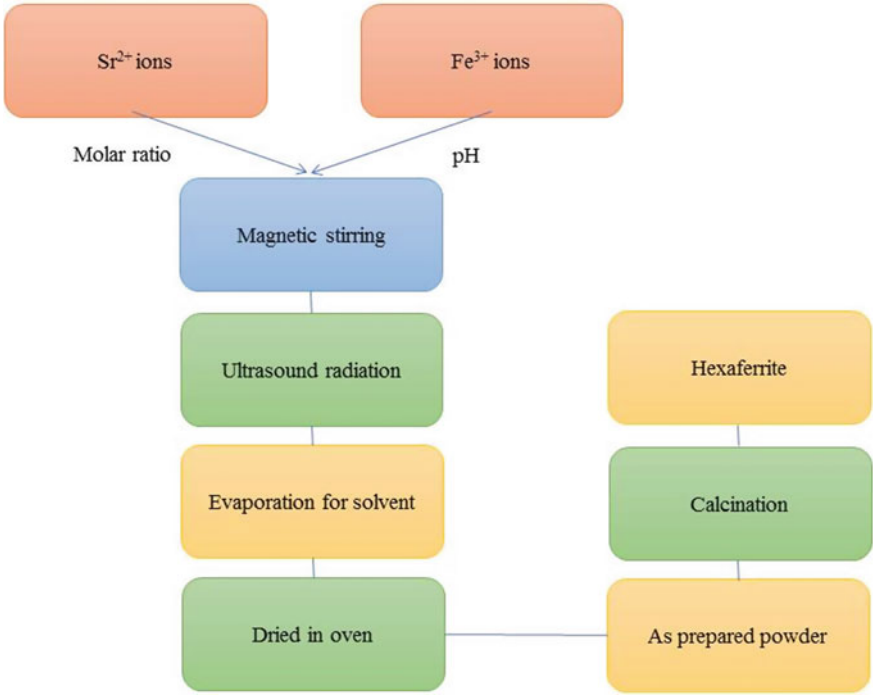

Fig. 6 Basic steps for the preparation of hexaferrite from sonochemical method

2.9 Aerosol Spray Pyrolysis Method

In aerosol spray pyrolysis method, soluble precursor metal salts are taken in liquid solution form and then atomized in a spray of fine droplets with the assistance of an atomizer. It is then passed through a hot wall tabular reactor transforming them to desired spherical and ultrafine particles. Lorentzou et al. [34] have stated that aerosol spray pyrolysis technique has been widely used for synthesizing ferrite powders, coatings, and especially magnetic particles and films. Gonzalez-Carreno et al. [35] have reported the impact of prepared aerosol spray pyrolysis method on the synthesis of barium ferrite nanoparticles. In the regards, metal nitrates were mixed together in deionized water after maintaining the atomic ratio (Fe/Ba) 1:2. The aqueous solution of citric acid was prepared and mixed with aqueous nitrates in 1:1 molar ratio. The homogeneous solution was obtained after the addition of ammonia solution. Then, solution was heat treated at 80 °C to remove excess amount of ammonia. Steam of fine and uniform droplets that get nebulized at a fixed flow rate 0.5 ml/min was produced from 2.10^{-2} M barium iron citrate precursor solution. Now droplets allow passing through furnace to evaporate solvent, 200–250 °C, and again dried barium iron citrate particles pass through second high-temperature (250–1000 °C) furnace to decomposition of citrates to obtain final particles. The product was collected with the help of

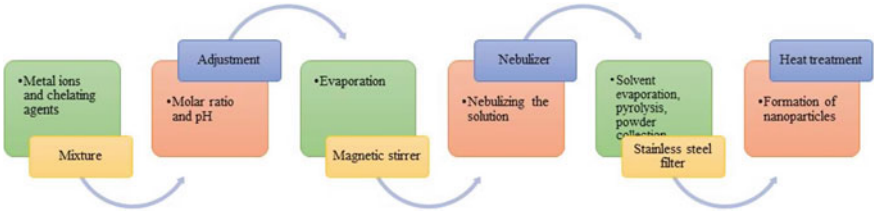

Fig. 7 Basic steps for the preparation of hexaferrite from aerosol pyrolysis

stainless steel filter having pore size, 0.02 mm. Finally, collected product was heat treated at 1000 °C for 1 h. Singhal et al. [36] have synthesized $BaMFe_{11}O_{19}$ (M = Fe, Co, Ni, and Al) by using aerosol route. The stoichiometric amounts of metal nitrates were dissolved in a water to prepare 5×10^{-2} M solution. A steady flow of aerosol was produced with the help of nebulizer in 40 psi air pressure. Fine droplets from the sample capillary were forays on an impact bead in the spray chamber that breaks them into smaller size (aerosol). These fined aerosols were mixed with air and enter into the furnace maintained at 600 °C which, with larger droplets, get filtered out in the spray chamber by flowing down the drain. Ferrites were deposited on Teflon-coated pan after various processes in succession, i.e., desolvation, vaporization, atomization, and oxidation. Yu et al. [37] have also reported barium hexaferrite nanoparticles from aerosol technique using regents, viz. $Fe(NO_3)_3.9H_2O$, $Ba(OH)_2.8H_2O$, and anhydrous citric acid molar ratio Ba^{2+}: Fe^{3+}:C_3 H_4 $(OH)(COOH)_3$ = 1:12:19. pH of solution was maintained at 7 by using NH_4OH. The prepared solution refluxed at 60 °C (3 h) so that carboxyl group of citric acid can chelate metallic ions in solution. Two-fluid-type nozzle was used to nebulize the solution, and the obtained aerosol was passed through the hot air flow (Fig. 7). Then, aerosol enters into the vertical glass chamber for pyrolysis followed by solvent evaporation. The temperature of hot air flow was maintained at 250 ± 5 °C and 150 ± 5 °C for inlet and outlet process, respectively. The obtained particles were kept in oven at 200 °C for 24 h. Finally, dried particles were heat treated at temperatures (500–800 °C) at a heating rate of 5 °C/min for 3 h.

2.9.1 Sol–gel Auto-Combustion

Sol–gel auto-combustion method is a wet chemical technique. It is preferred because of its simplicity, cost-effectiveness, is environment friendly, and gives accurate stoichiometry. In the synthesis process, all-metal nitrated precursors are dissolved in deionized water. Citric acid, which acts as a chelating agent, is separately dissolved in deionized water. Then the citric acid solution is added to the nitrate solution and mixed thoroughly by constant magnetic stirring. Ammonium hydroxide is added to the mixture in order to control the pH while constantly stirring at 80 °C until a gel is formed. The precursor gel is heated until the final product is synthesized in powder form. A series of M-type $SrAl_{2x}Fe_{12-2x}O_{19}$ hexagonal ferrites having

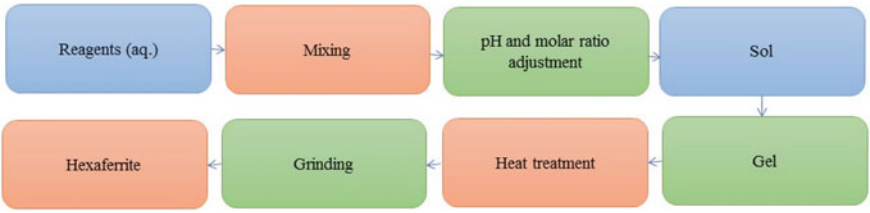

Fig. 8 Basic steps for the preparation of hexaferrite from sol–gel auto-combustion

x = (0.0,0.2,0.4,0.6,0.8,1.0) using sol–gel auto-combustion method taking strontium nitrate $Sr(NO_3)_3$, aluminum nitrate $Al(NO_3)_3$, and iron nitrate $Fe(NO_3)_3$ as precursors have been presented by Dilshad et al. [38] in their research work. The synthesis of Gd–Zn doped Br–Sr hexaferrites nanoparticles has been carried out by Huang et al. [39] from metal nitrates, viz. $Ba(NO_3)_2$, $Sr(NO_3)_2$, $Fe(NO_3)_3.9H_2O$, $Gd(NO_3)_3.6H_2O$, and $Zn(NO_3)_3.6H_2O$. The stoichiometric solution was prepared after mixing analytical grade reagents with chelating agent $C_6H_8O_7$ in deionized water. Metal to citric acid molar ratio was maintained at 1:1. NH_4OH solution was used to keep pH of bath at 7, and mixing of solution was done with the help of magnetic stirrer with gentle evaporation at 80 °C till the formation of a brownish gel. The gel started burning out as the temperature increases from 80 °C to 150 °C. The grinded powders were annealed at temperature of 1200 °C (2 h) in a muffle furnace (Fig. 8). Shariff et al. [40] have synthesized series of barium-strontium hexaferrite by using ($Ba(NO_3)_2$, $Sr(NO_3)_2$, $Fe(NO_3)_3.9H_2O$) as oxidizers and urea as fuel for combustion process. $Ba_{1-x}Sr_xFe_{12}O_{19}$; x = 0, 0.25, 0.5, 0.75, and 1 were prepared after maintaining molar ratio 1:9:31.66 for $Ba/Sr(NO_3)_2$: $Fe(NO_3)_3.9H_2O$):urea. Urea was used as a fuel for the combustion process owing to lesser hazardous characteristics and low cost for preparation of ferrites in respect to their counterpart, viz. oxalyldihydrazide, carbohydrazide, glycine, and alanine. Ammonia solution was added drop wise in precursor solution to achieve pH of 8 for the low annealing temperature formation of hexaphase in comparison with acidic region. The obtained brown-colored gel was preheated at 550 °C in furnace. It was observed that fuel get ignited and auto-combustion took place just after few minutes of preheating. A black-colored powder was obtained after combustion process as it grows like tree-like floppy structure. The obtained powder will be crushed with the help of mortar pestle and annealed at temperature 1000 °C for 2 h in a muffle furnace to achieve hexaferrite phase.

2.9.2 Green Synthesis

Green synthesis methods have gained much popularity in the past because of their simplicity, cost-effectiveness, good stability, lesser time consumption, eco-friendly, non-toxic by-products and can be easily scaled up for large-scale synthesis. In the green synthesis approach, the hazardous chemicals are replaced by some

organic/plant-based materials. However, there may be some disadvantages of biological materials like being unstable in aggressive environments, bioaccumulation, and the challenge of recycling, reusing, and regeneration. Kagdi et al. [41] have presented barium zinc hexaferrite by using combustion treatment method using ginger root extract as a green reducing agent. The solution of barium nitrate, zinc nitrate, and ferric nitrate was dissolved one by one in 100 ml ginger root extract which was extracted by boiling ~ 200 g fresh ginger root for 45 min in 200 ml distilled water. Ginger (Zingiber officinale) root extracts were used to prepare series of precursor solution and stirred on magnetic stirrer. The oil bath heating was used to obtain gel at 90 °C. The removal of water content from the gel was carried out in a muffle furnace at 100 °C for 20 h. The obtained powder subjected for heat treatment at 900 °C for 5 h followed by preheating at 550 °C after grounding the dried powder for 4 h to obtain desire product using green reducing agent (Fig. 9). The ginger extract was used for combustion during preparation because of good antioxidant properties that are associated with reducing power of biologically active compounds. The research work seems to be useful, economical, time-saving, and eco-friendly technique. Nickel ferrite by using green synthesis route with the help of different fuels has been reported by Kulkarni et al. [42]. Metal nitrates were dissolved in 200 ml of distilled water with the help of magnetic stirrer for 15 min. Then, clove extract was added to solution as eco-fuel to overcome the importance of harmful toxic chemicals. Clove extract was prepared from 20 g of clove boiled in 30 ml distilled water for 15 min on magnetic stirrer. The pH of solution was maintained at 9 and continuously stirred at 80–90 °C for 2 h. The temperature rose to 120 °C for ignition to obtain dried powder from viscous gel. Then, product was subjected for grinding process and sintered at 700 °C for 2 h to eliminate the impurities from the final product. Godara et al. [43] have derived hexaferrite nanoparticles by using natural, green, and eco-friendly Jamun pulp as a reducing agent. Barium nitrate ($Ba(NO_3)_2$ and ferric nitrate $Fe(NO_3)_3{\cdot}6H_2O$ were used as starting materials. The stoichiometric amount of $Ba(NO_3)_2$ (0.784 g) and $Fe(NO_3)_3{\cdot}6H_2O$(14.5 g) was dissolved in distilled water in a molar ratio 1:12 to prepare solution. Then, Jamun pulp of different concentration (0, 10, 20, 30, 40, 50, 60 g) was added to solution. The mixture of Jamun pulp and nitrates was subjected to continuous magnetic stirring at room temperature. Thereafter, sol was heated at 80–100 °C for 2–3 h to obtain blackish-brown viscous gel. Then gel was heat treated at 200–250 °C for 1–2 h for auto-combustion. Finally, prepared powder was calcined at 900 °C for 6 h to obtain crystalline $BaFe_{12}O_{19}$.

3 3D Printing of Ferrite Nanoparticles

3D printing has attracted the intention of several researchers to build 3D material by joining materials layer by layer. 3D printing is commonly known as additive manufacturing. 3D printing has wide range of importance in the field of medicine and electronics. 3D printing is very helpful in implants, drug delivery devices, medical imaging technologies, surgery, and 3D printing of living cells. Shamray et al. [44]

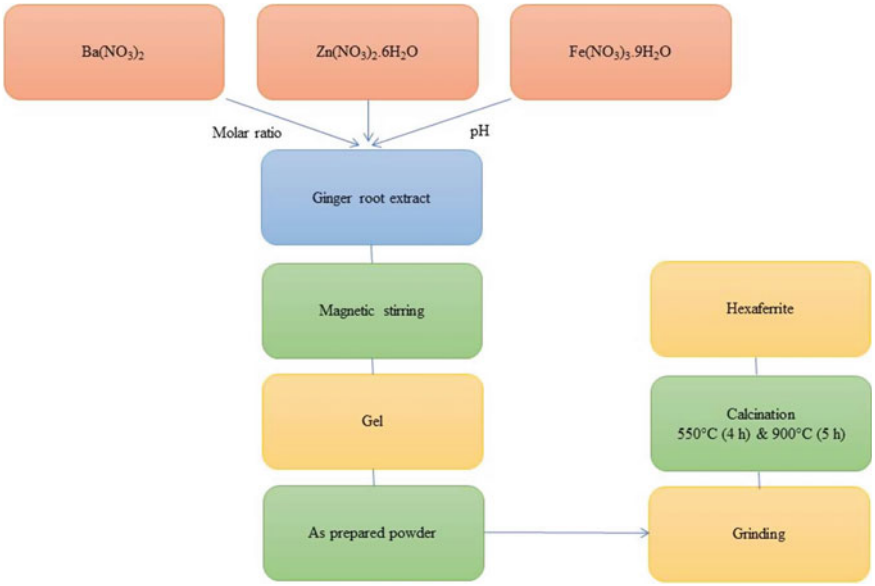

Fig. 9 Basic steps for the preparation of hexaferrite from green synthesis of ferrite nanoparticles

have obtained nickel zinc nanoferrites by using pyrochemical urea-nitrate method and highlighted that desired ferrite fraction in plastic for 3D printing is expected to be high to deliver high magnetic permeability. The fraction of ferrite was kept as low as in plastic to make smooth exit of material from the heated extrusion nozzle of the 3D printer. Polylactide was used as a matrix polymer, and during optimization, it was observed that higher the ferrite nano-powders fractions, higher the difficulties are there to print. Wang et al. [45] have described the dispersion of ferrite in filament and printed part of 3D printing of acrylonitrile butadiene styrene polymer-based nickel zinc ferrite magnetic composites. 3D printing development involves the selection, processing, and optimization as main components. Selection of printable thermoplastic matrix is the most important key step in development. Author uses acrylonitrile butadiene styrene polymer in this investigation for printing at low cost because of wide abundance. Acrylonitrile butadiene styrene polymer and ferrite were dissolved in acetone with the help of magnetic stirring. Sintered nickel zinc ferrites were dispersed in acetone and poured into the acrylonitrile butadiene styrene polymer-containing solution under stirring. The evaporation of acetone was carried out in fume cupboard after spreading the slurry on tray. The obtained composite was taken and then grounded to form pellets. Yang et al. [46] have presented a novel 3D gel printing to process complex-shaped strontium ferrite through hydroxyethyl methacrylate gelation system. Author presented the 3D printing of strontium ferrite in which firstly 3D models were designed and then sliced. Printed slurry was poured into a plastic syringe barrel with a nozzle. Gelation time was well adjusted by allowing N, N tetramethylethylenediamine and ammonium persulfate along with

slurry. It helps to print strontium ferrite part at a speed of 20 mm/s. Then, the prepared printed sample was further dried in an oven at 50 °C at 8 h. Thereafter, sample was subjected for sintering processing at 1300 °C for 2 h (4 °C/min) followed by heat treatment at 500 °C (1 h) in a tube furnace in an argon atmosphere.

4 Conclusion

Hexaferrites have been well prepared with versatile and economical methods such as solid-state reaction, sol–gel method, co-precipitation method, hydrothermal method, solvothermal method, citrate precursor method, reverse micelle method, sono-chemical method, aerosol spray pyrolysis method, and auto-combustion method. However, the involvement of highly flammable and toxic chemicals makes them non-environmentally friendly methods for the preparation of nanoparticles. Green synthesis approach was found to be suitable as an environmental-friendly technique to overcome the present concern raised by chemical industries. Except green synthesis route, all other methods involve harmful chemicals for the preparation of nanoparticles, whereas green synthesis involves natural extracts as reducing agent for the preparation as well as to possess good antioxidant properties.

References

1. Mathews SA, Babu DR (2021) Analysis of the role of M-type hexaferrite-based materials in electromagnetic interference shielding. Curr Appl Phys 29:39–53. https://doi.org/10.1016/j.cap.2021.06.001
2. Yu PY, Kang YM (2021) Tuning of electromagnetic wave absorbing properties in Fe-deficient $SrFe_{9.6-x}Co_{1.2}Ti_{1.2}O_{19}$ hexaferrite-epoxy composites. Curr Appl Phys 31:99–104. https://doi.org/10.1016/j.cap.2021.08.002
3. Dhage VN, Mane ML, Rathod SB et al (2021) Electric, dielectric and AC electrical conductivity study of Al^{3+} substituted barium hexaferrite nanoparticles synthesized by Sol-gel auto-combustion technique. Mater Today Proc 47:1982–1987. https://doi.org/10.1016/j.matpr.2021.04.119
4. Li LZ, Sokolov A, Yu CJ et al (2021) Effects of Y-Co co-substitution on the structural and magnetic properties of M-type strontium hexaferrites. Ceram Int 47:25514–25519. https://doi.org/10.1016/j.ceramint.2021.05.275
5. Abd-Elkader O, Al-Enizi AM, Shaikh SF et al (2022) The structure, magnetic, and gas sensing characteristics of W-substituted Co-ferrite nanoparticles. Crystals 12:393. https://doi.org/10.3390/cryst12030393
6. Hashhash A, Hassen A, Baleidy WS et al (2021) Impact of rare-earth ions on the physical properties of hexaferrites $Ba_{0.5}Sr_{0.5}RE_{0.6}Fe_{11.4}O_{19}$, (RE = La, Yb, Sm, Gd, Er, Eu, and Dy). J Alloys Compd 873:159812. https://doi.org/10.1016/j.jallcom.2021.159812
7. Zhang W, Li J, Yi S et al (2021) Influence of La-Nb co-substituted Sr ferrite on microstructure, spectrum and magnetic properties of hexaferrites. J Alloys Compd 871:159563. https://doi.org/10.1016/j.jallcom.2021.159563

8. Yang Y, Liu X, Feng S et al (2020) Effects of Pr-Al co-substitution on the magnetic and structural properties of M-type Ca-Sr hexaferrites. Chinese J Phys 63:337–347. https://doi.org/10.1016/j.cjph.2019.11.026
9. Shinde VS, Dahotre SG, Singh LN (2020) Synthesis and characterization of aluminium substituted calcium hexaferrite. Heliyon 6:e03186. https://doi.org/10.1016/j.heliyon.2020.e03186
10. Narang SB et al (2015) Comparative dielectric analysis of Co-Zr doped M-Type Barium HexaferritesBa$Co_xZr_xFe_{(12-2x)}O_{19}$ prepared by different wet chemical routes. Integr Ferroelectr 167(1):98–106. https://doi.org/10.1080/10584587.2015.1106882
11. Zhou S, Yang Y, Lei RY et al (2021) The effects of indium doping on the electrical, magnetic, and magnetodielectric properties of M-type strontium hexaferrites. J Magn Magn Mater 539:168333. https://doi.org/10.1016/j.jmmm.2021.168333
12. Vinnik DA, Prosvirin IP, Zhivulin VE et al (2020) Crystal growth, structural characteristics and electronic structure of $Ba_{1-x}Pb_xFe_{12}O_{19}$ (x = 0.23–0.80) hexaferrites. J Alloys Compd 844:156036. https://doi.org/10.1016/j.jallcom.2020.156036
13. Huang K, Yu J, Zhang L et al (2020) Synthesis and characterizations of magnesium and titanium doped M-type barium calcium hexaferrites by a solid state reaction method. J Alloys Compd 825:154072. https://doi.org/10.1016/j.jallcom.2020.154072
14. Zhang M, Liu Q, Zhu G et al (2019) Magnetic properties of Co and Ti co-doped strontium hexaferrite prepared by sol-gel method. Appl Phys A 125:191. https://doi.org/10.1007/s00339-019-2500-5
15. Chokprasombat K, Lohmaah A, Pinitsoontorn S et al (2022) Effects of bismuth and bismuth-copper substitutions on structure, morphology, and magnetic properties of sol-gel derived barium hexaferrites. J King Saud UnivSci 34:101682. https://doi.org/10.1016/j.jksus.2021.101682
16. Ashraf GA, Zhang L, Abbas W et al (2019) Magnetic and optical properties of Gd-Tl substituted M-type barium hexaferrites synthesized by co-precipitation technique. CurrApplPhys 19:506–515. https://doi.org/10.1016/j.cap.2019.02.005
17. Vadivelan S, Sowmiya S (2021) Structural and magnetic studies of nickel doped barium ferrite via co-precipitation method. Phys Open 9:100094. https://doi.org/10.1016/j.physo.2021.100094
18. Hu SL, Liu J, Yu HY et al (2019) Synthesis and properties of barium ferrite nano-powders by chemical co-precipitation method. J MagnMagn Mater 473:79–84. https://doi.org/10.1016/j.jmmm.2018.10.044
19. Jing Y, Jia L, Zheng Y et al (2019) Hydrothermal synthesis and competitive growth of flake-like M-type strontium hexaferrite. RSC Adv 9:33388–33394. https://doi.org/10.1039/C9RA06246G
20. Tang X, Hong RY, Feng WG et al (2013) Ethylene glycol assisted hydrothermal synthesis of strontium hexaferrite nanoparticles as precursor of magnetic fluid. J Alloys Compd 562:211–218. https://doi.org/10.1016/j.jallcom.2013.02.049
21. Shaikh SF, Ubaidullah M, Mane RS et al (2020) Types, synthesis methods and applications of ferrites. In: Mane RS, Jadhav VV (eds) Spinel ferrite nanostructures for energy storage devices. Micro and Nano technologies. Elsevier, pp 51–82. https://doi.org/10.1016/B978-0-12-819237-5.00004-3
22. Shafiu S, Sözeri H, Baykal A (2014) Solvothermal synthesis of $SrFe_{12}O_{19}$ hexaferrites: without calcinations. J Supercond Nov Magn 27:1593–1598. https://doi.org/10.1007/s10948-014-2490-7
23. Zheng X, Du Y, Wang Y et al (2012) Solvothermal synthesis and magnetic properties of La-substituted Barium Ferrite. Chem Lett 41:209–211. https://doi.org/10.1246/cl.2012.209
24. Thakur A, Kumar V (2020) Synthesis and characterization of holmium substituted M-type hexagonal strontium ferrite. J NanomaterSci 4:6–10
25. Satyapal HK, Singh RK, Kumar N et al (2020) Low temperature synthesis and influence of rare earth Nd3+ substitution on the structural, magnetic behaviour of M-type barium hexa ferrite nanomaterials. Mater Today Proc 28:234–240. https://doi.org/10.1016/j.matpr.2020.01.590

26. Kumar SS, Singh RK, Kumar N et al (2021) Structural, elastic, and multiferroic property of strontium ferrite nanoceramic prepared by sol–gel derived citrate precursor method. Mater Today Proc 46:8567–8572. https://doi.org/10.1016/j.matpr.2021.03.547
27. Koga N, Tsutaoka T (2007) Preparation of substituted barium ferrite $BaFe_{12-x}$ $(Ti_{0.5}Co_{0.5})_xO_{19}$ by citrate precursor method and compositional dependence of their magnetic properties. J Magn Magn Mater 313:168–175. https://doi.org/10.1016/j.jmmm.2006.12.020
28. Jacobo SE, Herme C, Bercoff PG (2010) Influence of the iron content on the formation process of substituted Co–Nd strontium hexaferrite prepared by the citrate precursor method. J Alloys Compd 495:513–515. https://doi.org/10.1016/j.jallcom.2009.10.172
29. Mudsainiyan RK, Jassal AK, Gupta M et al (2015) Study on structural and magnetic properties of nanosized M-type Ba-hexaferrites synthesized by urea assisted citrate precursor route. J Alloys Compd 645:421–428. https://doi.org/10.1016/j.jallcom.2015.04.218
30. Baig MM, Zulfiqar S, Yousuf MA et al (2020) Structural and photocatalytic properties of new rare earth La^{3+} substituted $MnFe_2O_4$ ferrite nanoparticles. Ceram Int 46:23208–23217. https://doi.org/10.1016/j.ceramint.2020.06.103
31. Sapkota B, Hasan MT, Martin A et al (2022) Fabrication and magnetoelectric investigation of flexible PVDF-TrFE/cobalt ferrite nanocomposite films. Mater Res Express 9:046302. https://doi.org/10.1088/2053-1591/ac6151
32. Palomino RL, Miró AMB, Tenorio FN et al (2016) Sonochemical assisted synthesis of $SrFe_{12}O_{19}$ nanoparticles. Ultrason Sonochem 29:470–475. https://doi.org/10.1016/j.ultsonch.2015.10.023
33. Sivakumar P, Shani L, Yeshurun Y et al (2016) Facile sonochemical preparation and magnetic properties of strontium hexaferrite ($SrFe_{12}O_{19}$) nanoparticles. J Mater Sci Mater Electron 27:5707–5714. https://doi.org/10.1007/s10854-016-4482-9
34. Lorentzou S, Agrafiotis CC, Konstandopoulos AG (2008) Aerosol spray pyrolysis synthesis of water-splitting ferrites for solar hydrogen production. Granular Matter 10:113–122. https://doi.org/10.1007/s10035-007-0069-8
35. Gonzalez-Carreno T, Morales MP, Serna CJ (2000) Barium ferrite nanoparticles prepared directly by aerosol pyrolysis. Mater Lett 43:97–101. https://doi.org/10.1016/S0167-577X(99)00238-4
36. Singhal S, Garg AN, Chandra K (2005) Evolution of the magnetic properties during the thermal treatment of nanosize BaMFe11O19 (M = Fe Co, Ni and Al) obtained through aerosol route. J MagnMagn Mater 285:193–198. https://doi.org/10.1016/j.jmmm.2004.07.039
37. Yu HF, Lin HY (2004) Preparation and thermal behavior of aerosol-derived $BaFe_{12}O_{19}$ nanoparticles. J Magn Magn Mater 283:190–198. https://doi.org/10.1016/j.jmmm.2004.05.020
38. Dilshad M, Khan HM, Zahid M et al (2022) Structural, optical and dielectric properties of aluminum-substituted $SrAl_{2x}Fe_{12-2x}O_{19}$ x = (0.0, 0.2, 0.4, 0.6, 0.8, 1.0) M-type hexagonal ferrites. J Mater Sci Mater Electron 33:21519–21530. https://doi.org/10.1007/s10854-022-08943-x
39. Huang K, Yu J, Zhang L, Xu J et al (2019) Structural and magnetic properties of Gd–Zn substituted M-type Ba–Sr hexaferrites by sol-gel auto-combustion method. J Alloys Compd 803:971–980. https://doi.org/10.1016/j.jallcom.2019.06.348
40. Shariff YKR, Choudhary HK, Khopkar V et al (2021) Sol-gel auto-combustion synthesis of Ba–Sr hexaferrite ceramic powders. Ceram Int 47:14907–14912. https://doi.org/10.1016/j.ceramint.2020.07.034
41. Kagdi AR, Pullar RC, Meena SS et al (2020) Studies of structural, magnetic and dielectric properties of X-type Barium Zinc hexaferrite $Ba_2Zn_2Fe_{28}O_{46}$ powder prepared by combustion treatment method using ginger root extract as a green reducing agent. J Alloys Compd 842:155120. https://doi.org/10.1016/j.jallcom.2020.155120
42. Kulkarni GD et al (2020) Green synthesis of $NiFe_2O_4$ nanoparticles using different fuels and their structural characterization. In: International Web Conference on Advanced Material Science and Nanotechnology (NANOMAT-2020), Nandgaon Khandeshwar India, June 2020. J Phys Conf Ser, vol 1644. IOP Publishing, p 012003. https://doi.org/10.1088/1742-6596/1644/1/012003

43. Godara SK, Dhaka RK, Kaur N et al (2021) Synthesis and characterization of Jamun pulp based M-type barium hexaferrite via sol–gel auto-combustion. Results Phys 22:103903. https://doi.org/10.1016/j.rinp.2021.103903
44. Shamray II et al (2020) Changes in the structure and properties of nickel-zinc spinel nanoferrites series for 3D-printing. In: International Russian Conference on Materials Science and Metallurgical Technology (RusMetalCon 2020), Chelyabinsk, Russian Federation, September 2020. IOP Conf Ser: Mater Sci, vol 969. IOP Publishing, p 012101. https://doi.org/10.1088/1757-899X/969/1/012101
45. Wang Y, Castles F, Grant PS (2015) 3D printing of NiZn ferrite/ABS magnetic composites for electromagnetic devices. MRS Online Proc Libr 1788:29–35. https://doi.org/10.1557/opl.2015.661
46. Yang F, Zhang X, Guo Z et al (2018) 3D gel-printing of Sr ferrite parts. Ceram Int 44:22370–22377. https://doi.org/10.1016/j.ceramint.2018.08.364

Chapter 4
Ferrite Nanoparticles for Water Decontamination Applications

Aayush Gupta and Raveena Choudhary

1 Need of Wastewater Treatment

> "If we move forward and don't clean up the messes of the past, they'll just get swept under the rug."—Erin Brokovich.

Water is a source of survival for all forms of life on earth. One cannot die without love and surely can without water. Globally, the supply of safe, secure, and inexpensive water has been one of the biggest difficulties faced in recent years. Fresh water availability per capita has been decreased as a result of the alarming rate of industrialization and population growth [1, 2]. Water covers over 71% of the surface of the globe. Of the total available water, around 97% is found in oceans and 3% is fresh water. Only 0.3% of the freshwater on earth's surface is located in fresh lakes, rivers, and streams, while 68.7% of the remaining fresh water is frozen in icecaps and glaciers. The remaining freshwater is found beneath the ground [2]. The water distribution over the earth's surface is depicted in a pie chart in Fig. 1.

Along with the very low availability of fresh water on the earth, industrialization and urbanization are also causing the deterioration of water quality. As a result, water crises are becoming unimaginably severe over the globe. Even though the planet's freshwater supply has mostly remained steady over time through constant recycling via the atmosphere and back. The rise in population implies that the rivalry for a plentiful supply of clean water for drinking, cooking, bathing, and supporting life grows more intense every year. According to a recent report by UNICEF, nearly 2/3rd of the world's population, i.e., 4.0 billion people endure extreme water scarcity for at

A. Gupta (✉)
Department of Mechanical Engineering, GLA University, Mathura 281406, India
e-mail: present.ayush@gmail.com

R. Choudhary
School of Physics and Materials Science, Thapar Institute of Engineering and Technology, Patiala 147004, India

P. Sharma et al. (eds.), *Engineered Ferrites and Their Applications*, Materials Horizons: From Nature to Nanomaterials, https://doi.org/10.1007/978-981-99-2583-4_4

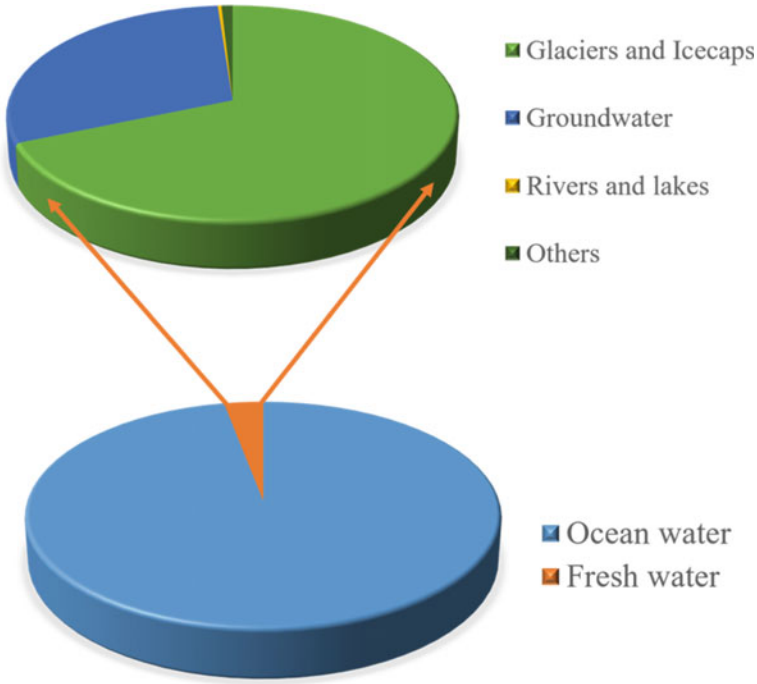

Fig. 1 Water distribution over the earth's surface

least one month each year. Due to the acute water shortage, 700 million people may be displaced worldwide by 2030 [3]. These key factors of water scarcity in the future are enough to be alarmed and step up for water conservation. Due to the dumping of polluted water effluents from industries to rivers and other freshwater streams, water-borne diseases are rising. According to recent data from a WHO assessment, at least 2 billion people drink polluted (feces) water. Microbial contamination brought on by feces contamination poses the biggest threat to the potable water. Drinking water contaminated by microorganisms increases the risk of contracting diseases such as diarrhea, cholera, typhoid, polio and contributes to the 4,85,000 annual deaths from diarrhea. The most dangerous chemicals in drinking water include arsenic, fluoride, and nitrate, but novel pollutants like pesticides, drugs, per- and polyfluoroalkyl substances (PFASs), and microplastics are now a source of public concern [4]. These pollutants generally emerge from wastewater from industries and households. Recycling wastewater effluents is therefore a top issue in every community worldwide in terms of environmental conservation and sustainable development.

2 Background of Photocatalytic Wastewater Treatment

The major water pollutants are of three types, viz. organic, inorganic, and microbial contaminants. The organic pollutants include pesticides, phthalates, phenols, dyes, and other VOCs from industries. These pollutants are usually carcinogenic and mutagenic in nature even present in very small fractions and can lower dissolved oxygen causing harm to humans and aquatic life. Metals, salts, and other substances free of carbon are examples of inorganic pollutants. From an ecotoxicological point of view, metal ions like Hg^{2+}, Pb^{2+}, Cr^{3+}, Cr^{4+}, Ni^{2+}, Co^{2+}, Cu^{2+}, Cd^{2+}, Ag^{+}, As^{5+}, and As^{3+} are toxic. In addition, the contamination caused by radioactive elements is a serious problem given their potentially dangerous long-term effects. Microbes/pathogens including bacteria, viruses, and parasites may only be present in very small concentrations in drinking water, but they are a major risk factor for the safety of water since they spread many infectious diseases. The pathogens such as bacteria, viruses, protozoa, and helminths are responsible for disease such as diarrhea, cholera, gastrointestinal illness [5–13].

Primary, secondary, and tertiary treatments are some of the processes in the treatment of wastewater as shown in Fig. 2. In the preliminary treatment procedure, heavy objects like sand, stones, etc. are separated from water using a range of processes, such as screening followed by grit removal, then pre-aeration, flow metering, and finally sampling. After initial treatment, primary treatment using sedimentation and floatation process removes the settleable organic solids. Biological techniques are employed in secondary treatment to further decompose organic materials, remove dissolved and colloidal particles (aquatic microorganisms). The most important and final stage entails a thorough tertiary treatment to clean the secondary-treated water and make it fit for consumption [14, 15]. There are tertiary treatments available to extract or degrade waste from wastewater using physical, chemical, and biological techniques (Fig. 2). These methods include electrochemical techniques, ozonation, adsorption, reverse osmosis, coagulation and flocculation, precipitation, and fungal decolonization [16–22]. For tertiary treatment, typical purification systems are either inefficient or excessively expensive. When using chemical techniques, ozonation is the least effective because of its short life and high expense, while the limitation of chlorination is that it may produce trihalomethane, a harmful disinfection by-product. Reverse osmosis is an expensive and ineffective physical approach for treating wastewater, as are flocculation and filtering [23]. When using biological methods, system handling becomes extremely important. Therefore, there is still a need for an effective, affordable, and manageable wastewater treatment method.

Among various wastewater treatment techniques, advanced oxidation process (AOP) compared to other techniques is rapid, effective, and inexpensive. It can overcome obstacles including hazardous by-products, high costs, and partial removal of pollutants. AOPs are employed for the complete mineralization of complex biorefractory pollutants from aqueous solution [1]. Different AOPs include Fenton-like reactions, ozonation, and photocatalysis which require costly catalysts, equipment and may lead to incomplete degradation to form toxic secondary products which adds

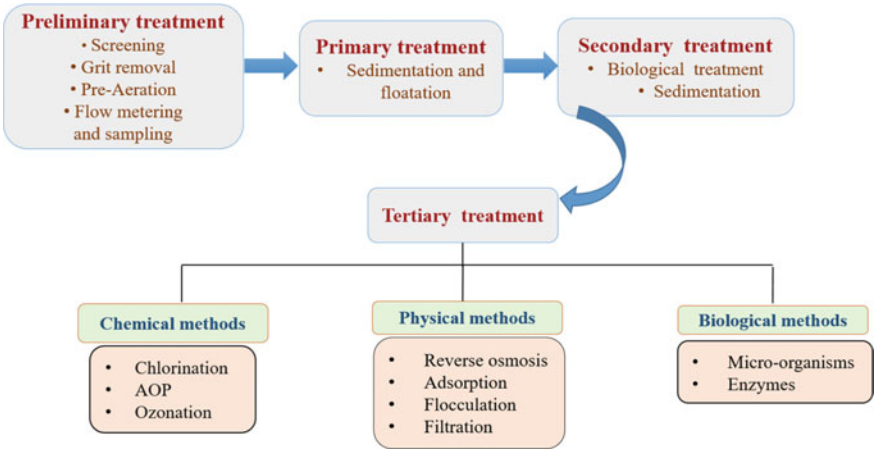

Fig. 2 Wastewater treatment stages

to environmental stress. One form of promising AOP technology is sunlight-driven photocatalysis. Solar irradiation has the ability to activate photocatalysts, resulting in the production of highly reactive photo-induced charge carriers that react with contaminants. In AOP photocatalytic process, the photocatalyst is generally mixed with the aqueous sample in which pollutants are present. The mechanism of photocatalysis is shown in Fig. 3. The basic principle on which AOP photocatalysis works involves the generation of exciton pair upon irradiation exposure of photocatalyst with electromagnetic radiation of energy, equal or greater than the optical band gap of the catalyst. The transition of electron (e^-) from the valence band to the conduction band occurs, and holes (h^+) are left in the valence band. Therefore, a photocatalyst with a smaller band gap is more likely to absorb more photons from visible light. The generated e^- and h^+ further react with water and dissolved oxygen in the water to form superoxide anion radicals and hydroxyl radicals. These radicals further react on the adsorbed pollutant on the surface of the catalyst to decompose it to form minerals and CO_2 [24]. The following equations represent the mechanism of photocatalysis:

$$\text{catalyst} + h\nu \rightarrow \text{catalst} + \text{h}^+ + \text{e}^-, \tag{1}$$

$$\text{catalyst}\left(\text{e}^-\right) + \text{O}_2 \rightarrow \text{O}_2^-, \tag{2}$$

$$\text{catalyst}\left(\text{h}^+\right) + \text{H}_2\text{O} \rightarrow \text{OH}^{\cdot}, \tag{3}$$

$$\text{O}_2^- + \text{OH}^{\cdot} + \text{pollutant} \rightarrow \text{CO}_2 + \text{H}_2\text{O}. \tag{4}$$

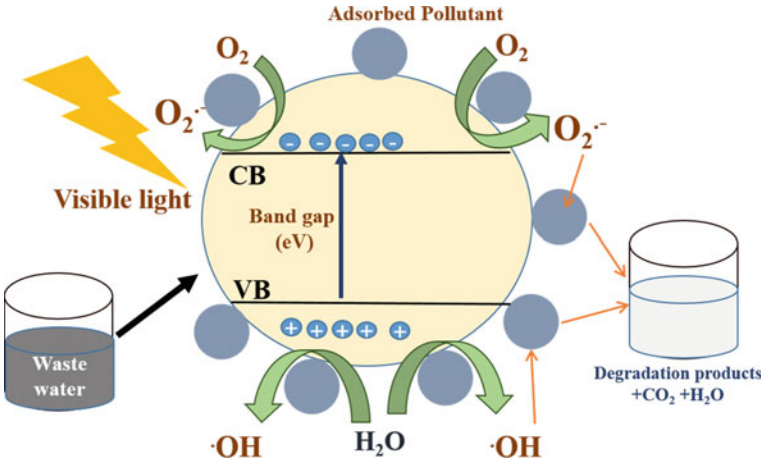

Fig. 3 Mechanism of photocatalytic wastewater treatment

3 Magnetic Materials as Photocatalyst

There are variety of materials which have been used so far as photocatalyst for wastewater treatment including metal oxide (ZnO, TiO_2, $BiTiO_3$, $SrTiO_3$, Fe_2O_3, BiOBr, $CaFe_2O_4$, $ZnFe_2O_4$, etc.), metal organic frameworks, carbon nanostructures (carbon nanosphere, carbon nanotube, carbon nitride, etc.), metal sulfide (ZnS, CdS, $CuInS_2$, etc.), piezoelectric materials, and noble metals (Pt, Ag, and Au). Due to its great chemical inertness, non-toxicity, abundance (0.44% of the earth's crust), and cost, titanium dioxide (TiO_2) is currently the most used photocatalyst. Possessing 3.2 eV as optical band gap, TiO_2 can absorb UV light ($\lambda < 387$ nm), which only makes up 5–8% of the whole solar spectrum. As a result, efforts have made on developing novel composite of TiO_2 with various components, such as carbon nanotubes, activated carbons, metal ions (Co, Ag, Au, etc.), and non-metals (nitrogen, carbon, sulfur, etc.). A good photocatalyst needs to have a low bandgap energy, with CB and VB at the proper positions to increase visible light activity. Other than that, a common problem with all the photocatalysts is their recovery from solution after use and thereafter their reuse, which restricts the scope of applications for photocatalysis [25–27].

Recently, magnetic materials have proven to be more useful for application of photocatalysis. The advantages of magnetic materials as photocatalysts over non-magnetic photocatalysts are their high efficiency, sustainability, and ease of preparation. When the particle size decreases (to nano-level), solid/liquid separation becomes increasingly challenging. On the other hand, magnetic filtering can be used for separation of catalyst from solution when using magnetic sorbents based on metal oxides. Additionally, using magnetic fields to remove particles from solutions is more efficient and effective (and frequently much faster) than centrifugation or filtering. The benefits of employing magnetic nanoparticles as an adsorbent in water treatment procedures include their high reusability, biocompatibility, selective solid/liquid

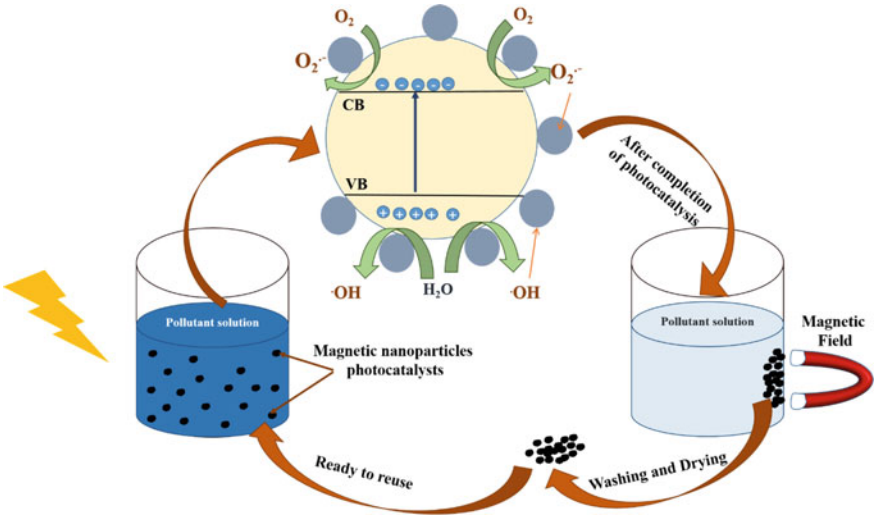

Fig. 4 Illustration of photocatalysis and removal of magnetic nanoparticles

separation using magnetic filtration, which is speedier than centrifugation and filtration procedures. However, the most important advantage of using magnetic materials is that catalysts are simply removed using a magnetic field from outside to separate the reaction liquid [28, 29]. The entire processes can be done with low cost in less time and improved reusability of the catalyst (Fig. 4).

Numerous types of magnetic materials have been fabricated, developed, and employed successfully in a variety of applications, including biomedicine, MRI, catalysis, spintronics, robotics, engineering, environmental remediation, etc. [2]. For a magnetic material being able to show best photocatalytic behavior under visible light, the following conditions must be satisfied:

- Their band gap should lie in the region of semiconductor (2–3 eV).
- Should be applicable at ambient temperature and pressures.
- Good selective adsorption.
- Lower rate of recombination of electrons and holes.
- Complete mineralization with no harmful by-products.

There are several methods to synthesize magnetic materials, including co-precipitation, solvothermal, hydrothermal, microemulsion, sonochemical, etc., which affect their magnetic properties, particle size, distribution, shape, and other characteristics. There are variety of metals which show magnetic properties, but the strongest magnetic materials consists of iron, cobalt, and nickel or their alloys [2]. All these magnetic photocatalysts are typically the composites made of magnetic material and non-magnetic photocatalytic material. In general, iron is used as one of the major components for the synthesis of magnetic photocatalysts. The most common and potentially useful magnetic minerals for water treatment are α-Fe_2O_3 (hematite),

β-Fe_2O_3 (maghemite), Fe_3O_4 (magnetite), and FeO (wustite) out of the eight known phases of iron oxides [30]. Initially, single-phase magnetic material such as Fe_2O_3 is used in environmental applications [31]. Rarely, reports are there on magnetic photocatalysts with a single phase that had high catalytic performance [32]. Most single-component, single-phase photocatalysts have a weak capacity for visible adsorption, which results in a low catalytic efficiency. Development of binary and ternary photoactive ferrites has been used to address this difficulty. The general formula for a material containing Fe^{3+} is MFe_2O_4, where M is a transition metal (Cu, Zn, Co, Mn, Ba, or Ni). Size- and shape-dependent magnetic response (saturation magnetization) of ferrites enables their utility as photocatalyst under external magnetic field. In terms of a photocatalytic application, the narrow band gap caused by the additional metal (M) enables ferrite as a very potent catalyst under visible radiation. Strong photocatalytic activity is demonstrated by ferrites, particularly when paired with other binary or photoactive materials such as $BiFeO_3$, $ZnFe_2O_4$, $CoFe_2O_4$, $NiFe_2O_4$ [33]. The examples of other binary ferrite photocatalysts along with synthesis method, pollutant, and efficiency of degradation are given in Table 1.

The interaction of a magnetic oxide with other oxide phase has also been extensively investigated as a way to produce highly photoactive materials. The catalytic activity can be significantly increased and charge recombination can be reduced when two different oxides are combined. Other than that, to overcome the difficulty of separation of photocatalyst along with the achievement of superior efficiency, combination of already available photocatalysts with the magnetic materials is came into existence. As TiO_2 is the most widely used catalyst, synthesis of magnetic photocatalyst in combination with TiO_2 has been studied broadly. For the very first time in 1994, Japanese patented the synthesis of Fe_3O_4/TiO_2 nanocomposites via titanium oxide deposition onto a magnetic core via hydrolysis of $TiOSO_4$, which led to its precipitation. Towata et al. in 1997 patented the dispersion of ferromagnetic particles in a TiO_2 suspension led to the creation of another magnetic photocatalyst [34]. Afterward, various researchers reported the deposition of photocatalyst onto magnetic core particles [35–38]. According to Beydoun et al. [35], charge carrier recombination of Fe_3O_4 could be caused by the contacts between the Fe oxide (core) and TiO_2 (shell) during illumination. Iron is less likely to be transported into the lower conduction band of the Fe_3O_4 core due to photogenerated electrons which are elevated to the conduction band of TiO_2. The iron oxide core's conduction band is preferred by the photogenerated holes in the valence band of TiO_2, which causes iron to oxidize and then leach iron ions into the solution. Therefore, it was concluded that interaction between magnetic Fe oxide and photoactive TiO_2 caused reduced photocatalytic activity when compared to solo TiO_2 against organic pollutant degradation. It was recommended to sandwich an inert layer between the magnetic core and TiO_2 shell to fend off photo-dissolution. The three-component photocatalyst is composed of three layers: (i) magnetic core, (ii) interlayer that prevents photo-dissolution and charge carrier recombination, and (iii) photocatalytic outer layer for the degradation of target molecule. Gad-Allah et al. [39] synthesized $TiO_2/SiO_2/Fe_3O_4$ composite as a magnetic photocatalyst in which silica was used as inert layer between TiO_2 and Fe_3O_4 to protect the magnetic and recombination of electron holes. In a similar

Table 1 Magnetic metal oxide-based photocatalysts with synthesis method, pollutant, and efficiency of degradation

Catalyst	Synthesis method	Saturation magnetization (emu/g)	Pollutant	Photocatalytic efficiency (%)	Ref.
Fe_3O_4@TiO_2	Hydrothermal	32.9	RhB	85	[43]
Fe_3O_4@MnO_2	Hydrothermal	–	Metal cations	88	[44]
$BiFeO_3$	Thermolysis	–	Doxorubicin	79	[45]
$ZnFe_2O_4$	Probe sonication	–	Acid red	98	[46]
$CoFe_2O_4$	Sol–gel	–	Reactive red	74	[47]
$NiFe_2O_4$	Co precipitation	31	Titan yellow	98.8	[48]
Fe_3O_4@ZnO	Hydrothermal	60.7	Phosphorous	92	[49]
Fe_3O_4@SnO_2	Hydrothermal	1.5	E. Coli inactivation		[50]
Fe_3O_4/g-C_3N_4	Hydrothermal	47.6	MB	98	[51]
Fe_3O_4@TiO_2	Sol–gel	–	Quinoline	95.6	[52]
Fe_3O_4@α-MnO_2	Two-step hydrothermal	39.9	BPA	92	[53]
Fe_3O_4@ZnO	Coprecipitation	24.2	AMX	90	[54]
rGO@Fe_3O_4@TiO_2	Sol–gel	–	MB	99	[55]
Fe_3O_4@MnO_2	Hydrothermal	32	Congo red	95	[56]
Cu@Fe@F_3O_4	Ball milling	38.56	MB	100	[57]
$CoFe_2O_4$	Wet chemical	–	4-nitrophenol	63	[58]
P25@graphene@Fe_3O_4	Solvothermal	5.26	RhB, MB, MO	100	[59]
TiO_2/$CuFe_2O_4$	Sol–gel		MB	57	[60]

manner, other reports also showed the use of silica or carbon as inert layer material between TiO_2 and magnetic core to form composite which was completely magnetically separable with high photocatalytic efficiencies [40–42]. Other material that has been extensively used as photocatalyst is zinc oxide (ZnO), which has a bandgap energy that is similar to that of TiO_2 (3.37 eV). Other benefits that have prompted researchers to extensively study its photoactivity include its electron mobility and inexpensive production costs. Researchers reported the synthesis of Fe_3O_4-embedded ZnO magnetic materials as semiconductor photocatalysts for wastewater treatment. Some other examples of important magnetic metal oxide-based photocatalysts with synthesis method, pollutant, and efficiency of degradation are given in Table 1.

Successful immobilization or covalent bonding of organic moieties and nonmetals, such as S, N, Cl, and P, onto magnetic photocatalysts has also been used to aid in the photodegradation of organic contaminants. It has been demonstrated that adding a well-selected organic modifier can produce a material with a greater

photoactivity than its pure inorganic counterpart. When a material is doped with a suitable dopant, such as N doping in TiO_2 photocatalyst leads to increased photoactivity. The substitution of N-atoms for oxygen in the lattice sites has been connected to an increase in photoactivity, and this will result to an occupied N_{2p} level above valence band of catalyst (O_{2p}). The semiconductor's new N_{2p} level is situated halfway between the valence and conduction bands enabling easier transportation of N_{2p} electrons to conduction band.

The common examples of organic/inorganic/magnetic photocatalysts involve the combination of ferrite with carbon, silica, poly(propylene oxide), polydopamine, poly(N-isopropylacrylamide), multiwalled carbon nanotubes, carbon spheres, graphene, etc., for usage in wastewater treatment via photocatalysis. Along with their appropriate magnetic properties—namely, being ferrimagnetic, ferromagnetic, and super paramagnetic (nanoparticle size < 10 nm)—their synthesis process is easy and inexpensive. According to their intended usage, these magnetic materials' size, shape, and magnetism may be easily changed, making it simple to disperse them in liquid media and maintain their stability for various applications. Additionally, these materials are biocompatible, chemically inert, thermally stable, and non-toxic or less hazardous [2].

In addition, numerous researches have been conducted in which the various magnetic properties, such as electron spin, external magnetic field, or size/morphology of the catalysts, were identified and might potentially have an impact on the photocatalytic efficiency of the magnetic material.

4 Properties of Magnetic Photocatalysts

The saturation magnetization, coercivity, magnetoresistance effect, etc. of magnetic materials' photocatalysts typically affect their effectiveness. These properties directly affect the rate of charge separation and recombination and hence the photocatalytic efficiency of the material. These properties are directly affected by externally applied magnetic field, tuning of electron spin, and size of the photocatalyst sample. In contrast to expectations, the photocatalytic process takes a period of 10^{-5}–10^{-3} s for the charge separation and transportation of excitons, which is significantly higher than the time of recombination (10^{-12}–10^{-3} s) in a typical semiconductor [61]. Here, the preparation of composite materials would solve the splitting and transfer of photoexcited electron–hole pairs-related issues. When a metal and semiconductor are combined, the semiconductor's energy band forms an interfacial electronic antiblocking layer, delaying the recombination of excitons. This results from the disparity between the Fermi level of the semiconductor and the work function of the metal. Another method to improve the separation and transmission of photogenerated electron–hole pairs is to apply an external magnetic field while the photocatalytic process is underway.

External magnetic field and Electron spin orientation

An acceptable, effective, non-contact way for increasing photocatalytic efficiency is to apply an external magnetic field. The magnetic field can alter the electrical configurations of the photocatalyst in its ground state, specifically the direction of the electron spin, in addition to producing the Lorentz force to split the photogenerated electrons and holes. Additionally, the chance that reaction intermediates will come into contact with catalyst-active sites is increased by an external magnetic field.

In case of non-ferromagnetic materials, external magnetic field does not impact electron spin orientation, and both show separate effect on the photocatalytic efficiency of the materials. When an external magnetic field is applied, a moving charged species in a magnetic field encounters a Lorentz force for non-ferromagnetic materials. Lorentz force is determined by the equation $F = q.v.B$, where q is the charge, v is the velocity, and B is the strength of the magnetic field. Light activates the electron–hole pairs during the photocatalytic reaction. They will experience opposing forces and deviate in the opposite direction when traveling in an external magnetic field as a result of their opposite charges. More carriers can interact with the catalyst surface and take part in the catalytic activity as a result of the longer lifetimes of electrons and holes.

Since charge and spin are two characteristics that electrons inherently possess. Spin orientations can be categorized as upward and downward, and inverse spin orientations will produce magnetic fields in the opposite direction. The electron spin states within a catalyst determine the electronic configurations of the catalyst's ground state, which in a notable way influence a catalyst's ability to absorb light, photogenerated carriers' splitting and recombination, and the intermedia species reaction barrier. Enhancing the effectiveness of electron transfer is possible through the dissipation-less spin transporting generated by spin polarization. Spin orientation can be tuned by adjusting the vacancies available in the catalyst via doping. In case of ferromagnetic sample, the spin orientation can be simply tuned by applying external magnetic field [62].

Electron spin states and outside magnetic fields have an impact on photocatalysis performance when ferromagnetic catalysts are exposed to a magnetic field. Electrons with spin preference can be produced by ferromagnetic catalysts, and these electrons will align with the external magnetic field. The interface of composite catalysts could easily permit the passage of electrons with precise spin alignments. A common trait is a negative magnetoresistance (MR) effect. The formula for MR can be given in Eq. (5) below:

$$\mathrm{MR} = [(R_H - R_0)/R_0] \times 100\%, \tag{5}$$

where the symbols R_H and R_0, respectively, stand for the resistances with and without a magnetic field. A substance exhibiting the MR effect can change its resistance when the magnetic field is present. Therefore, the resistance will drop in a magnetic field if a photocatalyst material displays a negative MR effect. A negative MR photocatalytic material will have its spin moments align parallel to one another in the presence

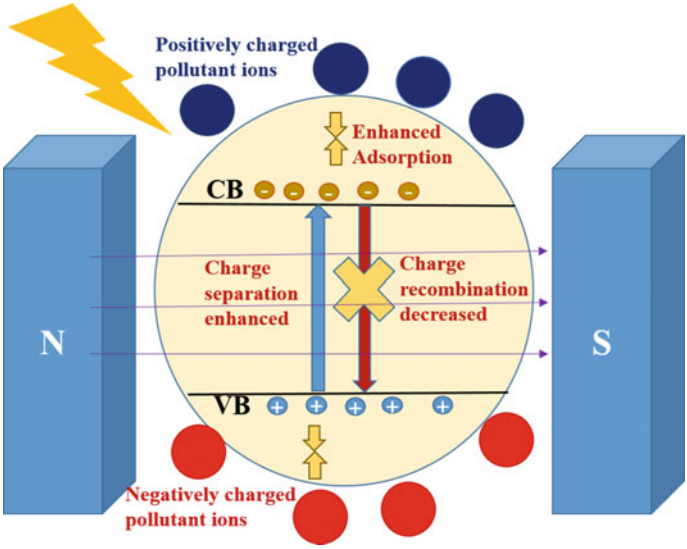

Fig. 5 Schematic of improved charge separation and enhanced photocatalysis via application of external magnetic field

of a magnetic field, which allows for more photogenerated carriers to participate in the surface photocatalytic processes. As a result, photogenerated carriers will be used more frequently, and photocatalytic performance will be improved with high sunlight conversion efficiency. In the meanwhile, a magnet can easily recycle photocatalysts having ferromagnetic properties [61, 63]. The schematic of charge separation with induced Lorentz force by applying external magnetic field and thus leading to enhanced photocatalytic activity is shown in Fig. 5.

Shi et al. [61] reported that hydrothermal and photoreduction methods used to create $ZnFe_2O_4$/Ag were used to deposit it on a 3D-cs substrate (to create 3D-cSZA) for increased surface area. In a 3D-cSZA photodegradation experiment, MO degraded 18% within 90 min and the photodegradation performance is further enhanced by the addition of a magnetic field, and at the same time, 24% of MO was degraded. Due to the photocatalyst's negative magnetic resonance (MR), when a magnetic field is provided, excessive electrons and holes can move to the surface to degrade pollutants, which are advantageous for increasing photocatalytic efficiency. Li et al. [64] reported the photocatalytic removal of Rhodamine B dye at equivalent rates of 59%, 74%, 83%, and 84% (magnetic fields 0, 3, 6, and 8 kOe, respectively) in the presence of α-Fe_2O_3/rGO nanocomposites. The applied magnetic field led to a notable increase in photocatalytic efficiency. In contrast, the photocatalytic efficiency of pure α-Fe_2O_3 was barely observed at zero magnetic field. When the α-Fe_2O_3/rGO nanocomposites were subjected to various magnetic fields, an apparent MR effect can be seen. While α-Fe_2O_3 nanoparticles did not exhibit MR impact due to alignment of magnetic

moment (α-Fe_2O_3 + rGO) and applied magnetic field lines, electronic spin orientation could easily pass through the resulted interface, which resulted in lowered resistance of α-Fe_2O_3/rGO nanocomposites when a magnetic field was applied. In a similar work, Wang et al. [65] used the composite photocatalyst of α-Fe_2O_3 and rGO (mass ratio, 10:1) in 1000 Oe magnetic field. The visible light-induced degradation efficiency of Congo red (CR) was improved from 60 to 87%. In comparison to pure α-Fe_2O_3, the composite photocatalyst had a greater negative MR and more vigorous magnetization intensity, according to magnetic behavior measurement. By applying a magnetic field, it was possible for the electrons with the precise spin alignments to flow over the contact with ease. He et al. [63] prepared $ZnFe_2O_4$/AgBr magnetic photocatalyst. The % degradation of Congo red using the synthesized photocatalyst without the external magnetic field was 40% in 90 min. The photodegradation efficiency of $ZnFe_2O_4$/AgBr was significantly increased by applying 1000 Oe of magnetic field; 53% of condo red was photodegraded in just 90 min. It was observed that only AgBr catalyst showed no changes in their photocatalytic efficiency with variation in magnetic field. Also, pure $ZnFe_2O_4$ showed significant enhancement in the photoactivity with external applied magnetic field. Therefore, it was concluded that due to its greater negative MR, $ZnFe_2O_4$/AgBr has the maximum photocatalytic activity when exposed to a magnetic field.

Hence, adding the magnetic field to photocatalytic processes is a useful and effective way to increase the efficiency of solar energy conversion while also improving adsorption on surfaces and charge separation.

Size and Morphology

The particle size induced magnetic features, e.g., coercivity and saturation magnetization, has already been well-documented. Depending on the material, saturation magnetization and coercivity for small nanoparticles up to a threshold size have been observed to increase as particle size has risen. The following equation gives the separating magnetic force (F_m) operating on the particles from solution with the help of external magnetic field:

$$F_m = \mu_0 . V_p . (M_p . N) H_a, \tag{6}$$

where V_p and M_p are the particle's volume and magnetism, respectively, and H_a is applied magnetic field strength. Therefore, the force needed to separate the magnetic particles from the solution increases with respect to increased particle size. The surface-to-volume ratio is decreased by increasing particle diameter, which lowers the photocatalytic material's effectiveness. So, in order to obtain the desired outcomes in these methods: improved photochemical kinetics and magnetic recovery, these parameters must be regulated [66].

The factors such as size, coercivity, saturation magnetization, which directly affect their performance, are influenced by the morphology of the nanoparticles in addition to the size and nature of the material. Exploring various nanomaterials morphologies is therefore vital to fully comprehend the potential benefits and drawbacks that each

one of them may have in relation to applications. The foundation for the development of advanced multicomponent magnetic systems will be the structure–properties relationship as well as the selection of synthesis techniques in terms of resilience, particle size uniformity, scalability, and chemical characteristics. The saturation magnetization directly affects the magnetic moment which in turns consequences the photocatalytic activity of the magnetic materials. An increase in photocatalytic degradation is related to the maximum net magnetic moment [67]. The cube-shaped particles exhibit the highest saturation magnetization, while rod-like particles exhibit the lowest, notwithstanding the difficulty in accurately controlling the morphology, particle size, and crystallinity of the nanosized particles [68]. Baghshahi et al. [68] reported that after 120 min of exposure to light, the photocatalytic MB removal efficiency of Fe_3O_4-TiO_2 NPs was greater than 90, 73, and 64% (spherical, cube, and rods, respectively). On the contrary, in another report by Baghshahi et al. [69], magnetite nanoparticles of different morphologies were developed by hydrothermal method with magnetic saturation of 60.74, 66.36, and 35.11 emu/g for the sphere, cube, and rod-like morphologies. The results were interpreted in terms of particle size, and the greater critical size of rod-shaped nanoparticles can be used to explain the magnetic drop in saturation. In contrast to spherical nanoparticles, the magnetic saturation of cubic nanoparticles rises with size.

Only a very few reports are available in which the effect of morphology in correlation with particle size of magnetic materials on their photocatalytic activity is explained. The variation in morphology contributes in the saturation magnetization of the magnetic material which in turn affects its photocatalytic activity, but the results are dependent on particle size too. In conclusion, both particle size and morphology play altogether to put an impact on the saturation magnetization and thus photocatalytic activity of the magnetic material.

5 Conclusion

This chapter explains how magnetic materials' structure–property connection affects their photocatalytic efficiency for removing organic contaminants from aqueous solutions. The availability of drinkable water is still a problem for mankind, aquatic vegetation, and animals. In this context, research teams have found a number of techniques for recycling spent water. Among them, the oxidation of organic pollutants (such as dyes, pigments, pesticides) by photocatalysis appears simple and quick, and it produces non-toxic by-products. The role of semiconducting magnetic nanoparticle in the photocatalysis has been explained in detail. Different types of magnetic materials, viz ferrites, their organic, inorganic, metallic composites, and their role in photocatalysis have been discussed thoroughly. However, a very few researchers studied the influence of these catalysts' magnetic properties on photocatalytic activity. In case of non-ferromagnetic materials, external magnetic field does not impact electron spin orientation, and both show separate effect on the photocatalytic efficiency of the materials. Electron spin states and outside magnetic fields have an impact on the

efficiency of photocatalysis when ferromagnetic catalysts are exposed to a magnetic field. Spin-preferential electrons can be produced by ferromagnetic catalysts, and these electrons will align with the surrounding magnetic field. The common trait is negative MRs. More photogenerated carriers can take part in the surface photocatalytic processes because a negative MR photocatalytic material will have its spin moments align parallel to one another in the presence of a magnetic field. As a result, photogenerated carriers will be used more frequently, and high sunlight conversion efficiency will enhance photocatalytic activity. Other than external magnetic field, effect of particle size and morphology on their photocatalytic activity was also discussed. It was concluded that the variation in morphology influences the saturation magnetization of the magnetic material, which in turn impacts its photocatalytic activity, but the outcomes also depend on particle size. To achieve a suitable magnetic performance for such photocatalytic applications, magnetic particles must be of the appropriate sizes and have a morphology that exhibits high saturation magnetization.

References

1. Saharan VK, Pinjari DV, Gogate PR, Pandit AB (2014) Advanced oxidation technologies for wastewater treatment: an overview. Elsevier Ltd
2. Sharma M, Kalita P, Senapati KK, Garg A et al (2016) Emerging pollutants—some strategies for the quality preservation of our environment, vol 11, pp 61–78
3. UNICEF. https://www.unicef.org/wash/water-scarcity
4. WHO. https://www.who.int/news-room/fact-sheets/detail/drinking-water
5. Song X, Wang Y, Wang K, Xu R (2012) Ind Eng Chem Res 51:13438
6. Yin J, Pei M, He Y, Du Y, Guo W, Wang L (2015) RSC Adv 5:89839
7. Konicki W, Cendrowski K, Bazarko G, Mijowska E (2015) Chem Eng Res Des 94:242
8. Bedin KC, Martins AC, Cazetta AL, Pezoti O, Almeida VC (2016) Chem Eng J 286:476
9. Kundu S, Chowdhury IH, Naskar MK (2018) J Chem Eng Data 63:559
10. Lazo-Cannata JC, Nieto-Márquez A, Jacoby A, Paredes-Doig AL, Romero A, Sun-Kou MR, Valverde JL (2011) Sep Purif Technol 80:217
11. Chen A, Li Y, Yu Y, Li Y, Xia K, Wang Y, Li S, Zhang L (2016) Carbon N Y 103:157
12. Song X, Gunawan P, Jiang R, Leong SSJ, Wang K, Xu R (2011) J Hazard Mater 194:162
13. Gong J, Liu T, Wang X, Hu X, Zhang L (2011) Environ Sci Technol 45:6181
14. Quach-Cu J, Herrera-Lynch B, Marciniak C, Adams S, Simmerman A, Reinke RA (2018) Water 10:13
15. Jayalekshmi JS, Minnu Biju SJ, Ajas DS, Muhammad PE (2021) Int J Eng Res Technol 1:3
16. Zhu M, Lee L, Wang H, Wang Z (2007) J Hazard Mater 149:735
17. Abid MF, Zablouk MA, Abid-Alameer AM (2012) J Environ Heal Sci Eng 9:1
18. Teh CY, Budiman PM, Shak KPY, Wu TY (2016) Ind Eng Chem Res 55:4363
19. Banerjee S, Sharma GC, Gautam RK, Chattopadhyaya MC, Upadhyay SN, Sharma YC (2016) J Mol Liq 213:162
20. Atchariyawut S, Phattaranawik J, Leiknes T, Jiraratananon R (2009) Sep Purif Technol 66:153
21. Vlyssides AG, Loizidou M, Karlis PK, Zorpas AA, Papaioannou D (1999) J Hazard Mater B70:41
22. Qu Y, Shi S, Ma F, Yan B (2010) Bioresour Technol 101:8016
23. Nageeb M (2013) Organic pollutants—monitoring, risk and treatment
24. Ren G, Han H, Wang Y, Liu S, Zhao J, Meng X, Li Z (2021) Nanomaterials 11
25. Ambashta RD, Sillanpää M (2010) J Hazard Mater 180:38

26. Zielińska-Jurek A, Bielan Z, Dudziak S, Wolak I, Sobczak Z, Klimczuk T, Nowaczyk G, Hupka J (2017) Catalysts 7
27. Masunga N, Mmelesi OK, Kefeni KK, Mamba BB (2019) J Environ Chem Eng 7:103179
28. Abdel Maksoud MIA, Fahim RA, Bedir AG, Osman AI, Abouelela MM, El-Sayyad GS, Elkodous MA, Mahmoud AS, Rabee MM, Al-Muhtaseb AH, Rooney DW (2022) Engineered magnetic oxides nanoparticles as efficient sorbents for wastewater remediation: a review, vol 20. Springer International Publishing
29. Orge CA, Soares OSGP, Ramalho PSF, Pereira MFR, Faria JL (2019) Catalysts 9
30. Singh P, Sharma K, Hasija V, Sharma V, Sharma S, Raizada P, Singh M, Saini AK, Hosseini-Bandegharaei A, Thakur VK (2019) Mater Today Chem 14:100186
31. Jacinto MJ, Ferreira LF, Silva VC (2020) J Sol-Gel Sci Technol 96:1
32. Wu T, Liu L, Pi M, Zhang D, Chen S (2016) Appl Surf Sci 377:253
33. Díez AG, Rincón-Iglesias M, Lanceros-Méndez S, Reguera J, Lizundia E (2022) Mater Today Chem 26
34. Towata A, Sando M (1997)
35. Beydoun D, Amal R, Low GKC, McEvoy S (2000) J Phys Chem B 104:4387
36. Abbas M, Parvatheeswara Rao B, Reddy V, Kim C (2014) Ceram Int 40:11177
37. Wei JH, Leng CJ, Zhang XZ, Li WH, Liu ZY, Shi J (2009) J Phys Conf Ser 149:012083
38. Zhang L, Wu Z, Chen L, Zhang L, Li X, Xu H, Wang H, Zhu G (2016) Solid State Sci 52:42
39. Gad-Allah TA, Fujimura K, Kato S, Satokawa S, Kojima T (2008) J Hazard Mater 154:572
40. Shi F, Li Y, Zhang Q, Wang H (2012) Int J Photoenergy 2012
41. Fan Y, Ma C, Li W, Yin Y (2012) Mater Sci Semicond Process 15:582
42. Yuan Q, Li N, Geng W, Chi Y, Li X (2012) Mater Res Bull 47:2396
43. Shi L, He Y, Wang X, Hu Y (2018) Energy Convers Manag 171:272
44. Zhao J, Liu J, Li N, Wang W, Nan J, Zhao Z, Cui F (2016) Chem Eng J 304:737
45. Dumitru R, Ianculescu A, Păcurariu C, Lupa L, Pop A, Vasile B, Surdu A, Manea F (2019) Ceram Int 45:2789
46. Surendra BS, Shashi Shekhar TR, Veerabhadraswamy M, Nagaswarupa HP, Prashantha SC, Geethanjali GC, Likitha C (2020) Chem Phys Lett 745:137286
47. Parhizkar J, Habibi MH, Mosavian SY (2019) SILICON 11:1119
48. Bameri I, Saffari J, Baniyaghoob S, Ekrami-Kakhki MS (2022) Colloids interface. Sci Commun 48:100610
49. Li N, Tian Y, Zhao J, Zhan W, Du J, Kong L, Zhang J, Zuo W (2018) Chem Eng J 341:289
50. Karunakaran C, SakthiRaadha S, Gomathisankar P, Vinayagamoorthy P (2013) Powder Technol 246:635
51. Liu X, Zhang T, Xu D, Zhang L (2016) Ind Eng Chem Res 55:11869
52. Jing J, Li J, Feng J, Li W, Yu WW (2013) Chem Eng J 219:355
53. Dong Z, Zhang Q, Chen BY, Hong J (2019) Chem Eng J 357:337
54. Dehghan S, Kakavandi B, Kalantary RR (2018) J Mol Liq 264:98
55. Banerjee S, Benjwal P, Singh M, Kar KK (2018) Appl Surf Sci 439:560
56. Yang Q, Song H, Li Y, Pan Z, Dong M, Chen F, Chen Z (2017) J Mol Liq 234:18
57. Yingzhe Z, Yuxing H, Qingdong Q, Fuchun W, Wankun W, Yongmei L (2018) Superlattices Microstruct 118:123
58. Sun M, Han X, Chen S (2019) Mater Sci Semicond Process 91:367
59. Cheng L, Zhang S, Wang Y, Ding G, Jiao Z (2016) Mater Res Bull 73:77
60. Li H, Zhang Y, Wang S, Wu Q, Liu C (2009) J Hazard Mater 169:1045
61. Shi C, Wang Y, He J, Feng D, Zhang R, Zheng L, Yang Z, Li H, Pan P, Zhao J, Zhang K, Cheng Y, Liu H (2022) Ceram Int 48:32314
62. Peng C, Fan W, Li Q, Han W, Chen X, Zhang G, Yan Y, Gu Q, Wang C, Zhang H, Zhang P (2022) J Mater Sci Technol 115:208
63. He J, Wang Y, Shi C, Wang M, Cao Z, Zhang R, Sun X, Bo J, Li W, Yang Z, Feng D, Zheng L, Pan P, Li H, Bi J, Zhao J, Zhang K, Cheng Y, Liu H (2022) Sep Purif Technol 284:120263
64. Li J, Pei Q, Wang R, Zhou Y, Zhang Z, Cao Q, Wang D, Mi W, Du Y (2018) ACS Nano 12:3351

65. Wang Y, Wang S, Wu Y, Wang Z, Zhang H, Cao Z, He J, Li W, Yang Z, Zheng L, Feng D, Pan P, Bi J, Li H, Zhao J, Zhang K (2021) J Alloys Compd 851:156733
66. Gómez-Pastora J, Dominguez S, Bringas E, Rivero MJ, Ortiz I, Dionysiou DD (2017) Chem Eng J 310:407
67. Cervera-Gabalda L, Zielińska-Jurek A, Gómez-Polo C (2022) J Magn Magn Mater 560:0
68. Baghshahi S, Yousefi F (2022) Trans Indian Ceram Soc
69. Baghshahi S, Yousefi F (2021) J Supercond Nov Magn 34:1949

Chapter 5
Ferrite Nanoparticles for Hyperthermia Treatment Application

Vineet Kumar, Nitesh Kumar, Manu Vineet Sharma, Sunil Kumar, and Attuluri Vamsi Kumar

1 Introduction

Because of biocompatibility and durable magnetic activity, nanoferrites are frequently used in biomedical applications, especially in magnetic hyperthermia treatments [1]. Through the use of dopant materials, biocompatible coatings, and preparation techniques, the effectiveness of nanoferrites is examined. Nanoferrites, which are known for having an exceptional heating mechanism, have been frequently employed in magnetic hyperthermia to destroy tumor cells [2]. Furthermore, the utility of nanoferrites in cancer treatments, magnetic hyperthermia inflict unambiguous necessities [3]. Dopant materials, biocompatible overlays, and preparation procedures are used to examine the performance of nanoferrites [4]. Due to having a specific characteristics, nanoferrites are frequently used in the treatment of various medical ailments in required amount [5].

Identifying the restrictions, delivering innovative nanoformulative materials which enhance magnetic characteristics by placing a biocompatible surface and magnetic nanoferrites are more efficient and performed better [6]. Research on these

V. Kumar (✉)
Department of Zoology, Dr. Yashwant Singh Parmar Govt. P.G. College Nahan, Himachal Pradesh, Sirmour 173001, India
e-mail: vineetkatoch975@gmail.com

N. Kumar
Department of Biosciences, Himachal Pradesh University, Summer Hill, Shimla, Himachal Pradesh 171005, India

M. V. Sharma
Department of Botany, Career Point, University, Hamirpur, Himachal Pradesh 176041, India

S. Kumar
ICMR-Regional Medical Research Centre, Gorakhpur, Uttar Pradesh 273013, India

A. V. Kumar
Department of Medical Lab Technology, Chandigarh University, Kharar, Punjab 40413, India

P. Sharma et al. (eds.), *Engineered Ferrites and Their Applications*, Materials Horizons: From Nature to Nanomaterials, https://doi.org/10.1007/978-981-99-2583-4_5

nanoferrite materials should be assessed in order to determine their application and efficacy in the treatment of various malignancies.

1.1 Ferrite Nanoparticles

Due to its numerous applications in a various disciplines, extending from biomedical to industrial, ferrite nanoparticles (FNPs), which are a large subgroup of magnetic nanoparticles (MNPs), have drawn a lot of attention. Fenton-like oxidation is one of the advanced oxidation processes (AOPs) that may effectively take away a range of contaminants from water. Spinel ferrite nanoparticles (SFs) have piqued the interest of researchers. Due to their unique physicochemical features, low cost, high catalytic activity, and interesting band gap have garnered a great deal of interest in recent years for use as a catalyst in this process. Similarly, their magnetic qualities allow for quick, simple, and low-cost separation from the reaction liquid [1–3].

The usage of many spinel ferrite nanoparticles as MFe_2O_4 has limitless potential as a catalyst in heterogeneous Fenton- and photo-Fenton-like oxidation. The use of spinel ferrite nanoparticles (SFNPs) to purify wastewater and water sources is done by using the magnetic and structural properties of these ferrimagnetic systems [4]. Additionally, the revival and recycling advantages of using ferrite nanoparticles in waste water treatment are due to the role of spinel ferrites in the photodegradation of organic molecules [2, 3, 5]**.**

It is necessary to identify the restrictions, and two potential solutions include developing innovative nanocomposite materials with improved magnetic characteristics due to the use of a biocompatible over lamina, as well as magnetic nanoferrites with improved performance and utility [6–10]. Ferrite nanoparticles are beneficial and depict very precise amalgamation rate for magnetic hyperthermia utilization.

"Nanoparticles" were formed by using a technique known as chemical co-precipitation. Manganese zinc ferrite (MZF) nanoparticles (NPs) were set up and used in the application of hyperthermia at room temperature [11–15]. The manufactured "ferrofluids" material could be employed to treat magnetic hyperthermia because heating potential may be reached within 65 s of hyperthermia temperature (42 °C) at lower 4 mg/mL levels. Due to their high heat-generating ability in a short time at a low concentration, the produced MZF nanoparticles offer a viable option for hyperthermia treatment [3, 7, 16]. Cobalt–zinc ferrite nanoparticles were devised by various techniques, and the produced NPs were comprehensively characterized on the basis of their utility [1, 14–16].

Heat production is considered to be caused by hysteresis, and CeGdZn–ferrite nanoparticles experience a decrease in temperature because ferromagnetic nanoparticles should experience diminishing returns on temperature rise. Future uses of cerium oxide nanoparticles with integrated gadolinium are highly promising due to their medicinal and diagnostic capabilities.

Ferrite nanoparticles (FNPs) have vast applications in a variety of sectors, including biomedicine, wastewater treatment, catalysis, and electrical devices [15,

17, 18]. Use of FNPs in electronic devices places a stronger emphasis in electronic materials such high-density recording medium, energy storage, microwave devices, and electromagnetic interference shielding [19–27]. Condition is recognized if a patient's fever is less than 95 °F (thirty-five degrees Celsius). Hypothermia, which can affect people of any age, is usually brought on by exposure to elements of cold weather like snow and ice. In addition, immersion in cold water may cause it [28]. As a result, studies on these nanoferrite materials are being conducted to determine their use and efficacy in cancer treatment. Future options for cancer therapy may include the improved ferrite-based nanoformulation, which increases their effectiveness in biological molecules [29–34].

2 Hyperthermia

The equilibrium between heat production and heat loss controls body temperature. All metabolic activities produce heat inside, and when surrounding temperatures are higher than body temperature, heat is evacuated from the nearby atmosphere [35]. The body's surfaces disperse heat. The skin is the most significant location for heat loss, although the lungs also contribute. Hyperthermia occurs when a person's body temperature increases above 37.5–38.3 °C (99.5–100.9 °F) without a change in internal body temperature. When thermoregulation fails, temperatures rise above normal. In the late afternoon, an adult's body temperature can reach 37.7 °C (99.9 °F) [36]. Hyperthermia is defined by an abnormally high body temperature, and at such elevations, body temperatures if exceeding 40 °C (104 °F) can be fatal [37].

More heat is produced or used by the body than is released. When the temperature rises too high, it turns into a medical emergency that needs to be treated right once to prevent death. The annual death toll from hyperthermia is around 500,000 [38]. When the body's heat-regulating mechanisms are overloaded by a fast temperature rise brought on by strong heat or a combination of heat and humidity, severe drug reactions and heat stroke occur [39]. The latter is an uncommon side effect of several medications, particularly those that affect the central nervous system. A rare adverse consequence of various types of general anesthesia is found in malignant hyperthermia. Additionally, a severe brain damage might cause hyperthermia. The fact that the body's temperature does not fluctuate distinguishes hyperthermia from fever [40].

2.1 Types of Hyperthermia

Hyperthermia is a condition where the body temperature rises above its normal range due to an external heat source. All forms of hyperthermia can be life-threatening if not properly treated (Fig. 1).

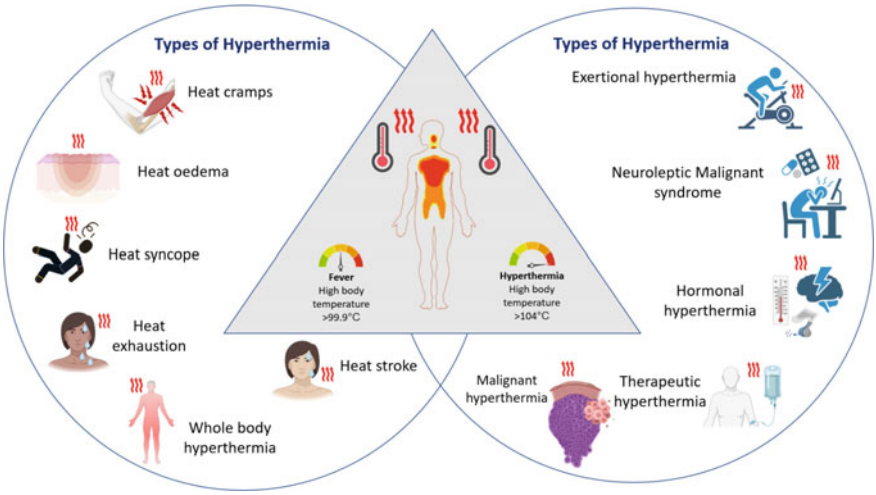

Fig. 1 Types of hyperthermia. *Source* created in BioRender.com

2.1.1 Heat Cramps

Excruciating muscular spasms in the arms, legs, or stomach during severe exertion, pulse rate is usually normal or rapid, and the skin is chilly and damp. The body maintains its regular temperature [38].

2.1.2 Heat Edema

A cutaneous ailment called heat edema is characterized by dependent vasodilator-induced pooling edema [38]. Heat dilates or expands blood vessels, which allows fluid from the body to fall into the hands or legs. A risk factor for heat edema is also the body's salt balance. The higher salt level pushes fluid into the hands and legs if salt removal is less than usual. Older persons are more susceptible to developing heat edema, particularly if they suffer from other medical disorders that impair their blood flow. A higher risk of heat edema may also exist for travelers from colder climes [41].

2.1.3 Heat Syncope

Heat syncope is fainting or light headedness brought on by overheating. The primary sign of heat syncope is fainting, whether or not it is accompanied by mental confusion. Peripheral artery dilatation, which results in reduced blood supply to the brain and dehydration, is the primary cause of heat syncope [42].

2.1.4 Heat Exhaustion

The skin might be chilly and wet. The heart rate will be quick and feeble, and the breathing will be quick and shallow. Heat exhaustion can lead to heat stroke if left untreated. Heavy sweat, pallor, muscular cramps, lethargy, weakness, disorientation, headache, nausea or vomiting, fainting, and other heat exhaustion symptoms are possible [38].

2.1.5 Heatstroke

A core body temperature of more than 40 °C (104 °F) and central nervous system involvement (delirium, decreased level of awareness, or ataxia) are two characteristics of heat stroke, which carries a risk of death. The body quickly heats up, the sweating mechanism malfunctions, and the body is unable to cool down when the body's capacity to regulate its temperature is compromised. In 10–15 min, a body temperature spike of 106 °F or more is possible [43]. When symptoms start to appear, it is imperative to seek prompt medical attention due to the extremely high morbidity and death rates associated with heat stroke. Even if the temperature returns to normal, heat stroke can be lethal. Heat shock protein release and a heightened immunological response may lead to intravascular coagulation and multiple organ failure. It is prudent to plan for acute renal failure. Patients who survive heat stroke frequently suffer from neurological dysfunction [44]. The following are some signs of heat stroke to watch out for: body temperature of higher than 40 °C (104 °F), a change in behaviour, such as agitation, hostility, or other odd behaviours; fainting, which is typically a warning sign; There is no perspiration despite the heat, a strong, fast pulse that later became slow and weak, as well as dry, flushed skin from vascular collapse, chilly skin, abnormalities in the electrocardiogram indicate cardiac injury, dizziness, or coma [45].

2.1.6 Exertional Hyperthermia

A physiological reaction to vigorous exercise is hyperthermia. Skeletal muscles can consume 20 times more energy when they are operating at maximum effort. Because the body only consumes around 25% of the energy utilized by muscles, a significant percentage of that energy is converted to heat, which is subsequently transferred from the muscle to the blood, increasing core temperature. Sweating and cutaneous vasodilation both help to expel heat. Accustomed athletes can evaporate up to 900 kcal per hour and create up to 2 L of sweat each hour [46]. However, environmental temperature and humidity have an upper limit on the capacity of compensating systems. Volume depletion also inhibits heat dissipation, but exertional hyperthermia is more accurately predicted by exercise volume than by dehydration level [46].

2.1.7 Neuroleptic Malignant Syndrome

Approximately 0.2% of individuals on neuroleptic medicines develop neuroleptic malignant syndrome, usually during the first 30 days of treatment [47]. Among the various phenothiazines, butyrophenones, and thioxanthenes connected to the condition, haloperidol is the most frequently implicated. The neuroleptic malignant syndrome is most likely caused by dopaminergic receptor blockage in the corpus striatum, which induces skeletal muscle stiffness, inhibits hypothalamic thermoregulation, and causes autonomic dysfunction, all of which influence heat dissipation [48].

Any patient using neuroleptic medications is at risk of developing the atypical response known as neuroleptic malignant syndrome. Hyperthermia causes a rise in body temperature exceeding 41 °C. Muscle stiffness, drug-induced movement disorders, changed awareness, and autonomic dysfunction may appear between 24 and 72 h (labile hypertension, diaphoresis, tachyarrhythmia, and incontinence). Hemoconcentration with increase in the number of white blood corpuscles, high concentration of sodium in blood, acidosis, electrolyte abnormalities, breakdown of muscle tissue, impaired kidney and liver function are among the laboratory findings [24].

2.1.8 Hormonal Hyperthermia

The most frequent endocrinologic cause of hyperthermia is thyrotoxicosis. Despite having hypermetabolism, thyrotoxicosis patients typically have normal or barely raised body temperatures [45]. Rectal temperatures of more than 40 °C are common during a thyrotoxic crisis [49]. Because a thyrotoxic crisis is frequently preceded by stress, all patients with this severe kind of thyrotoxicosis should be screened for concurrent illnesses. Catecholamines, like thyroid hormones, increase body temperature. During a pheochromocytoma crisis, hyperthermia can be dangerous, especially if increased norepinephrine levels produce hypermetabolism and cutaneous vasoconstriction. Adrenal insufficiency, hypoglycemia, and hyperparathyroidism have all been linked to moderate hyperthermia [49].

2.1.9 Therapeutic Hyperthermia

Traditional but unproven treatment for several musculoskeletal problems is regional hyperthermia [46]. Despite evidence that higher temperatures in humans boost a number of host defense systems, for a long time, fever treatment for infectious disorders has been discontinued [14]. However, nasal heating for viral nasopharyngitis is gaining popularity. Cancer adjuvant treatment using therapeutic hyperthermia is being investigated [5]. In 17% of individuals with recurrent superficial metastases, regional heat alone resulted in full remission and partial remissions in 23% of cases; however, these responses are often transitory. Less study has been conducted on the consequences of complete body hyperthermia. It is reported that medical data on the

maximum limits of tolerance are few, despite the fact that body temperatures have been elevated to 42.4 °C for up to four hours using a variety of methods [50].

2.1.10 Local Hyperthermia

It concentrates on relatively small tumors (3 to 5–6 cm in length) that are exposed or in cavities of the body that are easily accessible, like the rectum or esophagus [51]. Most frequently, supraficial, interstitial, intraminal, or intracavital applicators are utilized to provide heat to tumors using microwaves, radio waves, or ultrasound [51]. While normal tissue is sufficiently spared, local techniques can be used to heat small cancerous patches. Negative effects during hyperthermia sessions are avoided by concurrent cooling with water boluses, which maintains skin temperature at a level of about 37 °C and ensures electromagnetic connection of the applicator to the tissue. There is consequently less skin blistering and burning.

2.1.11 Regional or Part-Body Hyperthermia

It is a term for heating substantial body parts, such as the abdominal cavity, particular organs, or limbs, and is frequently applied to the treatment of well-developed tumours found in the pelvis, abdomen (carcinomas of the cervix, prostate, bladder, colorectal, and ovaries), or thighs (soft tissue sarcomas).

2.1.12 Whole-Body Hyperthermia (WBH)

A high body temperature is supposed to kill or drug-sensitize malignant cells that have spread throughout the body. Thermal chambers, hot water blankets, or infrared radiators are utilized to attain that goal (about 41.8–42.2 °C), along with the prevention of temperature loss and the restoration of electrolyte fluids [52].

2.1.13 Malignant Hyperthermia

Given a particular mix of sedatives and anesthetic during a medical treatment, malignant hyperthermia, a genetic disease, can make you susceptible to hyperthermia. During or after surgery, your body temperature may dangerously increase. A reaction to some drugs may occur in people with malignant hyperthermia the first time they are exposed to them, although it usually happens after multiple exposures. Anesthetics have an MH reaction frequency range of 1 in 10,000–1 in 250,000 [53]. It is estimated that as many as one in every 400 people has a genetic abnormality. The canine, equine, horse, and human populations are all at risk for developing MH. Classic MH symptoms result from a hypermetabolic reaction and include high body temperature, rapid heart rate, shallow breathing, increased carbon dioxide generation

and oxygen demand, acidosis, hyperkalemia, muscle stiffness, and rhabdomyolysis. If untreated, the condition is potentially fatal. The disease is recessive in pigs and dominant in humans. An unregulated rise in myoplasmic calcium causes pathophysiological changes by stimulating metabolic pathways associated with muscle activity [43, 53]. The ryanodine receptor is usually the cause of the disease. Approximately 400 variations in the RYR1 gene on chromosome 19q13.1 have been linked to MH.CACNA1S which has less than 1% variants; however, not all of them are causal. Muscle biopsy in vitro contracture response is utilized in diagnostic testing [46].

For vulnerable patients receiving general anesthesia with volatile medications, MH remains a severe risk factor. Various environmental factors and gene associated with MHS causes were identified. The reduced incidence of MH mortality and the effect of statin medications suggest that genetic variants previously linked with anesthetic-induced MH may now be associated with a considerably broader range of clinical manifestations. More research is needed to determine whether long-term mild hyperthermia therapy affects the activities of enzymes in various pathways linked to tumor cell metabolism and proliferation, stimulates immunology factors such as hsp70, which may activate the body's defense mechanisms, and specifically eliminates tumor cells. Tumor tissue's blood perfusion might rise from 1.5 to 2 times more under moderate hyperthermia (41–42 °C, 30 min) before the therapy.

3 Symptoms of Hyperthermia

The symptoms of hyperthermia vary depending on the type and severity of the condition (Fig. 2).

- Elevated core temperature.
- A splitting headache.

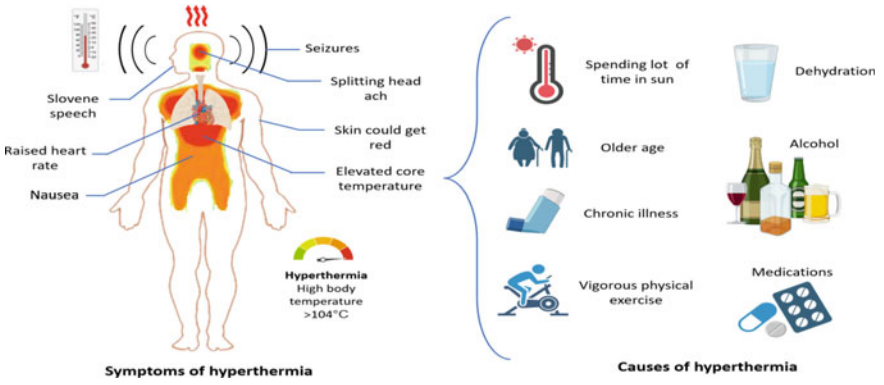

Fig. 2 Symptoms and causes of hyperthermia. *Source* created in BioRender.com

- The skin could get red.
- Irritability.
- Slovene speech.
- Seizures.
- Quick breathing.
- Nausea.
- Raised heart rate.

4 Causes of Hyperthermia

There are numerous causes of hyperthermia. A key reason is spending a lot of time in the sun. It mainly affects older persons and those who are chronically unwell and results in raised body temperature. Increased body temperature brought on by vigorous physical exercise in hot conditions is another cause of hyperthermia. This could happen to someone who is not used to the temperature and engages in strenuous activity. In hot temperatures, wearing too many clothes stops the body from perspiring and cooling off. Hyperthermia may also result from it. Alcohol use may impact how well the body cools. The body can become dehydrated through a lack of fluid consumption, which can potentially cause hyperthermia. Even taking some drugs can make you feel hot [14] (Fig. 2).

5 Hyperthermia Risk

Hyperthermia is more likely to occur in some people than others. Some of these include: drink too much alcohol; have electrolyte imbalances in their bodies; work in hot environments; dress tightly in the summer; struggle to sweat, cystic fibroid; under the age of four; over the age of 65; and long-term medical illnesses (heart, lung, kidney, or liver concerns) [54].

6 Diagnosis of Hyperthermia

A history that supports hyperthermia rather than a fever and an unusually high body temperature is typically used to diagnose hyperthermia [2]. Most frequently, this indicates that the individual had a heat stroke or was using a medication known to cause hyperthermia when their temperature rose (drug-induced hyperthermia). When determining the diagnosis, it is also taken into account whether there are signs and symptoms typical of fever-associated infections, such as extra pyramidal symptoms of neuroleptic malignant syndrome, which are related to hyperthermia syndromes.

Hyperthermia is disregarded if fever-reducing medications cause a drop in body temperature, even if the temperature does not fully return to normal [41].

7 Hyperthermia Treatment

Moving the patient to a cooler location is the first line of treatment for hyperthermia. The temperature can be lowered by submerging the patient in cool water or applying ice packs to their armpits, necks, or groynes. Evaporative cooling techniques can also be used effectively. Doctors spritz the patient with cool water and blast air over their entire body as part of this treatment. During this time, doctors may stop prescribing any drug. The medical professional might suggest flushing the body cavity with cool water and injecting IV fluids.

Due to their biocompatibility and permanent magnetic behavior, nanoferrites are widely used as top thermoseeds in biomedical applications, particularly in magnetic hyperthermia therapies. By using dopant materials, biocompatible overlays, and preparation techniques, the effectiveness of nanoferrites is examined. Therefore, this chapter examined the use of nanoferrites in the management of hypothermia therapy using nanoferrites made from various herbal preparations [8, 24, 30, 55].

8 Ferrite Nanoparticles for Biomedical Applications

Due to its use in several disciplines, notably the biomedical one where their increased magnetic properties allow for a range of imaging, diagnostic, and treatment options, ferrites, which are iron oxide nanoparticles, have fascinated a lot of interest lately. The high magnetic anisotropy and biocompatibility of ferrites based on Co, Ni, and Zn have shown potential for use in biomedical applications, despite the fact that many other kinds of ferrites have been developed and suggested for use in a variety of applications. There are several ways to create ferrites' nanoparticles, including hydrothermal sol–gel and co-precipitation. These methods produce a significant volume of ferrite powder and are very efficient [29–31]. Spinel ferrite nanoparticles (SFNPs) are used to purify wastewater and water sources according to the application of ferrite nanoparticles in wastewater treatment. The ferrimagnetic materials' magnetic and structural characteristics place a strong emphasis on green technology to control both inorganic and organic pollutants that have been adsorbed [6, 56–58].

8.1 Control of Hyperthermia with Herbal-Based Nanoparticles (NPs)

In order to cure hyperthermia, which can occasionally be fatal, there are many herbal therapeutic options. Our nature is full of so many herbals as hyperthermia may sometimes be life-threatening; there are several herbal-based therapy options available. Our environment is rich in medicinal plants. These days, scientists who study in the fields of molecular biology and nanotechnology are discovering the highly efficient therapeutic modalities based on nanoparticles for a very long period and have strong penetrating powers.

Combining herbal medicine with chemotherapy or radiation therapy slows the growth of tumors, makes conventional cancer therapy more effective, protects healthy cells after conventional therapy, maintains immunological function, and lessens the negative effects of conventional therapy. In a prospective, randomized, controlled, multicenter research, patients with advanced lung cancer who received traditional Chinese herbal medicine in addition to chemotherapy fared better than those who received chemotherapy alone in terms of progression-free survival (PFS) [40].

Hydrothermal treatment in the presence of medicinal cotton was used to construct MFe_2O_4 (M = Co, Fe, Mn) molecules. For each mixture, two sets of nanoparticles were created and characterized by using XRD, TEM, and SEM. The nanoparticle formed from the solution has the predicted spinel structure having various mean diameters (below 16 nm) [18] which was preserved in $CoFe_2O_4$. NP produced by hydrothermal synthesis in the presence of cotton performs well in hyperthermia [59].

Nanoparticles of Zn-doped $CuFe_2O_4$ were synthesized using a plant extract (NPs). Nanoparticles were characterized with a variety of techniques and thermal gravimetric analysis. On macrophage, healthy cells, and A549 lung cancer cells, Zn-doped $CuFe_2O_4$ NPs were tested for their cytotoxicity and anticancer properties [60].

Zn-doped $CuFe_2O_4$ is a multi-metallic material with good application and biocompatibility explored for the management, diagnostics of malignancies and communicable disorders. Furthermore, these nanomaterials with distinct optical and magnetic characteristics have been found to be appealing candidates for catalytic applications [61]. Patients with pancreatic cancer had a 4.5-month increase in median overall survival (OS) when traditional therapy was combined with herbal medications like Xiang-sha-Liu-Jun-Zi-Tang and herbal *Hedyotidis diffusa*. Furthermore, individuals with inoperable hepatocellular carcinoma had a superior median OS of 3.3 months following trans arterial chemoembolization (TACE) with herbal medicine granules [61].

The size and thermal behavior of magnetite nanoparticles have been biofunctionalized for use in hyperthermia applications. The green synthesis plays a part in managing and treating hyperthermia [63]. Superparamagnetic cobalt–zinc ferrites' nanoparticles have been used for green production, structure, cations' distribution, and bonding properties for Pb(II) adsorption and magnetic hyperthermia applications. It has been reported that Stevioside as a novel biosurfactant along with magnetic

nanoparticles shows a great potential and is used for the treatment of hyperthermia [48].

Covering the nanoparticles with the biosurfactant enhances the retention period of the nano-magnets in glioma cells in addition to improving cellular absorption of the nano-magnets [64]. Additionally, studies using rat C6 glioma cells in vitro revealed that the stevioside coating significantly enhanced calorimetric hyperthermia activity through particle size reduction, which is essential for magnetic hyperthermia-mediated cancer treatment, as reported in all previous studies [3, 22, 23, 31].

Colon cancer cells are eliminated through the green manufacture of Fe_3O_4 NPs utilizing a low-cost stabilizer made from a polyphenol-rich plant waste extract known for antioxidant and anticancer properties [65]. Crude extract from the fruit peel of *Garcinia mangostana* is used as a green stabilizer at various weight percentages (1, 2, 5, and 10 wt%) to easily produce Fe_3O_4 NPs. Following a magnetic hyperthermia analysis of the samples, an in vitro cytotoxicity assay shows a brand-new stabilizer for the biosynthesis of Fe_3O_4 NPs with desired physiochemical properties for potential use in the treatment of colon cancer and magnetic hyperthermia. A low-cost stabilizing and capping ingredient, *G. mangostana* fruit peel extract, enhances the colloidal stability and physiochemical characteristics of the Fe_3O_4 NPs for prospective hyperthermia therapy and anticancer therapies [66].

Green production of metal nanoparticles, ZnO.NPs utilizing plant extract from *Deverra tortuosa s*howed excellent potential. ZnO.NPs were constructed by employing an environmentally friendly extract of *D. tortuosa* aerial parts as a reducing and capping agent. Plant extract shows promising anticancer effect in vitro against two cancer cell lines (human colon adenocarcinoma "Caco-2" and human lung adenocarcinoma "A549"), and the synthesis of ZnO.NPs was confirmed (WI38) and tested against two different cancer cell lines, which showed extremely high levels of selective cytotoxicity both in the aqueous extract as well as in ZnO.NPs [67] (Fig. 3).

Plant extracts' uses in the green synthesis of silver nanoparticles are preferred due to its convenience, versatility, and easiness. *Caesalpinia pulcherrima* leaf extract is used to create silver nanoparticles (AgNPs). AgNPs demonstrated significant antibacterial action under controlled conditions [68], especially against Gram-negative bacteria. There are ample of studies which are advocating the beneficial effects of the nanoparticle against the bacterial and viral infections. The cytotoxicity impact was dose-dependent, and a genotoxic analysis showed that at lower concentrations, the substance was not toxic.

When paired with docetaxel, irinotecan, gemcitabine, or oxaliplatin, mild-temperature hyperthermia has a synergistic effect on tumor growth. This outcome might potentially be the consequence of processes that ensure the tumor's vascular perfusion so that chemotherapy medications can be given more effectively and with less drug resistance. Herbal medicine pill manufactured from the plant *Rhus verniciflua* is used for detoxifying, treating blood stasis and masses.

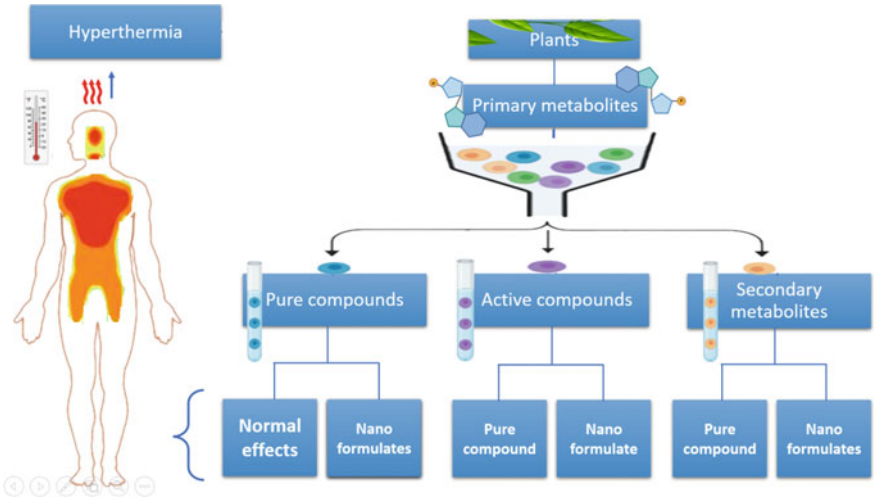

Fig. 3 Herbal-based nanoparticles' scheme for the treatment of hyperthermia [62]. *Source* created in BioRender.com

By stimulating apoptosis, blocking angiogenesis, and inhibiting proliferation, *Rhus verniciflua* showed its anticancer activity in cancer cells. NPs and hyperthermia can be used to treat cancer; the heat produced by the latter can occasionally damage healthy tissue when combined with strong chemotherapy. As an alternative to chemotherapy, plant-based herbal remedies and their combinations with hyperthermia can both slow the growth and clearance of tumors.

9 Conclusion

Nanoferrite proves to be beneficial for the hypothermia treatment. While mild-temperature hyperthermia enhances blood circulation and reoxygenates the tumor, high-temperature hyperthermia mostly induces hypoxia by directly injuring the tumor's blood vessels and triggering death. Combining it with radiation therapy, which behaves differently from high-temperature hyperthermia in its manifestation, may increase radiosensitivity by maintaining tumour vascular perfusion while suppressing DNA repair in the malignant tumour. The vasculature of a tumor is poorly structured and typically devoid of smooth muscles, making it very heat-sensitive. The damage from the angiogenesis would cause tumor cells to starve. Despite the existence of numerous significant reasons to lower body temperature, the comfort of the patient is rarely one of them. Contrarily, bodily cooling typically results in more discomfort than hyperthermia. Future treatments for hypothermia will be beneficial from the formulation of nanoferrites in conjunction with green therapy.

Acknowledgements We are grateful for the facilities offered by Dr. Yashwant Singh Parmar Govt. P.G. College Nahan, District Sirmour, Himachal Pradesh, and ICMR-Regional Medical Research Center for the Scholar's host institute.

References

1. Stefanou G, Sakellari D, Simeonidis K et al (2014) Tunable AC magnetic hyperthermia efficiency of Ni ferrite nanoparticles. IEEE Trans Magn 50.https://doi.org/10.1109/TMAG.2014.2345637
2. Mathew DS, Juang RS (2007) An overview of the structure and magnetism of spinel ferrite nanoparticles and their synthesis in microemulsions. Chem Eng J 129:51–65. https://doi.org/10.1016/J.CEJ.2006.11.001
3. Verde EL, Landi GT, Gomes JA et al (2012) Magnetic hyperthermia investigation of cobalt ferrite nanoparticles: comparison between experiment, linear response theory, and dynamic hysteresis simulations. J Appl Phys 111.https://doi.org/10.1063/1.4729271
4. Epstein Y, Yanovich R (2019) Heatstroke. N Engl J Med 380:2449–2459. https://doi.org/10.1056/NEJMRA1810762
5. Nandhini G, Shobana MK (2022) Role of ferrite nanoparticles in hyperthermia applications. J Magn Magn Mater 552:169236. https://doi.org/10.1016/J.JMMM.2022.169236
6. Salunkhe AB, Khot VM, Thorat ND et al (2013) Polyvinyl alcohol functionalized cobalt ferrite nanoparticles for biomedical applications. Appl Surf Sci 264:598–604. https://doi.org/10.1016/J.APSUSC.2012.10.073
7. Manohar A, Vijayakanth V, Pallavolu MR, Kim KH (2021) Effects of Ni—substitution on structural, magnetic hyperthermia, photocatalytic and cytotoxicity study of $MgFe_2O_4$ nanoparticles. J Alloys Compd 879.https://doi.org/10.1016/J.JALLCOM.2021.160515
8. Leonel AG, Mansur AAP, Carvalho SM et al (2021) Tunable magnetothermal properties of cobalt-doped magnetite-carboxymethylcellulose ferrofluids: smart nanoplatforms for potential magnetic hyperthermia applications in cancer therapy. Nanoscale Adv 3:1029–1046. https://doi.org/10.1039/D0NA00820F
9. Krishna Surendra M, Annapoorani S, Ansar EB et al (2014) Magnetic hyperthermia studies on water-soluble polyacrylic acid-coated cobalt ferrite nanoparticles. J Nanoparticle Res 16.https://doi.org/10.1007/S11051-014-2773-8
10. Shobana MK, Choe H (2016) Structural and electrical properties of Cr doped nickel ferrite. J Mater Sci Mater Electron 27:13052–13056. https://doi.org/10.1007/S10854-016-5446-9
11. Wang R, Zhao T, Zhuo J et al (2020) MAPK/HOG signaling pathway induced stress-responsive damage repair is a mechanism for Pichia pastoris to survive from hyperosmotic stress. J Chem Technol Biotechnol. https://doi.org/10.1002/jctb.6553
12. Rivera RK, Polse KA (1996) Effects of hypoxia and hypercapnia on contact lens-induced corneal acidosis. Optom Vis Sci. https://doi.org/10.1097/00006324-199603000-00009
13. Caizer C (2021) Computational study regarding $Co_xFe_3-xO_4$ ferrite nanoparticles with tunable magnetic properties in superparamagnetic hyperthermia for effective alternative cancer therapy. Nanomaterials 11:3294. https://doi.org/10.3390/nano11123294
14. Hayek SS (2019) Synthesis and characterization of CeGdZn-ferrite nanoparticles as magnetic hyperthermia application agents. Adv Mater Sci Eng 2019:1–8. https://doi.org/10.1155/2019/4868506
15. Darwish MSA, Kim H, Lee H et al (2019) Synthesis of magnetic ferrite nanoparticles with high hyperthermia performance via a controlled co-precipitation method. Nanomaterials 9.https://doi.org/10.3390/NANO9081176
16. Medina MA, Oza G, Ángeles-Pascual A et al (2020) Synthesis, characterization and magnetic hyperthermia of monodispersed cobalt ferrite nanoparticles for cancer therapeutics. Molecules 25.https://doi.org/10.3390/molecules25194428

17. Amiri S, Shokrollahi H (2013) The role of cobalt ferrite magnetic nanoparticles in medical science. Mater Sci Eng C 33:1–8. https://doi.org/10.1016/J.MSEC.2012.09.003
18. Narayanaswamy V, Al-Omari IA, Kamzin AS et al (2022) Tailoring interfacial exchange anisotropy in hard–soft core-shell ferrite nanoparticles for magnetic hyperthermia applications. Nanomaterials 12.https://doi.org/10.3390/NANO12020262
19. Shigeoka D, Yamazaki T, Ishikawa T et al (2018) Functionalization and magnetic relaxation of ferrite nanoparticles for theranostics. IEEE Trans Magn 54.https://doi.org/10.1109/TMAG.2018.2845132
20. Purnama B, Rahmawati R, Wijayanta AT, Suharyana (2015) Dependence of structural and magnetic properties on annealing times in co-precipitated cobalt ferrite nanoparticles. J Magn 20:207–210.https://doi.org/10.4283/JMAG.2015.20.3.207
21. Demirci E, Manna PK, Wroczynskyj Y et al (2018) Lanthanum ion substituted cobalt ferrite nanoparticles and their hyperthermia efficiency. J Magn Magn Mater 458:253–260. https://doi.org/10.1016/J.JMMM.2018.03.024
22. Ramana PV, Rao KS, Kumar KR et al (2021) A study of uncoated and coated nickel-zinc ferrite nanoparticles for magnetic hyperthermia. Mater Chem Phys 266.https://doi.org/10.1016/J.MATCHEMPHYS.2021.124546
23. Rayan DE-R, Ismail M (2019) Magnetic properties and induction heating ability studies of spinal ferrite nanoparticles for hyperthermia treatment of tumours. Egypt J Biomed Eng Biophys https://doi.org/10.21608/EJBBE.2019.5193.1022
24. Jalili H, Aslibeiki B, Hajalilou A et al (2022) Bimagnetic hard/soft and soft/hard ferrite nanocomposites: structural, magnetic and hyperthermia properties. Ceram Int 48:4886–4896. https://doi.org/10.1016/J.CERAMINT.2021.11.025
25. Lee SW, Bae S, Takemura Y et al (2007) Self-heating characteristics of cobalt ferrite nanoparticles for hyperthermia application. J Magn Magn Mater 310:2868–2870. https://doi.org/10.1016/J.JMMM.2006.11.080
26. Kim DH, Nikles DE, Johnson DT, Brazel CS (2008) Heat generation of aqueously dispersed $CoFe_2O_4$ nanoparticles as heating agents for magnetically activated drug delivery and hyperthermia. J Magn Magn Mater 320:2390–2396. https://doi.org/10.1016/J.JMMM.2008.05.023
27. Lickmichand M, Shaji CS, Valarmathi N et al (2019) In vitro biocompatibility and hyperthermia studies on synthesized cobalt ferrite nanoparticles encapsulated with polyethylene glycol for biomedical applications. Mater Today Proc 15:252–261. https://doi.org/10.1016/J.MATPR.2019.05.002
28. Rauf A, Badoni H, Abu-Izneid T et al (2022) Neuroinflammatory markers: key indicators in the pathology of neurodegenerative diseases. Molecules 27:3194. https://doi.org/10.3390/molecules27103194
29. Tatarchuk T, Shyichuk A, Sojka Z et al (2021) Green synthesis, structure, cations distribution and bonding characteristics of superparamagnetic cobalt-zinc ferrites nanoparticles for Pb(II) adsorption and magnetic hyperthermia applications. J Mol Liq 328.https://doi.org/10.1016/J.MOLLIQ.2021.115375
30. Kita E, Oda T, Kayano T et al (2010) Ferromagnetic nanoparticles for magnetic hyperthermia and thermoablation therapy. J Phys D Appl Phys 43.https://doi.org/10.1088/0022-3727/43/47/474011
31. Mallick A, Mahapatra AS, Mitra A et al (2018) Magnetic properties and bio-medical applications in hyperthermia of lithium zinc ferrite nanoparticles integrated with reduced graphene oxide. J Appl Phys 123.https://doi.org/10.1063/1.5009823
32. Aisida SO, Mahmood A, Ahmad I et al (2022) Bio-conjugate of magnesium ferrite nanoparticles in aqueous Allium cepa extract for self-heating potency. Appl Phys A Mater Sci Process 128.https://doi.org/10.1007/S00339-021-05145-W
33. Odenbach S (1998) Ferrofluids-magnetisable liquids and their application in density separation. Magn Electr Sep 9:1–25. https://doi.org/10.1155/1998/74963
34. Smitha P, Singh I, Najim M et al (2016) Development of thin broad band radar absorbing materials using nanostructured spinel ferrites. J Mater Sci Mater Electron 27:7731–7737. https://doi.org/10.1007/S10854-016-4760-6

35. Nasrin S, Chowdhury FUZ, Hoque SM (2019) Study of hyperthermia temperature of manganese-substituted cobalt nano ferrites prepared by chemical co-precipitation method for biomedical application. J Magn Magn Mater 479:126–134. https://doi.org/10.1016/J.JMMM.2019.02.010
36. Sneed PK, Stauffer PR, McDermott MW et al (1998) Survival benefit of hyperthermia in a prospective randomized trial of brachytherapy boost ± hyperthermia for glioblastoma multiforme. Int J Radiat Oncol Biol Phys 40:287–295. https://doi.org/10.1016/S0360-3016(97)00731-1
37. Karbelkar AA, Reynolds EE, Ahlmark R, Furst AL (2021) A microbial electrochemical technology to detect and degrade organophosphate pesticides. ACS Cent Sci 7:1718–1727https://doi.org/10.1021/acscentsci.1c00931
38. Casa DJ, Demartini JK, Michael F et al (2015) National athletic trainers' association position statement: exertional heat illnesses. 50:986–1000.https://doi.org/10.4085/1062-6050-50.9.07
39. Van Nostrand EL, Freese P, Pratt GA et al (2020) A large-scale binding and functional map of human RNA-binding proteins. Nature 583:711–719. https://doi.org/10.1038/S41586-020-2077-3
40. Truettner JS, Bramlett HM, Dalton Dietrich W Hyperthermia and mild traumatic brain injury: effects on inflammation and the cerebral vasculature. https://doi.org/10.1089/neu.2017.5303
41. Frink M, Floh S, Griensven M Van et al (2012) Facts and fiction : the impact of hypothermia on molecular mechanisms following major challenge 2012. https://doi.org/10.1155/2012/762840
42. Wills S (2015) Extremes of temperature: hyperthermia. Encycl Forensic Leg Med Second Ed 476–485.https://doi.org/10.1016/B978-0-12-800034-2.00175-0
43. Falk MH, Issels RD (2001) Hyperthermia in oncology. Int J Hyperthermia 17:1–18. https://doi.org/10.1080/02656730150201552
44. Seegenschmiedt MH, Sauer R (1993) Interstitial and intracavitary thermoradiotherapy.https://doi.org/10.1007/978-3-642-84801-8
45. Im DS (2021) Treatment of aggression in adults with autism spectrum disorder: a review
46. Elbeshir EIA (2016) Evaluation of thermal properties of ferrite nanoparticles for magnetic hyperthermia treatment. 5:2014–2017
47. Tarawneh R, Cummings JL (2017) Depression, psychosis, and agitation in stroke. Prim Cerebrovasc Dis Second Ed 767–774.https://doi.org/10.1016/B978-0-12-803058-5.00147-8
48. McGugan EA (2001) Hyperpyrexia in the emergency department. Emerg Med (Fremantle) 13:116–120. https://doi.org/10.1046/J.1442-2026.2001.00189.X
49. El-Radhi AS, Carroll J, Klein N (eds) (2009) Hyperthermia. In: Clinical manual of fever in children. Springer, Berlin, Heidelberg. https://doi.org/10.1007/978-3-540-78598-9_2
50. Onyedikachi OA, Aisida SO, Agbogu A et al (2022) Zinc ferrite nanoparticles capped with Gongronema latifolium for moderate hyperthermia applications. Appl Phys A Mater Sci Process 128.https://doi.org/10.1007/S00339-021-05244-8
51. Xing M, Mohapatra J, Beatty J et al (2021) Iron-based magnetic nanoparticles for multimodal hyperthermia heating. J Alloys Compd 871.https://doi.org/10.1016/J.JALLCOM.2021.159475
52. Kharat PB, Somvanshi SB, Khirade PP, Jadhav KM (2020) Induction heating analysis of surface-functionalized nanoscale $CoFe_2O_4$ for magnetic fluid hyperthermia toward noninvasive cancer treatment. ACS Omega 5:23378–23384. https://doi.org/10.1021/ACSOMEGA.0C03332
53. Wust P, Hildebrandt B, Sreenivasa G et al (2002) Hyperthermia in combined treatment of cancer. Lancet Oncol 3:487–497. https://doi.org/10.1016/S1470-2045(02)00818-5
54. Habash RWY (2018) Therapeutic hyperthermia. Handb Clin Neurol 157:853–868. https://doi.org/10.1016/B978-0-444-64074-1.00053-7
55. da Silva FAS, de Campos MF (2020) Study of heating curves generated by magnetite nanoparticles aiming application in magnetic hyperthermia. Brazilian J Chem Eng 37:543–553. https://doi.org/10.1007/S43153-020-00063-5
56. Koutsoumbou X, Tsiaoussis I, Bulai GA et al (2021) $CoFe_2$-xRExO$_4$ (RE = Dy, Yb, Gd) magnetic nanoparticles for biomedical applications. Phys B Condens Matter 606.https://doi.org/10.1016/J.PHYSB.2021.412849

57. Ansari M, Bigham A, Hassanzadeh Tabrizi SA, Abbastabar Ahangar H (2018) Copper-substituted spinel Zn-Mg ferrite nanoparticles as potential heating agents for hyperthermia. J Am Ceram Soc 101:3649–3661. https://doi.org/10.1111/JACE.15510
58. Peng E, Choo ESG, Chandrasekharan P et al (2012) Synthesis of manganese ferrite/graphene oxide nanocomposites for biomedical applications. Small 8:3620–3630. https://doi.org/10.1002/smll.201201427
59. Bañobre-López M, Teijeiro A, Rivas J (2013) Magnetic nanoparticle-based hyperthermia for cancer treatment. Reports Pract Oncol Radiother 18:397–400. https://doi.org/10.1016/J.RPOR.2013.09.011
60. Darvish M, Nasrabadi N, Fotovat F et al (2022) Biosynthesis of Zn-doped $CuFe_2O_4$ nanoparticles and their cytotoxic activity. Sci Rep 12.https://doi.org/10.1038/S41598-022-13692-2
61. Guo T, Dou F, Lin M et al (2019) Biological characteristics and carrier functions of pegylated manganese zinc ferrite nanoparticles. J Nanomater 2019.https://doi.org/10.1155/2019/6854710
62. https://help.biorender.com/en/articles/3619405-how-do-i-cite-biorender. Assessed 23 Oct 2022
63. https://www.cdc.gov/disasters/extremeheat/heattips.html. Assessed 23 Oct 2022
64. Laitano O, Leon LR, Roberts WO, Sawka MN (2019) Controversies in exertional heat stroke diagnosis, prevention, and treatment. J Appl Physiol 127:1338–1348. https://doi.org/10.1152/JAPPLPHYSIOL.00452.2019
65. Albino M, Fantechi E, Innocenti C et al (2019) Role of Zn^{2+} substitution on the magnetic, hyperthermic, and relaxometric properties of cobalt ferrite nanoparticles. J Phys Chem C 123:6148–6157. https://doi.org/10.1021/ACS.JPCC.8B10998
66. Thunugunta T, Reddy AC, Reddy LDC (2015) Green synthesis of nanoparticles: current prospects. Nanotechnol Rev 4(40):303–323
67. Selim YA, Azb MA, Ragab I, El-azim MHMA (2020) Green synthesis of zinc oxide nanoparticles using aqueous extract of Deverra tortuosa and their cytotoxic activities. Sci Rep 1–9.https://doi.org/10.1038/s41598-020-60541-1
68. Mahmoudi K, Bouras A, Bozec D et al (2018) Magnetic hyperthermia therapy for the treatment of glioblastoma: a review of the therapy's history, efficacy and application in humans. Int J Hyperth 34:1316–1328. https://doi.org/10.1080/02656736.2018.1430867

Chapter 6
Ferrite Nanoparticles for Telecommunication Application

Shiv Kumar and Ragini Raj Singh

Abbreviations

SNPs	Spinel Ferrite Nanoparticles
PCB	Printed Circuit Board
EMI	Electromagnetic Induction
VCR	Video Cassette Recorder
IEC	International Electrotechnical Commission
SMD	Surface Mount Device
DSL	Digital Subscriber Line
THD	Total Harmonic Distortion
RFI	Radio Frequency Interference

1 Introduction

Because of their higher resistivity, lower cost, easier availability to production, and greater magnetization qualities, ferrites are observed as superior magnetic materials over pure metals. They are widely employed in radar, audio–video and digital recording devices, bubble devices, memory devices of computer, satellite communication devices, and microwave equipments [1, 2]. The ferrites are widely used ranging from microwave to radio frequencies. The examples of ferrite usages include antenna cores in radio receivers, flyback transformers in TV picture tubes, and broadband transformers The other examples are mechanical filters, ultrasonic generators, moderators, phase shifters, and isolators. Ferrite is now utilized in computers, control

S. Kumar · R. R. Singh (✉)
Nanotechnology Laboratory, Department of Physics and Materials Science, Jaypee University of Information Technology, Waknaghat, Solan, India
e-mail: raginirajsingh@gmail.com

P. Sharma et al. (eds.), *Engineered Ferrites and Their Applications*, Materials Horizons: From Nature to Nanomaterials, https://doi.org/10.1007/978-981-99-2583-4_6

devices, and telephone exchanges. In case of antennae use in radio and television, the wavelengths associated are large in magnitude. The antennae would also need to be rather huge in order to match these wavelengths. However, antennae constructed of ferrite magnetic material can be quite small since magnetic materials have capability of focusing the received signal or electromagnetic wave to a significant factor. The issue becomes important when it comes to small portable radio or television sets.

Soft ferrite and hard ferrite are two familiar types of ferrite. Soft ferrite type of magnetic material is utilized as a transformer core primarily for electronic systems used in television, computers along with other industrial applications. Permanent magnets are made of hard ferrites and found their most usefulness in loudspeakers and micromotors. The high-frequency range should make use of the low-loss polycrystalline ferrites. The crucial technological characteristics for low- and high-frequency applications are saturation magnetization (MS), coercive force (HC), initial permeability I, and losses for applications with exceptional performance and characterized by initial permeability. In general, the ideal mix of these traits cannot be obtained for any given application. Most parameters for each given application can be controlled by adjusting compositions, adding additives, or changing preparation methods.

2 Properties of Ferrites Used in Telecommunication Applications and Their Tuning

Spinel ferrite nanoparticles (SNPs) have unique structural, electrical, magnetic, and optical capabilities that are advantageous for human technology. They have a general formula MFe_2O_4, M being one or more divalent metal cations such as Fe^{2+} Zn^{2+}, Ni^{2+}, Co^{2+}, Bi^{2+}, from transition metal ions to heavy metal ions. These SNPs have continuously maintained their importance for the last two decades by establishing themselves as suitable candidates for telecommunication applications due to their amazing magnetic properties, high resistivity and operating on a wide range of frequencies (from hundred Hz to GHz) [3, 4]. However, the properties of SNPs strongly depend upon the synthesis methods, selection of material compositions, and annealing temperatures [5, 6].

Comparing magnesium nickel ferrite ($Mg_xN_{1-x}Fe_2O_4$) nanoparticles to other doped ferrite materials, they exhibit higher magnetization (Ms), lower coercivity (Hc), and appropriate structural stability [7]. Furthermore, combined with good chemical and elastic stability, iron oxide NPs in some circumstances have Ms that are even greater than the most well-researched and recently available iron oxide NPs. With Fe^{3+} ions occupying the tetrahedral A-site and Mg^{2+} and Ni^{2+} ions occupying the octahedral B-sites, magnesium nickel ferrites have an inverted spinel structure [7, 8].

2.1 Elastic Parameters

The structural stability of ferrites plays an essential role in their use in the telecommunication industries. The substitution of tetrahedral or octahedral ions in ferrite lattice shows changes in the interatomic forces and the force constant. This results in variation in the stiffness constant C_{11}, C_{12} and elastic moduli Y, Bulk's modulus B, and shear modulus G [7]. In synthesis of materials and their industrial application as electrical and electronic materials, such elastic qualities may be crucial in overcoming physical stress [9]. Elastic properties of ferrites can be tuned by doping and altering annealing temperature during the synthesis of ferrites. For example, in magnesium, nickel ferrites annealed at two different temperatures of 900 and 1100 °C are observed to lose coercivity at 1100 °C compared to 900 °C; secondly, these ferrites gain elasticity at higher annealing temperatures [7].

2.2 Magnetic Parameters

The critical magnetic parameters used in telecommunication are saturation magnetization, coercivity, and hysteresis. The primary use of ferrites in the telecommunication industry is in the form of the core of transformers and antennae. The ferrites used should exhibit super-paramagnetism, i.e., low value of coercivity and high value of saturation magnetization. These properties can be tuned via annealing temperature.

Magnesium nickel ferrite ($Mg_xNi_{1-x}Fe_2O_4$, $x = 0.1875$, 0.3125, and 0.4375) nanoparticles are synthesized using the aqueous sol–gel method and annealed at 900 °C. The M–H curve for MgNi ferrite NPs for two compositions 0.1875 and 0.4375 is shown in Fig. 1.

The magnetic susceptibility is found to decrease with increasing Mg ion composition. Magnesium nickel ferrite ($MgNiFe_2O_4$) nanoparticles synthesized using the

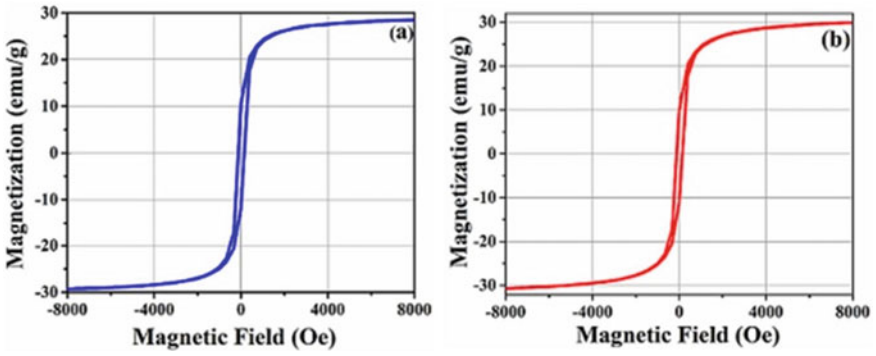

Fig. 1 M–H curve for $Mg_xNi_{1-x}Fe_2O_4$, $x =$ **a** 0.1875 and **b** 0.4375 annealed at 900 °C annealing temperature [6]. Reprinted with permission from Springer Nature

Table 1 Elastic parameters—bulk modulus (B), shear modulus (G), and Pugh's ratio (B/G)—and magnetic parameters—saturation magnetization (M_s) and coercivity (H_c) of MgNi ferrite NPs at 900 and 1100 °C annealing temperatures

Annealing temperature (°C)	Bulk's modulus (B)	Sheer modulus (G)	Pugh's ratio (B/G)	Saturation magnetization (M_s)	Coercivity (H_c)
900	66	63	1.06	28.97	137
1100	73	59	1.23	27.52	115.2

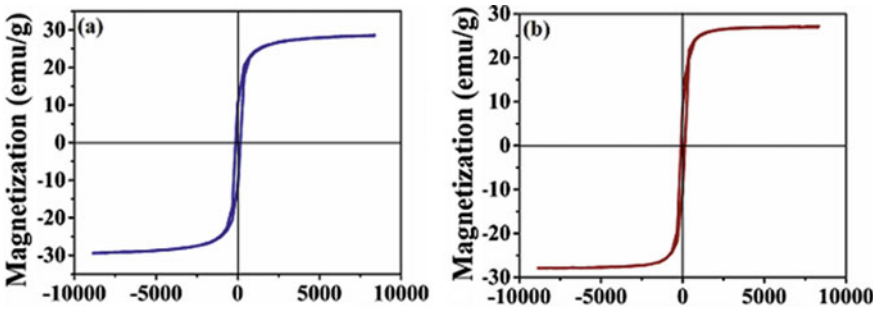

Fig. 2 M–H curve for MgNi ferrite NPs at **a** 900 °C **b** 1100 °C annealing temperatures [7]. Reprinted with permission from Elsevier

aqueous sol–gel method and annealed at 900 °C and 1100 °C were studied for their magnetic characteristics and are shown in Table 1 [7].

The saturation magnetization rises with annealing temperature, and coercivity is found to decrease. The M–H curves for MgNi ferrites' nanoparticles annealed at 900 and 1100 °C are shown in Fig. 2 [7].

The magnetic parameters can be tuned to over desired values by two means firstly by varying composition and secondly by annealing temperature. By accounting for the various ratios of iron content in chemicals, magnetic nickel ferrite nanoparticles (MNFNPs) can be tailored for a variety of technological applications in terms of their particle size, shape, and magnetic properties [10]. Using a straightforward and eco-friendly sol–gel method with water as the solvent, ferrite nanoparticles with metal doping-tunable magnetic characteristics were effectively created [11]. The case study used cobalt and zinc to dope the ferrite NPs. It was observed that with increasing cobalt and zinc concentration, saturation magnetization decreased, but coercivity in both the cases was not found to change as shown in Fig. 3 [4].

For another instance zinc manganese ferrite nanoparticles, saturation magnetization is found a function of annealing temperature as shown in Fig. 4 [12]. Here, saturation magnetization for $Zn_{0.3}Mn_{0.7}Fe_2O_4$ ferrite nanoparticles is measured at different temperatures 5–300 K, and saturation magnetization decreases with rise in temperature.

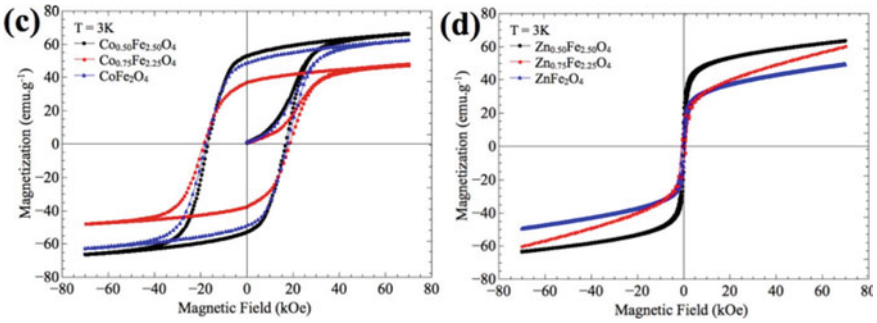

Fig. 3 Magnetization loop recorded at 3 K for sample $CoFe_2O_4$ (**a**) and $ZnFe_2O_4$ (**b**) [4]. Reprinted form an open access Journal, ACS Omega

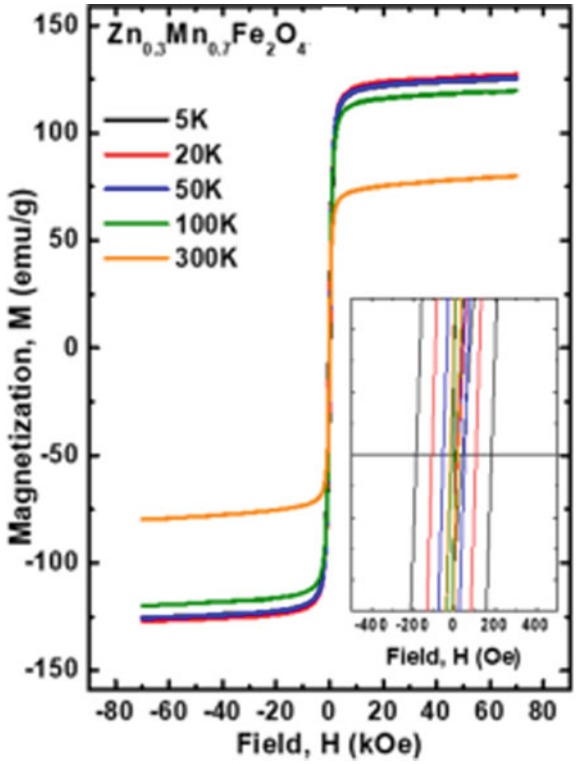

Fig. 4 Hysteresis curves at several temperatures (5–400 K) of $Zn_{0.3}Mn_{0.7}Fe_2O_4$ ferrite nanoparticles [12]. Reprinted with permission from ACS

3 Telecommunication Applications of Ferrites

In recent electronic communication system, the square-loop ferrite core is almost a new significant switching component. Ferrites have found several essential applications in the field of telecommunication as filters, beads, broadband transformers, etc., discussed in detail below.

3.1 The Square-Loop Ferrite Core as a Switching Element

Square-loop cores' potential for usage as switching and storage components has long been understood. The occurrence of positive or negative magnetic remanence is feasible by passing a current pulse through a winding, a core can be made to. Counting circuits and shift memory were the first products which are identified to use square-loop ferrite cores. Delay circuits are occasionally connected between the successive phases; however, diodes are generally used to prevent retroaction. However, it is possible to use transistors in place of diodes. With transistor-based amplification, the drive pulse power may be relatively modest, but the counting circuit's output power may be significantly higher [13]. There are various ferrites with square loops. Familiar among them is nickel ferrite ($NiFe_2O_4$) as shown in Fig. 5 [14].

3.2 Filters

LC filters are devices with one or more ferrites or chokes acting as inductive elements and one or more capacitor elements with a paper, plastic film, or ceramic dielectric combined. The ceramic capacitor type is called a feed-through capacitor, and one terminal is made up of the casing, soldered or bolted to the chassis. SMD variations are another option. Additionally, RC filters exist in which a series resistance and a metallized paper (MP) capacitor are coupled. A metallization alloy with increased resistance frequently makes up the resistor element. Arc suppression is the primary application for RC filters.

3.2.1 Ferrite Filters

Ferrite is a ceramic substance made of iron oxide and nickel, zinc, and manganese compounds. High-frequency electrical disturbances can be reduced and dissipated using ferrite filters and electronic components based on ferrite. These filters are effective at lowering EMI in electromagnetic equipment and circuits. Most power supplies and electronic devices emit electrical noise or EMI. Switching power supplies and the

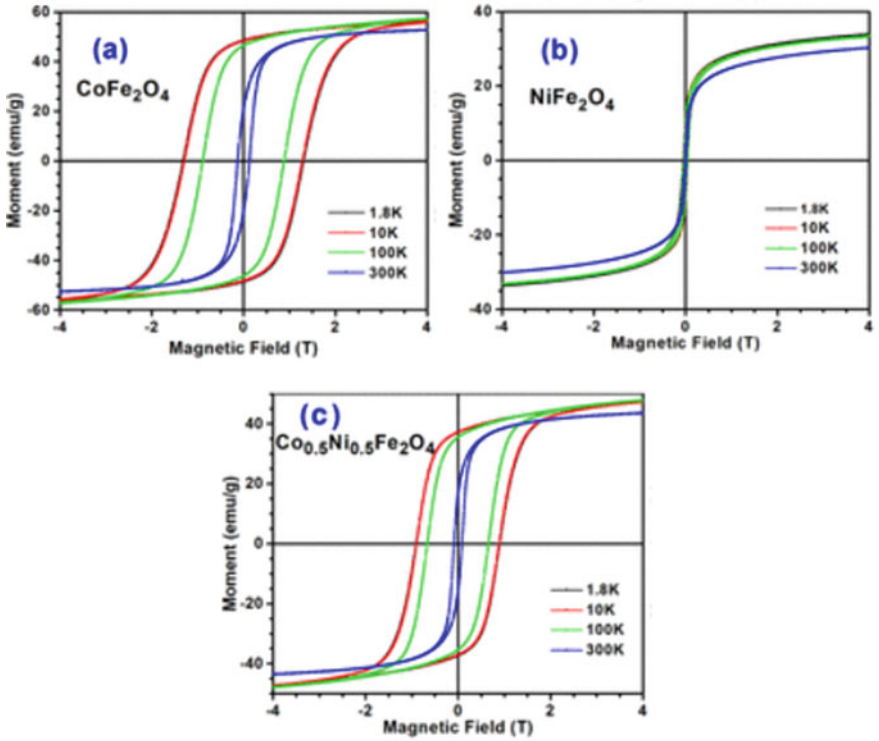

Fig. 5 Hysteresis loops of **a** $NiFe_2O_4$, **b** $CoFe_2O_4$, **c** $CoNiFe_2O_4$ [14]. Reprinted with permission from ACS

noise in communication networks produce high-frequency harmonics. These intrusive signals degrade quality by interfering with circuit signals. Ferrite cores, ferrite beads, and core inductors are a few examples of ferrite filters. Ferrite beads or rings are often used as filters in electrical circuits. They function as low-pass filters to stop high-frequency signals from entering a course. Ferrite cores or ferrite sleeves are widely used in cables for EMI suppression. Switching power converters also employ ferrite core inductors as filters. In the following sections, we will go into greater detail about ferrite core inductor filters, ferrite bead filters, and ferrite cores.

3.2.2 EMI Line Filters and Their Roles in Electrical Devices

The use of electrical devices in daily life is steadily expanding as consumer spending rises all around the world. Electronics are used in all aspects of life, whether in telecommunications, entertainment, networking, medicine, power conditioning, or information technology. However, did you know that these gadgets produce electromagnetic fields that cause outside interference in radio frequencies? In order to get rid

Fig. 6 EMI power line filter (CC BY-NC 2.0.)

of this, line filters, also known as EMI filters or RFI filters, were created. They assist in reducing the amount of Electromagnetic Interference (EMI) and Radio Frequency Interference (RFI) in the power and signal lines. They then send out pure signals to ensure the electronic devices work as intended. For example, a power line filter is shown in Fig. 6.

In professional settings like industrial, health care, and ITE, using a modular AC line filter integrated into a connector or as a chassis mount item is a usual practice for AC mains-powered equipment. The apparatus often includes a power supply or embedded AC–DC converter. This power supply may be rack- or PCB-mounted, as well as chassis-mountable. In every situation, the power supply will always meet the legal standards for emissions as a standalone component, typically EN55011/EN55032, for conducted and radiated interference.

Role/Functions of the Line Filter in Switching Power Supplies (SPS)

The EMI line filter blocks any unwanted current from passing through cables or wires while allowing required currents to flow freely. In addition, they stop electromechanical switches from generating an excessive peak voltage at the mains input that could damage the electronic control circuit. Contrary to what one might anticipate, filters work to lower the number of interference factors so that they are controllable. They are also referred to as EMI power line filters since they can reduce grid power noise.

Applications of the Line Filter

1. Home appliances, computers, military and aerospace systems, medical equipment, vehicle battery chargers, and energy management systems are just a few examples of applications for EMI line filters.
2. All of the machines mentioned above produce electromagnetic interference. In addition, line filters are becoming increasingly necessary, especially in residential appliances, to reduce noise. Machine interference is sometimes permissible in industrial settings, but rigorous rules are in place in domestic locations.

Importance of Line Filters

Because modern power conversion circuits employ high-frequency switching techniques, EMI power line filters are necessary. In order to lessen harmonic noise caused by quick variation in voltage and current from devices such as Switch Mode Power Supplies (SMPSs), inverter devices, various rectifiers, EMI filtering devices must adhere to the emission requirements established in the variety of international and military EMI standards. An EMI power line filter minimizes noise already on the power distribution system from entering equipment while also reducing harmonic energy propagating out onto the power distribution system. It needs an understanding of filter impedances and how they interact with circuit impedances over a wide frequency range to design an EMI power line filter. However, the installation and mounting details can equally affect the efficiency of an EMI power line filter. Elective compatibility can improve power systems to be more interference-resistant, have longer lifespans, and guarantee user safety. EMI line filters are essential to ensuring that the power systems have excellent electromagnetic compatibility (EMC). The quality of electronic components is assessed using the EMC indicator. Globally, its importance is rising quickly.

Experienced equipment designers know that using only compliant components does not ensure that an end product will pass an EMC compliance test. There are numerous causes. For instance, compliance tests on an AC–DC converter for equipment are carried out under exact circumstances, such as expected AC line impedance, output loading, cable length and routing, and part position concerning ground. These variables change when an end product is tested with this AC–DC converter installed internally, resulting in a different and frequently worse conducted EMI signature. On power cabling, radiated EMI from other components can also be picked up, raising conducted levels.

Structure of the EMI Line Filters

Capacitors, resistors, and inductors are used to create the passive filters known as EMI line filters. Additionally, UT ferrite cores are a crucial component of them. The electromagnetic signals are separated using them. As a result, the filters reduce EMI interference from the AC while transmitting AC to the power supply. In addition, they successfully reduce the EMI noise produced by power supplies. It helps to stop interference from entering the AC power system and affects how well electrical gadgets function.

Selection of EMI Line Filters

When choosing the EMI line filters, three factors must be considered: voltage and current, size and construction, and insertion loss. The environment in which the filter is used is not a significant consideration because it is typically potted. However, the

line filter's environmental characteristics are influenced by the temperature of the potting materials and filter capacitors.

To provide a baseline for the conducted emissions, it is even preferable if the power source to be filtered has passed preliminary EMC testing. The test findings will provide the manufacturer with information on the frequency and severity of the product failures. This information can be compared to the insertion loss of the EMI filter to see whether it provides adequate attenuation at frequencies where it failed the test.

It is better to measure system performance without a filter installed before determining how much more attenuation is necessary from an external filter to achieve standards. The attenuation curves in filter data sheets will hint at the filter's performance, but keep in mind that the datasheet performance is based on tests conducted under specific conditions, typically 50-Ω source and load impedance. Although a line impedance stabilizer network (LISN) can be used to standardize the AC source, the application load will probably be substantially different from the test conditions shown on the datasheet. It must ensure that all failed or marginal frequencies will be muted because attenuation across the frequency range varies.

3.2.3 Ferrite Cores and Ferrite Core Inductor Filters

Noises from EMI can affect cables. Cables can be a source of electrical noise and high-voltage spikes if not installed and appropriately protected. Without protection, voltage spikes and EMI can break down associated circuits or devices or harm hardware. The best choice for noise reduction in cables is ferrite cores. Ferrite cores (Fig. 7) can minimize noise levels and common-mode currents in electrical equipment because of their high magnetic permeability, low high-frequency loss, and low conductivity. They contribute to the performance improvement of power supply cables and make them perfect for various electrical applications. The installations of ferrite core filters can be EMI-shield cables. The efficiency of the ferrite filter varies depending on the type of ferrite core filter and when and where it is installed. Cables with ferrite cores cannot serve as antennas and cannot emit EMI noises as a result. Ferrite cores typically function as cable shields or EMI suppressors because they provide affordable filtering.

Either common-mode noises or differential noises occur in switching power converters. Inductors and capacitors are used to create LC filters, which are used to reduce the noise or EMI produced in switching power converters. To get the required filter attenuation properties of an LC filter, it is crucial to build the filter inductor. The magnetic or core materials must be employed for the inductor design to provide the appropriate filter attenuation properties.

Advanced modems are used to accelerate data transfer over standard (twisted pair) copper telephone lines in the emerging new telecom technology known as Digital Subscriber Line (DSL). Magnetic components built on ferrite cores perform several tasks in these DSL modems, including isolation, impedance matching, high-pass filtering, and low-pass filtering. To achieve the criteria on THD and insertion loss for

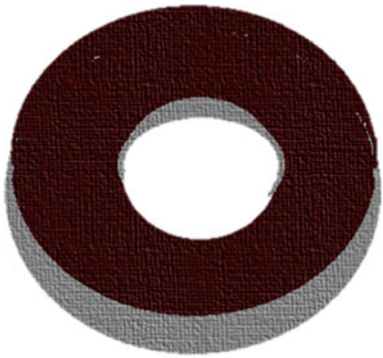

Fig. 7 Ferrite core

DSL wideband transformers, this application note shows how ferrite cores should be used.

Ferrite core inductors are common-mode or differential-mode filter inductors with their coils wound on a ferrite core. When utilized as filter inductors, ferrite core inductors are incredibly effective. They do a great job of eliminating EMI and high-frequency spikes from signals, enhancing the output quality and performance of the converter. Ferrite core inductors are widely used for switching power converter filtering applications because they are inexpensive, have low losses, and come in various forms with ferrite cores.

The installation location affects the choice of ferrite filter. Ferrite beads are the most significant filters for reducing sounds that are transmitted over PCB traces. In addition, ferrite cores are effective at lowering cable EMI. Several solutions could be available in a given application for a particular filtering need. One can design, simulate, and analyze the circuit with many filter options using Cadence's PCB design and analysis software to see which one performs best.

Ferrite cores perform differently in terms of decreasing electromagnetic interference depending on the materials and shapes employed because different materials have varying magnetic permeability and, consequently, different impedances. Utilizing ferrite materials also impacts the proportion of reactance to resistance. However, the ferrite core features frequently apply without regard to the ferrites.

3.3 Ferrite Beads

A wrapped coil and two terminals are the components of ferrite beads. Ferrite material typically consists of ceramic compounds with iron oxides combined with nickel, zinc, and manganese. Ferrite beads are shown in Fig. 8. Some varieties of ferrite chokes are ferrite beads. Another name for a ferrite bead is a ferrite clamp. It is a passive device intended to reduce high-frequency signals on a power supply line and enhance the power quality of your PCB.

Fig. 8 Ferrite beads (CC BY 2.0)

They are often positioned close to a power supply and ground line pair coming into a particular device. A good illustration is the laptop's power wire. In principle, any DC will result in a voltage drop proportional to the DC resistance through the ferrite bead. Ferrite beads are low-inductance ferrite inductors with low parasitic capacitance. They function more like a lossy inductor and lack any undesirable resonances.

Ferrite beads have poor qualitative attributes and a high self-resonant frequency. Ferrite beads provide high impedance in the RF and VHF frequency bands. Ferrite beads behave more like inductors in high-frequency applications than coil inductors if their resonance frequency is higher than the system frequency. When the resonance frequency is near a signal or system frequency, the ferrite beads behave like resistors and produce heat. Power loss from heat energy produced by ferrite beads in a circuit eliminates EMI noises. For EMI mitigation, ferrite beads are widely utilized in high-speed PCBs. At high frequencies, the PCB traces act as antennas. Using ferrite beads, the traces on a circuit board can lower EMI emissions and absorption.

4 Signal Transformers

In electronic devices, signal transformers are employed as a step-up/step-down, isolating, or impedance matching component. Signal transformers are typically not suitable for use with power transformers, which transport current, and vice versa. Typical electronics applications, such as telecommunications, radio frequency (RF), audio, video, and general-purpose purposes, all employ signal transformers. A transformer typically consists of two wire coils that are wrapped around a core; these coils are referred as the primary and secondary coils and are separated from one another by a medium like air, water, or metal. Typically, the primary coil is attached to a source that provides electricity or another signal. This signal causes an electromagnetic field and a voltage in the secondary coil when it is applied to the primary coil.

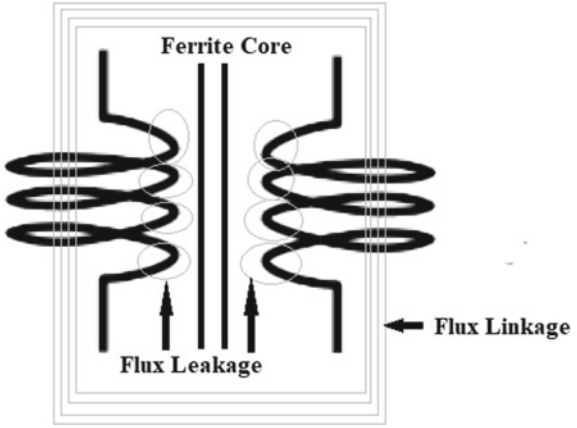

Fig. 9 Symbolic diagram of broadband transformer

Depending on the design and intended use of the device, a transformer can attenuate, boost, or simply isolate the applied signal based on the number of windings per coil. A symbolic diagram of signal transformer is shown in Fig. 9 which magnetic flus linkage and flux leakage are clearly shown.

The magnetic field, depicted by magnetic flux lines, travels along the direction with the least magnetic resistance (reluctance). Therefore, the first winding's flux does not entirely pass through the second winding. Leakage flux is the flow of current that does not join the two windings and wastes energy. Other energy losses like those in the transformer's core and windings also lower its efficiency, but we would not go into depth about them in this article. Reduce the distance between the two windings or stack the windings on top of one another to lessen the flux leakage. More of the flux may link both windings when the windings are correctly configured, which also reduces losses.

4.1 Broadband Transformers

Energy can be transmitted over various frequencies using magnetic devices referred to as "broadband transformers." They are wound on ferrite cores such as toroidal cores due to their improved permeability, higher efficiency, excellent RFI performance, good frequency responsiveness, and lack of leakage magnetic flux. Broadband transformers are designed to operate in various frequencies, each of which has a distinct one or more frequency ranges for X_L or X_C. Use high-permeability ferrite cores with tiny windings to provide the appropriate MF and HF spectral response for this. The core becomes evident to the circuit as the operating frequency rises. These transformers are widely used in low-power applications, such as telecommunications' equipment. The ferrite winding is only operating at its maximum efficiency during this period. The core can be seen via the circuit if you can see the lower frequency

range. It enables the winding to generate the necessary inductance in the operational range's low frequency.

The shunt reactance of transformers, which rises with frequency, is a significant characteristic. However, this only occurs if the material's permeability is constant or declining slower than the frequency rise. The best and most economical material for broadband transformers is ferrites. They always have a high initial permeability at lower cutoff frequencies and offer the highest impedance to undesired noise signals. Typically, ferrites are chosen based on attributes like the simplicity of winding, terminating, and specific technical design requirements of the transformer [15].

For instance, low- and medium-frequency transformer designs can use manganese zinc (Mn–Zn) ferrites. When these ferrites are used in broadband transformers, the core geometry should have the lowest possible ratio of DC resistance to inductance for a single turn. Gapped ferrite cores can regulate the decrease in shunt inductance for transformers with an overlying direct current.

On the other hand, ferrites with a toroidal core shape are ideal for high-frequency transformers. On the toroid, a few required turns can be damaged. But be aware that windings with fewer turns make achieving the necessary impedance ratios more difficult. The primary and secondary windings are linked to minimize leakage inductance. The various types of ferrite filters are described below.

4.1.1 Low- and Medium-Frequency Broadband Transformer

The most appropriate ferrite material for broadband transformer applications is one having the maximum initial permeability at low cutoff frequency levels. For low- and medium-frequency broadband transformer designs, Mn–Zn ferrites, namely Fair-Rite 77 or 78 material, show a great option. The most important transformer characteristic, i.e., shunt reactance (OL) shows an increase with frequency when the material permeability remains constant or found decreasing at a rate slower than the increase in frequency and holds good even if a transformer is made of manganese zinc ferrite, where frequency is situated at the upper end of the flat zone of the permeability of ferrite material vs. its frequency curve. The bandpass characteristics would not be greatly altered even though the full bandpass is located in the region where the initial permeability is showing decreasing trend. Reduce the R/L ratio by designing the core shape of broadband transformers utilizing manganese zinc ferrite material.

Alternatively stated, the dc resistance-to-inductance ratio for a single turn needs to be as low as possible. The International Electrotechnical Commission's list of pot cores in document IEC 60,133 is based on this minimal R/L ratio. Additionally, multiple core forms can be used to create these broadband transformers. The transformer's mechanical design constraints and other criteria, such as the simplicity of winding and terminating, frequently have an impact on the final core choice.

4.1.2 Broadband Transformer with a Superimposed Static Field

To avoid the reduction in shunt inductance, gapped cores can be employed in transformer designs with a superimposed direct current. Inductive direct current devices can be made with the use of Hanna curves. More information is provided in the section titled "The Effect of Direct Current on the Inductance of a Ferrite Circuit."

4.1.3 High-Frequency Broadband Transformer

The frequency ranges are not separated; however, for the sake of this study, it is considered that nickel–zinc ferrites are the preferred core material for high-frequency broadband transformer designs [16]. Typically, this occurs with transformer designs whose bandpass frequency is more than frequency of 500 kHz. This gains importance at these higher operating frequencies to consider the complex magnetic properties of the ferrite core material rather than employing the simple core material's constants recommended for low-frequency systems. Low shunt impedances are also crucial in these systems since transformers operable at high frequency are frequently found usability in circuits having low impedance. The design approach of decreasing R/L is no longer required because winding resistances are typically overcome with only a few spins. Instead, the design will focus on the shape and composition of the core to achieve the required shunt impedance at f and reduce the leakage inductance of the winding. When building high-frequency broadband transformers, it is important to take into account the material's permeability and losses, which have an impact on the shunt impedance. The following materials, coiled in a single turn through both holes, 73, 43, 61, and 67, are measured on the same 28–002,302 multi-aperture core. For high-frequency broadband, the toroidal core geometry is preferred. It is crucial to consider the material's permeability and losses while constructing high-frequency broadband transformers because they have an effect on the shunt impedance. It is preferred to use a toroidal core geometry for high-frequency broadband. This core shape will result in a transformer design with broader bandwidth as it has a shorter single-turn winding length than the same toroidal core of core constant C. Nickel zinc ferrite toroid has been successfully used in the design of numerous broadband transformers. Multi-aperture Ni–Zn ferrite cores must be considered if bandwidth requirements cannot be satisfied using toroid.

4.2 Power Conversion Transformers

Broadband transformers and filters for telecommunications and power converters are the principal applications for ferrite cores. However, various applications have different demands on a material's qualities, and as a result, other ferrite material compositions are employed.

Fig. 10 Power transformer (CC BY 2.0)

Although the quality of commercially available ferrites has steadily increased, several exceptional features reported from laboratories for a long time are still unavailable due to financial considerations. A typical picture of a power transformer is shown in Fig. 10. Compromises are frequently necessary as the best qualities cannot all be presented in one substance simultaneously. For ferrites, it is crucial to design new core types and coil formers that allow for autonomous handling. While there are many different core types for power converters, there are relatively few other material qualities.

In the telecommunications industry, ferrite–core inductors are frequently employed to provide accurate levels of inductance in LC filters for frequency-division multiplexers. A ferromagnetic material and an electromagnetic field interact non-reciprocally to form microwave ferrite devices. Tens were employed extensively in manufacturing high-voltage flyback transformers and TV tube deflection yokes. The technology of ferrites has gained increased significance over the last few decades. Along with introducing new technologies like radar, satellite communications, memory, and computer applications, there has also been a parallel expansion of the consumer markets for radio, television, VCRs, and finally, the internet. Ferrites' specifications have changed as the needs have. High-frequency switching mode power supplies were required to power computers and other digital devices as they transitioned from older analogue circuitry to more modern digital ones. In addition, ferrites have a significant market in the automotive sector, most recently in hybrid vehicles.

5 Conclusions

With "mature" technologies such as hard magnets, magnetic recording, and microwave devices, ferrites are well-known materials that have been studied and used for more than 50 years. However, the improvements in fabrication and application

technologies during the past ten years have been striking. While bulk ferrites remain an important class of magnetic materials, applications for nanostructured ferrites appear to be dramatically wider than those for bulk ferrites. The low cutoff frequency is primarily responsible for influencing one's choice toward selection of ferrite material. The Mn–Zn ferrites can be used in applications requiring a cutoff frequency of 500 kHz. Low- and medium-frequency transformers should have the core shape with the smallest DC resistance relative to the inductance. Using gapped cores and Hanna curves is advocated if a superimposed DC is present. For the requirement of high-frequency designs, nickel zinc ferrite is used. The toroidal and multi-aperture core topologies are advised. To minimizing the leakage inductance and self-capacitance of the windings, the number of turns should be reduced to a minimum possible number. Reduce leakage inductance by winding the primary and secondary windings in a bifilar or strongly linked configuration.

References

1. Goldman A (2006) Applications and functions of ferrites. Mod Ferrite Technol 217–226
2. Roess E (1982) Soft magnetic ferrites and applications in telecommunication and power converters. IEEE Trans Magn 18(6):1529–1534. https://doi.org/10.1109/TMAG.1982.1062068
3. Six W, Koolhof RA (1957) Some applications of square-loop ferrite cores in telecommunication switching circuits. Proc IEE-Part B: Radio Electron Eng 104(7S):491–501
4. Ortiz-Quiñonez JL, Pal U, Villanueva MS (2018) Structural, magnetic, and catalytic evaluation of spinel Co, Ni, and Co–Ni ferrite nanoparticles fabricated by low-temperature solution combustion process. ACS Omega 3(11):14986–15001
5. Mittal VK, Bera S, Nithya R, Srinivasan MP, Velmurugan S, Narasimhan SV (2004) Solid state synthesis of Mg–Ni ferrite and characterization by XRD and XPS. J Nucl Mater 335(3):302–310
6. Kumar S, Singh RR, Barman P (2021) Reitveld refinement and derivative spectroscopy of nanoparticles of soft ferrites (MgNiFe). J Inorg Organomet Polym Mater 31:528–541
7. Kumar S, Barman PB, Singh RR (2021) Estimation and association of structural, elastic and magnetic properties of magnesium-nickel-ferrite nanoparticles annealed at different temperatures. Mater Sci Eng, B 272:115362
8. Gubbala S, Nathani H, Koizol K, Misra RDK (2004) Magnetic properties of nanocrystalline Ni–Zn, Zn–Mn, and Ni–Mn ferrites synthesized by reverse micelle technique. Physica B 348(1–4):317–328
9. Rao BP, Rao KH (1997) Initial permeability dependence on the microstructural and compositional changes in Ni–Zn–Sc ferrites. Le J Phys IV 7(C1):C1-239
10. Lazarević ZŽ, Jovalekić Č, Milutinović A, Romčević MJ, Romčević NŽ (2012) Preparation and characterization of nano ferrites. Acta Physica Polonica, A 121(3)
11. Birajdar AA (2012) Introduction, types and applications of ferrites. SMP College Murom Osama Bad, India
12. Vinicius-Araujo M, Shrivastava N, Sousa-Junior AA, Mendanha SA, Santana RCD, Bakuzis AF (2021) Zn_xMn_{1-X} Fe_2O_4@ SiO_2: z Nd^{3+} core-shell nanoparticles for low-field magnetic hyperthermia and enhanced photothermal therapy with the potential for nanothermometry. ACS Appl Nano Mater 4(2):2190–2210
13. Kumar SS, Singh RK, Verma PK, Siddiqui MIH, Ali MA, Manash A (2021) Tuning of structural, elastic, luminescence, magnetic, and multiferroic properties of rare earth Ce^{3+} substituted strontium hexaferrite Ceramic magnetic nanomaterials for its industrial applications. Appl Phys A 127(10):1–12

14. Kulandaivel A, Jawaharlal H (2022) Extensive analysis on the thermoelectric properties of aqueous Zn-doped nickel ferrite nanofluids for magnetically tuned thermoelectric applications. ACS Appl Mater Interfaces
15. https://product.tdk.com/en/system/files?file=dam/doc/product/ferrite/ferrite/ferrite-core/catalog/ferrite_mz_sw_pq_en.pdf
16. Lima-Tenório MK, Oliveira LA, Guilherme MR, Tenório-Neto ET, Silva MF, Fernandes DM, Pineda EA (2017) Tuning the magnetic properties of ferrite nanoparticles by Zn and Co doping. Mater Lett 195:151–155

Chapter 7
Role of Ferrite Materials in Renewable Energy Harvesting

Surinder Paul, Bandna Bharti, and Rajesh Kumar

1 Introduction

1.1 Ferrite Materials

Ferrites are ceramic compound made of iron oxide (Fe_2O_3) which associated chemically with additional one or more metallic elements such as Barium, Strontium, Nickel, Manganese, Zinc, or other compounds [1]. They have an important ferromagnetic character, and therefore can be attracted to a magnet or magnetized as well as are nonconductive electrically. Ferrites are hard as well as soft in nature. Hard ferrites have high magnetic coercivity whereas soft show low value of magnetic coercivity. Hard ferrites always used to make magnets, small electric motors, refrigerator, and loudspeakers due to its high value of magnetic coercivity whereas soft ferrites because of its low magnetic coercivity used to make ferrite cores for transformers, inductors as well as for various microwave components in electronics industry. Soft as well as hard ferrites are frequently collective with core/shell nanostructures in order to improve their different properties [2]. Ferrites are technologically imperative materials which show three crystalline structures, first spinel's (AB_2O_4), second garnet ($A_3Fe_5O_{12}$), and third magneto plumbite ($AFe_{12}O_{19}$) in which A and B are ions of metal. Spinel ferrites is one of the simplest structure among these which primarily determined by the oxygen ion lattice. Figure 1 showing unit cell of spinel's structure. The oxygen anions in the structure are packed in FCC arrangement which contributes two types of interstitial voids between a sites tetrahedrally coordinated anions and B sites octahedrally coordinated anions [3]. Cation's distributions are determined by

S. Paul · R. Kumar (✉)
Department of Physics and Astronomical Science, Central University of Himachal Pradesh, Dharamshala 176206, India
e-mail: rajeshkumarf11@hpcu.ac.in

B. Bharti
Department of Chemistry, DAV University, Jalandhar, Punjab 144001, India

P. Sharma et al. (eds.), *Engineered Ferrites and Their Applications*, Materials Horizons: From Nature to Nanomaterials, https://doi.org/10.1007/978-981-99-2583-4_7

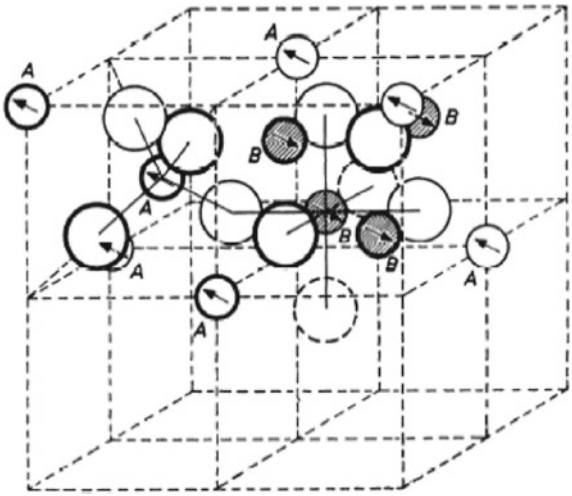

Fig. 1 Unit cell of spinel's structure. Reprinted with permission from Elsevier

different factors like ionic radii, crystal field effect as well as Madelung energy in spinel ferrites [4, 5].

Nanosized ferrites due to its unique properties like high coercivity, moderate saturation magnetization, high electrical resistivity, mechanical strength as well as high chemical stability show significant applications in the field of power electronics, sensors, recording materials, catalysts, spintronics as well as in drug delivery systems, etc. [6, 7]. Various properties like structural, electrical, and magnetic of the nanoferrite can be improved with doping of rare earth elements, transition elements as well as nonmetals. As per requirement as well as applications, a lot of materials include silica; ferrites, elemental carbon, Perovskites, titanium, alloys, noble metals, and polymers may be coated on ferrites in order to get extra functionality from these materials. First time the ferrite material was developed by Yogoro Kato and Takeshi Takei belongs to Tokyo Institute of Technology in 1930 [8]. Ferrite material can be produced by number of synthesis approaches. Application of the ferrite material is greatly affected by the synthesis process. Sol–gel process, Co-precipitation, Hydrothermal technique, Stearic acid gel method, solid-state methods are some well-known synthesis process by which ferrite material can be synthesized.

2 Applications of Ferrite Materials in Renewable Energy Harvesting

Environment-friendly energy harvesting devices has promoted great interest because of the rapid increasing demand for energy solution. It presents a great challenge to our technological future and humanity, as climate changes and environmental pollution are related to energy production and consumption. There are numerous types of

renewable energy sources exist in the environment that ranges from kinetic energy to solar energy and bio-energy. Recently much attention has been paid on energy harvesting technologies to seek energy from readily available sources like, water, air, heat, light, vibration, chemical reaction, and human motion into useful electrical energy for driving small scale device. In this section of the chapter, we shall carry out a detail discussion on the role of ferrite materials in renewable harvesting materials.

2.1 Ferrite Materials Used in Solar Cell

For renewable energy, solar energy is utilized as a significant source and enormously effective renewable resource owing to its energy performance, economic efficiency, and its ability to be used in different places. Ferrite materials are tremendously utilized for the fabrication of solar cell. Perovskite bismuth ferrites (BFO) on ZnO-based solar cell have been reported first time by using chemical solution method. In acidic and corrosive environment, ZnO has poor chemical stability therefore, in order to provide the protective coating on ZnO nanorods, a buffer method using amino silane have been used. After BFO coating, the amino silane coating was removed. Here, BFO acts as a blocking layer and avoid the recombination of electron with N719 because it does not immediately sensitize ZnO to visible light. By comparing the photovoltaic performance of ZnO and ZnO/BFO solar cell, it showed the enhancement from 0.64 mA cm^{-2} to 1.4 mA cm^{-2} and the efficiencies from 0.1 to 0.38% were also increased. The result showed that, the as prepared device displaying improve efficiency by a factor of 4 with the increase in the value of J_{sc} and $V_{oc,}$ respectively [9]. Zinc ferrite (ZF) is also used as a working electrode in dye sensitized solar cell (DSSC). Sol–gel method and thermal decomposition of different precursor were used for the fabrication of ZF electrode in DSSC. Scanning electron microscopy and field emission scanning electron emission studied revealed that, the ZF films were homogeneous and polycrystalline in nature. In this work, the coating of ZF was prepared by using doctor blade technique on fluorine doped tin oxide (FTO). By comparing four different precursors used for the preparation of ZF, the fill factor of ZF with titania thin layer as blocking layer shows maximum value [10]. In another report, auto combustion method was used for the preparation of spinel type barium zinc ferrite via using nitrates as precursor and glycine as fuel. The XRD study confirmed the existence of pure phase zinc ferrite and their crystallite size were varied from 39.5 to 47.6 nm. From optical studies it was confirmed that, with the change in the barium concentration, there was an increase in the optical band gap from 2.42 to 2.50 eV. The highest optimal energy conversion efficiency of 0.0027% was obtained in barium doped zinc ferrite nanoparticles which were confirmed by *J-V* measurements; however, the conversion efficiency of pure zinc ferrite was about 0.0014% [11]. r-NiF (reduced graphene oxide/nickel ferrite) nanocomposites have been reported with the help of hydrothermal method (one-pot). The as prepared r-NiF composite was applied as a catalytic counter electrode for DSSC. The r-NiF composite were inflexibly enfolded on rGO as conformed by HR-TEM, these results

also, illustrate the easy transfer of the electron across the counter electrode materials. DSSC achieved 8.41% of power conversion when r-NiF-25 sample was used as a catalytic electrode catalyst in iodine electrolytes. Also, without encapsulation the fabricated device sustains 88% efficiency up to forty days. Incident photon to current efficiency of DSSC for r-NiF-25 and Pt-based catalytic electrode reached highest absorption of 78% and 81% respectively, at 520 nm. The synergistic outcomes from the combination of conductive graphene and active NiF structure results in high catalytic activity of r-NiF-25 nanocomposites. These outcomes proposed that, r-NiF-25 nanocomposites can be recommended as an auspicious candidate to substitute Pt as a counter electrode in DSSCs [12]. Ceramic bismuth ferrite (BFO) thin film solar cell was fabricated and worked in an out of plane mode. In this work, researcher studied that, the above band gap voltage was actively connected to the alignment, thickness, and orientation of the BFO thin film conferring to the bulk photovoltaic effect, which were confirmed by XRD, SEM, and AFM studies. Oriented BFO thin film solar cell showed 6.9 V open circuit voltage. Also, the maximum open circuit voltage of 6.9 V heated at 500 °C on 600 nm thick cell was confirmed by the current density voltage traces as shown in Fig. 2. These results showed the ferroelectric behavior of the solar cell [13].

Hierarchical bismuth ferrite (BFO) and nanostructure of bismuth ferrite with Ag_2O was fabricated by means of hydrothermal method. Different analytical techniques were used to characterize the fabricated nanostructures. To fabricate DSSC, nanocomposites were used to prepare the photo anode. The addition of Ag_2O nanoparticles with BFO reduced the recombination of photo generated charges and improved the transportation of electrons. DSSC based on Ag_2O/BFO photo electrode displayed 4.25% efficiency of energy conversion and these results indicates

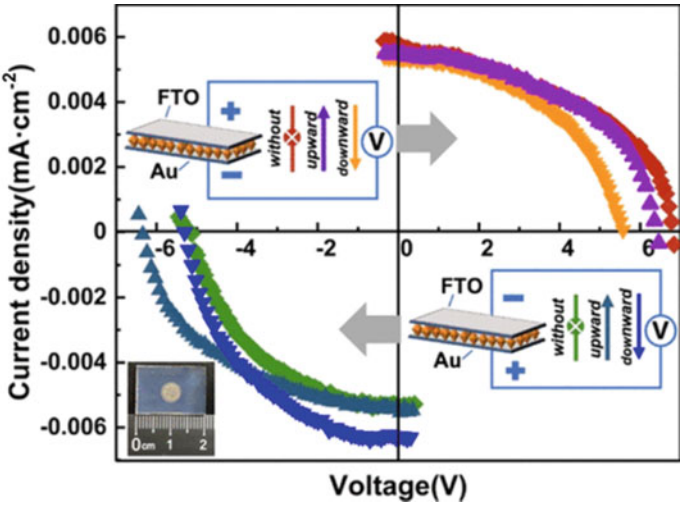

Fig. 2 The current density voltage traces of BFO [14]. Reprinted with permission from ACS

that, silver oxide doping in BFO can be utilized as working electrode in DSSC [15]. Besides DSSCs, perovskite solar cell has attained much attention because of their high efficiency of power conversion. Some research groups have used inorganic materials by replacing charge-transporting layers because inorganic materials are highly durable, environmentally friendly and their low cost. In this work, researchers basically focus on the inorganic electron transport and hole transport layers, zinc oxide and strontium ferrite, respectively, to rise the efficacy of the perovskite solar cell. High charge-collection ability and favorable band alignment make these materials very promising to apply in perovskite solar cell. From computational and experimental analysis, it was found that, the as fabricated device showed 8.83 and 7.80% power energy conversion. By using density functional theory, interface charge transfer and electronic properties illustrated that strontium ferrite was a suitable candidate for hole transfer layer. To achieve the excellent performance of solar cell, the numerical device modeling emphasized on the optimization of the thickness of hole transfer layer (100 nm), perovskite layers (300 nm), and defect density of the absorber (10^{16} cm^{-3}) [16]. A study revealed that, $LaFeO_3$:TiO_2 nanocomposite can be considered as a prominent source of renewable energy. $LaFeO_3$:TiO_2 nanocomposite was prepared by modifying $TiO_2$with inorganic perovskite $LaFeO_3$ which were used as an electron transport layer in perovskite solar cell. In this study, anatase phase of TiO_2 have been reported with an average diameter of approximate 18 nm and the particle size of $LaFeO_3$ was 55 nm. It was observed that, addition of optimum amount of $LaFeO_3$ to electron transfer layer decrease the charge carrier's recombination and charge carrier resistance. Higher performances perovskite solar cells devices were fabricated when $LaFeO_3$ was used in electron transfer layer. The value of V_{oc} and fill factor was 17.05% and 77.33% as displayed by PSC device [17]. Some research groups have implemented $BiFeO_3$ (BFO) thin films which act as an absorber in all photovoltaic devices. A complex solution of metal–organic precursor was used to fabricate the thin films at 673 K in air for 2 h. Uncontaminated form of BFO with rhombohedral structure was confirmed by XRD analysis. In this work, BFO/ZnO heterojunction solar cell was made by solution method. Open circuit voltage of 642 mV, short circuit density of 12.47 mA/cm^2 and fill factor of 50.4% was delivered by BFO/ZnO heterostructures solar cell. These findings illustrated that; the fabricated solar cell displayed a power conversion efficiency of 3.98%. Maximum external quantum efficiency close to 70% showed by the device as shown in Fig. 3a. Further, the time-resolved photoluminescence studied was performed, and the data were depicted in Fig. 3b. These data were in accordance to band-to-band transitions [18].

Some studies have reported the innovative and exceptional characteristics in the area of optoelectronics by integrating two-dimensional materials with ferroelectric thin films owing to their combined intrinsic attributes. Atomic layer deposition method was used to fabricate heterostructures device (bismuth ferrite/ZnO) with distinct electrodes to increase the power conversion efficiency. The power conversion efficiency of heterostructures device was enhanced from 4.1 to 7.4% via using graphene/tin oxide (hybrid transparent electrode). Enhance power conversion efficiency is the main parameter of BFO thin films which emphasize on the importance of

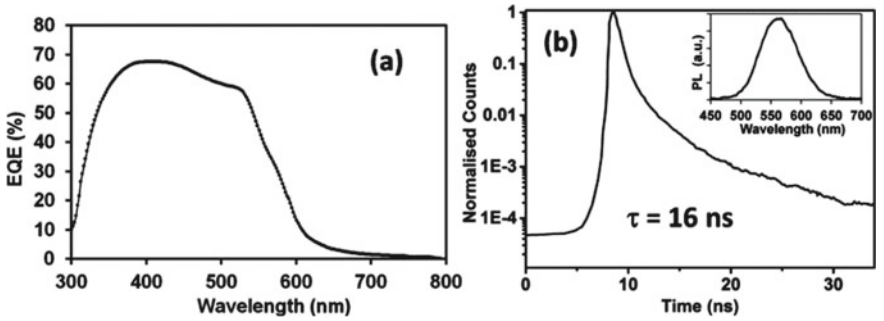

Fig. 3 **a** $BiFeO_3$ solar cell external quantum efficiency and **b** time-resolved photoluminescence, the inset depicts photoluminescence at room temperature [18]. Reprinted with permission from ACS

graphene as an electrode in BFO device which further implemented in optoelectronics and spintronics applications [19].

2.2 Ferrites Materials Used in Supercapacitors

Ternary transition metal ferrite mixed with nanocrystalline (MTTMF) was composed by sol gel approach and the composed materials were utilized as an electrode in supercapacitors. Creation of a single-phase spinel ferrite in NiCuF, NiCoF, and CuCoF were confirmed from the XRD analysis. The electrochemical performance of the nanoferrite was formed in order of CuCoF > NiCoF > NiCuF as confirmed by using impedance spectroscopy, two electrode configurations by galvanostatic approach and cyclic voltammetry. It was found from the analysis that, CuCoF at a scan rate of 5 mVs^{-1} shows maximum specific capacitance of 221 Fg^{-1}. Beside an outstanding cycling stability, an energy density of 7.9 kW kg^{-1} was attained at 1 Ag^{-1}. Based on these findings, it has been found that the increase electrochemical performance of MTTMF nanocomposites illustrated that, it can be utilized as an auspicious electrode for supercapacitors [20]. Copper ferrite nanoparticles connected with graphene nanosheets ($CuFe_2O_4$-GN) was fabricated by using one step solvothermal method. The method used for the preparation of ferrites also highlighted the reduction of graphene oxide and the development of $CuFe_2O_4$ was sustainable, manageable, ascendable, and effective. $CuFe_2O_4$ nanoparticles with a diameter of 100 nm were tightly and efficiently placed on GN. $CuFe_2O_4$-GN construction mechanism was discussed by evaluating the effect of stabilizing agent, concentration of the precursor, precipitation agent, etc. Also, galvanostatic charge–discharge and cyclic voltameter measurement were applied to evaluate the electrochemical properties of $CuFe_2O_4$-GN composite. The as prepared composite showed good cyclic stability, rate performance and enhanced electrochemical performance of 576.6 Fg^{-1} at 1 Ag^{-1}. These results showed better retention and greater specific

capacitance of the electrode materials [21]. Some research work shows that spinel ferrites are the possible energetic materials because of their theoretical capacity and act as an electrode for supercapacitors. A facile hydrothermal method was used for the preparation of $CoFe_2O_4$@graphene nanocomposite which was further worked as a cathode material. In this study, it was found that the weight ratio of ferrites to graphene shows a significant character in the working of the electrode. It was also found that, when the content of graphene was 40% then the specific capacitance could be enhanced to 579 Fg^{-1} at 1 Ag^{-1}. After that an asymmetrical supercapacitors (ASC) was developed by using Fe_3O_4@graphene nanocomposite as an anode material. The as fabricated device showed a promising energy density of 45.5 Wh at a power density of 840 W kg^{-1}, increase specific capacitance of 114.0 Fg^{-1} at a working voltage of 1.7 V. High cycling stability of 91% capacitance retention after 5000 cycles were showed by ASC device [22]. Some research groups have fabricated manganese ($MnFe_2O_4$) nanoparticles via using a hydrothermal method, after that the as synthesized nanoparticles were combined with nanosheets of exfoliated MoS_2. The combined nanoparticles and nanosheets were further used as supercapacitors. Even distribution of $MnFe_2O_4$ nanoparticles on a few layers of MoS_2 were confirmed by transmission electron microscopy. Reduction in the band gap of $MnFe_2O_4$ by MoS_2 was confirmed by UV–visible absorption photo spectroscopy which results an increased conductivity that is appropriate for the capacitance performance. These results revealed that the combination of MoS_2 nanosheets effectively improved the specific capacitance of $MnFe_2O_4$ from 600 to 2093 Fg^{-1} at 1 Ag^{-1} with power density and energy density of 213.64 W kg^{-1}, 46.51 Wh kg^{-1}, respectively. The fabricated device showed well charge–discharge cycling stability [23]. In another study, a simple one-pot co-precipitation method was used for the preparation of manganese cobalt ferrite ($MnCoFeO_4$). The fabricated device, at a scan rate of 1 mVs^{-1} shows a maximum specific capacitance of 675 Fg^{-1} with power and energy densities of 337.50 W kg^{-1}, 18.85 Wh kg^{-1}, respectively at a current density of 1.5 Ag^{-1}. Electrochemical impedance spectroscopy and galvanostatic charging-discharging was used to examine the cyclic stability of the prepared materials. It was found that, degradation of the super capacitive performance was only 7.14% after 1000 galvanostatic charging-discharging cycles which indicates outstanding long-term stability [24]. $Ni_{1-x}Mn_xFe_2O_4$ nanoparticles were used as a supercapacitor electrode material and fabricated by using hydrothermal method. This study also examined the effect of substitution of Ni with Mn on their electronic, structural, and electrochemical properties. Single-phase spinel structure was confirmed from the XRD results and the conversion of inverse structure of $NiFe_2O_4$ to the nearly normal structure of $MnFe_2O_4$ was revealed by Raman spectroscopy. With the increase in the content of Mn, the band gap was decreases. The sample revealed the outstanding performance and suitable cycling stability of the synthesized nanoparticles for supercapacitor as indicated by electrochemical characterization. Increase content of Mn also enhanced the specific capacitance up to 1221 Fg^{-1} for $MnFe_2O_4$ nanoparticles at a current density of 0.5 Ag^{-1}. The correspondence values of energy density and power density were 88.16 Wh kg^{-1} and 473.96 W kg^{-1}, respectively. This study also applied these nanoparticles in real life applications and demonstrated a density

functional theory to confirm the variation in the electronic and geometrical properties that could disturb the electrochemical performance [25]. For supercapacitor applications, Nickel ferrite/graphene nanocomposite were fabricated and implemented as an electrode. This work showed the importance of graphene nanosheet for dictating the morphology of the electrode materials and thus, increasing the performance of the electrode. Nickel ferrite/graphene nanocomposite were attained a specific capacitance of 207 Fg^{-1} which was almost four times higher than the nickel ferrite. 95% stable capacitance was displayed by the composites after 1000 cycles in 1 M sodium sulfate electrolyte. It was also found that the charge transfer resistance of the electrode reduced with graphene nanosheets as confirmed from the electrochemical impedance spectroscopy. The overall results illustrated the importance of the nanocomposite with longer cycle stability and better electrochemical performance [26]. Some research group used a polymeric route to prepare a nanocomposite of N-doped $CoFeO_4$/C (NCFC) with size of 10 nm. The prepared nanocomposites showed outstanding super capacitive performances in comparison of as compared to the pure nanoparticles of MFe_2O_4(M = Ni, Co, Cu, etc.). NCFC nanocomposites showed a specific capacitance of 474 Fg^{-1} at 5 mV/s scanning rate in 5 M KOH which was approximately five times higher than the pure nanoparticles of $CoFe_2O_4$. The corresponding energy densities of pure $CoFe_2O_4$ nanoparticles and NCFC nanocomposite were found to be approximately 23 and 116 Wh kg^{-1}, respectively. NCFC nanocomposites displayed less energy loss as confirmed from the galvanostatic charge–discharge measurements and for 50 segments the discharge time of NCFC nanocomposites were found to be around ten times greater in comparison to $CoFe_2O_4$ nanoparticles [27]. Thin film supercapacitor has established much attention since they can reach both high power densities and high energies densities which make them appropriate for practical application. Zinc ferrite ($ZnFe_2O_4$) thin film attached on multiwall carbon nanotube was prepared by ionic layer adsorption and reaction method (SILAR). The interaction of the composite electrode attains a maximum specific capacity of 217 $mAhg^{-1}$ at 5 mVs^{-1}, and this capacity is due to the contribution of inner and outer active surface of the composite electrode. The prepared device also showed a maximum specific power and specific energy of 377.86 W kg^{-1} and 12.80 Wh kg^{-1}, respectively, as shown in Fig. 4.

A hydrothermal method has been used to fabricate $CoFe_2O_4$@graphene nanocomposites as shown in Fig. 5. The prepared nanocomposite was used as a cathode material. The performance of as fabricated electrode depends on the ferrites to graphene weight ratio. It was found that, when the graphene content in composite was 40%, then the specific capacitance can be appreciably enhanced to 579 Fg^{-1} at 1 Ag^{-1}. After that, Fe_3O_4@graphene nanocomposites were used to construct asymmetric supercapacitor. With the working voltage of 1.7 V, asymmetric supercapacitor distributed an auspicious energy density of 45.5 Wh kg^{-1} and a specific capacitance of 114.0 Fg^{-1} at a power density of 840 W kg^{-1}. After 5000 cycles, 91% capacitance retention of asymmetric supercapacitor was found. It offers an innovative change to construct high performance ASCs with spinel ferrites-based graphene nanocomposites as electrodes [22]. Numerous studies related to the use of ferrite materials in supercapacitor have been reported in the literature as given in Table 1.

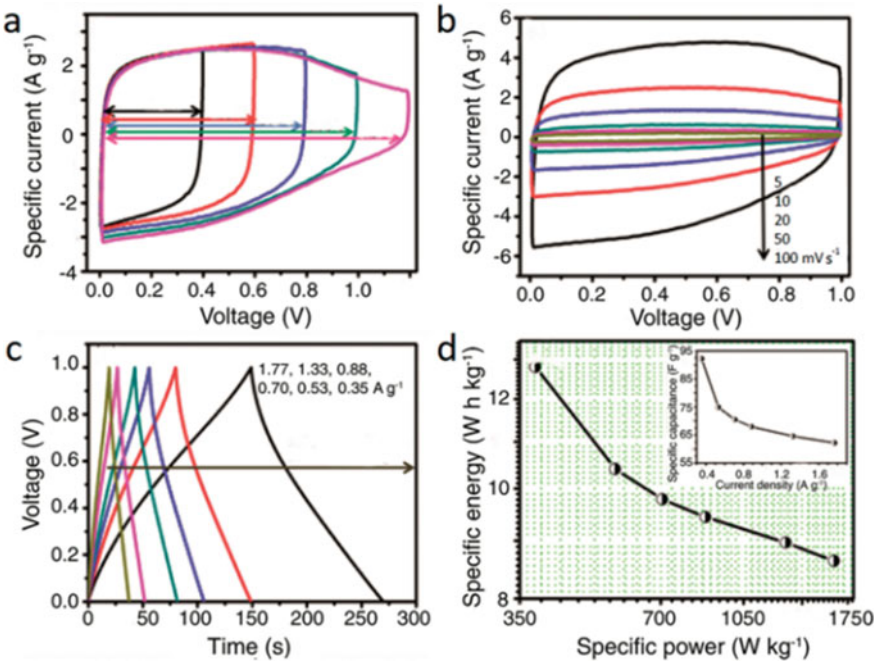

Fig. 4 ZFO–CNT//ZFO–CNT SSS **a** Capacitance retention with cycle number **b** Nyquist plot before and after stability testing. **c** Nyquist plot before and after stability testing **d** phase angle versus log frequency before and after stability testing. Reproduced with permission [28]; copyright 2018, EurJIC

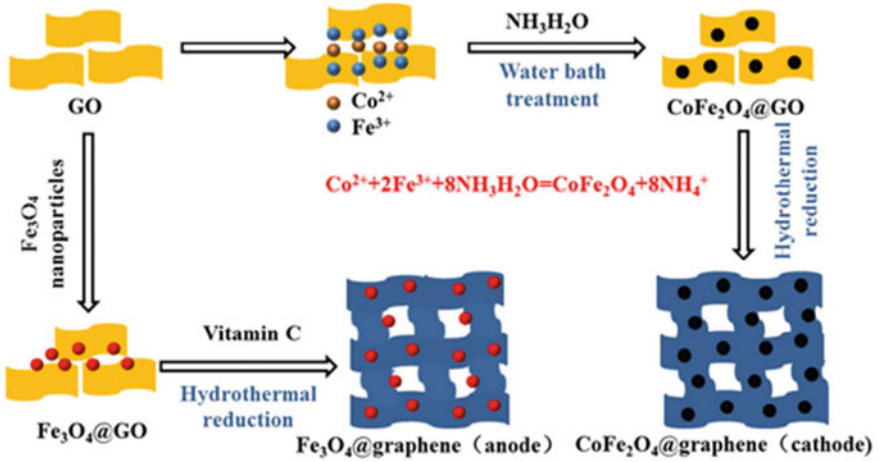

Fig. 5 Synthesis process of $CoFe_2O_4$@graphene and Fe_3O_4@graphene. Reproduced with permission [22]; copyright 2018, ACS

Table 1 Role of different ferrite materials in supercapacitor

Name of the ferrite materials	Use	Specific capacitance	Power density ($W\ kg^{-1}$)	Energy density ($Wh\ kg^{-1}$)	Cycle life	Reference
$Ni/NiFe_2O_4$@Carbon nanocomposite	Electrode	1710 Cg^{-1} for a given current density of 2 Ag^{-1}	3440	62	5000	[29]
Ternary hybrid CoF/G/PANI	Electrode	1123 Fg^{-1} for a given current density of 1 Ag^{-1}	2680	240	2000	[30]
$CoFe_2O_4$ thin films	Electrode	258.5 Fg^{-1} for a given current density of 0.5 mA cm^2	3277	17	1500	[31]
$Ni_{1-x}Co_xFe_2O_4$ solid solution	Electrode	237 Fg^{-1} for a given current density of 1 Ag^{-1}	4208	10.3	4000	[32]
$Ni_{1-x}Mn_xFe_2O_4$ nanoparticles	Electrode	1221 Fg^{-1} for a given current density of 0.5 Ag^{-1}	473.96	88.16	–	[25]
α-$LiFe_5O_8$/NiO	Electrode	134 Cg^{-1} for a given specific current of 4 Ag^{-1}	621	30	5000	[33]
Ternary hybrid CoF/G/PANI	Electrode	1123 Fg^{-1} for a given current density of 1 Ag^{-1}	2680	240	2000	[30]
$NiFe_2O_4$ nanoparticles	Electrode	398 Cg^{-1} for a given current density of 1 Ag^{-1}	14.49	27.71	6500	[34]

(continued)

Table 1 (continued)

Name of the ferrite materials	Use	Specific capacitance	Power density ($W\ kg^{-1}$)	Energy density ($Wh\ kg^{-1}$)	Cycle life	Reference
$MnCoFeO_4$ material	Electrode	675 Fg^{-1} for a given scan rate of 1 mVs^{-1}	337.50	18.85	200 1000	[24]
$CuFe_2O_4$-GN composite	Electrode	576.6 Fg^{-1} for a given current density of 1 Ag^{-1}	1.1	15.8	1000	[21]
$CuFe_2O_4$-rGO//rGO	Nanocomposite-cathode and rGO as anode	163 Fg^{-1} for a given current density of 4 Ag^{-1}	2600	38	10,000	[35]
BFO-RGO nanocomposite	Electrode	928.43 Fg^{-1} for a given current density 5 Ag^{-1}	950	18.62	1000	[36]
$ZnFe_2O_4$ nanoflake@$ZnFe_2O_4$/C nanoparticle heterostructures thin films	Electrode	1884 Fg^{-1} for a given current density of 5 mA cm^{-2}	3.9	81	35,000	[37]
Holey C@$ZnFe_2O_4$ nanoflakes	Electrode in ionic liquid	190 Fg^{-1} for a given current density of 1 Ag^{-1}	0.87	81.4	50,000	[38]

2.3 Ferrites Materials Used in Batteries

In recent years, ferrites materials have been mostly considered for lithium-ion batteries (LIBs). But, due to the serious volume expansion during lithiation/delithiation and low electronic conductivity have restricted the enhancement of capacity and long-life processing of batteries. Therefore, in order to overcome these obstacles, some researchers have used some modifications on ferrites materials. Fluorine doped $ZnFe_2O_4$ have been fabricated via using a quick quenching method. It was used as an anode in LIBs and its performance were examined by electrochemical activity. The method used in this process was not only produces fluorine doping but it also improves the disorder of the atom, which can shield the capacity of swelling to a larger amount. Simultaneously, quenching produces more active sites and induces lattice defects. The prepared anode has the highest specific capacity of 950 mAh g^{-1} after stabilization at 0.5 Ag^{-1}. A high current density of 5 Ag^{-1}, also shows a distinctive rate performance up to 312 mAh g^{-1}. However, the rate performance of ZFO without doping was 200 mAh g^{-1}, which was lower than the fluorine doped ZFO. Hence, from these finding it was confirmed that, the method used in this work efficiently enhanced the electrochemical performance of $ZnFe_2O_4$ [39]. Some research groups have reported the shortcoming of in depth detailed of copper-based ferrites anode architecture with increased electro activity for lithium-ion batteries. To overcome this shortcoming, a research group has reported an advance synthesis method in which copper ferrites attached with reduced graphene oxide ($CuFeO_2$@rGO and Cu/$CuFe_2O_4$@rGO) and act as eminent-working electrodes. It was observed that, in the final configuration the reduced graphene provides increase specific surface area and induces a conductive channel for ion/electron to hold the copper ferrites volume expansion. A high reversible capacity of 587 mAh g^{-1} after 100 cycles at 200 mAg^{-1} was shown by sheet-on-sheet $CuFeO_2$@rGO electrode. Especially, Cu/$CuFe_2O_4$@rGO hybrid, which merges the utilization of reduced graphene and copper nanomaterials, demonstrate a substantial improvement in the properties of lithium storage. It exhibited a robust cycling capability of 1102 mAh g^{-1} after 250 cycles at 800 mA g^{-1} and higher rate capability of 723 mAh g^{-1} at 800 mA g^{-1}. Hence, these results offer an approach for the development of multivalent metal oxide in different device applications where lithium can be stored [40]. After this, in the initial cycles, the conversion electrode formed on ternary or binary oxides are identified to faces some electrode kinetics problem that is interconnected with electrochemical stability, loss of columbic efficiency and diffusion of solid-state lithium. Some research groups have found that, the reason behind the solid-state diffusion during the conversion reaction was grain boundary effect; however, the reason for the electrochemical stability was unrevealed. To overcome this problem some study has reported the utilization of conversion electrode fabricated with nanosized $NiFe_2O_4$. Along with conversion electrode, an alginate binder was also used, which act as an admirable high-rate electrode. In this work, over many cycles 98% of the primary charge storage of $NiFe_2O_4$ electrode was re-established. $NiFe_2O_4$ nanoparticles can distribute 740 mAh g^{-1} capacities at a current rate 1 C with superior dimensions

retention. From these results it has been found that, the ternary metal oxide-based electrode will act as an anode for lithium-ion batteries [41]. Nanocrystalline $NiFe_2O_4$ have been prepared by using citric acid assisted sol gel method. The as synthesized materials were tested as negative electrode for lithium-ion batteries. The stable reversible capacity of 786 mAh g^{-1} with capacity retention of over 85% was exhibited by $NiFe_2O_4$ electrode, after 100 cycles at a constant current density of 0.5 Ag^{-1}. A specific capacity of 365 mAh g^{-1} was attained by $NiFe_2O_4$ electrode, when cycled at a current density of 10 Ag^{-1}. At this current density, $NiFe_2O_4$ nanoparticles as an anode showed outstanding capacity. In this work, it was also revealed that, nickel was present in both metallic nickel and nickel oxide phases and found the reason of partial irreversible capacity while iron was active in the electrochemical reaction with full reversibility [42] (Fig. 6).

Another study reported a hydrothermal method assisted with a microwave for the fabrication of $Fe_{3-x}Sn_xO_4$ nanoparticles which was affixed on reduced graphene oxide with the change in the content of Sn. The as synthesized materials were utilized as anode materials in lithium-ion battery as shown in Fig. 7. After 100 cycles, $Fe_{2.76}Sn_{0.24}O_4$/rGO composite showed a greater reversible capacity of 1428 mAh g^{-1} at a given value of 200 mAg^{-1}, which illustrate the better working of tin-based anode materials. In this work, authors have also investigated the atomic structure and electronic state of the electrode using XAS techniques during a progress of cycles. The rise capacity during cycling was due to the contribution of the decomposition, reversible formation of PGF and the whole reoxidation of tin-tin oxide. Beside this, a newly formed α–FeOOH was found which was due to the reduction of LiOH after 100 cycles [43].

Some research groups have reported the two-step synthesis to produce chromium ferrites ($CrFe_2O_4$) nanoparticles monohybrids and multi-walled carbon nanotubes (MWCNTs). These two-step syntheses include co-precipitation method and ultrasonication assisted route. In the first step, nanoparticles of $CrFe_2O_4$ were synthesized by co-precipitation method, and in the second step, diffusion of $CrFe_2O_4$ on

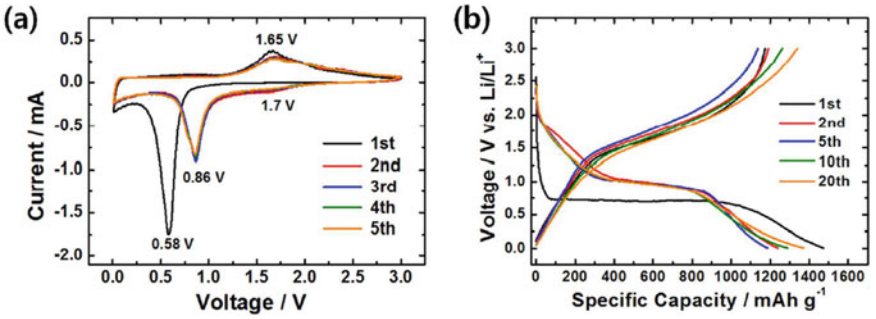

Fig. 6 **a** Curves of cyclic voltammetry scanned at a given value of 0.1 mVs^{-1} and **b** profile of charge/discharge outline with a current density of 0.1 Ag^{-1}. Reproduced with permission [42]; copyright 2017, ACS

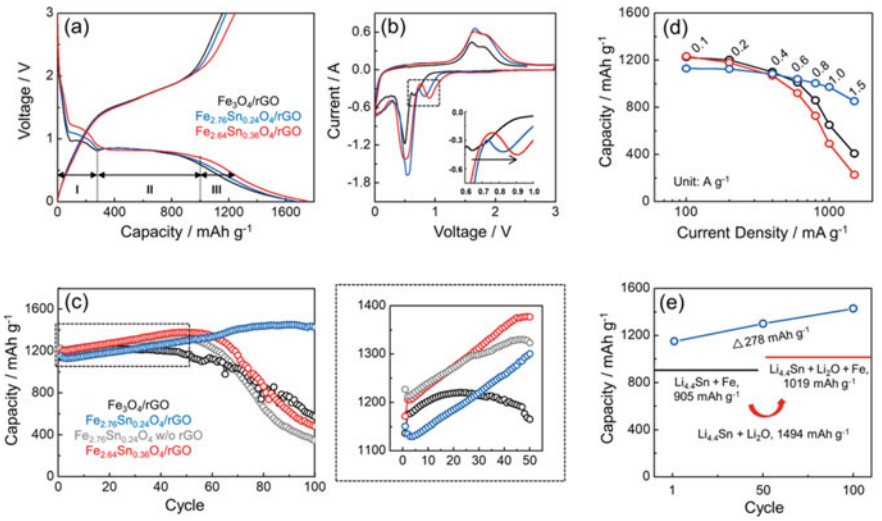

Fig. 7 $Fe_{3-x}Sn_xO_4$/rGO composites **a** first voltage profiles; **b** first cyclic voltammetry curves; **c** cycle performance and the $Fe_{2.76}Sn_{0.24}O_4$ composite without rGO; **d** different current densities from 0.1 to 1.5 Ag^{-1}; **e** capacities of the $Fe_{2.76}Sn_{0.24}O_4$/rGO composite. Reproduced with permission [43]; copyright 2019, ACS

MWCNTs were done by using ultra-sonication assisted route. To obtain the final product $(MWCNTs)_x/CrFe_2O_4$ toluene was used for the dispersal of $CrFe_2O_4$ on MWCNTs. SEM results illustrated that, the as prepared nanoparticles were evenly distributed on MWCNTs and the pulverization of active materials that confirm the transport of electron ion efficiency during lithiation and delithiation was revealed by the analysis of SEM images $(MWCNTs)_x/CrFe_2O_4$. Accordingly, at various values of current densities these monohybrids displayed superior cyclic performances. The as synthesized monohybrid displayed good Li^+ storage properties with increase cyclic stability, better columbic efficiency, and enhanced reversible discharge capacity after 100 cycles. These finding presented a low-cost route to synthesized nanohybrid which act as an anode materials for lithium-ion batteries [44].

Apart from lithium-ion batteries, lithium-sulfur batteries have been studied as the most auspicious energy storage systems, because of their improved hypothetical definite capacity (1675 mAh g^{-1}) and energy density (2600 Wh g^{-1}). Still, it was very stimulating to resolve the problem of low loss kinetics and shuttling of lithium polysulfide. To solve these problems some studies have reported the synthesis of nanoparticles of copper ferrite deposited on carbon nanofibers that is doped with nitrogen via the combination of hydrothermal and electro spun treatments (CF/NC). The as produced materials were used as a collector (positive current) containing Li_2S_3 catholyte for Li–S batteries. CF nanoparticles addition played an essential role in seizing polysulfide's in both chemical and physical adsorption. Also, because of the efficient catalytic effect which result in the promoted sulfur conversion and permitted remarkably enhanced utilization of sulfur, cyclic stability, and longer rate capability.

A cell with CF/NC transported an outstanding cycling stability of 609 mAh g^{-1} after 300 cycles at 0.2 C, under 5.75 mg sulfur loading. At 0.1 C the high initial capacity of the cell was 9.4 mAh under a 12.15 mg loading of sulfur [45]. In another study, a ferromagnetic one-dimensional porous Fe_3O_4@C electrode (1D-Fe_3O_4@C) as a sulfur host has been reported. The as prepared electrode showed a strong binding effect on polysulfide's through physical adsorption and Lorentz forces, hence lowering the shuttle effect. The reason behind this finding was its 1D structure. Simultaneously, the porous morphology of the prepared materials encourages the loading of sulfur and during cycling, enfolds the large volume changes. Superior specific capacity and excellent high-rate cyclability was exhibited by 1D-Fe_3O_4@C, which was confirmed by the capacity retention rate of 95.1 and 92.7% respectively, for 200 cycles [46].

2.4 Ferrite Materials Used in Fuel Cell

Fuel cell is a device which can converts chemical energy into electrical energy and heat excluding direct release as well as combustion of nitrous oxides (NO_x), carbon oxides (CO_x), and sulfur oxides (SO_x). There are various types of fuel cells like molten carbonate, alkaline, polymer electrolyte membrane, solid oxide, and phosphoric acid fuel cell. As solid materials are used for the fabrication of solid oxide fuel cell that's why it is different among other types of fuel cells and oxygen ions traveling through the fuel cell to produce electricity. Efficiency of solid oxide fuel cell can arrive at up to 60% and goes up to 80% on heat recovery [47]. Electrolyte, cathode, anode, and interconnects are main components of solid oxide fuel cell. Ferrite material more frequently used to prepare the components of the solid oxide fuel cell to obtain better efficiency from the cell without polarization loss of the material during working of the cell. Working diagram of solid oxide fuel cell is shown in Fig. 8.

Oxygen (air) enters at the cathode side of the cell, where reduction of oxygen molecules in to oxygen ions takes place. Generally, porous ceramic materials are used as cathode, so that conduction of electron as well as ions takes place easily. The oxygen ions migrate toward anode through the electrolyte which is a dense layer of ceramic, predominately an ionic conductor. At anode, gaseous fuel (Hydrogen) enters the cell and react with oxygen ions migrated from cathode through electrolyte; as a result, oxidation of hydrogen take place thereby generates the electrons. From external circuit, electrons travel toward cathode from anode side which maintains permanent supply of oxygen ions for electrolyte and generate sufficient electric power along with water and heat as byproduct [49–52]. Perovskite-type oxides materials commonly uses as cathode material of SOFCs. The general formula of perovskite is ABO_3, in which A and B both have + 6 positive charge. 'A' cations are the combination of rare and alkaline earth metals (such as La, Ca, Ba, and Sr, etc.) which are bigger in size and coordinated with 12 oxygen anions on the other hand 'B' cations are reducible transition metals (such as Mn, Ni, Cr, Co, and Fe, etc.)

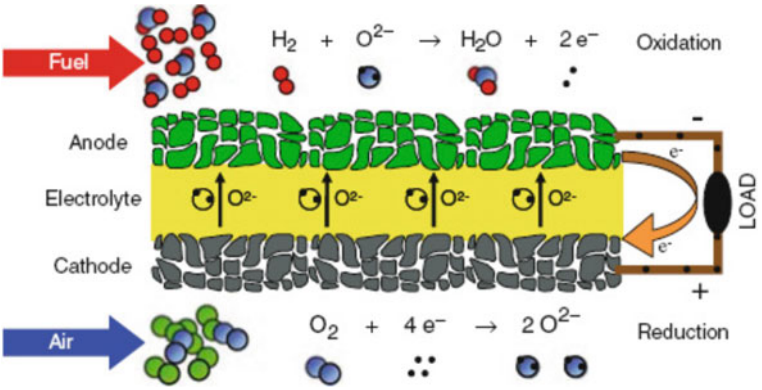

Fig. 8 Working diagram of solid oxide fuel cell. Reproduced with permission [48]; copyright 2006, Springer

which are much lesser in size and therefore coordinated with 6 oxygen anions [53, 54]. Figure 9 shows a typical structure of ABO_3 perovskite [55].

At the B-site of ABO_3 perovskite cathode material, Fe substituted cathode is more stable than Co substituted because Fe^{3+} ion has stable electronic configuration $3d^5$ therefore conversion of Fe^{3+} to Fe^{4+} is very small. The maximum power density makes the Sr-doped $LaFeO_3$ (LSF) promising cathode for SOFCs. $La_{0.80}Sr_{0.20}FeO_3$ (LSF) cathode achieves maximum power densities 0.90–0.95 W cm^{-2} at temperature 750 °C and 0.7 V and outstanding stability. In addition, area specific resistance of the ferrite-based cathode $La_{0.80}Sr_{0.20}FeO_3$ significantly reduced to 0.1 Ω cm^2 at temperature 800 °C, and TECs are near to those of the CGO and YSZ electrolyte [56].

Doping of Sr to $LaFeO_3$ (LSF) create charge imbalance, this charge neutrality is compensated either by creation of Fe^{4+} ion or by oxygen vacancy. At high temperature, oxygen vacancies are formed in LSF by losing oxygen and due to this hole concentration decreases. When the partial pressures of oxygen (e.g., air or O_2) are very high, holes are the leading charge carriers but at lesser partial pressures of

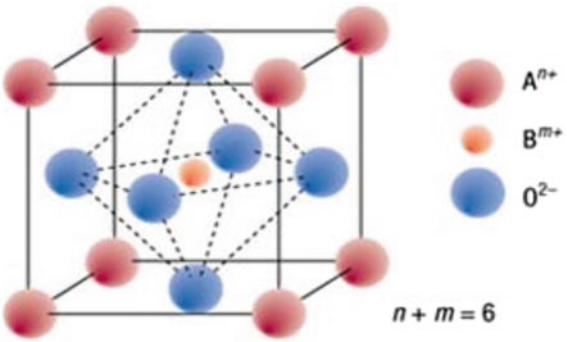

Fig. 9 Unit cell of structure of the ABO_3 perovskite. Reproduced with permission [55]; copyright 2003, Nature Materials

oxygen charge imbalance are neutralized by the creation of vacancies of oxygen in the material. The total conductivity of ferrite is therefore due to mobility of the electron or hole instead of oxygen ions; therefore, whole conductivity in ferrite is due to hole conduction [57]. $Ln_{0.50}M_{0.50}FeO_{3-\delta}$Perovskites (Ln = La, Nd, Pr; M = Sr, Ca, and Ba) A-site cation disorder affect the electronic and electrochemical performance. They observed highest conductivity and working for Lanthanum-based materials and reported that slight cationic radii covering cathode materials will react extra energetically with electrolytes [58].

3 Conclusions

Recently, semiconducting industry receiving much consideration in the field of energy harvesting, the promising field that used semiconductor. In order to achieve semiconducting materials, nanotechnology is used to fabricate different materials used for the fabrication of various devices. A general introduction of various types of ferrites nanomaterials and their application in different field were discussed. Different ferrites nanomaterials such as perovskite bismuth ferrites, NiF_2O_4, $MnFe_2O_4$, Ni/$NiFe_2O_4$@carbon nanocomposites, $CuFe_2O_4$-rGO//rGO, $ZnFe_2O_4$ nanoflakes@$ZnFe_2O_4$/C, etc. were discussed in this chapter. These ferrites nanomaterials were used in various applications such as organic solar cell, dye sensitized solar cell, photovoltaic cell, photo detector, photodiodes, supercapacitors, batteries, and fuel cell. The demand for solar cells, supercapacitors, fuel cell, batteries transistor, and diodes are increasing tremendously every year due to their enormous range of applications. In case of supercapacitor, ferrite nanomaterials enhance the energy density and specific super capacitance of as prepared device by showing good cyclic stability, better retention, rate performance, and higher electrochemical performance. In case of fuel cell, the electrochemical capacitance and power density were improved by ferrite nanomaterials where it worked as an anode material. Ferrites materials are also used in batteries, but due the less electronic conductivity, these materials have limited the long-life utilization of batteries. Therefore, to overcome these limitations, the ferrites nanomaterials are modified by different metals and nonmetals. The modified ferrites materials have showed high current densities, larger specific capacitance. Hence by using ferrite nanomaterials, various types of energy storage and energy conversion devices were utilized to minimize the energy crisis.

References

1. Carter CB, Norton MG (2007) Ceramic Materi: Sci Eng. 212–15. ISBN 978-0-387-46270-7
2. Girgis E, Wahsh MM, Othman AG, Bandhu L, Rao KV (2011) Synthesis, magnetic and optical properties of core—shell $Co_{1-x}Zn_xFe_2O_4/SiO_2$ nanoparticles. Nanosc Resear Lett 6(1):1–8
3. Nair DS, Kurian M (2018) Chromium-zinc ferrite nanocomposites for the catalytic abatement of toxic environmental pollutants under ambient conditions. J Hazard Mater 344:925–941

4. Jacob BP, Thankachan S, Xavier S, Mohammed EM (2013) Effect of Tb^{3+} substitution on structural, electrical and magnetic properties of sol–gel synthesized nanocrystalline nickel ferrite. J Alloys Compd 578:314–319
5. Kurian M, Nair DS, Rahnamol AM (2014) Influence of the synthesis conditions on the catalytic efficiency of $NiFe_2O_4$ and $ZnFe_2O_4$ nanoparticles towards the wet peroxide oxidation of 4-chlorophenol. React Kinet Mech Catal 111(2):591–604
6. Paul S, Manokamna, Kumar A, Sharma DK, Singh A, Kumar A (2022) Rasayan J Chem 15(1):210–216. https://doi.org/10.31788/RJC.2022.1516751
7. Paul J, Philip J (2020) Design optimization and stability enhancement of modified inter-digital capacitive humidity transducer with cobalt ferrite nanoparticles as dielectric. Trans Inst Meas Contr 42:4
8. Okamoto A (2009) The invention of ferrites and their contribution to the miniaturization of radios. In: IEEE Globecom workshops. pp 1–42
9. Loh L, Briscoe J, Dunn S (2014) Enhanced performance with bismuth ferrite perovskite in ZnO nanorod solid state solar cells. Nanoscale 6(12):7072–7078
10. Habibi MH, Habibi AH, Zendehdel M, Habibi M (2013) Dye-sensitized solar cell characteristics of nanocomposite zinc ferrite working electrode: effect of composite precursors and titania as a blocking layer on photovoltaic performance. Spectrochim Acta Part A Mol Biomol Spectrosc 110:226–232
11. Tholkappiyan R, Vishista K (2014) Synthesis and characterization of barium zinc ferrite nanoparticles: working electrode for dye sensitized solar cell applications. Sol Energy 106:118–128
12. Samson VAF, Bernadsha SB, Britto JF, Raj MVA, Madhavan J (2022) Synthesis of $rGO/NiFe_2O_4$ nanocomposite as an alternative counter electrode material to fabricate Pt-free efficient dye sensitized solar cells. Diam Relat Mater 109406
13. Liang KY, Wang YF, Yang Z, Zhang SP, Jia SY, Zeng JH (2021) Above-band-gap voltage from oriented bismuth ferrite ceramic photovoltaic cells. ACS Appl Energy Mater 4(11):12703–12708
14. Kurian M, Thankachan S (2021) Open Ceramics 8(2021):100179. https://doi.org/10.1016/j.oceram.2021.100179
15. Ahamad T, Aldalbahi A, Alshehri SM, Alotaibi S, Alzahly S, Wang ZB, Feng PX (2021) Enhanced photovoltaic performance of dye-sensitized solar cells based Ag_2O doped $BiFeO_3$ hetrostructures. Sol Energy 220:758–765
16. Tangra AK, Kanoun MB, Goumri-Said S, Kanoun AA, Musselman K, Kaur J, Lotey GS (2022) Low-cost inorganic strontium ferrite a novel hole transporting material for efficient perovskite solar cells. Nanomaterials 12(5):826
17. Moradi F, Shariatinia Z, Safari N, Mohajerani E (2022) Boosted performances of mesoscopic perovskite solar cells using $LaFeO_3$ inorganic perovskite nanomaterial. J Electroanal Chem 916:116376
18. Tiwari D, Fermin DJ, Chaudhuri TK, Ray A (2015) Solution processed bismuth ferrite thin films for all-oxide solar photovoltaics. J Phys Chem C 119(11):5872–5877
19. Afzal AM, Javed Y, Hussain S, Ali A, Yaqoob MZ, Mumtaz S (2020) Enhancement in photovoltaic properties of bismuth ferrite/zinc oxide heterostructure solar cell device with graphene/indium tin oxide hybrid electrodes. Ceram Int 46(7):9161–9169
20. Bhujun B, Tan MT, Shanmugam AS (2017) Study of mixed ternary transition metal ferrites as potential electrodes for supercapacitor applications. Results Phys 7:345–353
21. Zhang W, Quan B, Lee C, Park SK, Li X, Choi E, Diao G, Piao Y (2015) One-step facile solvothermal synthesis of copper ferrite–graphene composite as a high-performance supercapacitor material. ACS Appl Mater Interfaces 7(4):2404–2414
22. Wang H, Song Y, Ye X, Wang H, Liu W, Yan L (2018) Asymmetric supercapacitors assembled by dual spinel ferrites@ graphene nanocomposites as electrodes. ACS Appl Energy Mater 1(7):3206–3215
23. Sharifi S, Rahimi K, Yazdani A (2021) Highly improved supercapacitance properties of $MnFe_2O_4$ nanoparticles by MoS_2 nanosheets. Sci Rep 11(1):1–15

24. Elkholy AE, Heakal FET, Allam NK (2017) Nanostructured spinel manganese cobalt ferrite for high-performance supercapacitors. RSC Adv 7(82):51888–51895
25. Sharifi S, Yazdani A, Rahimi K (2020) Incremental substitution of Ni with Mn in $NiFe_2O_4$ to largely enhance its supercapacitance properties. Sci Rep 10(1):1–15
26. Soam A, Kumar R, Sahoo PK, Mahender C, Kumar B, Arya N, Singh M, Parida S, Dusane RO (2019) Synthesis of nickel ferrite nanoparticles supported on graphene nanosheets as composite electrodes for high performance supercapacitor. Chem Select 4(34):9952–9958
27. Alshehri SM, Ahmed J, Alhabarah AN, Ahamad T, Ahmad T (2017) Nitrogen-doped cobalt ferrite/carbon nanocomposites for supercapacitor applications. ChemElectroChem 4(11):2952–2958
28. Raut SS, Sankapal BR, Hossain MSA, Pradhan S, Salunkhe RR, Yamauchi Y (2018) Zinc ferrite anchored multiwalled carbon nanotubes for high-performance supercapacitor applications. Eur J Inorg Chem 2018(2):137–142
29. Athika M, Prasath A, Sharma AS, Devi VS, Duraisamy E, Elumalai P (2019) Ni/$NiFe_2O_4$@ carbon nanocomposite involving synergistic effect for high-energy density and high-power density supercapattery. Mater Res Exp 6(9):095503
30. Mousa MA, Khairy M, Shehab M (2017) Nanostructured ferrite/graphene/polyaniline using for supercapacitor to enhance the capacitive behavior. J Solid-State Electrochem 21(4):995–1005
31. Nikam SM, Sharma A, Rahaman M, Teli AM, Mujawar SH, Zahn DRT, Patil PS, Sahoo SC, Salvan G, Patil PB (2020) Pulsed laser deposited $CoFe_2O_4$ thin films as supercapacitor electrodes. RSC Adv 10(33):19353–19359
32. Malima NM, Khan MD, Choi J, Gupta RK, Mashazi P, Nyokong T, Revaprasadu N (2021) Solventless synthesis of nanospinel $Ni_{1-x}Co_xFe_2O_4$ ($0 \leq x \leq 1$) solid solutions for efficient electrochemical water splitting and supercapacitance. RSC Adv 11(49):31002–31014
33. William JJ, Babu IM, Muralidharan G (2019) Lithium ferrite (α-$LiFe_5O_8$) nanorod based battery-type asymmetric supercapacitor with NiO nanoflakes as the counter electrode. New J Chem 43(38):15375–15388
34. Mordina B, Kumar R, Neeraj NS, Srivastava AK, Setua DK, Sharma A (2020) Binder free high performance hybrid supercapacitor device based on nickel ferrite nanoparticles. J Energy Storage 31:101677
35. Makkar P, Gogoi D, Roy D, Ghosh NN (2021) Dual-purpose $CuFe_2O_4$-rGO-based nanocomposite for asymmetric flexible supercapacitors and catalytic reduction of nitroaromatic derivatives. ACS Omega 6(43):28718–28728
36. Maitra D, Anand C, Ghosh BK, Chandel M, Ghosh NN (2018) One-dimensional $BiFeO_3$ nanowire-reduced graphene oxide nanocomposite as excellent supercapacitor electrode material. ACS Appl Energy Mater 1(2):464–474
37. Vadiyar MM, Kolekar SS, Chang JY, Ye Z, Ghule AV (2017) Anchoring ultrafine $ZnFe_2O_4$/Nanoparticles on 3D $ZnFe_2O_4$ nanoflakes for boosting cycle stability and energy density of flexible asymmetric supercapacitor. ACS Appl Mater Interfaces 9(31):26016–26028
38. Vadiyar MM, Bandgar SB, Kolekar SS, Chang JY, Ling YC, Ye Z, Ghule AV (2019) Holey C@ $ZnFe_2O_4$ nanoflakes by carbon soot layer blasting approach for high performance supercapacitors. ACS Appl Energy Mater 2(9):6693–6704
39. Zhao Q, Peng P, Zhu P, Yang G, Sun X, Ding R, Gao P, Liu E (2022) F-doped zinc ferrite as high-performance anode materials for lithium-ion batteries. New J Chem 46(20):9612–9617
40. Wang J, Deng Q, Li M, Jiang K, Zhang J, Hu Z, Chu J (2017) Copper ferrites@ reduced graphene oxide anode materials for advanced lithium storage applications. Sci Rep 7(1):1–12
41. Kumar PR, Mitra S (2013) Nickel ferrite as a stable, high capacity and high-rate anode for Li-ion battery applications. RSC Adv 3(47):25058–25064
42. Islam M, Ali G, Jeong MG, Choi W, Chung KY, Jung HG (2017) Study on the electrochemical reaction mechanism of $NiFe_2O_4$ as a high-performance anode for Li-ion batteries. ACS Appl Mater Interfaces 9(17):14833–14843
43. Um JH, Palanisamy K, Jeong M, Kim H, Yoon WS (2019) Phase dynamics on conversion-reaction-based tin-doped ferrite anode for next-generation lithium batteries. ACS Nano 13(5):5674–5685

44. Mumtaz M, Lashari NUR, Hassan M, Tangsee S, Khan MT (2021) Multi-walled carbon nanotubes and chromium ferrites nanoparticles nanohybrids as anode materials for lithium-ion batteries. J Alloy Compd 872:159654
45. He Y, Bi M, Yu H, Zhang C, Majeed A, Shen X, Yao S (2021) Nanoscale $CuFe_2O_4$ uniformly decorated on nitrogen-doped carbon nanofibers as highly efficient catalysts for polysulfide conversion in lithium-sulfur batteries. ChemElectroChem 8(23):4564–4572
46. Huang Y, Li Z, Zhu T, Gao X, Lv X, Ling M, Wan Z, Xia Y (2021) Ferromagnetic 1D-Fe_3O_4@C microrods boost polysulfide anchoring for lithium–sulfur batteries. ACS Appl Energy Mater 4(4):3921–3927
47. Singhal SC (2000) Solid State Ionics 135:305
48. Serra JM (2006) Nano-structuring of solid oxide fuel cells cathodes. Top Catal 40(1–4):123–131
49. Manokamna, Paul S, Kumar A, Singh A, Singh KL, Bhargav G, Singh AP (2021) Mater Today: Proc 45:4639–4645. https://doi.org/10.1016/j.matpr.2021.01.095
50. Liu M, Lynch ME, Blinn K, Alamgir F, Choi Y (2011) Rational SOFC material design: new advances and tools. Mat Today Invited Rev 14:534
51. Devi S, Ahmed N, Manokamna, Singh A, Paul S (2022) Mater Today: Proc 60(3):1989–1993. https://doi.org/10.1016/j.matpr.2022.01.214
52. Menzler NH, Batfalsky P (2012) Fuel cell science and engineering: materials processes, systems and technology. Wiley Science, USA
53. Skinner SJ (2001) Recent advances in Perovskite-type materials for solid oxide fuel cell cathodes. Int J Inorg Mater 3:113–121
54. Paul S, Manokamna, Kaur S, Malhi PS, Singh A, Kumar A (2019) Int J Innovative Technol Exploring Eng 9–1:324–328
55. Boukamp BA (2003) Fuel cell: the amazing perovskite anode. Nat Mater 2:294–296
56. Simner SP, Bonnett JF, Canfield NL, Meinhardt KD, Sprenkle VL, Stevenson JW (2002) Optimized lanthanum ferrite-based cathodes for anode supported SOFCs. Electrochem Solid-State Lett 5:A173
57. Zhou XD, Anderson HU (2005) SOFC-IX: solid oxide fuel cells IX, electrochemical society proceedings, Quebec PQ, Canada. pp 1479–1486
58. Vidal K, Rodriguez-Martinez LM, Ortega-San-Martin L, No ML, Rojo T, Arriortua MI (2011) Fuel Cells 11:51–58

Chapter 8
Ferrite Nanocomposites for EMI Shielding Applications

Neha Thakur, Shubhpreet Kaur, Indu Sharma, and Gulshan Kumar

1 Introduction

The fast development of new gadgets and the adoption of fully interconnected circuits have created a new form of pollution identified as EMI. The usage of electromagnetic technologies has increased significantly during the past ten years, especially in communication systems, health sciences, and security devices. Significant effort has been put into the extensive development of wireless electronic equipment. These technological applications result in electromagnetic (EM) pollution and interference in the environment. EMI has evolved into a significant matter that not only impacts human health but also interacts with the functioning of electrical gadgets. Therefore, shielding is necessary to protect electronics connected to strategic systems from severe electromagnetic radiation that cannot be avoided, such as from transformers, airplanes, nuclear reactors, control mechanisms, and communications networks [1, 2]. Exploiting a brand-new material with significant electromagnetic wave absorption qualities is a good strategy to solve these issues. This absorber is useful for attenuating electromagnetic radiation by magnetic or dielectric loss, and it can be used to reduce the electromagnetic response from metal substrates like airplanes, ships, tanks, anechoic chamber walls, and electronic devices [3]. Electrostatic discharge (ESD) is the most common EMI cause. Even a non-technical person can easily identify this ubiquitous phenomenon as audio static, damaged satellite coverage in the type of screen sparkles, and the select that can be detected on compatible devices whenever

N. Thakur · I. Sharma (✉)
Department of Physics, Career Point University, Hamirpur, Himachal Pradesh 176041, India
e-mail: indu.phy@cpuh.in

S. Kaur
Multifunctional Material Laboratory, Department of Physics, Guru Nank Dev University, Amritsar, Punjab 143005, India

G. Kumar
Department of Botany, Career Point University, Hamirpur, Himachal Pradesh 174061, India

P. Sharma et al. (eds.), *Engineered Ferrites and Their Applications*, Materials Horizons: From Nature to Nanomaterials, https://doi.org/10.1007/978-981-99-2583-4_8

a light is turned up. Upon exposure to electromagnetic radiation, EMI also origin health risks like as drowsiness, sleeplessness, anxiety, and headaches [4]. In order to decrease their impact, electronic devices should be shielded or cased to ensure that no electromagnetic waves enter or leave the equipment. A material or piece of device that has been appropriately shielded both decreases any undesired emissions from that instruments and shields it from any potential interference from outside electromagnetic radiations or signals. A surface that is conductive or magnetic can successfully shield EM waves using reflection, absorption, and multireflection mechanisms. This property is known as EMI shielding efficiency (EMI-SE) [5]. Radiated or conducted electromagnetic interference can either reject or impact an electrical system. Conduction interaction of electromagnetic radiations can be avoided by utilizing frequency filters or inductors in the circuit design. On the other hand, radiation can be prevented by physically shielding the source. Thus, EMI shielding attempts to block or decrease EM radiation from emitters by utilizing materials capable of interfacing with such signals. In order to reduce the possibility of electrical equipment failure due to electromagnetic pollution and sound, newly discovered EM shields and absorbing substances have now been created and manufactured [6]. The equilibrium of complex permeability and permittivity may result in an increase in the ability to absorb EM waves when impedance matching conditions are satisfied. The most common way to achieve impedance matching is to combine a magnetic material with dielectric elements. Hexaferrites are a category of materials with magnetic properties that have numerous uses in technology, particularly in electronic equipments [7]. Resonance frequency absorbers (ferrites) and dielectric absorption were used to identify electromagnetic interference absorption (foams). Due to the excessive thickness of dielectric absorbent, resonance frequency absorbers were used as effective electromagnetic absorbers. M-type hexaferrites are among the most practical and promising EMAs. Magnetic moments, storage systems, and recording, as well as electrical and electromagnetic absorption materials, are only a few uses for ferromagnetic barium hexaferrites [8]. Substances for electromagnetic pulse (EMP) shielding and materials for EMI shielding are directly connected. A brief electromagnetic energy explosion, including those generated by electricity and nuclear detonation, is known as an EMP. Antennas, which operate in both the radio frequency and microwave bands, are relevant applications for highly conductive elements that are characteristic of EMI shielding technologies [9]. Anand et al. [10] reported zirconium-substituted barium hexaferrite nanomaterials as well as reduction graphene oxide fillers in a polyvinylidene fluoride matrix to create ultra-light and adaptable polymeric films for electromagnetic radiation absorption and high electromagnetic shielding. Primarily, Zr-doped barium M-type hexaferrite ($BaZrFe_{11}O_{19}$) was prepared by sol–gel autocombustion, and RGO was produced using a simplified Hummers route accompanied by a heat removal process. The resulting adjustable films have an electromagnetic interference shielding efficiency of 48.59 dB at frequency range 11.1 GHz for a 10 weight percent addition of $BaZrFe_{11}O_{19}$ in polymer composites with a very thin thickness of 0.2 mm. The significance of energy absorption of 40.98 dB is caused by increased electrical resistivity and magnetic loss both of which are shown to be reduced with the addition of fillers formed of ferrite. These findings show that

reduced graphene oxide fillers with minimal substituted barium M-type hexaferrite nanofillers implanted in polymeric nanocomposites films probably one of the potential radiations shielding materials for radio detection and ranging and weapons systems. Bheema et al. [11] report the interference shielding effectiveness of epoxy composite samples that contain barium M-type hexaferrite nanomaterials as well as graphene nanocrystal over the X-band (8–12.4 GHz). Shooshtary Veisi et al. [12] investigated the synthesis of copper and zirconium-substituted barium strontium M-type hexaferrite/poly (ortho-toluidine) nanomaterials as microwave shielding in the Ku-band frequency spectrum 12–18 GHz using in situ polymerization of ortho-toluidine. In comparison with the additional samples inside the Ku-band frequency range (12–18 GHz), the vector network analyzer measurement of the BSCZH/POT nanocomposite with a 2 mm thickness revealed that it had the maximum microwave absorbance of almost 90% for Cu/Zr-doped barium strontium hexaferrites/POT for ($X = 0.2$). The results suggest that the new entity, a nanocomposite, could be employed as a powerful electromagnetic interface shield to protect against electromagnetic radiation. Tohidifar [13] studied the electromagnetic interference (EMI) shielding and broadband electrical characteristics of a multi-walled carbon nanotube (MWCNT)/barium titanate nanocomposites. Furthermore, adding 6 weight percent ($Bi_2O_3 + B_2O_3$) to a 1.5 mm nanocomposite containing dissimilar weight percent MWCNT resulted in an electromagnetic interference shielding effect significantly larger than 28 dB, indicating that this innovative nanomaterials is a highly effective choice for electromagnetic absorbance and electromagnetic fields applications. Dalal et al. [2] using a simple in situ chemical oxidative polymerization process, poly(3,4-ethylenedioxythiophene)/reduction graphene oxide/$PbTiO_3$ nanocomposites have been created. The manufacturing technique produces core–shell-shaped nanocomposites with $PbTiO_3$ as the main filler and reduction graphene oxide as the second filler in a matrix of poly(3,4-ethylenedioxythiophene). The outcome is an improved electromagnetic shielding efficacy rating of 51.94 dB in the frequency range of 12.4–18 GHz. Using thermal gravimetric analysis and Fourier transmission infrared spectroscopy, the nanocomposites were further investigated.

The present and prospective wireless technologies require the use of suitable shielding materials in order to protect the devices from harmful radiation and prevent compromises in their performance and durability. Due to the growing demands of portable devices, current generation electronics need shielding materials that are flexible and light [14].

2 Mechanism of EMI Shielding

A specific kind of plane wave is an electromagnetic wave. Its direction of propagation is parallel to the magnetic and electric fields' plane. The intensity of the energy increases with frequency. The far-field region was the focus of electromagnetic interference shielding research, and the shielding substance was conductible. Transmission line theory is a widely established analytical theory that combines ease

of calculation with great precision and clarity [15]. The three EMI attenuation mechanisms are reflection, absorption, and multiple reflections. The main method, reflection, depends on the presence of moving charged particles (electrons or holes) that participate in electromagnetic radiation interaction. However, higher conductivity may not be essential for protection; the shield would prefer to be electrically conductive. Shielding did not necessarily require connectedness in the conductive network; however, conduction does. The reflect reduction is determined by the proportions of the electrical conductivity of copper and the magnetic permeability of copper, respectively [16]. Absorption is frequently a second method of EMI protection. The barrier should have both electrical and magnetic eddy currents that coincide with the electromagnetic energy in the radiation to absorb considerable amounts of radiation. Electric dipoles can be created using materials with high dielectric strengths. The presence of magnetic dipoles can also be produced by several additional components having a higher magnetic permeability, which can be improved by using many layers of magnetic films to decrease the number of magnetic domain boundaries [17]. Figure 1 demonstrates an incoming electromagnetic (EM) wave passing through a hard object. Absorption loss is an objective of $\sigma_r.\mu_r$ and is proportional to shielding thickness. Although reflection generally decreases with frequency, absorption generally increases as frequency increases. Multiple reflections are the third shielding method. At the shield's surfaces or interfaces, several wave reflections occur. Large surface areas or contacts must be available for this mechanism to function [18]. Schoellkopf's theory states that when electromagnetic waves reach the shielding material's surface, some of them are directly reflected (SE_R) because of an impedance misaligned. The remaining electromagnetic radiations are received by substances as absorption coefficients (SE_A), and portions that are reduced by numerous reflections are known as multiple reflection coefficients (SE_M) [19].

This equation is used to calculate the microwave-absorbing capabilities of nanomaterials, which are the total of the absorption value, reflection, and multiple reflection factors.

$$SE_T\,(\mathrm{dB}) = SE_A + SE_R + SE_M \tag{1}$$

The terms SE_R, SE_M, and SE_A, respectively, stand for the shielding efficiency resulting from absorption, reflections, and multiple reflections.

Electromagnetic interference shielding effect is known as the logarithmic proportion of radiation input power (P_i) to radiation output power (P_o), as determined by Eq. 2 [20].

$$SE_T\,(\mathrm{dB}) = -10\log\left(\frac{P_T}{P_I}\right) = -20\log\left(\frac{E_T}{E_I}\right) = -20\log\left(\frac{B_T}{B_I}\right) \tag{2}$$

where T or I stand for the incoming and emitted radiations occurring on the protecting layer of a material, accordingly, and P, E, or B stand for the power, electric, and magnetic field intensities, respectively [21].

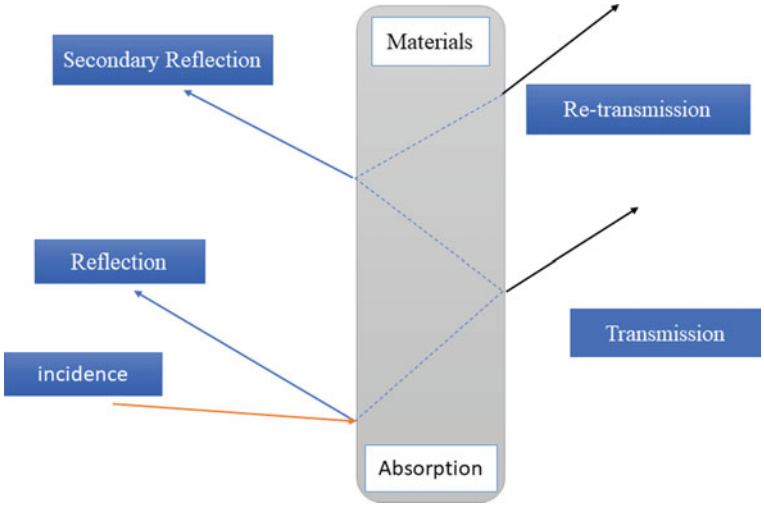

Fig. 1 Demonstration of incoming electromagnetic (EM) wave passing through a hard object

A network analysis can be used to detect electromagnetic interference shielding effectiveness. Scalar (SNA) and vector (VNA) network analyses are the two different categories of network analysis. A VNA measures the magnitude and stages of different signals, whereas a SNA merely detects the amplitude of signals. Complex signals, such as relative permittivity or permeability, cannot be assessed with a SNA, but they can be measured with ease using a VNA. Complex scattering variables can quantitatively describe the incident and emitted vibrations in a two different vector network analyzer (or S parameters). The evaluation of reflection and transmission ratios involves each four (S_{11}, S_{21}, S_{12}, and S_{22}) or a couple (S_{11}, S_{21}) of the S factors of the substance being tested, making it the most often used method for carrying out such conversion's material under test. A VNA, a sample holder, coaxial wires, and an adaptor make up the entire EMI-SE measuring setup. When an electromagnetic wave encounters an absorber layer, the transmission electromagnetic wave can be detected by the variable ($S11$ or $S22$), and the reflection electromagnetic wave is evaluated by the variable ($S12$ or $S21$). Figure 2 illustrates how EM waves interface with shielding substances [20].

The transmission and reflection ratios are expressed by the two-port connection system's S_{11} (or S_{22}) and S_{12} (or S_{21}) variables. Absorbance (A), transmittance (T), and reflectance (R) through the blocking layer can be identified as follows based on the analysis of S variables [22]:

$$T = |S_{12}|^2 \left(= |S_{21}|^2\right) \tag{3}$$

$$R = |S_{11}|^2 \left(= |S_{22}|^2\right) \tag{4}$$

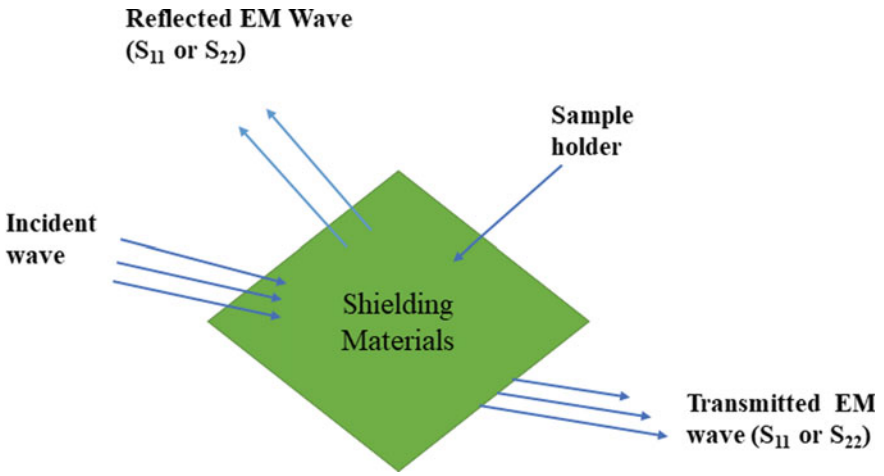

Fig. 2 EM wave shows connection with shielding substances

The absorption coefficient (A) is calculated using the electromagnetic radiation power equilibrium formula (incoming wave strength, $I + A + R + T$).

$$A = I - R - T \tag{5}$$

where $I - R$ stands for the intensity values of the electromagnetic radiation that efficiently penetrate the components in this case after reflection, generating absorption, and transmission impacts [23]. Figure 3 represents the scattering variables by VNA.

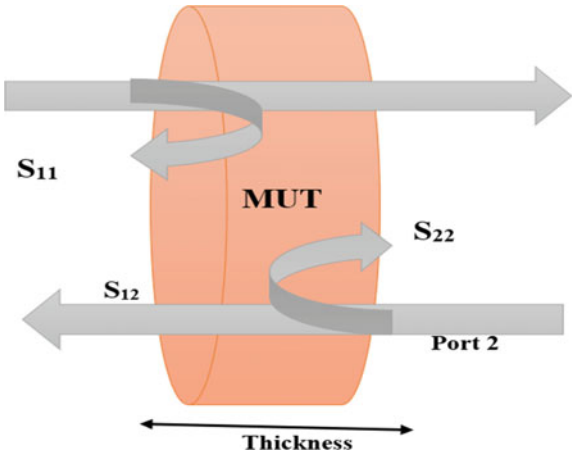

Fig. 3 Scattering variable via vector network analyzer

2.1 Measurements of EMI Shielding Effectiveness

There is a particular test to determine the effectiveness because not all EMI enclosures perform at the same level of efficiency. The most popular techniques for determining how effective a material is at shielding are

1. Open field method
2. Coaxial transmission line technique
3. Shielded box route
4. Shielded room route

1. **Open field method**

The open field technique and free storage technique evaluates the shielding efficiency of an interconnected electrical device of separate finished items in an open area, free of a metallurgical surrounding. With the help of an antenna positioned at different ranges from the equipment, the method assesses the conductivity of the transmissions and the intensity of the diffraction pattern. This specific test was created to simulate typical application areas for gadgets. In locations devoid of material properties, antennas are constructed (outside of testing equipment). Figure 4 shows an average noise sensor that detects EMI rates and saves the output.

2. **Coaxial transmission line technique**

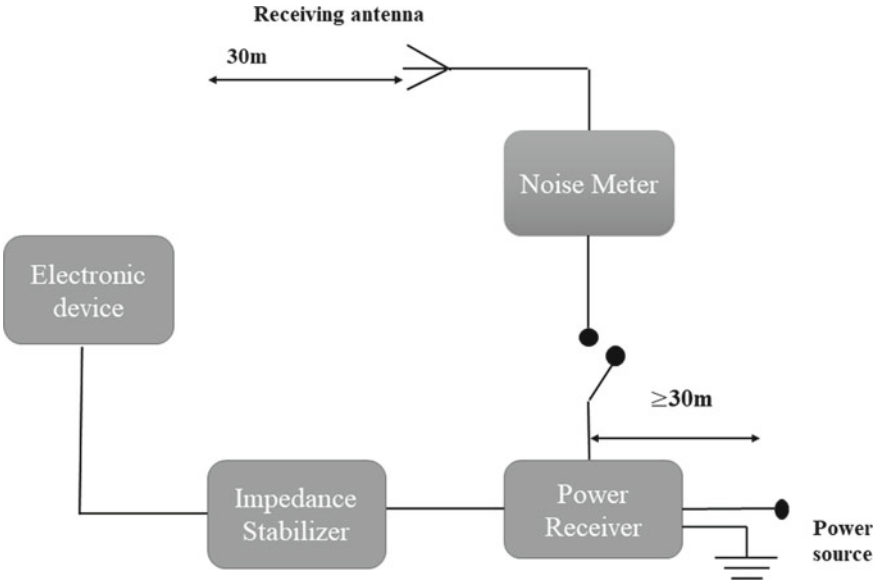

Fig. 4 Systematic representation of open field test

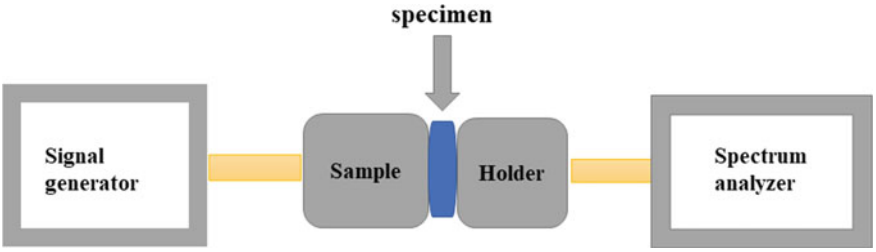

Fig. 5 Systematic representation of coaxial transmission line technique

This experiment is typically used to assess the efficiency of flat materials as shields. This experiment, which uses the Doppler Effect, is thought to be the most popular one and consists of a network analyzer and two coaxial connectors for keeping the sample (Fig. 5). It gets around the problem with insulated box tests, where we get similar results from various labs. In the coaxial container, the sample is injected between the component pieces and exposed to an electric field in all directions. Using an insulated screw, the direct electrical connections are minimized [24].

3. **Shielded box route**

The barrier box technique is frequently utilized to measure test specimens made of various shield elements side by side. The study involves a metal container with a mechanically impermeable wall that has a test outlet and a receiver module installed in it. From outside the box, a receiving antenna is positioned, and the amplitude of the signals it receives is listed through both the access part and the port with the test sample concealing it. Figure 6 demonstrates this feature. This technique's disadvantage is that it's challenging to establish a sufficient electrical connection between prepared samples and the shielded container. The other difficulty is its comparatively small frequency range of 500 MHz.

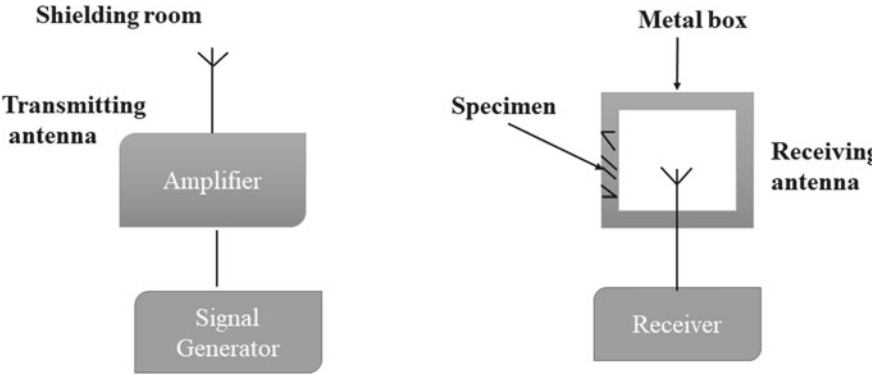

Fig. 6 SE measurements of shielding box

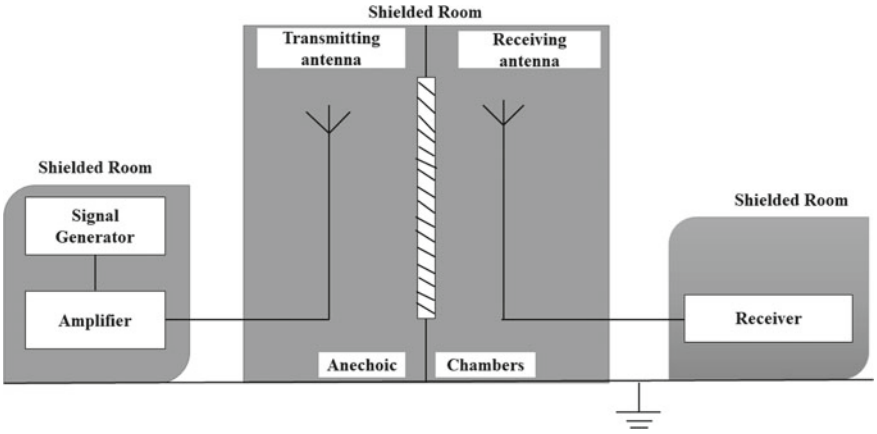

Fig. 7 SE measurement of shielded room

4. **Shielded room route**

The most advanced technique, the shielded room system, was created to eliminate the restriction of the shielded box concept. The measurement technique, signal producer, sending antenna, received power, and recorder are all separated in different rooms to prevent interference, but the main idea is the same as with the shielded box technique. Furthermore, the test specimen area is significantly expanded, often on the scale of 2.5 m^2 in area, and the antennas are placed in acoustical chambers the size of a room. This is demonstrated in Fig. 7, where it can be seen that, as compared to the shielded group that understands the basic concepts, the frequency band over which valid findings may be achieved is much increased, and the data repeatability is greatly enhanced [25].

2.2 Shielding Effectiveness Through Reflection

Reflection loss (SE_R) is connected compared to the incident's relative consistency electromagnetic wave and the shielding material's surface impedance, whose generalized form is defined as [26]

$$SE_R = -10 \log_{10}\left(\frac{\sigma_T}{16 f \epsilon_r \mu_r}\right) \tag{6}$$

where σ_T is the total conductivity (T) is measured in S/cm. According to Eq. 6, SE_R is a function of the shielding material's ratio of σ_T to μ_r or (σ_T/μ_r). Furthermore, Eq. 6 clearly implies that, for a specific shielding substance with fixed T and r, SE_R is shown to decrease with rising f.

2.3 Shielding Effectiveness Through Absorption

Electric and magnetic fields present in the microwave radiation can interact with the shielding material's constructed dipole and cause Ohmic losses. Electric and magnetic dipoles are necessary for a shielding material to absorb EM radiation. Across the shield's thickness, the strength of the EM waves' propagation decreases exponentially. The signal produced in the shielding (Ohmic loss) and hysteresis loop losses are the main causes of the absorption. The following relationship can be used to determine the size of SE_A [27]:

$$\mathrm{SE_A} = -8.68t\left(\frac{\sigma_T \omega \mu_R}{2}\right)^{\frac{1}{2}} \tag{7}$$

Here, thickness of barriers is denoted by t, and the ratio of the shield electrical conductivity of substance to its permeability determines how much SE_A will occur. Electromagnetic radiation absorption can be further improved by thickening the barrier. The absorption scales with frequency, in contrast to the reflection mode. The interdependence is a logarithmic function even if the reflection gets smaller as the frequency increases. As a result, frequency-dependent EM radiation attenuation increases overall.

2.4 Shielding Effectiveness Through Multiple Reflection

The significant inside surface of materials and composites with fillers exhibits a multiple reflection process. Multiple reflections typically reduce the overall protection factor if the medium is less than the surface region and can be disregarded if the material is thicker than the surface region [28].

Skin Depth An electric charge decreases and reaches $1/e$ times the power of the arriving at depth, known as skin depth (δ), when a plane wave penetrates a conductive substance, as shown by

$$\delta = \frac{1}{\sqrt{\pi f \mu \sigma}} \tag{8}$$

where σ is the conductivity, the wave's frequency is denoted by f, and μ represents the shield's magnetic permeability [29].

Multiple reflections, or reflections at many surfaces or at the material crossing, make up the third mechanism [30].

$$\mathrm{SE}_M = 20\log\left(1 - e^{\frac{-2t}{\delta}}\right) = 20\log\left(1 - e^{\frac{\mathrm{SE}_A}{10}}\right) \tag{9}$$

SE_M and SE_A are connected with one another according to Eq. 6. The mathematical morphological structure heavily relies on SE_M. The intensity of electromagnetic waves is insignificant when they arrive at the second border of the shielding materials, so SE_M can be disregarded for comparatively thick shielding materials. Simply include, the SE_M can be disregarded when the SE_A of the protector materials is below 10 dB [31].

3 Reflection Loss

The electromagnetic wave absorption qualities of the samples were calculated from the variation of reflection loss versus frequency in the X-band region (8–12 GHz) and Ku-band (12–18 GHz) frequency bands. Transmission line concept states that the reflection loss of an electromagnetic field on an only one surface of a material supported by a perfect conductor can be described as follows:

$$\mathrm{RL(dB)} = 20 \log \left| \frac{Z_{\mathrm{in}} - Z_0}{Z_{\mathrm{in}} + Z_0} \right| \tag{10}$$

Here, Z_0 denotes the free space characteristic impedance and Z_{in} represents the normalized input impedance at the interface between free space and materials, as given by the following relation [32].

4 Properties Associated with Electromagnetic Interference Mechanism

4.1 Tangent Loss (Dielectric and Magnetic)

Ferrites' dielectric characteristics depend on many different variables, including the varieties of charge carriers, which in turn are based on the fabrication, annealing temperatures, chemical nature, ionic potential, and particle density [33].

The angle between both the stage of displacement or and the entire current is represented by the tangent of the dielectric loss. Complex permittivity ε, concept that written as, is also what distinguishes a dielectric material's magnetic properties.

$$\varepsilon = \varepsilon' - j\varepsilon'' \tag{11}$$

Here, ε' represents the actual factor of permittivity and ε'' denotes the fictional component of permittivity [32]. The complex permittivity is made up of an actual permittivity (ε') component that summarizes a material's capacity to reserve energy when exposed to an electric field, as well as factors that influence the dispersion of the

electromagnetic current and the process of waves passing by way of the substance and an assumed permittivity (ε'') component that affects both reduction and power absorption [6].

The type of power released by the ferrite nanoparticles during electron transmission in the dielectric system is revealed by the dielectric loss (tanδ) [34]. The loss of electron can be calculated as a loss tangent and stated as per the Debye polarization relaxation equation.

$$\tan\delta = \frac{\varepsilon''}{\varepsilon'} = \frac{(\varepsilon_s - \varepsilon_\infty)\omega\tau}{\varepsilon_s + \varepsilon_{\infty\omega^2\tau^2}} \tag{12}$$

where $\varepsilon_s, \varepsilon_\infty, \omega$ and τ represent the stable dynamic constant, high-frequency dynamic constant, frequency and the frequency, the breakdown period of polarization, respectively [35].

The EMI shielding processes of an EMI shielding material can be known by evaluating the magnetic complex permeability as

$$\mu_r = \mu_r' - j\mu_r'' \tag{13}$$

where μ_r' indicates the imaginary part and $j\mu_r''$ denotes the magnetic storage of the electromagnetic radiation. The tangent of the magnetic loss can be applied to determine the losses which are shown in Eq. (15) [36].

$$\tan\delta_\mu = \frac{\mu_r''}{\mu_r'} \tag{14}$$

4.2 Source of Dielectric Loss

The conduction loss (ε_c'') plus relaxing loss (ε_r''), which make up the majority of the dielectric loss signal, make up the imaginary part of permittivity (ε''). The theory of Debye describes the ε'' as follows:

$$\varepsilon'' = \varepsilon_c'' + \varepsilon_r'' \tag{15}$$

$$\varepsilon_c'' = \frac{\sigma_{\mathrm{dc}}}{\omega\varepsilon_0} \tag{16}$$

$$\varepsilon_r'' = \frac{\varepsilon_s - \varepsilon_\infty}{1 + \omega^2\tau^2}\omega\tau \tag{17}$$

where static permittivity is ε_s, ε_∞ denotes the high-frequency limit permittivity, σ_{dc} represents the direct current conductivity, and the relaxation period is τ. The electric

loss in carbon membranes is the cause of composites' conduction loss. The defective dipole and interfacial polarization phenomena are the main causes of the relaxation loss [37].

According to the Havriliak–Negami equation, the complex dielectric constant comprises two components: polarization process and conductivity impact [38].

$$\varepsilon_r = \varepsilon_\infty + \frac{\Delta\varepsilon}{[1 + iW\tau_{\mathrm{HN}})^{\alpha_{\mathrm{HN}}}]^{\gamma_{\mathrm{HN}}}} - i\frac{\sigma_0}{W^s\varepsilon_0} \tag{18}$$

where $\Delta\varepsilon$ denotes the dielectric relaxation intensity, W represents the frequency of the electromagnetic field oscillation, α_{HN} and γ_{HN} are the relaxation spectra shape parameters, and the $-i\sigma/W^s\varepsilon_0$ component indicates the conductivity effect, here σ_0 is the sample's dc conductance and s is the conduction mechanism.

4.3 Source of Magnetic Loss

According to the theory of Ferromagnetic resonance, the frequency of natural resonance (f_r) can be shown by the given function [39]:

$$f_r = \frac{\gamma}{2\pi}H_{\mathrm{eff}} \tag{19}$$

$$H_{\mathrm{eff}} = \frac{4|K_1|}{3\mu_0 M_s} \tag{20}$$

where gyromagnetic ratio denoted by $\frac{\gamma}{2\pi}$, H_{eff} represents the effective magnetic field, K_1 refers to the magneto-crystalline anisotropic coefficients.

5 Parameters Governing EMI Shielding Mechanism

5.1 Impedance Compatibility Requirement

The impedance compatibility requirement can be determined by using following relationships:

$$Z = Z_1/Z_0 \tag{21}$$

$$Z_1 = (\mu_r/\varepsilon_r)^{\frac{1}{2}}Z_0 \tag{22}$$

$$|\varepsilon| = (\varepsilon'^2 + \varepsilon''^2)^{\frac{1}{2}} \tag{23}$$

$$|\mu| = (\mu'^2 + \mu''^2)^{\frac{1}{2}} \tag{24}$$

Here, Z_1 is the absorbing material's impedance, Z_0 is the free space impedance, and μ_r and ε_r are complex variables for permeability and permittivity.

If the electromagnetic absorbing material exhibits ideal impedance matching, the output coefficient should be zero, implying that $Z_1 = Z_0$. Similarly, the μ_r value must equal ε_r [40].

5.2 Attenuation Constant

The constant of attenuation (α) also shows the impacts of the shields' internal attenuation capacity. This is the rate at which microwave fields disperse and may be determined using the equation below [41].

$$\alpha = \frac{\sqrt{2\pi f}}{c} * \mu''\varepsilon'' - \mu'\varepsilon' + \sqrt{(\mu''\varepsilon'' - \mu'\varepsilon')^2 + (\mu'\varepsilon'' + \mu''\varepsilon')^2} \tag{25}$$

where 'c' denotes the velocity of light.

6 Conclusion and Prospect

This Chapter includes ferrites nanocomposites for EMI shielding and microwave absorption application. This chapter also includes the electronic properties of the materials such as complex permeability, permittivity, and tangent loss (dielectric and magnetic). All of this connected with electromagnetic interference. The EMI-SE are important for research and development of the protective material's structural system. The creation of innovative materials with enhanced shielding capabilities is another challenge. Increasing the use of available information for accessibility is the most essential part. The method of electromagnetic shielding, various EMI concepts, and theoretical analysis features such as reflection, absorption, and multiple reflections, as well as methods for determining EMI-SE, are all explained in detail.

References

1. Verma M, Singh AP, Sambyal A, Singh BP, Dhawanb SK, Choudhary V (2015) Barium ferrite decorated reduced graphene oxide nanocomposite for effective electromagnetic interference shielding. R Soc Chem 17:1610–1618. https://doi.org/10.1039/C4CP04284K

2. Dalal J, Lather S, Gupta A, Dahiya S, Maan AS, Singh K, Dhawan SK, Ohlan A (2018) EMI shielding properties of laminated graphene and $PbTiO_3$ reinforced poly(3,4-ethylenedioxythiophene) nanocomposites. Compos Sci Technol 165:222–230. https://doi.org/10.1016/j.compscitech.2018.07.016
3. Sun X, He J, Li G, Tang J, Wang T, Guo Y, Xue H (2013) Laminated magnetic graphene with enhanced electromagnetic wave absorption properties. J Mater Chem C 1:765–777. https://doi.org/10.1039/C2TC00159D
4. Geetha S, Satheesh Kumar KK, Rao CRK, Vijayan M, Trivedi DC (2009) EMI shielding: methods and materials—a review. J Appl Polym Sci. https://doi.org/10.1002/app.29812
5. Wilson R, George G, Joseph K (2020) An introduction to materials for potential EMI shielding applications: status and future. In: Material for potential EMI shielding application. pp 1–8. https://doi.org/10.1016/B978-0-12-817590-3.00001-4
6. González M, Pozuelo J, Baselga J (2018) Electromagnetic shielding materials in GHz range. Chem Rec 18:1–11. https://doi.org/10.1002/tcr.201700066
7. Tran N, Lee MY, Jeong WH, Phan TL, Tuan NQ, Lee BW (2021) Thickness independent microwave absorption performance of La-doped BaFe12O19 and polyaniline composites. J Magn Magn Mater 538:168299. https://doi.org/10.1016/j.jmmm.2021.168299
8. Abdollahi F, Yousefi M, Hekmati M, Khajehnezhad A, Afghahi SSS (2019) Magnetic and microwave absorption properties of barium hexaferrite doped with La^{3+} and Gd^{3+}. J Nanostruct 9:576–586. https://doi.org/10.22052/JNS.2019.03.019
9. Chung DDL (2020) Materials for electromagnetic interference shielding. 255:123587. https://doi.org/10.1016/j.matchemphys.2020.123587
10. Anand S, Pauline S, Joseph Prabagar C (2020) Zr doped Barium hexaferrite nanoplatelets and RGO fillers embedded Polyvinylidenefluoride composite films for electromagnetic interference shielding applications. Polym Testing. 86:106504. https://doi.org/10.1016/j.polymertesting.2020.106504
11. Bheema RK, Ojha AK, Praveen Kumar AV, Etika KC (2022) Synergistic influence of barium hexaferrite nanoparticles for enhancing the EMI shielding performance of GNP/epoxy nanocomposites. Compos Nanocompos 57:8714–8726. https://doi.org/10.1007/s10853-022-07214-8
12. Shooshtary Veisia S, Yousefi M, Amini MM, Shakeri AR, Bagherzadeh M, Afghahi SSS (2021) Magnetic properties, structural studies and microwave absorption performance of $Ba_{0.5}Sr_{0.5}Cu_xZr_xFe_{12-2x}O_{19}$/poly ortho-toluidine ($X = 0.2,0.4, 0.6, 0.8$) ceramic nanocomposites. Inorg Chem Commun 132:108802. https://doi.org/10.1016/j.inoche.2021.108802
13. Tohidifar MR (2014) Highly-efficient electromagnetic interference shielding and microwave dielectric behaviour of a ($Bi_2O_3 + B_2O_3$)-doped MWCNT/$BaTiO_3$ ceramic nanocomposite. Ceram Int 12(15):13613–13622. https://doi.org/10.1016/j.ceramint.2018.04.197
14. Kumar P (2019) Ultrathin 2D nanomaterials for electromagnetic interference shielding. Adv Mater Interface 1901454:1–24. https://doi.org/10.1002/admi.201901454
15. Wang H, Li S, Liu M, Li J, Zhou X (2021) Review on shielding mechanism and structural design of electromagnetic interference shielding composites. Macromol Mater Eng 2100032:1–13. https://doi.org/10.1002/mame.202100032
16. Yang S, Lozano K, Lomeli A, Foltz HD, Jones R (2005) Electromagnetic interference shielding effectiveness of carbon nanofiber/LCP composites. Compos A: Appl Sci Manufact 36:691–697. https://doi.org/10.1016/j.compositesa.2004.07.009
17. Chung DDL (2001) Electromagnetic interference shielding effectiveness of carbon materials. Carbon 39:279–285. https://doi.org/10.1016/S0008-6223(00)00184-6
18. von Klemperer CJ, Maharaj D (2009) Composite electromagnetic interference shielding materials for aerospace applications. Compos Struct 91:467–472. https://doi.org/10.1016/j.compstruct.2009.04.013
19. Wang L, Ma Z, Zhang Y, Chen L, Cao D, Gu J (2021) Polymer-based EMI shielding composites with 3D conductive networks: a mini-review. SusMatWillay 1–19. https://doi.org/10.1002/sus2.21

20. Kondawar SB, Modak PR (2020) Theory of EMI shielding. Department of Physics, Rashtrasant Tukadoji Maharaj Nagpur University, Nagpur, India, pp 9–25. https://doi.org/10.1016/B978-0-12-817590-3.00002-6
21. Iqbal S, Shah J, Kotnala RK, Ahmad S (2018) Highly efficient low-cost EMI shielding by barium ferrite encapsulated polythiophene nanocomposite. J Alloys Compunds 1–24. https://doi.org/10.1016/j.jallcom.2018.11.307
22. Hong YK, Lee CY, Jeong CK, Lee DE, Kim K, Joo J (2003) Method and apparatus to measure electromagnetic interference shielding efficiency and its shielding characteristics in broadband frequency ranges. AIP 1098. https://doi.org/10.1063/1.1532540
23. Faisal M, Khasim S (2013) Broadband electromagnetic shielding and dielectric properties of polyaniline-stannous oxide composites. J Mater Sci: Mater Electron 24:2202–2210. https://doi.org/10.1007/s10854-013-1080-y
24. Hema S, Sreedha S (2021) Ferrite-based polymer nanocomposites as shielding materials: a review. Chem Papers 75:3697–3710. https://doi.org/10.1007/s11696-021-01664-1
25. Geetha S, Satheesh Kumar KK, Rao CRK, Vijayan M, Trived DC (2006) EMI shielding: methods and materials—a review. J Appl Polym Sci. https://doi.org/10.1002/app.29812
26. Sankaran S, Deshmukh K, Basheer Ahamed M, Khadheer Pasha SK (2018) Recent advances in electromagnetic interference shielding properties of metal and carbon filler reinforced flexible polymer composites: a review. Compos A 114:49–71. https://doi.org/10.1016/j.compositesa.2018.08.006
27. Pawar SP, Biswas S, Kar GP, Bose S (2016) High frequency millimetre wave absorbers derived from polymericnanocomposites. Polymer 84:398–416. https://doi.org/10.1016/j.polymer.2016.01.010
28. Aswathi MK, Rane AV, Ajitha AR, Thomas S, Jaroszewski M (2018) EMI shielding fundamental. In: Material science. https://doi.org/10.1002/9781119128625.CH1
29. Zahid M, Siddique S, Anum R, Fayzan Shakir M, Nawab Y, Rehan ZA (2021) M-type barium hexaferrite-based nanocomposites for EMI shielding application: a review. J Supercond Nov Magn 34:1019–1045. https://doi.org/10.1007/s10948-021-05859-1
30. Liang C, Gu Z, Zhang Y, Ma Z, Qiu H, Gu J (2021) Structural design strategies of polymer matrix composites for electromagnetic interference shielding: a review. Nano-Micro Lett 13:181. https://doi.org/10.1007/s40820-021-00707-2
31. Mosleh Z, Kameli P, Poorbaferani A, Ranjbar M, Salamati H (2016) Structural, magnetic, and microwave absorption properties of CE-doped barium hexaferrite. J Magn Magn Mater 397:101–107. https://doi.org/10.1016/j.jmmm.2015.08.078
32. Mousavi Ghahfarokhi SE, Bazdar F, Kazeminezhad I, Mohammadzadeh Shobegar E, Chamran S, Iran A (2020) Effect of Ni^{2+} substitution on the structural, magnetic and dielectric properties of $PbFe_{12-x}Ni_xO_{19}$ nanoparticles. https://orcid.org/0000-0002-4495-5859
33. Beheshti KA, Yousef M (2021) Magnetic and microwave absorption of $BaMg_xZr_xFe_{12-2x}O_{19}$ polyaniline nanocomposites. J Alloys Compd 859:1–9. https://doi.org/10.1016/j.jallcom.2020.157861
34. Mohammed J, Suleiman AB, Carol TTT, Hafeez HY, Sharma J, Maji PK, Kumar SG, Srivastava AK (2018) Enhanced dielectric and optical properties of nanoscale barium hexaferrites for optoelectronics and high frequency application. Chinese Phys B 27:128104. https://doi.org/10.1088/1674-1056/27/12/128104
35. Yin X, Kong L, Zhang L, Cheng L, Travitzky N, Greil P (2014) Electromagnetic properties of Si–C–N based ceramics and composites. 59(6):326–355. https://doi.org/10.1179/1743280414Y.0000000037
36. Jiang D, Murugadoss V, Wang Y, Lin J, Ding T, Wang Z, Shao Q, Wang C, Liu H, Lu N, Wei R, Subramania A, Guo Z (2019) Electromagnetic interference shielding polymers and nanocomposites—a review. Polym Rev 280–337. https://doi.org/10.1080/15583724.2018.1546737
37. Cheng C, Fan R, Wang Z, Shao Q, Guo X, Xie P, Yin Y, Zhang Y, An L, Lei Y, Ryu YE, Shankar A, Guo Z (2007) Tunable and weakly negative permittivity in carbon/silicon nitride composites with different carbonizing temperatures. Carbon 125:103–112. https://doi.org/10.1016/j.carbon.2017.09.037

38. Quan B, Liang X, Ji G, Cheng Y, Liu W, Ma J, Zhang Y, Li D, Xu G (2017) Dielectric polarization in electromagnetic wave absorption: review and perspective. J Alloys Compd 728:1065–1075. https://doi.org/10.1016/j.jallcom.2017.09.082
39. Yadav RS (2021) Advanced spinel ferrite nanocomposites for electromagnetic interference shielding applications. Micro Nano Technol
40. Lv H, Ji G, Liang XH, Zhanga H, Du Y (2015) A novel rod-like MnO_2@Fe loading on graphene giving excellent electromagnetic absorption properties. J Mater Chem C 3:5056–5064. https://doi.org/10.1039/C5TC00525F
41. Yang Z, Zhang Y, Wen B (2019) Enhanced electromagnetic interference shielding capability in bamboo fiber@polyaniline composites through microwave reflection cavity design. Compos Sci Technol 178:41–49. https://doi.org/10.1016/j.compscitech.2019.04.023

Chapter 9
Ferrite Nanoparticles for Sensing Applications

Parul Raturi, Iliyas Khan, Gaurav Joshi, Samir Kumar, and Sachin Gupta

1 Introduction

Micro- and nanostructured spinel ferrites have become increasingly popular in recent years due to their numerous ranges of applications. The spinel ferrites or iron-containing ferrites are the complex oxide-based crystal structure having a face-centered cubic core. They are usually designated by the general formula XFe_2O_4 and are usually formed by the combination of a trivalent iron(III) ion (Fe^{3+}) with a series of the same or another metal cation (X, where X includes the divalent cation Co, Ni, Zn, Mg, Mn, etc.) [1, 2]. Recent research has focused on spinel ferrites due to their nanoscale superparamagnetic characteristics, chemical and thermal stability with a variety of compositions [3]. The substitution of Fe ions with other metal cations can also affect the electronic structure of Fe_3O_4 [4, 5]. Since the magnetic, electrical, mechanical, and optical properties of ferrites can be easily tuned, they are considered promising materials for various sensors such as magnetoresistance,

P. Raturi
Department of Physics, Omkaranand Sarswati Government Degree College, Devpryag, Uttarakhand 249301, India

I. Khan
Department of Pharmacy, School of Chemical Sciences and Pharmacy, Central University of Rajasthan, Ajmer 305817, India

G. Joshi
Department of Pharmaceutical Science, Hemvati Nandan Bahuguna Garhwal (A Central) University, Srinagar, Garhwal, Uttarakhand 246174, India

S. Kumar (✉)
Department of Electronics and Information Engineering, Korea University, Sejong 30019, Korea
e-mail: skumar@korea.ac.kr

S. Gupta (✉)
Department of Physics, Bennett University, Greater Noida 201310, India
e-mail: sachin.gupta@bennett.edu.in

P. Sharma et al. (eds.), *Engineered Ferrites and Their Applications*, Materials Horizons: From Nature to Nanomaterials, https://doi.org/10.1007/978-981-99-2583-4_9

thermal, mechanical and chemical sensors, actuators, and gas sensors. It is possible to tune these properties either by adding dopants or by creating metal or metal oxide structures using diverse types of materials. Ferrites also have the advantage of being inexpensive materials.

So far, various combinations of spinel ferrites have been described in the literature, including magnetite spinel, cuprospinel (containing copper), jacobsite (containing manganese), franklinite (containing iron, manganese or zinc), ulvospinel (containing titanium), magnesioferrite (containing magnesium) or trevorite (containing nickel) spinels [6]. Due to high selectivity, high sensitivity, low cost, low operating temperature, low detection limits, fast response time, wide dynamic range of application, and long-term stability, spinel ferrites are the ideal material for the development of sensors [7]. The field of spinel ferrite has continuously expanded in recent years. Searching the Scopus database for the keywords 'spinel ferrite' AND sensor yielded 2033 documents (as of November 8, 2022), of which 1777 were research-based articles, Fig. 1a. Sensors are particularly developed (based on the number of publications) in the broader fields which include materials science (1476 documents), physics and astronomy (1050 documents), chemical engineering (663 documents), engineering (538 documents), chemistry (373 documents), and biochemistry, genetics, and molecular biology (63 documents), see Fig. 1b. The analysis shows that the field in which spinel ferrite is used is new and developing at a rapid pace, particularly because of its utility in chemistry as a chemosensor and in related biology or health sciences as a biosensor.

In this chapter, recent developments and improvements in the use of ferrites in chemical and biological sensing techniques are presented. There are numerous details

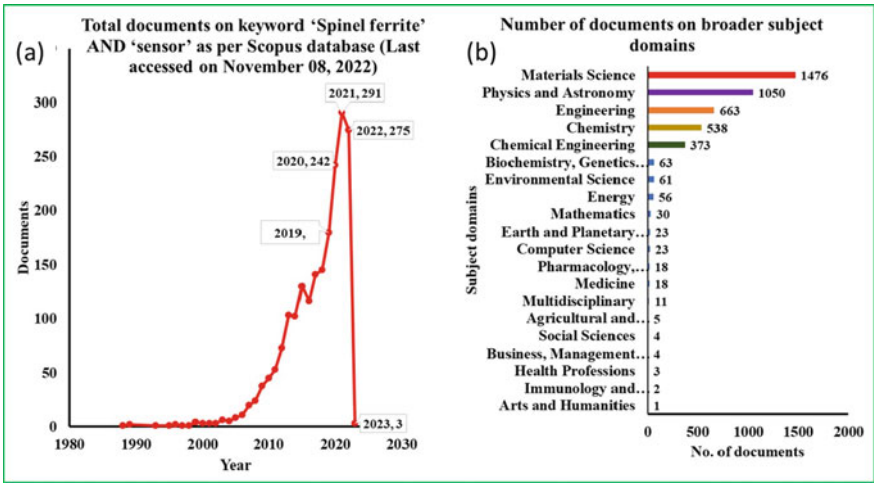

Fig. 1 **a** Searches of the Scopus database for the keywords 'spinel ferrite' AND sensor yielded 2033 documents (as of November 8, 2022). **b** Publications on relevant topics in the broader field of science and technology

in the literature on the current trends in spinel ferrites for various technologies [8–14]. In a study, Goncalves et al. reviewed the contributions and compared the main strategies to develop XFe_2O_4 materials for improved electrochemical sensing applications [15]. In another study, Sutka and Gross have summarized recent advances in synthetic methods for the preparation of spinel ferrites. In addition, recent progress in the use of spinel ferrites for gas sensors [10, 16], chemical sensors [17], biosensors [18], temperature sensors [19], stress sensors [20], and biomedical applications [13, 21, 22] has been summarized. Nevertheless, we are not aware of any review that describes the entire potential of spinel ferrites as different sensors in a single article. Thus, the prime aim of this review is to focus on the latest advances in spinel-ferrite-based materials for various sensing applications. In addition, the advantages and disadvantages of using these spinels as well as the future prospects and directions are critically discussed.

2 Sensing with FNPs

2.1 Gas and Humidity Sensors

A gas sensor detects toxic gases and vapors that are harmful to humans. The need for sensitive, stable, and selective gas sensors for the detection of toxic gases is becoming increasingly important. There are a variety of applications for gas sensors made from spinel ferrites, both industrial and medical. Metal ferrites can detect a range of gases, including carbon monoxide, liquefied petroleum gas, hydrogen sulfide, gasoline, and methane. It is becoming increasingly important to integrate sensors into smart devices for remote sensing. As a result, compactness and compatibility with operating systems are driving the progress of electrical sensors. Solid-state gas sensors based on new materials are becoming more popular [23]. Ferrite-based gas sensors are mechanically resilient, affordable, and have excellent sensing characteristics. When a chemical reaction on ferrite surfaces leads to the transfer of electrons between gas molecules and ferrite surfaces, the electrical conductivity or resistance changes. We will briefly review recent advances in ferrite-based gas sensors. The numerous methods used to synthesize ferrites are beyond the scope of this chapter and can be found elsewhere.

2.1.1 Gas Sensing Mechanism

The response of spinel ferrites to target gases is like that of a semiconductor gas sensor. Spinel ferrite sensors are also based on the intricate interaction of the gas–solid interface, which changes the electrical conductivity [24]. They work on the principle that gasses adsorb to surfaces and cause changes in capacitance or electrical resistance. An oxygen molecule adsorbs to the surface of a spinel-ferrite-based sensor

when it is exposed to air. In doing so, it accepts free electrons from the conduction band and forms oxygen anions. In the presence of a reducing agent, such as CO, the reducing agent reacts with the adsorbed O^- and releases the trapped electron into the conduction band, lowering the resistance. In ferrite, a surface-controlled reaction occurs, as shown in the following expression, in which oxygen from the air having the test gas analyte is adsorbed and ionized from the surface.

$$O_2(\text{gas}) \leftrightarrow O_2(\text{ad}) \tag{1}$$

$$O_2(\text{ad}) + e^- \leftrightarrow O_2^-(\text{ad}) \tag{2}$$

$$O_2^-(\text{ad}) + e^- \leftrightarrow O^{2-}(\text{ad}) \tag{3}$$

This equation denotes the gaseous and oxygen adsorbed components, respectively, as gas and ad. When reducing gases (R) are present, they may be absorbed at the exterior of the sensor, as given in Eq. (4).

$$R \leftrightarrow R(\text{ad}) \tag{4}$$

The reaction between the adsorbed gas and the adsorbed oxygen species, such as O^- (ad) and $O_2{}^-$(ad), continues according to Eqs. (6) and (7).

$$R(\text{ad}) + O^-(\text{ad}) \leftrightarrow RO(\text{ad}) + e^- \tag{5}$$

$$R(\text{ad}) \pm O^{2-}(\text{ad}) \leftrightarrow RO(\text{ad}) \pm e^{2-} \tag{6}$$

$$RO(\text{ad}) \leftrightarrow RO(\text{gas}) \tag{7}$$

Exposure of the target gas (reducing gas) to *n*- and *p*-type metal oxide sensors results in a change in resistance, as shown in Fig. 2a.

Using $ZnFe_2O_4$ gas sensors, for example, acetone can be detected between (147–397)°C and a reaction is triggered as shown in Eq. (7) and Fig. 2b.

$$C_3H_6O = 8O^- \rightarrow 3CO_2 + 3H_2O + 8e^- \tag{8}$$

When an analyte gas is exposed to adsorbed O^-, the gas reacts with the trapped electron and donates it to the conduction band, resulting in a decrease in resistance. As shown in Fig. 2b, an analogous reaction occurs when $ZnFe_2O_4$ gas sensors detect acetone (Eq. 8). On the other hand, if the target gas is an oxidant (acceptor), such as, NO, Cl_2, NO_2, the reaction with chemisorbed oxygen ions leads to an increase in the potential barrier by causing further electron loss from the depletion layer. As a result of the described process, the conductivity of the oxide layer decreases, or in other words, its resistance increases. There are differences in the reactions and adsorption

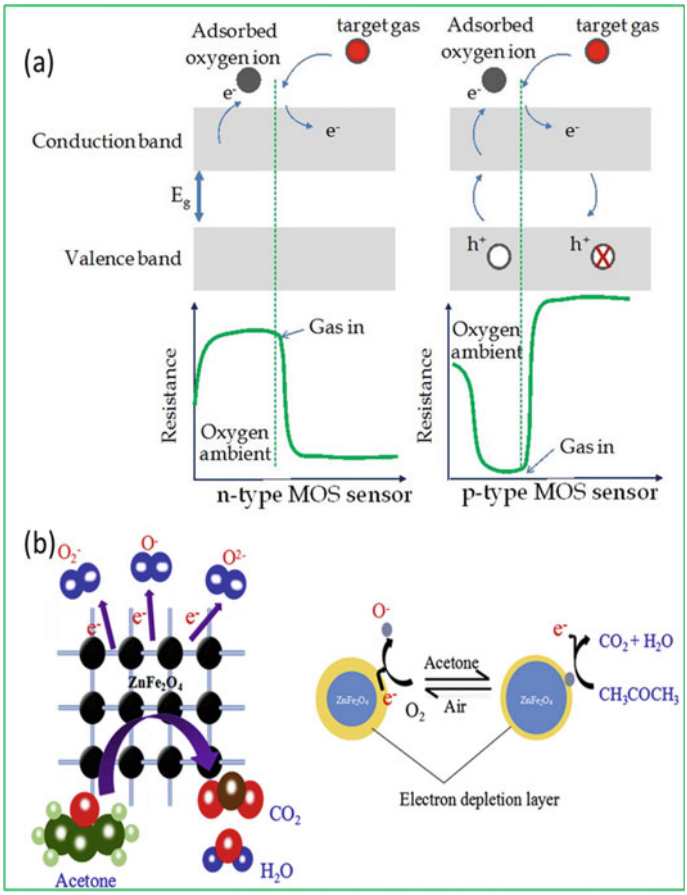

Fig. 2 **a** Diagram showing the change in sensor resistance when exposed to the target gas (reducing gas) for *n*- and *p*-type metal oxide sensors. ©2012 Supab Choopun, Niyom Hongsith and Ekasiddh Wongrat. Adapted from S. Choopun, E. Wongrat, N. Hongsith, in Metal-Oxide Nanowires for Gas Sensors, INTECH Open Access Publisher, **2012**, originally published under CC BY 3.0 license. Available from: https://doi.org/10.5772/54385. **b** Schematic illustrating the acetone sensing mechanism of the $ZnFe_2O_4$ gas sensor. Reproduced with permission [25]. An illustration of chemisorbed oxygen creating a depletion region in a ferrite particle. Copyright 2019, Ceramics International 45, 11,143–11,157 (2019). This diagram shows an example of chemisorbed oxygen forming a depletion zone on a ferrite particle

processes that determine the sensing properties of distinctive gases. Oxygen species play a crucial role in the process by supplying suitable reactants. The addition of catalytically active compounds improves the sensing capability of the device.

2.1.2 Spinel Ferrite Gas Sensors

Spinel ferrite is an excellent material for gas sensing due to its unique crystal structure and high surface activity. The high activation energy of oxygen adsorption on the surface of the material also allows it to react rapidly with reducing gases. According to a study by de Oliviera et al., the enhanced gas sensing capability of $ZnFe_2O_4$ nanoparticles may be associated with the (110) surface having low reactivity to O_3, allowing reversibility and stronger gas response, thereby minimizing sensor surface saturation [25]. In response to the urgent demand for high-performance gas sensors, a comprehensive series of metal-doped mixed ferrite materials and heterostructure gas sensor materials have been produced [26–33].

The operating temperature, humidity, and gas concentration can have a significant effect on the gas sensor function of a ferrite. In addition, morphology characteristics, including specific surface area, contact area, porosity, grain size, and grain stacking and aggregation order, are also influential factors [34]. For example, the porosity of the sensor plays an important role in determining sensitivity because the analyte is absorbed by the porous pores on the surface of the sensor. Yadav et al. and Joshi et al. have shown that the large pore size of the ferrite sensor affects its sensitivity to LPG and ethanol, respectively [35, 36]. Specific surface area, which is the ratio of total ceramic surface area to the mass of the ceramic, also affects gas sensing properties. Gas sensing can be improved by materials with smaller particle sizes and large specific surface areas [37, 38]. As a result, spinel ferrites have different gas sensing properties depending on their nano/microstructure, such as nanoparticles [33], nanorods [34], and micro/nanospheres [35]. Consequently, researchers have considered the creation of special shapes and structures to achieve the desired results.

One of the most studied gas sensors is nickel/nickel-doped ferrites, which can detect gasses such as LPG [39], acetone [40, 41], methanol [40], ammonia [42–45], methane [46, 47], chlorine [48], trimethylamine [49], toluene [50, 51], carbon monoxide [47], carbon dioxide [52, 53], nitrogen monoxide [54], nitrogen dioxide [55], hydrogen [56, 57], hydrogen sulfide [48, 58, 59], and as well as humidity [10, 11, 60–62]. The earliest report on the use of $NiFe_2O_4$ thick films for gas sensing is by Kamble et al., who synthesized nanocrystals using chemical co-precipitates and screen-printed thick films [63]. They reported a maximum sensitivity of 96% to 1000 ppm Cl_2 at 60 °C and a reaction time of 12 min. Recently, an experimental and numerical study by Kumar et al. compared the performance of a nanostructured nickel ferrite ($NiFe_2O_4$) sensing layer based on its interaction with ammonia gas (NH_3) [42]. They synthesized nickel ferrite nanostructures auto-combustion synthesis [64]. The measured response of the sensor to a concentration of 1000 ppm ammonia at 410 K was 65.29%, while the simulated response at the same ammonia concentration and operating temperature was 72%. They found that the nanocrystallite size of the fabricated nickel ferrite material was the main reason for the increased sensor response at lower concentrations of the target gas. Due to the smaller average crystal size (17 nm), the surface of the sensor can interact more easily with the target gas. Consequently, the adsorption of analytes on the sensor surface was significantly higher. In addition, various studies have investigated the influence of substitution

with copper [65], lithium [57], manganese [66], palladium [48], silver [67], tin [68], zinc [69], and cobalt [70] on nickel ferrite.

Zinc ferrite ($ZnFe_2O_4$) is another commonly used metal oxide semiconductor that exhibits excellent gas sensing properties for reducing gasses. Numerous efforts have been made to fabricate $ZnFe_2O_4$ nanomaterials, metal-doped $ZnFe_2O_4$ mixed materials, and heterostructure gas sensor materials [26, 71–77]. Recently, Li et al. reported a typical one-step hydrothermal synthesis method for the preparation of pure, ultrasmall $ZnFe_2O_4$ nanoparticles, which exhibited excellent selectivity for NO_2 molecules [77]. $ZnFe_2O_4$-based sensors displayed a high response ($R_{gas}/R_{air} =$ 247.7), a fast response time ($T_{res} = 6.5$ s), and fast recovery time ($T_{rec} = 11$ s) to 10 ppm NO_2 at an ambient temperature of 125 °C. They demonstrated by theoretical calculations that NO_2 molecules adsorb with a negative adsorption energy of 1.32 eV and 0.35 electrons are transferred from the Zn and Fe atoms of $ZnFe_2O_4$ to NO_2 molecules during this process. In addition, the presence of an oxygen gap can also lead to a higher adsorption energy and charge transfer between $ZnFe_2O_4$ and NO_2.

In recent years, there has been an explosion of research in the field of spinel ferrites. This is due to their superior sensing performance, ease of fabrication, low cost, and sensitivity to a variety of flammable, explosive, toxic, and harmful reducing gases. In addition, the commonly used nickel ferrites and zinc ferrites, there are several other ferrites and their combinations (cobalt ferrite and doped cobalt ferrites [36, 78–84], copper ferrites and doped copper ferrites [85–92], cadmium ferrites and doped cadmium ferrites [89, 93–98], magnesium ferrites and doped magnesium ferrites [99–105], manganese ferrites and doped manganese ferrites [106–110], and lithium and doped lithium ferrites [57, 87]) are widely used in the development and application of various nanostructure materials for gas sensors. Table 1 showing the optimal parameters for several metal ferrites used as gas sensors is provided below. For gas sensing to work effectively, consistent nanostructure and morphology are critical. Therefore, spinels with controllable morphology are being studied in increasing detail. Currently, only a few of the common spinel structures have been studied in detail. The synthesis temperature and reaction time of most spinel structures prohibit their use in gas sensing. Therefore, the ability to effectively control the morphology of the material and improve the gas response should be further developed in spinel-type materials. There are also several factors that complicate the spinel structure, including the low accuracy of the theoretical model of gas sensing. Therefore, more detailed research is needed to better understand the mechanism.

2.1.3 Spinel Ferrites as Humidity Sensors

Humidity and its monitoring are of critical importance in the pharmaceutical and drug industries. Given the importance of humidity measurement, the research of Petrila et al. led to the development of copper–zinc spinel ferrites in which iron was replaced by tungsten [154]. In a similar context, Zafar et al. developed TMBHPET, a thin-film spinel–cobalt–ferrite nanoparticle with a high and sympathetic potential

Table 1 Various metal ferrites used as sensors for different gases and their optimized parameters

Ferrites	Synthesis method	Temperature calcination	Operating	Sensitivity	Selectivity	Concentration (ppm)	Crystallite size (nm)	Particle size (nm)	Response time	Recovery time	Reference
Ag-$NiFe_2O_4$	Solid state	800 °C	–	43	Acetone	–	–	–	1 s	~ 10 s	[111]
$CdFe_2O_4$	Sol–gel self-auto-combustion	1000 °C	350 °C	–	LPG, C_2H_5OH, and acetone	150	300	–	–	–	[112]
$CdFe_2O_4$	Oxalate Co-precipitate	–	350 °C	85% 35% 30%	C_2H_5OH LPG Cl_2	–	30		200–250 s	250–300 s	[113]
$CdFe_2O_4$	Chemical co-precipitate	600 °C and 800 °C	380 °C	90%	C_2H_5OH	200	15	–	15 s	35 s	[114]
$Co_{0.01}Mn_{0\text{-}02}Fe_{1.98}O_4$	Self-combustion	1000 °C	230 °C	–	C_2H_5OH, CH_4, and LPG	–	100–500	0.1 μm	–	–	[115]
$Co_{0.8}Ni_{0.2}Fe_20_4$	Sol–gel citrate	600 °C	210 °C	–	NH_3	200	30	25–35	50 s	–	[116]
$Co_{1-x}Fe_2O_4$	Chemical spray pyrolysis	900 °C	150 °C	90%	NO_2	100	45–65	–	1.62	–	[117]
$Co_{1-x}Ni_xFe_2O_4$	Co-precipitate	550 °C	325 °C	–	CO and C_2H_5OH	10–1000	10–20	–	–	–	[36]
$CoFe_2O_4$	Hydrothermal	75 °C	150 °C	71.9	C_2H_5OH	10	–	15–20	–	–	[118]
$CoFe_2O_4$	Chemical spray pyrolysis	900 °C	150 °C	90%	NO_2	80	200–400	–	5 s	117 s	[119]
$CoFe_2O_4$	Wet chemical	175 °C	227 °C	–	NH_3	25	40	–	–	–	[120]
$CoFe_2O_4$	Spray pyrolysis	900 °C	150 °C	–	NO_2	5–8	100–200	–	5–9 s	130–60 s	[121]
$CuFe_2O_4$	Sol–gel auto-combustion	700 °C	80 °C	–	H_2S	25	32	35.8 ± 5.3 s	51.5 ± 3.4 s	–	[122]
$CuFe_2O_4$	Sol–gel spin coating	500 °C	25 °C	1.96	LPG	500	13	12	60 s	400 s	[123]

(continued)

Table 1 (continued)

Ferrites	Synthesis method	Temperature calcination	Operating	Sensitivity	Selectivity	Concentration (ppm)	Crystallite size (nm)	Particle size (nm)	Response time	Recovery time	Reference
$CuFe_2O_4$	Sol–gel self-auto-combustion	1000 °C	350 °C	90%	C_2H_5OH, acetone, and LPG	150	700	–	3 min	4 min	[124]
$CuFe_2O_4$	Auto-combustion	600 °C and 900 °C	300 °C	–	LPG	1000	~ 9 to 45	40–60	–	–	[125]
$Li_{0.5}SmxFe_{2.5-x}O_4$	Sol–gel self-auto-combustion	850 °C	60 °C	80–87% < 40%	Methanol and C_2H_5OH LPG and NH_3	200	100–200	–	~ 3 min	~ 5 to 6 min	[126]
$Li_{0.5}Sm_xFe_2O_4$	Sol–gel self-combustion	850 °C	25 °C	80–87%	C_2H_5OH, methanol	200	–	0.2–0.15 μm	3 min	5–6 min	[126]
Li-$CuFe_2O_4$	Co-precipitation	900 °C	340–355 °C	83.82%	LPG	0.5–4 vol%	17	7–17	2.7 min	19.36 min	[67]
$Mg_{0.5}Zn_{0.5}FeO_4$	Wet chemical	750 °C	375 °C	~ 60%	Acetone	50	~ 23	~ 58	32 s	2–3 min	[127]
$Mg_{0.5}Zn_{0.5}FeO_4$	Wet chemical	750 °C	350 °C	~ 39%	C_2H_5OH	50	~ 23	~ 58	24 s	1 min	[127]
$Mg_{1-x}LiFe_2O_4$	Solid-state reaction	300 °C	200 °C	–	Humidity	10–80%	–	110–200	180-360 s	435–780 s	[128]
$Mg_{1-x}Zn_xFe_2O_4$	Wet chemical	300–900 °C	320 for CO and 380 °C for H_2	44% for CO and 65% for H_2	CO and H_2	1660	11	–	–	–	[129]
$MgFe_2O_4$	Sol–gel auto-combustion	1173 K	250 °C	71%	LPG	200	–	30–38	–	–	[130]
$MgFe_2O_4$	Co-precipitation	900 °C	335 °C	3.0	Petrol	5	40	1 μm	–	–	[131]
$MgFe_2O_4$	Solid-state reaction	700 °C	275 °C	–	C_2H_5OH	10–1000	–	15–30	–	–	[128]
$MgFe_2O_4$	Sol–gel auto-combustion	450–500 °C	598 K	73% 50%	C_2H_5OH CH_3OH	5	–	15–20	–	–	[132]

(continued)

Table 1 (continued)

Ferrites	Synthesis method	Temperature calcination	Operating	Sensitivity	Selectivity	Concentration (ppm)	Crystallite size (nm)	Particle size (nm)	Response time	Recovery time	Reference
$MgFe_{2-x}Ce_xO_4$	Sol–gel auto-combustion	973 K and 1173 K	25 °C	94%	Acetone	100–300	28–34	0.07–0.2 µm	20 s	65 s	[133]
$Mn_{0.2}Ni_{0.8}Fe_2O_4$	Hydrothermal	–	250 °C	0.99	Humidity	1000–8000	27	–	450 s	90 s	[134]
$MnFe_2O_4$	Chemical Co-precipitate	–	–	93.6% 80.6%	NO_2 SO_2	–	10.7	–	1 s	5 min	[135]
$MnFe_2O_4$	Solution assisted combustion	–	300 K	83.5	NH_3	–	–	30–35	–	–	[136]
$Ni_{1-x}CO_xFe_2O_4$	Spin coating	800 °C	260 °C	70%	C_2H_5OH	150	20–29	–	–	10 min	[137]
$Ni_{1-x}Co_xMn_xFe_2O_4$	Hydrazine	500 °C	180 °C	60%	LPG	1000	10–15	–	< 1 min	–	[138]
$Ni_{1-x}Zn_x$ Fe_2O_4	Sol–gel self-auto-combustion	880 °C	275 °C	–	Acetone	500	–	–	–	–	[139]
$NiFe_2O_4$	Co-precipitate	400 °C	300 °C	96%	Cl_2	1000	8.36	–	2 min	–	[63]
$NiFe_2O_4$	Sol–gel self-auto-combustion	600 °C	350 °C 300 °C	–	C_2H_5OH	50	23	–	88 s	220 s	[140]
$NiFe_2O_4$	Sol–gel self-auto-combustion	600 °C	230 °C	~ 88% ~ 76%	Acetone Alcohol	200 200	–	15–25	–	–	[87]
$NiFe_2O_4$	Hydrothermal	–	Room temperature	–	LPG	–	8.9–11.3	12.3–14.7	–	–	[138]
$NiFe_2O_4$	Sol–gel self-auto-combustion	550 °C	350 °C	2.1	LPG	2000	23	11	~ 70	~ 180	[141]
$NiFe_2O_4$	Glycine combustion route	500 °C and 700 °C		142%	LPG	200	31 and 38	–	–	–	[142]
$NiFe_2O_4$	Co-precipitate	400 °C	–	62.3	LPG	4 vol%	–	–	220 s	250 s	[143]

(continued)

Table 1 (continued)

Ferrites	Synthesis method	Temperature calcination	Operating	Sensitivity	Selectivity	Concentration (ppm)	Crystallite size (nm)	Particle size (nm)	Response time	Recovery time	Reference
PANI-$CdFe_2O_4$	Chemical polymerization	300 °C	–	50.83	LPG	1000	24	–	50 s	100 s	[144]
Pd-$MgFe_2O_4$	Molten salt	700 °C		60%	LPG	200	15–20	–	5 s	5 min	[145]
$Sn_{0.2}Ni_{0.8}Fe_2O_4$	Co-precipitate	900 °C	25 °C	68.43%	Sulfur hexafluoride	80	39	34.5–35.01	3.76 s	23.21 s	[146]
$Zn_{1-x}Cux\ Fe_2O$	Sol–gel auto-combustion	630 °C	250 °C	53.35%	LPG	0.6 vol%	28–47	–	6.25 min	3.5 min	[147]
$ZnFe_2O_4$	Molten salt route	700 °C	250 °C	300 for H_2S and rest < 60	H_2S, NO_2, SO_2, C_2H_5OH and acetone	200	15–20	16	3 s	< 3 min	[148]
$ZnFe_2O_4$	Sol–gel self-auto-combustion	1000 °C	350 °C	90%	C_2H_5OH, LPG, and acetone	150	100	–	2 min	4 min	[149]
$ZnFe_2O_4$	Sol–gel self-auto-combustion	500 °C	25 °C	140%	LPG	2000	10	30–40	60 s	300 s	[150]
$ZnFe_2O_4$	Ultrasonic spray pyrolysis	–	280 °C	10	CO	500	–	200	–	–	[151]
$ZnFe_2O_4$	Auto-combustion	560 °C	250 °C	–	C_2H_5OH	200–800	–	10	70 s	90 s	[152]
$Zn_{0.6}Mn_{0.4}Fe_2O_4$	Sol–gel self-auto-combustion	550 °C	300 °C	–	C_2H_5OH	200	–	30–35	–	–	[153]

Reproduced with permission from [10]

for measuring relative humidity [155]. Naik et al. disclosed exactly how the sensitivity of copper–ferrite nanoparticles could be improved by substitution with bismuth [156]. The developed material possessed a high sensitivity factor at both low and high relative humidity, allowing direct practical application in industries where humidity monitoring is one of the critical factors. In exploring the moisture-sensing properties of spinel ferrites, Patil et al. developed magnesium-substituted zinc ferrites as a nanomaterial that utilizes the principle of adsorption in humidity sensing [157]. The developed nanoparticles were found to be highly sensitive in the range of 40–75% of relative humidity. In another exciting moisture-sensing study, Priya et al. developed a $MgFe_2O_4$-based ferrite material using citric juice-assisted green synthesis techniques [158]. The developed ferrites were found to be sensitive to a broader range of 10–95% relative humidity. In another study, Jeseentharani et al. developed a series of spinel ferrites (MFe_2O_4, where M includes cobalt, copper, magnesium, nickel, and zinc) [159]. All the ferrites were properly characterized by the group, and it was found that among the developed ferrites, the zinc ferrites have the highest sensitivity with a very high recovery time. Rana et al. reported gadolinium-substituted spinel ferrites in a similar context using a chemical co-precipitation technique [160]. The developed material was investigated for its conductivity-based moisture measurement capability, which was found to be sensitive in the range of 10–80% relative humidity. Hiremath et al. also investigated the doping effect of rubidium on magnesium ferrites on their moisture measurement capability [161]. The group found that the doped ferrites were sensitive and stable with minimal hysteresis, making them an effective material for moisture-sensitive devices. A similar doping effect of lithium and cobalt on the sensitivity of ferrites to moisture measurement was observed by Ateia et al. [162]. Based on their studies, the group concluded that the developed material could be used in commercially available humidity sensors. In another doping experiment, nickel–magnesium spinel ferrites doped with yttrium were fabricated by Rao et al. for humidity sensing [163]. The group found that the doped sensors were very sensitive and stable over a wider range of relative humidity for up to six months. In addition, the sensing properties of zinc-based spinel ferrites were explored by Nitika et al., who investigated the moisture sensitivity of the spinels they developed at different annealing temperatures [164]. The group found high to excellent sensitivity of their advanced materials when annealed at 700 °C, due to increased crystallinity and decreased lattice strain.

2.2 Bio and Chemical Sensors

Due to their excellent absorption properties for electromagnetic waves, spinel ferrites are employed in the field of chemical sensing. In the following subsections, important highlights and recent advances of spinel ferrites in the detection of organic and inorganic chemicals as well as in the detection of pharmaceuticals are presented.

2.2.1 Spinel Ferrites as Chemical Sensors

Spinel ferrites are used as sensors due to their selectivity and sensitivity to various organic and inorganic chemicals. Among the critical recent advances in this field is the work of Chapelle et al., who have developed a copper oxide-based spinel ferrite to detect carbon dioxide through a combination of in situ reduction techniques and afterglow in air [127]. The developed sensor was sensitive enough to measure the concentration of carbon dioxide present up to 5000 ppm effectively in the atmosphere. Another example is the development of graphene oxide nanoparticles made with zinc-containing spinel ferrite nanoparticles by Tajik et al. [165]. The group used the application of the same for the detection of Sudan I, which is considered hazardous and carcinogenic and can irritate eyes, skin, or respiratory tract in the atmosphere. The sensor formed was effective in recording the oxidation of Sudan I and helped in detecting traces of Sudan down to a threshold of 0.02 μM. In a similar context, Gunasekaran et al. reported the $Co_xFe_{3-x}O_4$ cobaltites as ethanol sensing materials [166]. The developed powders were deposited on alumina substrates and analyzed for their response under ethanol gas pulses. Similarly, a nanocrystalline spinel of zinc-substituted cobalt ferrite ($Zn_xCo_{1-x}Fe_2O_4$) was developed as an efficient ethanol sensor by Powar et al. [37]. The thick ZCF developed achieved maximum gas response and selectivity for 100 ppm ethanol at 30 °C. In addition, a zinc ferrite ($ZnFe_2O_4$)-based nanostructure with the potential to detect ethanol was developed by Nemufulwi et al. [167]. The ethanol sensor is of critical importance because it has applications in numerous fields such as chemical reactions, ethanol bioproduction, breath analysis, and food quality control. Another persistent chemical is formaldehyde, a volatile organic compound that has been linked to numerous health risk factors, including sick building syndrome. The WHO has mandated a limit of 0.08 ppm formaldehyde for a 30-min exposure, above which fatal effects, including death, have been reported. To successfully detect formaldehyde in the atmosphere, Rahman et al. developed spinel $ZnFe_2O_4$ nanorods using formaldehyde as a model compound [168]. The performance of the chemical sensors showed better stability, higher sensitivity, and repeatability. Another chemical, phenylhydrazine, whose high exposure is associated with nausea, vomiting, headache, dizziness, fatigue, and long-lasting allergies. Therefore, to monitor its concentration, Al-Heniti and his group developed $Cd_{0.5}Mg_{0.5}Fe_2O_4$ cadmium-based ferrite nanoparticles using a simple co-precipitation method [169]. The fabricated sensor showed a high sensitivity of 7.01 μA mM/cm^2 with a detection limit of 3.125 mM in 10.0 s. In another study, Katowah et al. reported a poly(pyrrole-co-toluidine) copolymer and cobalt ferrite ($CoFe_2O_4$) as an electrochemical sensor for the selective detection of lead using the in situ oxidative polymerization technique [170]. The concentration of lead in air should be less than 0.1 μg/m^3. When this limit is exceeded, lead exposure is associated with damage to various body systems, including the nerves, kidneys, immune system, and reproductive organs. Exposure to lead is also associated with decreases in blood oxygen capacity.

2.2.2 Spinel Ferrites as Biosensors

The development and progress in nanoparticles are leading to the advancement in sensitive biosensors, which are finding wider applications in various fields such as medical research, drug development, and therapeutics [171]. Magnetic nanomaterials are often used as a source for biosensing due to their magnetic behavior. The latest instrumentation tactics are widely used for magnetic materials detection and sensing. Some biosensors use magnetic nanoparticles as markers and sensing methods, such as (i) magneto-resistive sensor: In these sensors, magnetic particles are attached to the surface of the sensor, which changes the magnetic fields and ultimately leads to electrical changes in the sensor [172, 173]. (ii) Magnetic relaxation switches (MRSw): In these sensors, the targeted aggregation/disaggregation of magnetic nanoparticles is used to identify biomolecules [174, 175] (Table 2). (iii) Magnetic particle relaxation sensors: These sensors utilize the relaxation of magnetic moments in the particles [176]. The relaxation is the basis of this assay [177, 178].

Nowadays, metal oxide nanoparticles are widely used to develop low-cost glucose biosensors. Monunith et al. reported polyethylene glycol (PEG) grafted manganese ferrite (PEG-$MnFe_2O_4$) nanoparticles for glucose sensors (enzymatic and non-enzymatic) [183]. They found that GO_x@ PEG-$MnFe_2O_4$ had higher selectivity for glucose than other interferents and that this enzymatic sensor had better reproducibility and lifetime. Sakthivel et al. developed spinel-nickel ferrite, $NiFe_2O_4$ nanosheets ($NiFe_2O_4$ NSs) [184]. They reported selective electrocatalytic reduction of hydrogen peroxide with nickel ferrite. $NiFe_2O_4$ nanosheets were employed for estimation of H_2O_2 in human blood and rat brain serum samples. Sarala et al. prepared and reported that the efficacy of nickel ferrite ($NiFe_2O_4$) against breast cancer (MCF-7) cell lines was investigated using an MTT assay [185]. The detection of trace acetone gasses is important for the diagnosis of diabetes. In this sequel, Zhou et al. developed zinc ferrite ($Zn_xFe_{3-x}O_4$) sensing materials that showed signals for trace acetone in the breath of diabetic patients [186]. Similarly, rosuvastatin was detected in human plasma using *p*-$CuFeO_2$ NPs. The developed chemical sensor showed appropriate oxidation behavior for ROS oxidation from 0.2 to 22.0 nM with 0.077 nM LOD [187].

Table 2 Magnetic nanoparticles used for biosensing applications

Particles	Size (nm)	Composition	Characteristics	References
MP	1000	Dynabeads	MRSw	[179]
Iron oxide	56	Quantum magnetics	SQUID	[180]
Cubic FeCO	12.8	Oxidized shell	GMR	[181]
Magnetic beads	130, 250	Micromod Partikeltechnologie	SQUID	[182]

2.2.3 Spinel Ferrites as Pharmaceutical Sensors

Pharmaceuticals are vital to humans, but their misuse and unethical disposal are responsible for environmental pollution that has negatively impacted human health. Therefore, the need to detect these pharmaceuticals in the environment is a very important and critical aspect. Spinel ferrites have also proven to be effective and sensitive sensors for the detection of pharmaceuticals in the environment. An important example of this is the study by Hasanpour et al., who developed a voltammetric sensor based on copper ferrite spinels embedded in multi-walled carbon nanotubes [188]. The developed sensor was able to detect dacarbazine as it oxidized. Although dacarbazine is used as an anticancer agent, it is also an irritant and can cause hypersensitivity reactions in patients with liver failure that can be severe to fatal. The voltammetric sensor developed proved to be extremely sensitive, being able to detect dacarbazine at concentrations as low as 0.08 μmol/L. Osman et al. synthesized spinel $Ba_{0.5}Co_{0.5}Fe_2O_4$ nanoparticles using thermal glycol technique for potential application as an electrochemical sensor for ciprofloxacin [189]. Furthermore, Morales et al. reported $Cu_{0.3}Co_{0.7}Fe_2O_4$-based spinel ferrite and its application as an electrode modifier [190]. The developed ferrite showed excellent electrocatalytic activity, leading to a possible usage as an electrochemical sensor for *N*-acetyl-*p*-aminophenol. In another study, Taei et al. presented the preparation of magnetic cobalt ferrite nanoparticles ($CoFe_2O_4$) and multi-walled CNTs for the rapid and sensitive detection of doxorubicin [191]. Chemicals such as diclofenac and morphine are simultaneously detected with spinel $MgFe_2O_4$ nanoparticles. The $MgFe_2O_4$-based sensor has been used to enrich morphine and diclofenac in serum and urine samples [192].

2.3 Spinel Ferrites as Temperature Sensors

Temperature sensors play a key role in many technical applications. In daily life, we use various technologies such as smartphones, thermometers, microwave ovens, and refrigerators in which temperature sensors are used. The development of ferrite temperature sensors for biomedical applications can help monitor the local temperature in a living body. Local temperature is an important parameter to study of health problems in a living body. For example, thermal imaging (temperature scanning) is used in medical diagnostics, which can help detect metabolism and various medical problems such as inflammation or tumors in a living body [193–195]. To measure local temperature of a body, several magnetic resonance imaging-based thermometry (tMRI) methods have been employed [196]. Among these, most accurate and widely used method is proton resonance frequency (PRF) [197]. While this method achieves an accuracy of 1 °C for immobile tissue, it has its limitations when working with adipose tissue because of its sensitivity to tissue movement in the body [195]. To solve these problems, suitable magnetic contrast agents have been proposed that have a temperature-dependent magnetic moment. The magnetic

moment of these particles changes with local temperature, resulting in a temperature-dependent local inhomogeneous field and changing the width of the nuclear magnetic resonance (NMR) signal, which is reflected in the intensity of the MRI signal. Since the field strongly depends on temperature, the determination of the absolute temperature can be done from the intensity of T^*_2 weighted MRI images [198]. Easy tuning of magnetic parameters (such as magnetic moments and Curie temperature) and their biocompatibility enable ferrite nanoparticles to find a special place in MR thermometry applications. Various ferrites nanoparticles such as iron-based ferrites (Fe_3O_4, Fe_2O_3), Ni–Zn ferrite, Mg–Zn ferrite ($Mg_{1-x}Zn_xFe_2O_4$), and Cu–Zn ferrites ($Cu_{1-x}Zn_xFe_2O_4$) have been investigated for MRI temperature sensors [198–200]. To develop MRI temperature sensors, two properties of ferrites should be carefully studied: magnetic properties and toxicity (biocompatibility). To obtain MRI images with high-temperature resolution, the ferrite nanoparticles should have their Curie temperature close to the temperature range of interest (usually the temperature of body) and have a strong temperature dependency on magnetization, which can be determined by magnetic measurements. As for the toxicity of ferrites mentioned above, Mg–Zn ferrites have been reported to have low toxicity and are the most suitable candidates for tMRI [195, 198, 200, 201]. Thus, in the remainder of part, we will review various properties of Mg–Zn ferrites as representatives of ferrites. It has been reported that Mg ferrite ($MgFe_2O_4$) shows Curie temperature of 713 K along with a saturation magnetization value of 27 emu/g [202]. The high Curie temperature of Mg ferrite makes it impractical for tMRI [203]. Therefore, the researchers replace Mg with Zn, which lowers the Curie temperature of Mg–Zn ferrites ($Mg_{1-x}Zn_xFe_2O_4$) [198]. The Curie temperature and saturation magnetization can be tuned by varying the Zn concentration, which is caused by a change in the distribution of cation between tetrahedral and octahedral sites. Therefore, it is important to monitor and control the cation distribution during the development of ferrite composition to obtain the best possible ferrite for tMRI applications. The reports show that the cation distribution in ferrites can be analyzed by X-ray diffraction, and then the magnetic properties can be analyzed by Moessbauer and magnetometry studies [198].

Figure 3a shows the Mössbauer spectra of $MgFe_2O_4$ and one of the Mg–Zn composition [$(Mg_{0.36}Zn_{0.64})_{0.8}Fe_{2.2}O_4$], recorded at temperatures of 80 and 300 K, respectively. The data were fitted using input parameters obtained from Rietveld refinement of XRD patterns and are shown by solid lines [198]. From the Moessbauer spectra, it appears that there are well-defined absorption peaks that were fitted to determine the value of the hyperfine field (B_{hf}) and to analyze the sites occupied by Fe^{3+} cations (A) and [B]. Despite the additional Fe cations per formula unit in [$(Mg_{0.36}Zn_{0.64})_{0.8}Fe_{2.2}O_4$] compared to its parent $MgFe_2O_4$ ferrite, the Moessbauer spectra (Fig. 3b) show a relaxation character suggesting a lower blocking temperature than that of the $MgFe_2O_4$ ferrite.

To know the temperature dependence of magnetization and the Curie temperatures of Mg–Zn ferrites, the magnetization measurements must be performed. Figure 3c shows magnetization measurements of Mg–Zn ferrites as a function of temperature and Zn concentration. From Fig. 3d, the magnetization has a strong temperature dependence, which makes these ferrite nanoparticles suitable for tMRI.

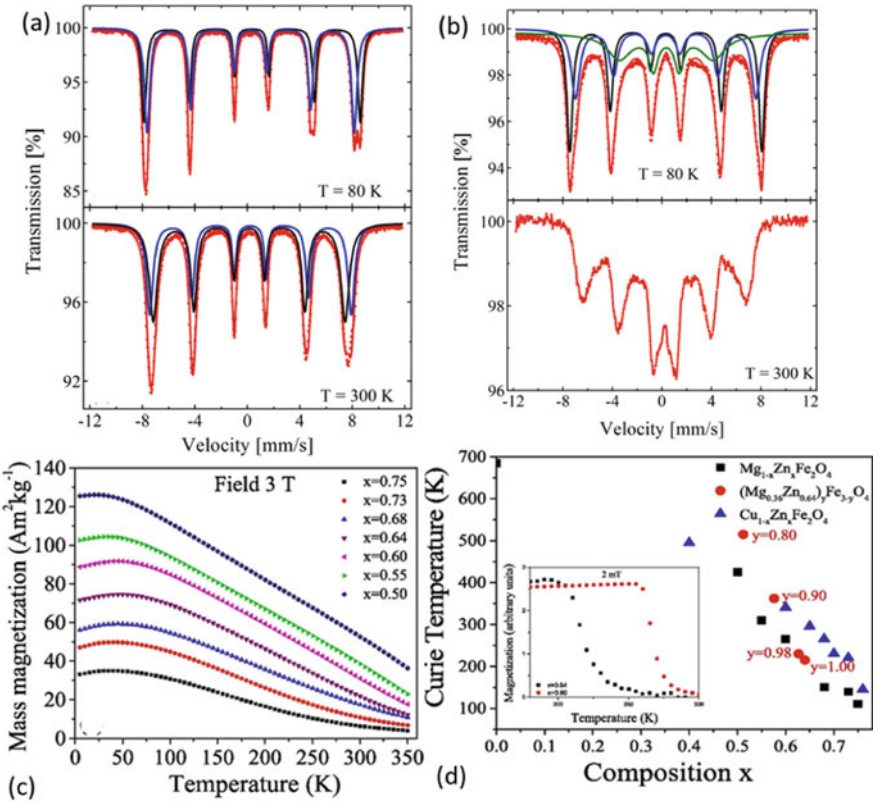

Fig. 3 Mössbauer spectra of **a** $MgFe_2O_4$ and **b** Mg–Zn ferrite $[(Mg_{0.36}Zn_{0.64})_{0.8}Fe_{2.2}O_4]$ performed at 80 and 300 K. The solid line in the graph shows fitting of the data. Reproduced with permission from [200]. **c** Magnetization as a function of temperature at applied field of 3 T for $Mg_{1-x}Zn_xFe_2O_4$ and **d** Zn concentration dependence of Curie temperature. The inset shows magnetization as a function of temperature at 2mT field

Mg–Zn and Cu–Zn ferrite nanoparticles with polydispersity of 0.402 and 0.640 and size of 742.2 ± 5.2 and 715.5 ± 126.9 nm, respectively, were investigated for toxicity by Alghamdi et al. [198], as reported by the authors, after 24 h, there were no statistically significant differences in mitochondrial function between macrophages exposed to different types and doses of nanoparticles. This shows that exposure of the sample has no effect on cell viability. However, the cell responses to these particles as inflammation show that Mg–Zn ferrites are better than Cu–Zn ferrites, and therefore, in terms of toxicity, Mg–Zn ferrites are good candidates for tMRI applications.

After checking the suitability of ferrites, one can have these ferrites examined by MRI. Figure 4 shows axial MRI images of the phantom as a function of temperature taken with an agar gel phantom based on Ringer's solution for three representative Cu–Zn ferrites ($Cu_{1-x}Zn_xFe_2O_4$) with x concentration 0.65, 0.70, and 0.73 [195]. The authors observed a clear dependence of MRI brightness on temperature—brightness

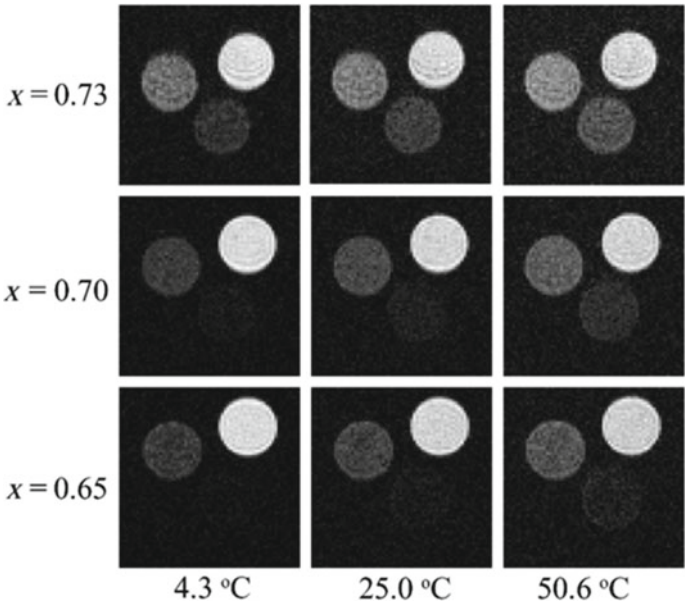

Fig. 4 MR image as a function of temperature for a phantom Cu–Zn ferrite ($Cu_{1-x}Zn_xFe_2O_4$) with x concentration 0.65, 0.70, and 0.73

increases with temperature. Moreover, the image brightness is also influenced by the ferrite composition and the molar concentration of the nanoparticles [195]. Therefore, the temperature dependence of magnetic nanoparticles plays a crucial role in tMRI.

Some ferrite materials, e.g., $Cu_{0.35}Zn_{0.65}Fe_2O_4$, have also been found to be promising for magnetic cooling, as these materials have very large relative cooling power (RCP) [204, 205].

2.4 Stress Sensors

Stress is a mechanical property of solids and is defined as force per unit area. Mechanical stress is used for the development of various sensors. These sensors are in high demand in emerging technological applications such as medicine, robotics, and the automotive industry. One of the phenomena used in the stress sensor is magnetostriction. Change in dimensions of a magnetic material upon application of a magnetic field is defined as magnetostriction [206]. Change in dimensions of the materials is due to rotation of domains and movement of domain walls when external magnetic field is applied. The dimensions can either expand or contract, and therefore, the materials are referred to as positive or negative magnetostrictive materials. Since magnetostriction is due to the coupling between magnetic and elastic force, application of these materials in stress sensors is great for scientific and technological

Table 3 Comparison of magnitude of magnetostriction (λ) and dλ/dH in some promising ferrite compositions

Composition	Magnetostriction (λ) in ppm	$(d\lambda/dH)_{max}(10^{-9}\ A^{-1}\ m)$	Reference
$CoFe_2O_4$	− 212	1.37	[212]
$Co_{1.1}Ge_{0.1}Fe_{1.8}O_4$	− 241	− 2.6	[212]
$Co_{1.1}Al_{0.1}Fe_{1.9}O_4$	− 140	− 2.9	[212]
$CoMn_{0.2}Fe_{1.8}O_4$	− 234	− 1.78	[213]

developments. Co-ferrites have emerged as promising candidates for application in stress sensors due to their large magnetostriction effect, strong stress sensitivity, high Curie temperatures, low cost (compared to rare earth-based materials), chemical stability, and robustness [207, 208]. Researchers have also replaced Co-ferrites with various transition metal elements [some of which are listed in Table 3] and studied their magnetoelastic properties [207, 209, 210]. For sensors based on magnetostriction, the slope of the magnetostriction (λ) with the magnetic field (H) dλ/dH is the crucial parameter, since it gives the sensitivity of the magnetic induction to stress (dB/d) [211].

2.5 Magnetoresistance Sensors

In the current time, magneto-electronics plays a key role in sensor applications. Popular among them are magnetoresistance sensors (MR). The property of change in electrical resistance when magnetic fields are applied in magnetic materials is called magnetoresistance. It is generally defined as the change in resistance with respect to the resistance in a magnetic field [214–216]. The formula for MR is given as follows:

$$\mathrm{MR} = \frac{\Delta R}{R} = \frac{R(H) - R(H=0)}{R(H)}, \tag{9}$$

where R is the electrical resistance of a material and H is the applied magnetic field. The large change in the electrical resistance of a material or device upon application of external magnetic field is of great technological importance for the development of many types of sensors (such as biosensors, magnetic sensors, and navigation sensors) and memory [214].

There can be different types of MR effects, some of which are widely used in technological applications are described as following:

1. Anisotropic magnetoresistance (AMR): This is the first MR effect reported by Thomson in 1857 [217]. The magnitude of AMR in a sample depends on the relative direction of magnetization to the applied current. It has been observed that the electrical resistivity of a ferromagnetic material is maximum when the

direction of the applied current coincides with the magnetization, and minimum when the current and magnetization directions are at right angles. However, the reverse trend is also observed for some materials. Thus, it may also depend on the materials. The AMR effects are comparatively small (less than 5%).

2. Giant magnetoresistance (GMR): GMR has greater impact than AMR [218, 219]. The discovery of GMR effects led to intensive research in the field of magnetic sensors and devices. This led to a new emerging branch of electronics called spintronics, where researchers can benefit from both electron and spin properties. Before the discovery of GMR, AMR effects were used for magnetic sensors and memory. GMR is observed in a multilayer system having two ferromagnetic layers, which are separated by a non-magnetic metallic layer. Figure 5a shows a schematic of a multilayer system that produces the GMR effect. When the current is applied, the electron moves from one magnetic layer to the non-magnetic layer and reaches the interface of the second magnetic layer (depending on the thickness of the non-magnetic layer). Now, if the magnetization in the second magnetic layer has the same orientation as that of the first (ferromagnetic coupling), the electron enters the second magnetic layer, resulting in low resistance. On the other hand, if the magnetization of the second layer is antiparallel (antiferromagnetic coupling), the electron is scattered, resulting in a high resistance. In this way, one can represent a low and a high resistance as 0 and 1, and this property is used in sensors and devices.
3. Tunneling magnetoresistance (TMR): A device in which a thin insulating layer is sandwiched between two magnetic layers (as shown in Fig. 5a) is called a tunnel junction. The electron tunnels through the insulating barrier in such structures and the effect are called tunneling magnetoresistance [220, 221]. The TMR value depends on the spin polarization in the magnetic layers—the higher the spin polarization, the larger the TMR effects. In general, the TMR effects are larger than the GMR effect.

As mentioned earlier, MR effects can be used to develop various types of magnetic sensors and storage devices. The advantage of magnetic sensors over others, such as electrical, is that they have less background noise and therefore have a good signal-to-noise ratio. To exploit this potential, it is very important to search for different materials that can exhibit greater MR effects. Among the various magnetic materials, ferrites such as Fe_3O_4, $FeTi_2O_4$, Mn-doped Fe_2O_4, and $Fe_{1-x}Cu_xCr_2S_4$ nanoparticles exhibit interesting magnetoresistive properties and are promising for magnetic and MR-based sensors [222].

Cancer in various parts of the body is very common nowadays, which can also be life-threatening. Early medical examination and detection of these cancer cells is very important, and for this purpose, biosensors can be a life-saving tool. Using magnetic Fe_3O_4 nanoparticles on an InSb semiconductor channel, Kim et al. demonstrated a GMR-based biosensor as shown in Fig. 5b, c [223]. The authors reported that Fe_3O_4 NPs were linked to the target antigen by the selective antibody in the reagent solution, and a detection antibody fixed on an InSb channel selectively bound to the complex of antigen, antibody, and Fe_3O_4 NPs [223]. Due to the Lorentz force, a static field is

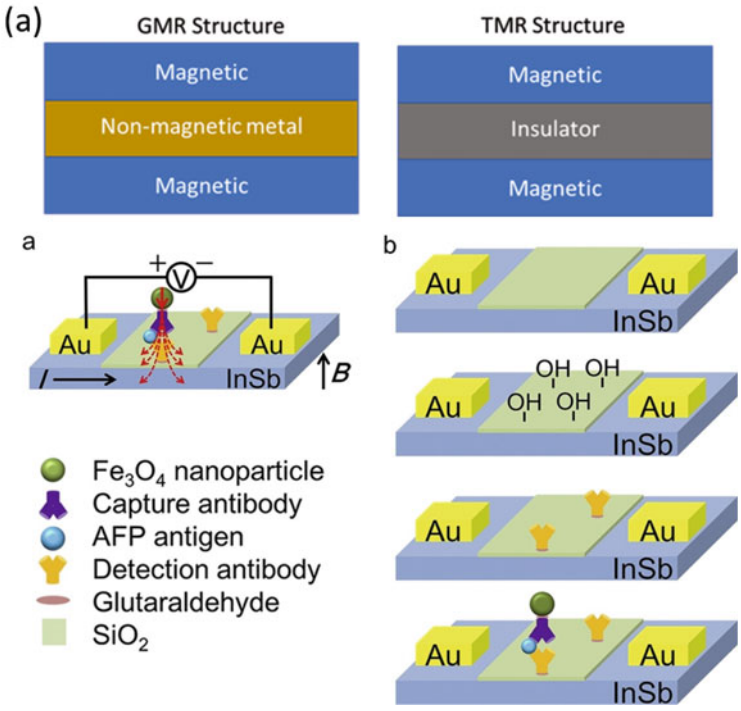

Fig. 5 **a** Schematic for GMR and TMR multilayer structures. **b** Schematic of MR-based InSb biosensor using ferrite nanoparticles. **c** Fabrication of deice and different sensing process. Reproduced with permission from [182]

generated by the detected magnetic nanoparticle and the generated field changes the resistance of the InSb semiconductor channel. The change in resistance due to the magnetic field, i.e., magnetoresistance, provides the antigen concentration, which is proportional to the number of Fe_3O_4 nanoparticles on the sensor surface. It has been shown that the sensor can detect antigen concentrations as low as 1 pg/ml and has good selectivity and reusability [223, 224]. The sensor can be used to detect antigens from blood sample in liver cancers. The GMR-based biosensor with Fe_3O_4 NPs was developed by Chen et al. for the early detection of gastric cancer cells [225, 226]. In addition to biosensors, MR-based ferrite nanoparticles are also used in spintronics and other magnetic applications [227, 228].

2.6 Ferrites as Components of Optical and Plasmonic Sensors

Nanotechnology focuses on the development of materials with superior electrical, optical, biological, and magnetic properties. Magnetic nanomaterials are of particular

interest among nanomaterials with additional properties due to their unique physicochemical structure and the numerous applications associated with modulating the size distribution, magnetic moment, and many other properties of magnetic nanomaterials. The application of magnetic nanomaterials varies significantly depending on their size and other characteristics, such as their surface properties [229, 230]. For example, magnetic nanoparticles (MNPs) smaller than 28 nm exhibit superparamagnetic properties suitable for biomedical applications, while MNPs larger than 28 nm are widely used for electronic instruments and magnetic separation due to their ferrimagnetic properties [231]. Magnetic and plasmonic NPs are most commonly used by researchers for biomedical applications, but both have their limitations [232, 233]. It is possible to improve the performance of the resulting material by combining magnetic and plasmonic properties. A disadvantage of magnetic nanoparticles is their tendency to corrode, aggregate, and be toxic in water, while plasmonic materials are limited by their low biological sensitivity. By combining magnetic properties with plasmonic materials, a highly sensitive hybrid can be produced. Magneto-plasmonic (MNP) particles exhibit both magnetic and plasmonic properties, and the interaction between the plasmonic shell and magnetic core leads to symmetric effects in bioimaging and thermotherapy. In their study, Hat et al. showed that Fe_3O_4 nanoparticles coated with Au shell exhibited a decrease in saturation magnetization from (64.9–59.2) emu g^{-1}. A similar trend was observed by Zhou et al. However, there was no change in coercivity in either case, indicating that the magnetization of Fe_3O_4 nanoparticles is not affected by the addition of Au [234–236]. MPNs can be classified into three categories based on their chemical structure: pure metals, metal oxides, and magnetic nanocomposites. The classification of MPNs for various applications is shown in Fig. 6.

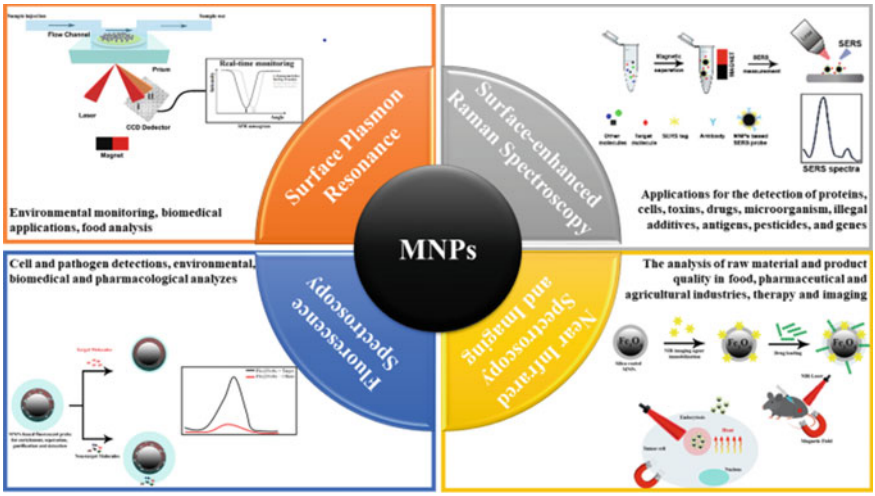

Fig. 6 Biomedical and environmental applications of optical (bio)sensor systems with magnetic nanoparticles (MNPs). Reproduced from [237] originally published under CC BY 4.0 license

Due to their instability and wide size distribution, metal MPNs are less commonly used than metal oxide MPNs. In addition to structure, environment and fabrication techniques also affect the properties of MPNs [238, 239]. Chemical methods or 'bottom-up' synthesis processes are commonly used to synthesize MPNs, such as high-temperature thermal decomposition, flow injection synthesis, electrochemical methods, and sol–gel synthesis [238, 240]. Chemical methods are preferred over physical methods because they provide controllable process conditions, while microorganism-based approaches, such as bioreduction, allow large production volumes, stability, reproducibility, and high yields. The fabrication of multifunctional composites, such as Fe_3O_4@Au and Fe_3O_4@Ag, involves two processes: (1) immobilization of the core and (2) core–shell structure [241–243]. The term 'biosensor' refers to a device that consists of a transducer and a biological sensing element [244]. Biosensors use physical, chemical, optical, electrochemical, and thermal processes to convert the signal obtained from biological interactions into information [245–247]. Electrochemical and electrical transducers are the most advanced transducers used in biosensors. However, these systems suffer from the limitations of using oxidizing/reducing agents [248]. Optical biosensors based on optical transducers play a prominent role in the field of sensing due to their high detection accuracy and cable-free design [244, 248]. The optical biosensor is capable of multiplex detection, remote sensing, and immunological electromagnetic interference. Sensors based on absorption, surface plasmon resonance (SPR), and photoluminescence provide a next-generation optical biosensing platform [235, 249–251]. Surface-enhanced Raman spectroscopy (SERS), fluorescence spectroscopy, near-infrared spectroscopy, and SPR are among the optical sensing techniques that utilize MPNs [232, 237, 252–256].

An important aspect of nanophotonics is plasmonics, which explains the enhancement of the optical near field in the subwavelength range by the interaction between electromagnetic radiation and conduction electrons in metallic nanostructures [257–260]. Plasmonics describes the confinement of electromagnetic waves in a dimension equal to or smaller than the wavelength [261, 262]. The use of SERS as a plasmonic detector for biomolecules has been intensively explored in the last decades. By using SERS, the Raman signals from biomolecules can be amplified by several orders of magnitude [233, 250, 263, 264].

2.6.1 Surface Plasmon Resonance Sensors

The SPR phenomenon is the result of a complex physical phenomenon caused by the incidence of light on a conductive noble metal layer. It takes place at the interface between a medium with a low refractive index (buffer) and a medium with a high refractive index (sensor glass surface) [265]. A reduction in the amplitude of the incident light occurs when free electrons in the metal layer absorb the energy of the incident photons. In 1968, the SPR effect was successfully explained [266], while this effect was not mentioned in the field of biosensors until fifteen years later, in 1983, by Liedberg et al. [267]. Before SPR, optical methods based on absorption

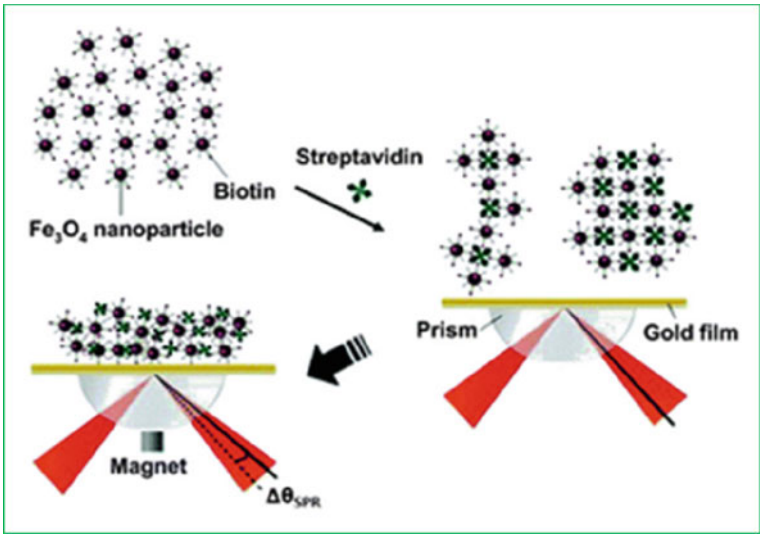

Fig. 7 Surface plasmon resonance (SPR)—signal amplification with MNPs [272]. Reproduced with permission of the Royal Society of Chemistry

and fluorescence were developed and used by researchers [268, 269]. SPR is limited in its ability to detect low molecular weight and low concentration biomolecules, but it is a viable method for detecting high molecular weight and high concentration biomolecules. The use of MPNs in SPR sensing makes it possible to detect analytes in complex samples [270, 271]. The basic principle of the SPR sensing system is shown in Fig. 7. Using gold nanospheres modified with magnetic nanoparticles, Sun et al. reported hollow biosensors for the detection of rabbit IgG [272]. Fe_3O_4 MNPs were used to capture the target molecules from the medium. A polydopamine solution was used to prevent the nanoparticles from agglomerating. Compared to conventional SPR biosensors, the gold nanostructures were able to detect rabbit IgG at a lower concentration than conventional biosensors. Comparing the SPR signals of the hollow gold nanospheres with those of the magneto-sandwich immunoassay, an eightfold increase was observed for the magneto-sandwich immunoassay compared to the hollow gold nanospheres [273]. Another report describes the development of an SPR biosensor based on immobilized AuNPs/MNPs conjugates and MNPs for the detection of thrombin at a concentration of 100 nM. The SPR angular shift was increased fivefold for the conjugated system of AuNPs and MNPs.

2.6.2 Near Infrared Spectroscopy Sensors

Near infrared spectroscopy (NIRS) is a type of vibrational spectroscopy that measures the absorption of electromagnetic radiation in the range of 750–2500 nm [274]. A series of absorption bands corresponds to the respiration of C–H bonds, C–O bonds,

O–H bonds, and N–H bonds [275]. Both qualitative and quantitative analyzes of molecules can be performed using these spectra. Compared to UV and visible radiation, NIR radiation is less scattered and penetrates the body more easily, making it ideal for obtaining information from inside the body [276]. This method is simple, fast, and requires only a small amount of sample without pretreatment, making it suitable for a variety of applications, including commodity analysis, pharmaceutical testing, and agricultural testing [277, 278]. Functional NIRS has recently been developed as a new generation tool, especially for biomedical applications such as neuroimaging and glucose monitoring [279–282].

Due to the superior properties of magnetic nanoparticles, they are used in NIRS as MRI and targeting agents by improving the therapy and resolution by improving the therapy system and imaging. Zhou et al. used indocyanine green as an agent for NIR imaging and Fe_3O_4 magnetic nanoparticles as an MRI agent [283]. In another report, Yang et al. used Fe_3O_4 MNPs modified with NIR dye for dual imaging involving NIR and MRI imaging [284]. The Fe_3O_4 MNPs modified with NIR dye conjugates showed better response than conventional dyes. In addition, the researchers observed high MRI sensitivity, good structural stability, and efficient NRI signals with polymer-coated MNPs. A combination of polyrol and Fe_3O_4 magnetic core was used by the researchers to develop a strategy for cancer therapy and imaging, as shown in Fig. 8 [285]. When the magnetic field is applied, the Fe_3O_4 magnetic core is used to target the tumor, while the PPY shell is used as an NIR absorber for photothermal ablation of the tumor while preventing the release of Fe^{2+}/Fe^{3+} from the Fe_3O_4 MNPs [286]. Huang et al. used Fe_3O_4 MNPs coated with Chlore6 on their surface for imaging and therapy of Gastric cancer [286]. Cho et al. designed an injectable hydrogel and collagen nanocarrier for phototherapy, drug delivery, and imaging. Magnetic nanoparticle-mediated NIRS has also been used to detect pathogens [287]. Plasmon absorption, magnetic separation, and thermal ablation were used to simultaneously detect multiple pathogens in a single sample using gold nanorods and Fe_3O_4-based multifunctional biosensors [288–290]. Fe_3O_4 nanoparticles were used for pathogen taring, imaging, and subsequent photothermal therapy, but gold nanoparticles were used for multiple detection because of the plasmonic property of gold [273, 291]. Lee et al. developed a hydrogel-based thermosensitive microrobot for drug delivery by using NIR stimuli [292]. The fabricated microrobot efficiently performed drug delivery for the treatment of cancer cells through in vitro assays with Hep3B cells by using NIR and electromagnetic stimulation.

2.6.3 Fluorescence Spectroscopy and Imaging

Magnetofluorescent materials are of particular importance due to their optical properties, e.g., in bioimaging and bioimaging of fluorescent materials combined with the possibility of magnetic field guidance [292–294]. Fluorescent materials are suitable for biological applications due to their robust optical and chemical properties [295–298]. Because of their high sensitivity, fast response, and low cost, fluorescent

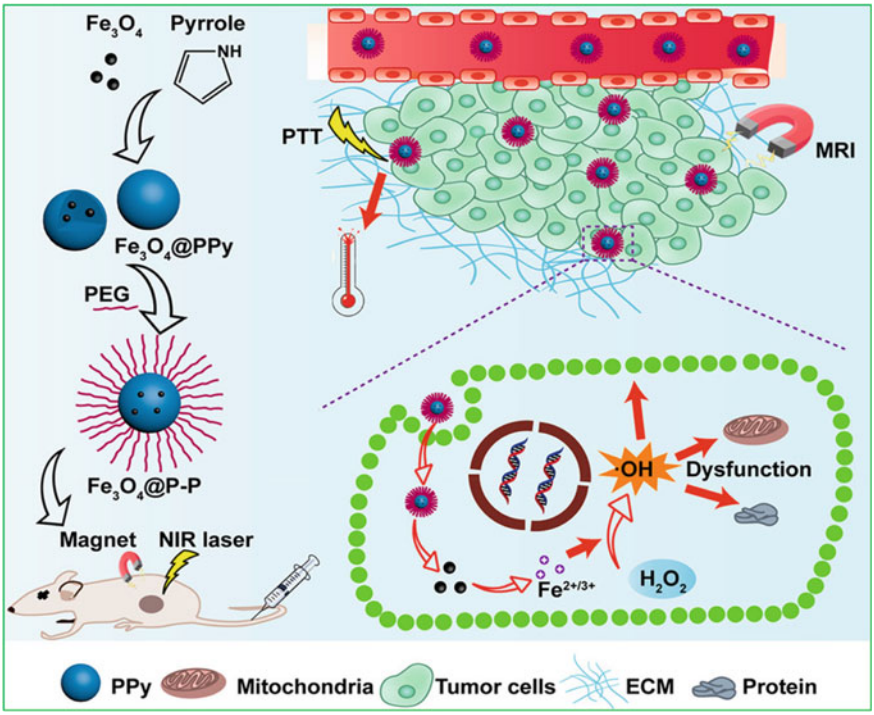

Fig. 8 Synthesis pathway of Fe_3O_4@ PP nanoparticles and assumed synergistic anticancer mechanism of Fe_3O_4@ PP nanoparticles. Reprinted with permission from [284]. Copyright American Chemical Society 2018

particles are also useful for sensing applications. However, they also have the disadvantage of inevitably emitting false signals due to nonspecific adsorption. Therefore, magnetic particles are used to separate the target from complicated matrices to avoid false signals. Magnetoflourometric sensing methods are used to detect a wide range of substances, including toxins, drugs, heavy metals, bacteria, cells, DNA, etc. [299–301]. Liu et al. used magnetic fluorescent materials for the separation of DNA [302]. The use of these materials increased the adsorption capacity and reduced the amount of material needed for the experiment. In another report, MNPs were used as concentrating agents in combination with dye-doped silica nanoparticles for fluorescence [303]. Laser-induced fluorescence microscopy was used to detect the target, and an improvement in the detection limit was observed compared with conventional methods. Zarei-Ghobadi et al. proposed genosensors for DNA detection by using photoluminescence quenching of fluorescent quantum dots in the presence of magnetic nanoparticles with large surface area suitable for quenching [304]. Because of their high biocompatibility, low cost, and high adsorption capacity, these biosensors are useful for biosensing. A novel magnetofluorescent material was developed for the detection of mycotoxins by combining $NaYF_4$: Ce/Tb a with Fe_3O_4.

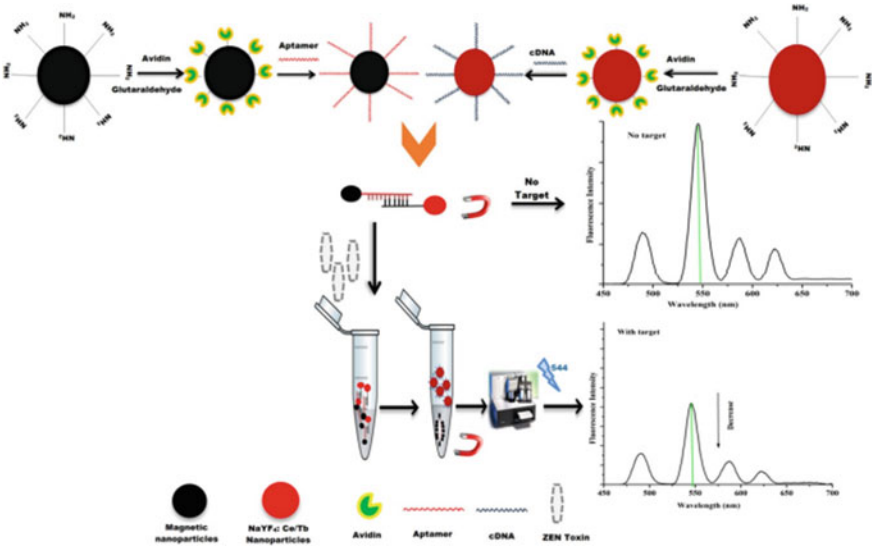

Fig. 9 Detection principle based on MNPs as capture probe and fluorescent nanoparticles as a signal probe. Reprinted with permission from [304]

This nanocomposite was stable, specific, fast, and practical. The scheme for the magnetofluorescent assay is shown in Fig. 9 [305]. In addition, the researchers used nickel powder enclosed in microchannels to generate a local magnetic field. This study documents the use of red fluorescent MNPs in biology, chemistry, and tissue engineering [306, 307].

2.6.4 Surface-Enhanced Raman Scattering Sensors

SERS is a surface sensitive technique used for the detection of analytes at very low concentrations and with high molecular sensitivity [233, 308–312]. The interaction between incident light and nanostructures is the foundation of SERS. It is based on the surface plasmon-induced amplification of molecular Raman scattering [313]. This technique is also suitable for the detection of single molecules and provides finer details of the chemical structure and confirmation [314]. The amplification of the Raman signal is contributed by the electromagnetic enhancement due to the effect of the electromagnetic field of the target stimulated by surface plasmons of the nanostructures, and another contribution of the Raman signal is provided by the chemical enhancement [315]. Electromagnetic enhancement is the main factor of molecular Raman scattering; therefore, high enhancement factor in Raman spectra can be achieved by changing the optical properties. SERS selectivity and sensitivity are affected by the size, shape, and composition of nanostructures [316–319]. SERS substrates are used for the detection of microorganisms, cells, and

environmental pollutants because of their high selectivity and sensitivity [320–326]. Magnetic nanoparticles are particles whose properties can be manipulated by an external magnetic field and whose size ranges from 1 to 100 nm [327]. Due to their excellent physicochemical properties, magnetic nanoparticles are used for biosensing and many other fields [328, 329]. However, due to their high chemical activity, these particles tend to agglomerate or oxidize, so their functionalization improves their stability. It is possible to overcome the limitations of MNPS by combining them with plasmonic nanostructures. In general, MNPs are used in SERS applications in two different ways. In the first method, they are used as a capture probe for purification, separation, and enrichment, and then participate in the detection process by interacting with the SERS component. In the second approach, a SERS modified magnetic core is used in conjunction with a plasmonic component, such as a silver or gold shell, as both a capture probe and a SERS probe. Although this approach has several advantages over the previous ones, depending on the type of analysis to be performed, another approach may be more appropriate [238]. Zengin et al. used hybrid MNPs as probes and polymer functionalized Au nanoparticles as SERS substrates. This MNPs sandwich assay was then used for the detection of tau protein, with a detection limit of about 25 fM [330]. In another report, detection of microRNA was performed using functionalized magnetic nanoparticles (Fe_3O_4@Ag) [331]. However, researchers have extensively studied the various synthetic methods for the preparation of MNPs and the use of MNPs in SERS, and there is still much scope for further applications of MNPs in SERS.

3 Conclusions and Outlook for MNP Sensors

An overview of recent advances and trends in the fabrication of various sensors based on spinel-ferrite materials is presented in this chapter. Recent years have seen a great deal of interest in nanoparticle-based optical sensing systems based on MNPs because of their unique properties, such as biocompatibility, low toxicity, chemical stability, large surface area, and ease of fabrication. This field is still in its infancy, but spinel ferrites have the potential to offer a wide range of applications. These devices are ideal for detecting and quantifying species that are still poorly understood, such as antibiotics and chemicals, using electroanalytical methods. Ferrite spinel has been combined with 2D materials such as graphene and other substances to produce remarkable results. In addition, plasmonic nanoparticles of noble metals can be combined to produce sensors with excellent performance, opening up a wide range of potential applications. Spinel-type ferrites are highly versatile gas sensor materials that will find more and more industrial applications as technology advances. Ferrites not only offer high sensitivity and selectivity but are also stable over the long term. Although spinel ferrites have been widely explored as sensors, their properties have not yet been fully explored, so further research is needed. In the near future, it is likely that ferrite spinels will be used in many sensors incorporating new technologies.

References

1. Xie X, Wang B, Wang Y, Ni C, Sun X, Du W (2022) Chem Eng J 428:131160
2. Kurian M, Thankachan S (2021) Open Ceramics 8:100179
3. Masunga N, Mmelesi OK, Kefeni KK, Mamba BB (2019) J Environ Chem Eng 7:103179
4. Park JW, Jang AN, Song JH, Park CY, Lee YS (2013) J Nanosci Nanotechnol 13:1895
5. Rani GPJ, Saravanan J, Sheet S, Rajan MAJ, Lee YS, Balasubramani A, Kumar GG (2018) Electrocatalysis 9:102
6. Vedrtnam A (2020) Mechanical Engineering Department, Invertis University, Bareilly, UP, India-243001, K. Kalauni, S. Dubey, A. Kumar, and Departamento de Arquitectura, Escuela de Arquitectura -Universidad de Alcalá, Spain, AIMS Mater. Sci. **7**, 800 (2020)
7. Hao A, Ning X (2021) Front Mater 8
8. Dalawai SP, Kumar S, Aly MAS, Khan MZH, Xing R, Vasambekar PN, Liu S (2019) J Mater Sci: Mater Electron 30:7752
9. Dippong T, Levei EA, Cadar O (2021) Nanomaterials (Basel) 11:1560
10. M. A. Njoroge, N. M. Kirimi, and K. P. Kuria, Crit. Rev. Solid State Mater. Sci. 1 (2021).
11. Narang SB, Pubby K (2021) J Magn Magn Mater 519:167163
12. Sharma SK (ed) (2021). Springer International Publishing, Cham
13. Srinivasan SY, Paknikar KM, Bodas D, Gajbhiye V (2018) Nanomedicine (Lond) 13:1221
14. Ahmad SI (2022) J Magn Magn Mater 562:169840
15. Gonçalves JM, de Faria LV, Nascimento AB, Germscheidt RL, Patra S, Hernández-Saravia LP, Bonacin JA, Munoz RAA, Angnes L (2022) Anal Chim Acta 1233:340362
16. Mathpal MC, Niraula G, Chand M, Kumar P, Singh MK, Sharma SK, Soler MAG, Swart HC (2021) Topics in mining, metallurgy and materials engineering. Springer International Publishing, Cham, pp 437–475
17. dos Santos OAL, Sneha M, Devarani T, Bououdina M, Backx BP, Vijaya JJ, Bellucci S (2021) J Electrochem Soc 168:067506
18. Shobana MK (2021) Mater Sci Eng B 272:115344
19. Ramakrishnaiah T, Prasanna GD, Chaturmukha VS, Reddy S, Kumaraswamy S, Naveen CS (2022) Sens Rev 42:164
20. Vinosha PA, Manikandan A, Judith Ceicilia AS, Dinesh A, Francisco Nirmala G, Preetha AC, Slimani Y, Almessiere MA, Baykal A, Xavier B (2021) Ceram Int 47:10512
21. Amiri M, Salavati-Niasari M, Akbari A (2019) Adv Colloid Interface Sci 265:29
22. Abdel Maksoud MIA, Ghobashy MM, Kodous AS, Fahim RA, Osman AI, Al-Muhtaseb AH, Rooney DW, Mamdouh MA, Nady N, Ashour AH (2022) Nanotechnol Rev 11, 372
23. Šutka A, Gross KA (2016) Sens Actuators B Chem 222:95
24. Yuan C, Ma J, Zou Y, Li G, Xu H, Sysoev VV, Cheng X, Deng Y (2022) Adv Sci e2203594
25. Cristina de Oliveira R, Pontes Ribeiro RA, Cruvinel GH, Ciola Amoresi RA, Carvalho MH, Aparecido de Oliveira AJ, Carvalho de Oliveira M, Ricardo de Lazaro S, Fernando da Silva L, Catto AC, Simões AZ, Sambrano JR, Longo E (2021) ACS Appl Mater Interfaces 13:4605
26. Li W, Wu X, Chen J, Gong Y, Han N, Chen Y (2017) Sens Actuators B Chem 253:144
27. Lv L, Cheng P, Wang Y, Xu L, Zhang B, Lv C, Ma J, Zhang Y (2020) Sens Actuators B Chem 320:128384
28. Zhang H, Hu J, Li M, Li Z, Yuan Y, Yang X, Guo L (2021) Sens Actuators B Chem 349:130734
29. Bag A, Kumar M, Moon D-B, Hanif A, Sultan MJ, Yoon DH, Lee N-E (2021) Sens Actuators B Chem 346:130463
30. Wu K, Luo Y, Li Y, Zhang C (2019) Beilstein J Nanotechnol 10:2516
31. Park K-R, Kim RN, Song Y, Kwon J, Choi H (2022) Materials (Basel) 15:399
32. Zhang H, Gao S, Feng Z, Sun Z, Yan X, Li Z, Yang X, Pan G, Yuan Y, Guo L (2022) Sens Actuators B Chem 368:132100
33. Al-Enizi AM, Abd-Elkader OH, Shaikh SF, Ubaidullah M, Abdelkader MO, Mostafa NY (2022) Coatings 12:1355
34. Srivastava R, Yadav BC (2012) Int J Green Nanotech 4:141

35. Yadav AK, Singh RK, Singh P (2016) Sens Actuators B Chem 229:25
36. Joshi S, Kamble VB, Kumar M, Umarji AM, Srivastava G (2016) J Alloys Compd 654:460
37. Powar RR, Parale VG, Phadtare VD, Wategaonkar SB, Mane RK, Gunjkar JL, Patil DR, Piste PB, Park H-H, Zambare DN (2021) Mater Today Chem 22:100607
38. Guillén-López ES, López-Urías F, Muñoz-Sandoval E, Courel-Piedrahita M, Sanchez-Tizapa M, Guillén-Bonilla H, Rodríguez-Betancourtt VM, Blanco-Alonso O, Guillén-Bonilla A, Morán-Lázaro JP (2021) Mater Today Commun 26:102138
39. Srinivasamurthy KM, Manjunatha K, El-Denglawey A, Rajaramakrishna R, Kubrin SP, Pasha A, Jagadeesha Angadi V (2022) Mater Chem Phys 275:125222
40. Rezaeipour A, Dehghani S, Hoghoghifard S (2022) IEEE Sens J 22:16464
41. Zhang S, Jiang W, Li Y, Yang X, Sun P, Liu F, Yan X, Gao Y, Liang X, Ma J, Lu G (2019) Sens Actuators B Chem 291:266
42. Kumar A, Kashyap R, Kumar R, Singh R, Prasad B, Kumar M, Kumar D (2022) J Electron Mater 51:4040
43. Kashyap R, Kumar R, Devi S, Kumar M, Tyagi S, Kumar D (2019) Mater Res Express 6:125034
44. Sonwane ND, Kondawar SB (2022) Synth Met 284:117004
45. Qayoom M, Irfan S, Malik GF, Shah KA, Lone MQ, Kumar RTR, Dar GN (2022) J Mater Sci Mater Electron
46. Chaudhuri A, Mandal K, Pati SP, Das D (2018) Mater Res Express 5:065056
47. George J, Abraham KE (2021) J Mater Sci Mater Electron 32:13220
48. Janudin N, Kasim NAM, Feizal Knight V, Norrrahim MNF, Razak MAIA, Abdul Halim N, Mohd Noor SA, Ong KK, Yaacob MH, Ahmad MZ, Yunus WMZW (2022) Polymers 14
49. Zhai C, Zhang H, Du L, Wang D, Xing D, Zhang M (2020) CrystEngComm 22:1286
50. Zou Y, Wang H, Yang R, Lai X, Wan J, Lin G, Liu D (2019) Sens Actuators B Chem 280:227
51. Iqbal B, Laybourn A, ul-Hamid A, Zaheer M (2021) Ceram Int 47:12433
52. Patil SN, Ladgaonkar BP, Pawar AM (2019) Department of Electronics, Tuljaram Chaturchand College, Pune, Maharashtra, India, Department of Electronics, Shankarrao Mohite College, Solapur, Maharashtra, India, and Department of Electronics, Tuljaram Chaturchand College, Pune, Maharashtra, India. I-Manag s J Mater Sci 7:42
53. Tarttelin Hernández P, Kuznetsov MV, Morozov IG, Parkin IP (2019) Mater Sci Eng B Solid State Mater Adv Technol 244:81
54. Manikandan V, Petrila I, Kavita S, Mane RS, Denardin JC, Lundgaard S, Juodkazis S, Vigneselvan S, Chandrasekaran J (2020) J Mater Sci Mater Electron 31:16728
55. Koli PB, Kapadnis KH, Deshpande UG (2019) J Nanostruct Chem 9:95
56. Manikandan V, Mirzaei A, Vigneselvan S, Kavita S, Mane RS, Kim SS, Chandrasekaran J (2019) ACS Omega 4:12919
57. Manikandan V, Kim J-H, Mirzaei A, Kim SS, Vigneselvan S, Singh M, Chandrasekaran J (2019) J Mol Struct 1177:485
58. Mutkule SU, Tehare KK, Gore SK, Gunturu KC, Mane RS (2019) Mater Res Bull 115:150
59. Shedam RM, Kashid PP, Mathad SN, Deshmukh RB, Shedam MR, Gadkari AB (2022) Physics and Chemistry of Solid State 23:626
60. Manikandan V, Sikarwar S, Yadav BC, Mane RS (2018) Sens Actuators A Phys 272:267
61. Manikandan V, Sikarwar S, Yadav BC, Vigneselvan S, Mane RS, Chandrasekaran J (2021) J Exp Nanosci 16:43
62. Ranga R, Kumar A, Kumari P, Singh P, Madaan V, Kumar K (2021) Mater Charact 178:111269
63. Kamble RB, Mathe VL (2008) Sens Actuators B Chem 131:205
64. Sivakumar P, Ramesh R, Ramanand A, Ponnusamy S, Muthamizhchelvan C (2011) Mater Res Bull 46:2204
65. Rao P, Godbole RV, Bhagwat S (2016) Mater Chem Phys 171:260
66. Ranjith Kumar E, Siva Prasada Reddy P, Sarala Devi G, Sathiyaraj S (2016) J Magn Magn Mater 398:281
67. Jiao W-L, Zhang L (2012) Trans Nonferrous Met Soc China 22:1127
68. Manikandan V, Li X, Mane RS, Chandrasekaran J (2018) J Electron Mater 47:3403

69. Pathania A, Thakur P, Trukhanov AV, Trukhanov SV, Panina LV, Lüders U, Thakur A (2019) Results Phys. 15:102531
70. Chaudhari PR, Gaikwad VM, Acharya SA (2022) Ferroelectrics 587:76
71. Cao Y, Jia D, Hu P, Wang R (2013) Ceram Int 39:2989
72. Ni Q, Sun L, Cao E, Hao W, Zhang Y, Ju L (2019) Appl Phys A Mater Sci Process 125
73. Zhang W, Shen Y, Zhang J, Bi H, Zhao S, Zhou P, Han C, Wei D, Cheng N (2019) Appl Surf Sci 470:581
74. Nemufulwi MI, Swart HC, Mhlongo GH (2021) Mater Res Bull 142:111395
75. Zhang C, Wu Q, Zheng B, You J, Luo Y (2018) Ceram Int 44:20700
76. Varpe AS, Deshpande MD (2022) J Alloys Compd 892:162124
77. Li K, Luo Y, Liu B, Gao L, Duan G (2019) J Mater Chem A Mater Energy Sustain 7:5539
78. Kumar ER, Kamzin AS, Janani K (2016) J Magn Magn Mater 417:122
79. Sankaran KJ, Suman S, Sahaw A, Balaji U, Sakthivel R (2021) J Magn Magn Mater 537:168231
80. Durga Prasad P, Hemalatha J (2019) J Magn Magn Mater 484:225
81. Paul J, Philip J (2020) Mater Today 25:148
82. Raut SD, Awasarmol VV, Ghule BG, Shaikh SF, Gore SK, Sharma RP, Pawar PP, Mane RS (2018) Mater Res Express 5:065035
83. Montahaei R, Emamian HR (2022) Ceram Int 48:26629
84. Jabbar R, Sabeeh SH, Hameed AM (2020) J Magn Magn Mater 494:165726
85. Manikandan V, Singh M, Yadav BC, Vigneselvan S (2018) J Electron Mater 47:6366
86. Wang X, Gong L, Zhang D, Fan X, Jin Y, Guo L (2020) Sens Actuators B Chem 322:128615
87. Manikandan V, Singh M, Yadav BC, Denardin JC (2018) J Sci Adv Mater Devices 3:145
88. Mahapatra PL, Das S, Keasberry NA, Ibrahim SB, Saha D (2022) SSRN Electron J
89. Tumberphale UB, Jadhav SS, Raut SD, Shinde PV, Sangle S, Shaikh SF, Al-Enizi AM, Ubaidullah M, Mane RS, Gore SK (2020) Solid State Sci 100:106089
90. Anh LN, Loan TT, Thanh NK, Duong NP, Nguyet DTT, Hong NM (2021) J Nanosci Nanotechnol 21:2641
91. Manikandan V, Singh M, Yadav BC, Mane RS, Vigneselvan S, Mirzaei A, Chandrasekaran J (2020) Mater Chem Phys 240:122265
92. Ranjith Kumar E, Jayaprakash R, Sarala Devi G, Siva Prasada Reddy P (2014) Sens Actuators B Chem 191:186
93. Bagwan AM, Waikar MR, Sonker RK, Chakarvarti SK, Sonkawade RG (2022) Smart nanostructure materials and sensor technology. Springer Nature Singapore, Singapore, pp 285–307
94. Shaikh SF, Ubaidullah M, Mane RS, Al-Enizi AM (2020) Spinel ferrite nanostructures for energy storage devices. Elsevier, pp 51–82
95. Gadkari AB, Shinde TJ, Wali AA, Vasambekar PN (2021) Adv Mater Proc 4:88
96. Ebrahimi HR, Usefi H, Emami H, Amiri GR (2018) IEEE Trans Magn 54:1
97. Chethan B, Ravikiran YT, Vijayakumari SC, Rajprakash HG, Thomas S (2018) Sens Actuators A Phys 280:466
98. Sarrami H, Ebrahimi HR, Emami H (2021) IEEE Trans Magn 57:1
99. Powar RR, Phadtare VD, Parale VG, Pathak S, Sanadi KR, Park H-H, Patil DR, Piste PB, Zambare DN (2020) Mater Sci Eng B Solid State Mater Adv Technol 262:114776
100. Sumangala, Pasquet I, Presmanes L, Thimont Y, Bonningue C, Venkataramani N, Prasad S, Baco-Carles V, Tailhades P, Barnabé A (2018) Ceram Int 44:18578
101. Patil JY, Nadargi DY, Mulla IS, Suryavanshi SS (2019) Heliyon 5:e01489
102. George J, Abraham (2021) Physica B Condens Matter 610:412958
103. Gumbi SW, Mkwae PS, Kortidis I, Kroon RE, Swart HC, Moyo T, Nkosi SS, Appl ACS (2020) Mater Interfaces 12:43231
104. Zhang R, Wang Y, Zhang Z, Cao J (2018) ChemistrySelect 3:12269
105. Mkwae PS, Kortidis I, Kroon RE, Leshabane N, Jozela M, Swart HC, Nkosi SS (2020) J Mater Res Technol 9:16252
106. Sandu I, Presmanes L, Alphonse P, Tailhades P (2006) Thin Solid Films 495:130

107. Akhlaghi N, Najafpour-Darzi G (2021) J Ind Eng Chem 103:292
108. Deivatamil J, Abel N, Dyana T, Prince J (2021) Solid State Commun 339:114500
109. Deivatamil JA, Mark M, Raghavan T, Jesuraj JP (2021) Inorg Chem Commun 123:108355
110. Nagarajan V, Thayumanavan A, Chandiramouli R (2018) J Inorg Organomet Polym Mater 28:121
111. Patil RP, Nikam PN, Patil SB, Talap PD, Patil DR, Hankare PP (2015) Sens Lett 13:785
112. Verma A, Thakur OP, Prakash C, Goel TC, Mendiratta RG (2005) Mater Sci Eng B Solid State Mater Adv Technol 116:1
113. Kotnala RK, Shah J, Singh B, Kishan H, Singh S, Dhawan SK, Sengupta A (2008) Sens Actuators B Chem 129:909
114. Darshane S, Mulla IS (2010) Mater Chem Phys 119:319
115. Kazin AP, Rumyantseva MN, Prusakov VE, Suzdalev IP, Maksimov YV, Imshennik VK, Novochikhin SV, Gaskov AM (2010) Inorg Mater 46:1254
116. Xu Y, Sun D, Hao H, Gao D, Sun Y (2016) RSC Adv 6:98994
117. Liang Y-C, Liu S-L, Hsia H-Y (2015) Nanoscale Res Lett 10:1059
118. Manikandan V, Tudorache F, Petrila I, Mane RS, Kuncser V, Vasile B, Morgan D, Vigneselvan S, Mirzaei A (2019) J Magn Magn Mater 474:563
119. Abdel Maksoud MIA, El-Sayyad GS, Ashour AH, El-Batal AI, Abd-Elmonem MS, Hendawy HAM, Abdel-Khalek EK, Labib S, Abdeltwab E, El-Okr MM (2018) Mater Sci Eng C Mater Biol Appl 92:644
120. Khandekar MS, Tarwal NL, Patil JY, Shaikh FI, Mulla IS, Suryavanshi SS (2013) Ceram Int 39:5901
121. Gedam NN, Padole PR, Rithe SK, Chaudhari GN (2009) J Solgel Sci Technol 50:296
122. Gadkari AB, Shinde TJ, Vasambekar PN (2015) AIP Publishing LLC
123. Kotresh S, Ravikiran YT, Tiwari SK, Vijaya Kumari SC (2017) J Electron Mater 46:5240
124. Rezlescu N, Doroftei C, Popa PD (2007) Rom J Phys 52:353
125. Liu X, Xu Z, Shen Y (1997) Yunnan University Natural Sciences
126. Zhang P, Qin H, Lv W, Zhang H, Hu J (2017) Sens Actuators B Chem 246:9
127. Chapelle A, Oudrhiri-Hassani F, Presmanes L, Barnabé A, Tailhades P (2010) Appl Surf Sci 256:4715
128. Yu L, Cao S, Liu Y, Wang J, Jing C, Zhang J (2006) J Magn Magn Mater 301:100
129. Singh S, Yadav BC, Gupta VD, Dwivedi PK (2012) Mater Res Bull 47:3538
130. Tao S, Gao F, Liu X, Toft Sørensen O (2000) Mater Sci Eng B Solid State Mater Adv Technol 77:172
131. Fazio E, Spadaro S, Corsaro C, Neri G, Leonardi SG, Neri F, Lavanya N, Sekar C, Donato N, Neri G (2021) Sensors (Basel) 21:2494
132. Mangalaraja RV, Ananthakmar S, Manohar P, Gnanam FD, Awano M (2004) Mater Sci Eng A. Struct Mater 367:301
133. Costa ACFM, Morelli MR, Kiminami RHGA (2001) J Mater Synth Process 9:347
134. Valenzuela R, Fuentes MC, Parra C, Baeza J, Duran N, Sharma SK, Knobel M, Freer J (2009) J Alloys Compd 488:227
135. Junliang L, Wei Z, Cuijing G, Yanwei Z (2009) J Alloys Compd 479:863
136. Thakur P, Sharma R, Kumar M, Katyal SC, Negi NS, Thakur N, Sharma V, Sharma P (2016) Mater Res Express 3:075001
137. Satyanarayana L, Madhusudan Reddy K, Manorama SV (2003) Sens Actuators B Chem 89:62
138. Dey A (2018) Mater Sci Eng B Solid State Mater Adv Technol 229:206
139. Issa B, Obaidat IM, Albiss BA, Haik Y (2013) Int J Mol Sci 14:21266
140. Kapse VD (2015) Res J Pharm Biol Chem Sci
141. Jones FW (1938) Proc R Soc Lond 166:16
142. Yamazoe N (1991) Sens Actuators B Chem 5:7
143. Wang X-F, Ma W, Jiang F, Cao E-S, Sun K-M, Cheng L, Song X-Z (2018) Chem Eng J 338:504
144. Rathore D, Mitra S (2016) AIP Conf. Proc. 1728:020166
145. Xue H, Li Z, Wang X, Fu X (2007) Mater Lett 61:347

146. Godbole R, Rao P, Bhagwat S (2017) Mater Res Express 4:025032
147. Chapelle A, Yaacob MH, Pasquet I, Presmanes L, Barnabé A, Tailhades P, Plessis JD, Kalantar-zadeh K (2011) Sens Actuators B Chem 153:117
148. Bharti DC, Mukherjee K, Majumder SB (2010) Mater Chem Phys 120:509
149. Mukherjee K, Majumder SB (2010) Electrochem Solid State Lett 13:J25
150. Singh S, Singh A, Yadav RR, Tandon P (2014) Mater Lett 131:31
151. Park CO, Akbar SA (2003) J Mater Sci 38:4611
152. Mukherjee K, Majumder SB (2010) Talanta 81:1826
153. Gadkari AB, Shinde TJ, Vasambekar PN (2013) Sens Actuators B Chem 178:34
154. Petrila I, Tudorache F (2013) Mater Lett 108:129
155. Zafar Q, Azmer MI, Al-Sehemi AG, Al-Assiri MS, Kalam A, Sulaiman K (2016) J Nanopart Res 18:12
156. Chavan P, Naik LR (2018) Sens Actuators B Chem 272:28
157. Patil SN, Pawar AM, Tilekar SK, Ladgaonkar BP (2016) Sens Actuators A Phys 244:35
158. Shunmuga Priya R, Chaudhary P, Ranjith Kumar E, Balamurugan A, Srinivas C, Prasad G, Yadav BC, Sastry DL (2021) Ceram Int 47:15995
159. Jeseentharani V, George M, Jeyaraj B, Dayalan A, Nagaraja KS (2013) J Exp Nanosci 8:358
160. Rana A, Thakur OP, Kumar V, Pant RP, Singh B (2014) Sens Lett 12:1378
161. Hiremath VG, Yahia IS, Zahran HY, Chethan B, Malimath GH, Ravikiran YT, Angadi VJ (2022) J Mater Sci: Mater Electron 33:11591
162. Ateia MA, Ateia EE, Mosry M, Arman MM (2022) Appl Phys A Mater Sci Process 128:884
163. Rao P, Chikate RC, Bhagwat S (2016) New J Chem 40:1720
164. Nitika, Rana A, Kumar V (2021) Appl Phys A Mater Sci Process 127:609
165. Tajik S, Ahmadi SA, Askari MB, Beitollahi H (2022) J Iran Chem Soc 19:3127
166. Gunasekaran V, Presmanes L, Sinnarasa I, Thimont Y, Cam Dinh TM, Barnabe A, Thailhades P, Menini P (2019) 2019 5th experiment international conference (Exp.at'19). IEEE
167. Nemufulwi MI, Swart HC, Mdlalose WB, Mhlongo GH (2020) Appl Surf Sci 508:144863
168. Rahman MM, Khan SB, Faisal M, Asiri AM, Alamry KA (2012) Sens Actuators B Chem 171–172:932
169. Al-Heniti SH, Umar A, Zaki HM, Dar GN, Al-Ghamdi AA, Kim SH (2014) J Nanosci Nanotechnol 14:3765
170. Katowah DF, Hussein MA, Alam MM, Gabal MA, Sobahi TR, Asiri AM, Uddin J, Rahman MM (2019) ChemistrySelect 4:10609
171. Min C, Shao H, Liong M, Yoon T-J, Weissleder R, Lee H (2012) ACS Nano 6:6821
172. Li F, Kosel J (2014) Biosens Bioelectron 59:145
173. Markevicius V, Navikas D, Miklusis D, Andriukaitis D, Valinevicius A, Zilys M, Cepenas M (2020) Sensors (Basel) 20:3541
174. Bamrungsap S, Shukoor MI, Chen T, Sefah K, Tan W (2011) Anal Chem 83:7795
175. Cai S, Liang G, Zhang P, Chen H, Zhang S, Liu B, Kong J (2011) Analyst 136:201
176. Engelmann UM, Pourshahidi AM, Shalaby A, Krause H-J (2022) J Magn Magn Mater 563:169965
177. Koh I, Josephson L (2009) Sensors 9:8130
178. Lee J-H, Huh Y-M, Jun Y-W, Seo J-W, Jang J-T, Song H-T, Kim S, Cho E-J, Yoon H-G, Suh J-S, Cheon J (2007) Nat Med 13:95
179. Koh I, Hong R, Weissleder R, Josephson L (2008) Angew Chem Int Ed Engl 47:4119
180. Chemla YR, Grossman HL, Poon Y, McDermott R, Stevens R, Alper MD, Clarke J (2000) Proc Natl Acad Sci U S A 97:14268
181. Srinivasan B, Li Y, Jing Y, Xu Y, Yao X, Xing C, Wang J-P (2009) Angew Chem Int Ed Engl 48:2764
182. Strömberg M, Göransson J, Gunnarsson K, Nilsson M, Svedlindh P, Strømme M (2008) Nano Lett 8:816
183. Monunith A, Rajan S, Sahu NK (2020) Mater Res Express 7:094001
184. Sakthivel K, Mani G, Chen S-M, Lin S-H, Muthumariappan A, Mani V (2018) J. Electroanal Chem (Lausanne Switz) 820:161

185. Sarala E, Vinuth M, Naik MM, Reddy YVR (2022) J Hazard Mater Adv 8:100150
186. Zhou T, Cao S, Sui N, Tu J, Zhang T (2021) Sens Actuators B Chem 344:130152
187. El-Wekil MM, Abdelhady KK, Abdel Salam RA, Hadad GM, Ali R (2019) Microchem J 147:1133
188. Hasanpour F, Taei M, Fouladgar M (2018) Russian J. Electrochem 54:70
189. Osman NSE, Thapliyal N, Alwan WS, Karpoormath R, Moyo T (2015) J Mater Sci Mater Electron 26:5097
190. Morales J, Silgado-Cortázar DG, Rosero-Martínez JM, Basante-Delgado SF, Mendez-Albores E, Aperador-Chaparro WA, Gómez-Cuaspud JA (2021) ECS Trans 100:117
191. Taei M, Hasanpour F, Salavati H, Mohammadian S (2016) Mikrochim Acta 183:49
192. Basiri F, Taei M (2017) Mikrochim Acta 184:155
193. Ramírez-Torres A, Rodríguez-Ramos R, Sabina FJ, García-Reimbert C, Penta R, Merodio J, Guinovart-Díaz R, Bravo-Castillero J, Conci A, Preziosi L (2017) J Theor Biol 426:152
194. Rieke V, Butts Pauly K (2008) J Magn Reson Imaging 27:376
195. Alghamdi NA, Hankiewicz JH, Anderson NR, Stupic KF, Camley RE, Przybylski M, Zukrowski J, Celinski Z (2018) Phys Rev Appl 9:054030
196. Winter L, Oberacker E, Paul K, Ji Y, Oezerdem C, Ghadjar P, Thieme A, Budach V, Wust P, Niendorf T (2016) Int J Hyperthermia 32:63
197. Depoorter J, Dewagter C, Dedeene Y, Thomsen C, Stahlberg F, Achten E (1994) J Magn Reson B 103:234
198. Alghamdi N, Stroud J, Przybylski M, Żukrowski J, Cruz Hernandez A, Brown JM, Hankiewicz JH, Celinski Z (2020) J Magn Magn Mater 497:165981
199. de Brito VLO, De Almeida LFA, Hirata AK, da Cunha Migliano AC (2010) Prog Electromagn Res Lett 13:103
200. Hankiewicz JH, Alghamdi N, Hammelev NM, Anderson NR, Camley RE, Stupic K, Przybylski M, Zukrowski J, Celinski ZJ (2017) AIP Adv 7:056703
201. Hankiewicz JH, Stoll JA, Stroud J, Davidson J, Livesey KL, Tvrdy K, Roshko A, Russek SE, Stupic K, Bilski P, Camley RE, Celinski ZJ (2019) J Magn Magn Mater 469:550
202. Smit J, Wijn HPJ (1959) Eindhoven, The Netherlands
203. Chikazumi S, Graham CD (1997) Physics of ferromagnetism. Oxford University Press
204. Hamad MA, Hemeda OM, Alamri HR, Mohamed AM (2021) Phys Lett A 394:127204
205. Gupta S, Suresh KG (2015) J Alloys Compd 618:562
206. Luborsky FE, Livingston JD, Chin† GY (1996) Physical metallurgy. Elsevier, pp 2501–2565
207. Rao GSN, Kumar SA, Rao KH, Rao BP, Gupta A, Caltun O, Dumitru I, Kim C (2007) 2007 2nd IEEE international conference on nano/micro engineered and molecular systems. IEEE
208. Murayama R, Akizuki Y (2022) Sens Actuators A Phys 333:113294
209. Siva KV, Kumar A, Chelvane JA, Arockiarajan A (2022) Mater Sci Eng B Solid State Mater Adv Technol 284:115885
210. Paulsen JA, Ring AP, Lo CCH, Snyder JE, Jiles DC (2005) J Appl Phys 97:044502
211. Song S-H (2007) Magnetic and magnetoelastic properties of M-substituted cobalt ferrites (M=Mn, Cr, Ga, Ge). Office of Scientific and Technical Information (OSTI)
212. Nlebedim IC, Ranvah N, Melikhov Y, Williams PI, Snyder JE, Moses AJ, Jiles DC (2009) IEEE Trans Magn 45:4120
213. Khaja Mohaideen K, Joy PA (2013) Curr Appl Phys 13:1697
214. Felser C, Fecher GH, Balke B (2007) Angew Chem Int Ed Engl 46:668
215. Liang S, Sutham P, Wu K, Mallikarjunan K, Wang J-P (2022) Sensors (Basel) 22:5563
216. Zhao W, Tao X, Ye C, Tao Y (2022) Sensors (Basel) 22:1021
217. Thomson W (1857) Proc R Soc Lond 8:546
218. Baibich MN, Broto JM, Fert A, Nguyen Van Dau F, Petroff F, Etienne P, Creuzet G, Friederich A, Chazelas J (1988) Phys Rev Lett 61:2472
219. Djamal M, Ramli R (2017) Magnetic sensors—development trends and applications. InTech
220. Moodera JS, Nassar J, Mathon G (1999) Annu Rev Mater Sci 29:381
221. Prathipkumar S, Hemalatha J (2020) Ceram Int 46:258

222. Wang Y-H (2010) Nanocrystals and thin films of oxide and chalcogenide spinels for spintronic applications. The University of Alabama
223. Kim SJ, Lee S-W, Song JD, Kwon Y-W, Lee K-J, Koo HC (2018) Sens Actuators B Chem 255:2894
224. Sun X, Zhi S, Lei C, Zhou Y (2016) Biomed Microdevices 18:60
225. Chen L, Bao C-C, Yang H, Li D, Lei C, Wang T, Hu H-Y, He M, Zhou Y, Cui D-X (2011) Biosens Bioelectron 26:3246
226. Liu N, Wang S, Wang J, Lv J, Cheng Q, Ma W, Lu Y (2022) IEEE Sens J 22:13529
227. Kotnala RK, Shah J (2015) Handbook of magnetic materials. Elsevier, pp 291–379
228. Ren C, Bayin Q, Feng S, Fu Y, Ma X, Guo J (2020) Biosens Bioelectron 165:112340
229. Thejas R, Soundarya TL, Nagaraju G, Swaroop K, Prashantha SC, Veena M, Melagiriyappa E, Naveen CS (2022) Materials Letters: X 15:100156
230. Ahmad U, Afzia M, Shah F, Ismail B, Rahim A, Khan RA (2022) Mater Sci Semicond Process 148:106830
231. Bao Y, Wen T, Samia ACS, Khandhar A, Krishnan KM (2016) J Mater Sci 51:513
232. Wang J, Wu X, Wang C, Rong Z, Ding H, Li H, Li S, Shao N, Dong P, Xiao R, Wang S, Appl ACS (2016) Mater Interfaces 8:19958
233. Lai H, Xu F, Wang L (2018) J Mater Sci 53:8677
234. Corma A (1997) Chem Rev 97:2373
235. Fan X, White IM, Shopova SI, Zhu H, Suter JD, Sun Y (2008) Anal Chim Acta 620:8
236. Liu X, Hu Y, Zheng S, Liu Y, He Z, Luo F (2016) Sens Actuators B Chem 230:191
237. Üzek R, Sari E, Merkoçi A (2019) Magnetochemistry 5:59
238. Mohammed L, Gomaa HG, Ragab D, Zhu J (2017) Particuology 30:1
239. Kumar S, Kumar P, Shakher Pathak C (ed) (2021) Silver micro-nanoparticles—properties, synthesis, characterization, and applications. IntechOpen
240. Rocha-Santos TAP (2014) Trends. Analyt Chem 62:28
241. Francis R, Joy N, Aparna EP, Vijayan R (2014) Polym Rev (Phila. Pa) 54:268
242. Mahmoudi M, Sant S, Wang B, Laurent S, Sen T (2011) Adv Drug Deliv Rev 63:24
243. Sharifabad ME, Mercer T, Sen T (2015) J Appl Phys 117:17D139
244. Coulet PR, Blum LJ (2019) Biosensor principles and applications. CRC Press
245. Suvarnaphaet P, Pechprasarn S (2017) Sensors (Basel) 17:2161
246. Seo D, Han E, Kumar S, Jeon E, Nam M-H, Jun HS, Seo S (2022) Biosensors 12:47
247. Kumar S, Seo S (2023) Biosensors 13:385
248. Tereshchenko A, Bechelany M, Viter R, Khranovskyy V, Smyntyna V, Starodub N, Yakimova R (2016) Sens Actuators B Chem 229:664
249. Gahlaut SK, Pathak A, Gupta BD, Singh JP (2022) Biosens Bioelectron 196:113720
250. Kumar S, Gahlaut SK, Singh JP (2022) Appl Surface Sci Adv 12:100322
251. Kumar S, Namura K, Suzuki M (2019) Proc SPIE 10894:1089414
252. Kumar S, Fukuoka T, Takahashi R, Yoshida M, Utsumi Y, Yamaguchi A, Namura K, Suzuki M (2021) Mater Lett 286:129106
253. Kumar S, Kanagawa M, Namura K, Fukuoka T, Suzuki M (2023) Appl Nanosci 13:155–163
254. Kumar S, Goel P, Singh DP, Singh JP (2014) Appl Phys Lett 104:023107
255. Lakowicz JR, Ray K, Chowdhury M, Szmacinski H, Fu Y, Zhang J, Nowaczyk K (2008) Analyst 133:1308
256. Yadav S, Senapati S, Kumar S, Gahlaut SK, Singh JP (2022) Biosensors (Basel) 12:1115
257. Kumar S, Tokunaga K, Namura K, Fukuoka T, Suzuki M (2020) J Phys Chem C Nanomater Interfaces 124:21215
258. Maier SA (n.d.) Plasmonics: fundamentals and applications. Springer
259. Flory F, Escoubas L, Le Rouzo J, Berginc G (2018) Europhys News 49:18
260. Vladimir Bochenkov ABAPN, Baumberg J, Noginov M, Benz F, Aldewachi H, Schmid S, Podolskiy V, Aizpurua J, Lin K, Ebbesen T, Kornyshev AA, Hutchison J, Matczyszyn K, Kumar S, de Nijs Franci B (2015) Faraday Discuss 178:435
261. Song G, Zhang W (2017) Plasmonics 12:179
262. Liz-Marzán LM, Murphy CJ, Wang J (2014) Chem Soc Rev 43:3820

263. Kumar S, Kumar P, Das A, Shakher Pathak C (2020) Recent advances in nanophotonics—fundamentals and applications. IntechOpen
264. Tang S, Li Y, Huang H, Li P, Guo Z, Luo Q, Wang Z, Chu PK, Li J, Yu X-F, Appl ACS (2017) Mater Interfaces 9:7472
265. Gosu R, Zaheer SM (2021) In: Zaheer SM, Gosu R (eds) Methods for fragments screening using surface plasmon resonance. Springer, Singapore, pp 1–4
266. Ritchie R, Arakawa E, Cowan J, Hamm R (1968) Phys Rev Lett 21:1530
267. Liedberg B, Nylander C, Lundström I (1983) Sens. Actuators 4:299
268. Gunasekaran S, Paulsen MR, Shove GC (1985) J Agric Eng Res 32:209
269. Hiller B, McDaniel JC, Rea EC Jr, Hanson RK (1983) Opt Lett 8:474
270. Nguyen HH, Park J, Kang S, Kim M (2015) Sensors 15:10481
271. Yang D, Ma J, Peng M, Zhang Q, Luo Y, Hui W, Jin T, Cui Y (2013) J Nanosci Nanotechnol 13:5485
272. Lee KS, Lee M, Byun KM, Lee IS (2011) J Mater Chem 21:5156
273. Li S, Wu Q, Ma P, Zhang Y, Song D, Wang X, Sun Y (2018) Talanta 180:156
274. (2016) The concise handbook of analytical spectroscopy: theory, applications, and reference materials. World Scientific, pp 1–55
275. Reich G (2005) Adv Drug Deliv Rev 57:1109
276. Sakudo A (2016) Clin Chim Acta 455:181
277. Roggo Y, Chalus P, Maurer L, Lema-Martinez C, Edmond A, Jent N (2007) J Pharm Biomed Anal 44:683
278. Büning-Pfaue H (2003) Food Chem 82:107
279. Chen M, Blumen HM, Izzetoglu M, Holtzer R (2017) J Neuroimaging 27:453
280. Fantini S (2014) Biomedical optics 2014. OSA, Washington, D.C.
281. Jernelv IL, Milenko K, Fuglerud SS, Hjelme DR, Ellingsen R, Aksnes A (2019) Appl Spectrosc Rev 54:543
282. Al-Nabulsi J, Abu Owida H, Ma'touq J, Matar S, Al-Aazeh E, Al-Maaiouf E, Bleibel A (2022) Bull Electr Eng Inform 11:1926
283. Zhou H, Hou X, Liu Y, Zhao T, Shang Q, Tang J, Liu J, Wang Y, Wu Q, Luo Z, Wang H, Chen C, Appl ACS (2016) Mater Interfaces 8:4424
284. Yang H-M, Park CW, Park S, Kim J-D (2018) Colloids Surf B Biointerfaces 161:183
285. Wu H, Cheng K, He Y, Li Z, Su H, Zhang X, Sun Y, Shi W, Ge D, Biomater ACS (2019) Sci Eng 5:1045
286. Huang P, Li Z, Lin J, Yang D, Gao G, Xu C, Bao L, Zhang C, Wang K, Song H, Hu H, Cui D (2011) Biomaterials 32:3447
287. Cho S-H, Kim A, Shin W, Heo MB, Noh HJ, Hong KS, Cho J-H, Lim YT (2017) Int J Nanomed 12:2607
288. Wang C, Irudayaraj J (2010) Small 6:283
289. Stafford S, Serrano Garcia R, Gun'ko Y (2018) Appl Sci (Basel) 8:97
290. Mikoliunaite L, Talaikis M, Michalowska A, Dobilas J, Stankevic V, Kudelski A, Niaura G (2022) Nanomaterials (Basel) 12:2860
291. Namura K, Hanai S, Kondo S, Kumar S, Suzuki M (2022) Adv Mater Interfaces 9:2200200
292. Lee H, Choi H, Lee M, Park S (2018) Biomed Microdevices 20:103
293. Ruan J, Ji J, Song H, Qian Q, Wang K, Wang C, Cui D (2012) Nanoscale Res Lett 7:309
294. Icten O, Kose DA, Matissek SJ, Misurelli JA, Elsawa SF, Hosmane NS, Zumreoglu-Karan B (2018) Mater. Sci Eng C Mater Biol Appl 92:317
295. Singh DP, Kumar S, Singh JP (2015) RSC Adv
296. Chen O, Riedemann L, Etoc F, Herrmann H, Coppey M, Barch M, Farrar CT, Zhao J, Bruns OT, Wei H, Guo P, Cui J, Jensen R, Chen Y, Harris DK, Cordero JM, Wang Z, Jasanoff A, Fukumura D, Reimer R, Dahan M, Jain RK, Bawendi MG (2014) Nat Commun 5:5093
297. Kim S-K, Sung H, Hwang S-H, Kim M-N (2022) Biochip J 16:175
298. Myeong S, Chon B, Kumar S, Son H-J, Kang SO, Seo S (2022) Nanoscale Adv. 4:1080
299. Zheng J, Nie Y, Hu Y, Li J, Li Y, Jiang Y, Yang R (2013) Chem Commun (Camb) 49:6915
300. Jin M, Liu X, van den Berg A, Zhou G, Shui L (2016) Nanotechnology 27:335102

301. Wan Y, Sun Y, Qi P, Wang P, Zhang D (2014) Biosens Bioelectron 55:289
302. Liu C-H, Sahoo SL, Tsao M-H (2014) Colloids Surf B Biointerfaces 115:150
303. Kim S, Ko J, Lim HB (2013) Anal Chim Acta 771:37
304. Zarei-Ghobadi M, Mozhgani S-H, Dashtestani F, Yadegari A, Hakimian F, Norouzi M, Ghourchian H (2018) Sci Rep 8:15593
305. Niazi S, Wang X, Pasha I, Khan IM, Zhao S, Shoaib M, Wu S, Wang Z (2018) Talanta 186:97
306. Yu X, Wen C-Y, Zhang Z-L, Pang D-W (2014) RSC Adv 4:17660
307. Xie H-Y, Zuo C, Liu Y, Zhang Z-L, Pang D-W, Li X-L, Gong J-P, Dickinson C, Zhou W (2005) Small 1:506
308. Kumar S, Goel P, Singh JP (2017) Sens Actuators B Chem 241:577
309. Kumar S, Lodhi DK, Singh JP (2016) RSC Adv 6:45120
310. Wang C, Wang C, Wang X, Wang K, Zhu Y, Rong Z, Wang W, Xiao R, Wang S, Appl ACS (2019) Mater Interfaces 11:19495
311. Sun Y, Xu L, Zhang F, Song Z, Hu Y, Ji Y, Shen J, Li B, Lu H, Yang H (2017) Biosens Bioelectron 89:906
312. Kumar S, Doi Y, Namura K, Suzuki M (2020) ACS applied bio materials 3:3226
313. Pathak CS, Kumar S (ed) (2022) Recent developments in atomic force microscopy and Raman spectroscopy for materials characterization. IntechOpen, London, UK
314. Campion A, Kambhampati P (1998) Chem Soc Rev 27:241
315. Stiles PL, Dieringer JA, Shah NC, Van Duyne RP (2008) Annu Rev Anal Chem 1:601
316. Kumar S, Namura K, Kumaki D, Tokito S, Suzuki M (2020) Results Mater 8:100139
317. Cheng H-W, Luo J, Zhong C-J (2015) Front Chem Sci Eng 9:428
318. Büchner T, Drescher D, Merk V, Traub H, Guttmann P, Werner S, Jakubowski N, Schneider G, Kneipp J (2016) Analyst 141:5096
319. Sun X, Li H (2016) Curr Nanosci 12:175
320. Kumar S, Taneichi T, Fukuoka T, Namura K, Suzuki M (2021) Cellulose 28:10803
321. Kumar S, Goel P, Singh DP, Singh JP (2014) AIP Conf Proc 1591:872
322. Rajput A, Kumar S, Singh JP (2017) Analyst 142:3959
323. Kumar S, Lodhi DK, Goel P, Neeti, Mishra P, Singh JP (2015) Chem Commun 51:12411
324. Goel P, Kumar S, Sarkar J, Singh JP, Appl ACS (2015) Mater Interfaces 7:8419
325. Kadir M, Nemkayeva R, Baigarinova G, Alpysbayeva B, Assembayeva A, Smirnov V (2023) Physica E Low Dimens Syst Nanostruct 145:115499
326. Xing T, Qian Q, Ye H, Wang Z, Jin Y, Zhang N, Wang M, Zhou Y, Gao X, Wu L (2022) Biosens Bioelectron 212:114430
327. Materón EM, Miyazaki CM, Carr O, Joshi N, Picciani PHS, Dalmaschio CJ, Davis F, Shimizu FM (2021) Appl Surface Sci Adv 6:100163
328. Weller D, Moser A (1999) IEEE Trans Magn 35:4423
329. Baghayeri M, Nazarzadeh Zare E, Mansour Lakouraj M (2014) Biosens Bioelectron 55:259
330. Zengin A, Tamer U, Caykara T (2013) Biomacromol 14:3001
331. Pang Y, Wang C, Wang J, Sun Z, Xiao R, Wang S (2016) Biosens Bioelectron 79:574

Chapter 10
Ferrite Nanoparticles for Energy Storage Applications

Samta Manori, Ashok Manori, and Ravi Kumar Shukla

1 Introduction

A rapid rise in the global population, scarcity of fossil fuels and increasing rate of ecological pollution is leading us towards the high demand for utilization of eco-friendly and sustainable energy resources. Supercapacitors, batteries and fuel cells are among the major energy storage devices. These energy storage devices must possess high power density, fast charge/discharge rates and long cycle life [1]. Ferrite nanoparticles (FNPs) are a member of a wide group of magnetic nanoparticles which have attracted the interests of researchers across the globe owing to their numerous applications in different areas such as biomedical, waste-water treatment, catalytic and energy storage devices. FNPs are basically metal oxides consisting of spinel structure having general formula AB_2O_4, with A as divalent and B as trivalent metallic cations located at two separate crystallographic positions. The tetrahedral site is occupied by A while B occupies octahedral site [2]. These A and B cations are coordinated to oxygen atoms tetrahedrally and octahedrally, respectively. Ferrites must have at least iron (III) in their chemical formula. $MnFe_2O_4$, where M = Mn, Co, Ni, Cu and Zn, are some of the examples of ferrites. Most of the ferrites show superparamagnetic (SPM) behaviour with size less than or nearly equal to 20 nm. A single unit cell of ferrite consists of 64 tetrahedral and 32 octahedral sites for cations [3, 4]. Distribution of metallic cations over these sites depends upon the affinity of the cations towards these positions. This further depends upon various factors like stabilization energy, ionic radii, size of interstices and synthesis conditions and

S. Manori (✉) · R. K. Shukla
Advanced Functional Smart Materials Laboratory, Department of Physics, School of Physical Sciences, DIT University, Dehradun, Uttarakhand 248009, India
e-mail: samta.manori@gmail.com

A. Manori
Department of Electrical Engineering, Women Institute of Technology, Dehradun, Uttarakhand 248009, India

P. Sharma et al. (eds.), *Engineered Ferrites and Their Applications*, Materials Horizons: From Nature to Nanomaterials, https://doi.org/10.1007/978-981-99-2583-4_10

methods employed [5]. The distribution of cations greatly influences the magnetic properties of ferrites. The net magnetic moment of FNPs is the difference between the electron spins which are parallel within each lattice site and anti-parallel between two sub-lattice sites [6, 7]. The saturation magnetization values of FNPs having same size and composition may thus vary if there exists any difference in distribution of cations over both the sites. Depending upon the distribution of cations, three different types of spinel structures can exist: normal, inverse and mixed. If we represent a ferrite with general formula given by $\left(M_{1-x}^{2+}\right)\left(Fe_{x}^{3+}\right)\left[M_{x}^{2+}Fe_{2-x}^{3+}\right]O_4$, where x is the degree of inversion, B sites are occupied by ions which are inside the square brackets and A sites are occupied by ions that are outside the square brackets. Here, the value of x decides the type of spinel structure. For normal spinel structure, $x = 0$; for mixed spinel structure, $0 < x < 1$ and for inverse spinel structure, $x = 1$ [8]. $ZnFe_2O_4$ is a normal spinel ferrite, while common examples of inverse spinel ferrites are Fe_3O_4 and $NiFe_2O_4$. $MnFe_2O_4$ ($Mn_{0.8}Fe_{0.2}$ $[Mn_{0.2}Fe_{1.8}]O_4$) is a mixed spinel ferrite. Irrespective of their type, FNPs must acquire different properties for different applications. For applications in the biomedical field, the FNPs should show SPM behaviour at room temperature [9]. The FNPs must show remarkable reactivity, high capacity for adsorption and optimum saturation magnetization values to ease the removal of pollutants from water and waste water by external magnetic field [10].

For energy storage applications, various ferrites have been explored. Among various spinel ferrites, Co and Ni ferrites are environment friendly, cost-effective and show large magneto crystalline anisotropy and chemical stability and superior electrochemical performance for supercapacitor [11]. Supercapacitors are categorized as pseudo-, electric double layer-, and hybrid capacitors based on mechanisms used for storing the charge. In case of electric double layer capacitors (EDLC), the electric energy storage occurs at the interface of electrode and electrolyte, and hence, their specific capacitance depends on the surface area of the electrode [12]. The reversible faradic reactions taking place between electrode and electrolyte are the main source of electric energy storage in pseudo-capacitors [13]. In EDLC, the electrodes are made up of carbon-based materials like graphene, carbon nanotubes, etc., because of their high electrical conductivity and surface area. The limitation with carbon-based materials is their low specific capacitance value for which they avoided for any practical application [14]. In pseudo-capacitors, the electrodes are made with conducting polymers and metal oxides which again face the problem of poor electrical conductivity and cycle stabilities, thus preventing their applications for energy storage [15, 16]. To overcome these limitations, hybrid supercapacitors are made with electrode materials consisting of carbon-active and metal oxides composites [17]. In case of hybrid supercapacitors, the energy storage occurs due to two processes: redox reactions that are fast and reversible and ion adsorption/desorption taking place at the interface of electrode and electrolyte [18]. Spinel ferrites have proved as promising materials for applications in supercapacitors due to their improved and exceptional electrochemical activity in comparison to single metal oxides.

2 Ferrites for Energy Storage

2.1 Cobalt Ferrite ($CoFe_2O_4$)

Cobalt ferrite possesses remarkable magnetic, mechanical (hardness) as well as chemical (stability) properties, thus making it promising material for applications in magnetic devices [19]. Apart from these properties, it also shows good electrochemical properties as a supercapacitor. Nanoflakes of $CoFe_2O_4$ prepared by chemical bath deposition method have been used as supercapacitors. A stainless steel substrate having thickness ~ 5 to 7 μm was used to deposit these nanoflakes. A three electrode system was used to investigate the electrochemical behaviour of the nanoflakes with 1 M NaOH electrolyte. A specific capacitance of ~ 366 F/g with interfacial capacitance 0.110 F/g was observed at a scan rate of 5 mV/s. After 1000 cycles, these $CoFe_2O_4$ nanoflakes preserved around 90.6% capacitance.

Another study by Pawar et al. have obtained nanoparticles of $CoFe_2O_4$ with average size ~ 20 nm by using sol–gel method [20]. The nanoparticles were studied for supercapacitor applications and found to possess pseudo-capacitor properties with 1 M NaOH as an electrolyte in a three electrode system. The specific capacitance in this case was found to be 15 F/g at a current density 0.6 A/g as determined from the galvanostatic charge discharge method. Poor conductivity of $CoFe_2O_4$ nanoparticles might be responsible for such a lower value of specific capacitance. These electrochemical properties of $CoFe_2O_4$ nanoparticles were improved by synthesis of nanocomposite of $CoFe_2O_4$/FeOOH by one-step hydrothermal process [21]. A mixture of $CoFe_2O_4$/FeOOH nanocomposite, carbon black and polyvinylidene fluoride (PVDF) with 80:10:10 wt% ratio was used as an electrode which showed improved value of capacitance at large values of current thus making them suitable for supercapacitor applications. The structure showed a loss of 8.7% of capacitance after 1000 cycles.

Thin films of mesoporous $CoFe_2O_4$ also showed high value of specific capacitance ~ 370 F/g at scan rate of 2 mV/s in 1 M NaOH [22]. As the scan rate increases to 100 mV/s, the capacitance value is reduced to ~ 170 F/g. The film was prepared using pyrolysis technique with aqueous medium with substrate temperature at ~ 475 °C. The mesoporous film of $CoFe_2O_4$ showed nanosized grains with power density of ~ 30 kW/kg and energy density ~ 27 Wh/kg. Nanoparticles of $CoFe_2O_4$ were synthesized using the methods of hydrothermal and coprecipitation with precursors made up of nitrates, chlorides and acetates, giving average particle size of ~ 11 to 26 nm and surface area ~ 34 m^2/g [23]. These nanoparticles showed large specific capacitance of ~ 430 F/g in 6 M NaOH electrolyte at 0.5 A/g. The nanoparticles showed a remarkable retention of capacitance with ~ 98.8% capacitance after 6000 cycles at current density ~ 10 A/g. Another composite of $CoFe_2O_4$ and reduced graphene oxide (RGO) was studied for supercapacitor applications which showed high specific capacitance of ~ 123 F/g at current density of ~ 5 mA/cm^2. However, the structure showed a loss of ~ 22% capacitance after 1000 cycles [24].

Xiong et al. have synthesized ternary nanocomposites of $CoFe_2O_4$/graphene/polyaniline which were characterized for high performance supercapacitors [25]. Hydrothermal method was used to synthesize the $CoFe_2O_4$ nanoparticles and graphene nanosheets, and after that, in-situ polymerization process was used to coat them with polyaniline. Large value of specific capacitance ~ 1133 F/g was observed for 1 mV/s in 1 M KOH electrolyte. A large capacitance retention of ~ 96% was obtained after 6000 cycles. The reason behind the large capacitance value is that the electron transfer process and surface area of the electrode are enhanced by using graphene nanosheets. Polyaniline gives rise to the pseudocapacitance in $CoFe_2O_4$ nanoparticles.

2.2 *Manganese Ferrite ($MnFe_2O_4$)*

Electrodes made up of $MnFe_2O_4$ show good capacitive properties in aqueous electrolyte as the charge is stored by pseudocapacitance mechanism [1, 26]. Shin-Liang Kuo et al. have synthesized $MnFe_2O_4$ by using coprecipitation method and found that the charge in this case is stored by insertion/extraction mechanism of proton into/from the lattice sites occupied by both the Mn- and Fe-ions [27]. Electrochemical properties were studied by using three electrode systems where $MnFe_2O_4$ powder was mixed with carbon black and PVDF which was further coated on the current collector. Overall specific capacitance of ~ 63 F/g was obtained with $MnFe_2O_4$ electrode giving 115 F/g of specific capacitance. Another study involved the effect of using surfactants with $MnFe_2O_4$ synthesized by solvothermal method on their electrochemical properties [28]. The capacitance values were found to be larger for $MnFe_2O_4$ colloidal nanoclusters as compared to hollow spheres of $MnFe_2O_4$ in aqueous $LiNO_3$ electrolyte. This rise in capacitance value might be due to the reduction in the tension at the interface between electrode and electrolyte introduced by the surfactants which promotes the diffusion of Li ions. Vignesh et al. have studied the capacitor performance of $MnFe_2O_4$ spherical nanoparticles synthesized by coprecipitation method for different electrolytes [29]. A specific capacitance of 173, 31 and 430 F/g was obtained for electrolytes of 3.5 M KOH, 1 M $LiNO_3$ and1 M Li_3PO_4, respectively. The best rate performance was obtained for 3.5 M KOH electrolyte which can retain the capacitance even at higher current densities. Electrochemical properties of colloidal clusters of $MnFe_2O_4$ nanocrystal were studied in configuration of symmetric supercapacitors using various electrolytes in aqueous form [30]. The specific capacitances of $MnFe_2O_4$ electrodes were obtained as 97.1, 93.9, 74.2 and 47.4 F/g for 2 M KOH, 2 M NaOH, 2 M LiOH and 2 M Na_2SO_4 electrolytes, respectively. It was observed that $MnFe_2O_4$ structure showed better retention of capacitance of about 76% for 6 M KOH electrolyte after 2000 cycles.

Nanocomposites of $MnFe_2O_4$ with graphene showed improved super capacitance properties [26, 31]. A maximum supercapacitance of ~ 276 F/g at a scan rate of 10 mV/s with 6 M KOH electrolyte was obtained for RGO/$MnFe_2O_4$ nanocomposites made by one-pot hydrothermal technique [32]. Current collectors made up

of flexible graphite sheets have been used to fabricate flexible supercapacitor of $MnFe_2O_4$/graphene which possessed supercapacitance of 120 F/g at 1 A/g with retention capacitance of 105% after 5000 cycles [26]. A hybrid capacitor made up of $MnFe_2O_4$ and crumpled graphene sheet showed a supercapacitance of 195 F/g at a scan rate of 0.5 A/g with 0.05 M KCL electrolyte [31]. A ternary nanocomposite of $MnFe_2O_4$/graphene/polyaniline prepared by facile two-step approach showed a specific capacitance of 307.2 F/g at 0.1 A/g with retention capacitance 76.4% after 5000 cycles.

2.3 Zinc Ferrite ($ZnFe_2O_4$)

Zinc ferrite is the most commonly used electrode for supercapacitor applications due to various properties like its strong redox behaviour, better chemical stability, non-toxicity and high storage capacity of 2600 F/g [33, 34]. The morphology of $ZnFe_2O_4$ can be easily tuned to get nanoparticles, nanorods and nanoflakes, thus offering a large surface area for storage of charge [35, 36]. Vadiyar et al. used different electrolytes to study the surface wettability and storage capacity for $ZnFe_2O_4$ nanoflakes [37]. The CV curves obtained for this study for all the electrolytes showed pseudo-capacitive behaviour. Thin film of $ZnFe_2O_4$ synthesized by using the method of successive ionic layer adsorption and reaction showed high value of specific capacitance ~ 470 F/g with scan rate of 5 mV/s in an aqueous electrolyte of 1 M NaOH [38]. A power density of 277 W/kg and energy density of 4.47 Wh/kg was obtained with $ZnFe_2O_4$ thin film-based supercapacitors. A binder free thin film of $ZnFe_2O_4$ showed specific capacitance of 615 F/g at a current density of 3 mA/cm^2 [39]. $ZnFe_2O_4$ nanoparticles with average size 20–30 nm were synthesized using combustion method and showed specific capacitance of ~ 1200 F/g at 1 mA/cm^2 [19]. An asymmetric supercapacitor with negative electrode made up of $ZnFe_2O_4$ and positive electrode made up of nickel hydroxide was analysed for electrochemical properties. Nanoflakes of 3D aligned $ZnFe_2O_4$ on a flexible substrate of stainless steel mesh resulted in improved characteristics as an electrode in an asymmetric supercapacitor configuration with $Ni(OH)_2$ [40]. The device gave specific capacitance of ~ 1600 F/g at 1 mA/cm^2 with 97% retention capacity over 8000 cycles.

Microspheres of $ZnFe_2O_4$ prepared by using solvothermal method gave specific capacitance of 131 F/g having retention capacity of 92% after 1000 cycles [41]. Vadiyar et al. have prepared heterostructure electrodes of self-assembled $ZnFe_2O_4$ nanoflakes at $ZnFe_2O_4$/C nanoparticles for application in high performance supercapacitors [36]. The electrode structure showed high specific capacitance of ~ 1800 F/g at 5 mA/cm^2. With heterostructure of $ZnFe_2O_4$ nanoflakes at $ZnFe_2O_4$/C nanoparticles as negative electrode and RGO as positive electrode, a specific capacitance of ~ 350 F/g was obtained. The supercapacitor showed 98% retention capacity after 35,000 cycles. A structure of $ZnFe_2O_4$ nanoparticles dispersed in nitrogen-doped RGO gave a specific capacitance of ~ 240 F/g at 0.5 A/g [35]. The structure retained ~ 80% capacitance after 5000 cycles. Nanorods of $ZnFe_2O_4$ with RGO gave specific

capacitance of ~ 1400 F/g at a scan rate of 10 mV/s for 2 M KOH electrolyte with retention capacitance of 93% after 5000 cycles [42]. The enhanced electrochemical behaviour was ascribed to larger surface area offered by RGO with better electrical conductivity. Thin films of porous $ZnFe_2O_4$ nanoflakes gave large capacitance of ~ 760 F/g at 5 mA/cm^2 with energy and power density of 106 Wh/kg and 18 kW/kg, respectively. The electrode system showed a good retention property of 88% after 5000 cycles.

2.4 Nickel Ferrite ($NiFe_2O_4$)

Nickel ferrite is also one of the promising materials for supercapacitor applications [43, 44]. Large number of studies are done on $NiFe_2O_4$ and its nanocomposites for electrode applications in supercapacitors. Sub-micron sized $NiFe_2O_4$ nanoparticles prepared by molten salt process gave high specific capacitance of ~ 18 F/g at 10 mV/s [45]. Nanospheres of $NiFe_2O_4$ showed specific capacitance of ~ 120 F/g at 8 A/g, and the capacitance was found to increase with KOH concentration [46]. Mesoporous nanoparticles of $NiFe_2O_4$ were synthesized by one-step hydrothermal method with surface area ~ 150 m^2/g and gave specific capacitance of ~ 1000 F/g at 1 A/g using a three electrode system with 2 M KOH electrolyte [47]. However, the structure gave 30% loss in capacitance after 500 cycles. A high specific capacitance of ~ 450 F/g was obtained for $NiFe_2O_4$ prepared by combustion route with better cyclic stability over 1000 charging and dis-charging cycles [48]. Various studies have been done on graphene-based materials which are mixed with $NiFe_2O_4$ to get improved capacitive properties. A specific capacitance of ~ 200 F/g was obtained for $NiFe_2O_4$/graphene nanocomposite in a 1 M Na_2SO_4 electrolyte [49]. Porosity of the electrode improved the electrochemical properties as well as capacitance stability of about 95% over 1000 cycles. Wang et al. have prepared RGO-$NiFe_2O_4$ nanocomposites using hydrothermal method with varying pH values (8, 10, 12 and 14). They have found that nanocomposites synthesized at pH value 10 exhibited the largest surface area (~460 m^2/g) and showed specific capacitance of ~ 220 F/g at 5 mV/s [50].

Nanocomposites of conducting polymers like PANI with $NiFe_2O_4$ were reported by various groups which showed improved electrochemical properties [51]. A high specific capacitance of ~ 450 F/g was obtained for PANI/$NiFe_2O_4$ nanocomposites with 80% retention capacitance over 1000 cycles. Another study on $NiFe_2O_4$ composites with multiwalled carbon nanotubes (MWCNTs) prepared by one-pot hydrothermal method using hexamethylene tetramine (HMT) have observed a high specific capacitance of ~ 1290 F/g at 1 A/g [44]. The electrode showed capacitive retention of 80% over 500 cycles in 2 M KOH. $NiFe_2O_4$ nanoparticles deposited on a flexible carbon cloth using hydrothermal method showed high specific capacitance of ~ 1130 F/g for 1 M H_2SO_4 and ~ 920 F/g for 6 M KOH electrolytes [52]. The conductive 3D network of carbon cloth and the large surface area of the nanoparticles contributed towards the high capacitance value. A binder free electrode made from

$NiFe_2O_4$ nanocone forests on a carbon cloth showed a high specific capacitance of 697 F/g at scan rate of 5 mV/s [53]. An $NiFe_2O_4$ on carbon cloth-based nanocomposite designed as a solid state supercapacitor showed large specific capacitance of 584 F/g at 5 mV/s as well as good cyclic stability of 93.57% capacitive retention after 1000 cycles. Thus, the device can be used as a promising material for supercapacitor applications. In the case of $NiFe_2O_4$, the capacitive performance is found to be highly dependent on the synthesis method. $NiFe_2O_4$ synthesized by sol–gel method gave high specific capacitance of 97 F/g which could be due to small grain size and pores obtained from sol–gel method.

Nanocomposites of 1D $NiFe_2O_4$ and graphene synthesized using hydrothermal method gave a specific capacitance of ~ 480 F/g at 0.1 A/g [54]. The electrode showed improved cyclic stability of only 1% degradation after 10,000 cycles as compared to $NiFe_2O_4$ electrode, which showed 40% loss in capacitance. Conducting network of graphene and large number of redox active sites can be responsible for excellent electrochemical properties of $NiFe_2O_4$/graphene nanocomposites. Ternary nanocomposites of nitrogen doped graphene/$NiFe_2O_4$/polyaniline gave specific capacitance of ~ 650 F/g at 1 mV/s [55]. The retention capacity of the system was found to be 90% for over 10,000 cycles with energy and power density of ~ 92.7 Wh/kg and 110.8 W/kg, respectively.

3 Conclusions

In this chapter, various ferrites ($CoFe_2O_4$, $MnFe_2O_4$, $ZnFe_2O_4$, and $NiFe_2O_4$) and their nanocomposites were discussed for their applications in energy storage devices, specifically, supercapacitors. Firstly, the common structure of ferrites was discussed with literature survey on various synthesis methods used for the synthesis of ferrite nanostructures. It is reported by various groups that the electrochemical properties of ferrites are highly dependent on the synthesis process used and the synthesis conditions employed. The properties of a supercapacitor are also controlled by the surface morphology, shape and size of the nanostructures. Nanocomposites of ferrites with graphene and reduced graphene oxide enhance their electrochemical performance due to their large electrical conductivity. Nanoflakes of ferrite composites offer the most promising electrochemical performance over other structures.

References

1. Bashir B, Shaheen W, Asghar M, Warsi MF, Khan MA, Haider S, Shakir I, Shahid M (2017) J Alloys Compd 695:881
2. Kefeni KK, Msagati TAM, Mamba BB (2017) Mater Sci Eng B Solid-State Mater Adv Technol 215:37
3. Mathew DS, Juang RS (2007) Chem Eng J 129:51

4. Yadav RS, Havlica J, Masilko J, Kalina L, Wasserbauer J, Hajdúchová M, Enev V, Kuřitka I, Kožáková Z (2016) J Magn Magn Mater 399:109
5. Reddy DHK, Yun Y (2016) Coord Chem Rev 315:90
6. Lee N, Yoo D, Ling D, Cho MH, Hyeon T, Cheon J (2015) Chem Rev 115:10637
7. Sharifi I, Shokrollahi H, Amiri S (2012) J Magn Magn Mater 324:903
8. Gomes JA, Sousa MH, Tourinho FA, Mestnik-filho J (2005) J Magn Magn Mater 289:184
9. Akbarzadeh A, Samiei M, Davaran S (2012) Nanoscale Res Lett 7:1
10. Mahmoud ME, Abdelwahab MS, Fathallah EM (2013) Chem Eng J 223:318
11. Malarvizhi M, Meyvel S, Sandhiya M, Sathish M, Dakshana M, Sathya P, Thillaikkarasi D, Karthikeyan S (2021) Inorg Chem Commun 123:108344
12. Wang K, Cao Y, Wang X, Andrea M, Luo B, Gu Z, Liu J, Hoefelmeyer JD, Fan Q (2016) J Power Sources 307:462
13. Reddy ALM, Ramaprabhu S (2007) J Phys Chem C 111:7727
14. Teng Y, Liu E, Ding R, Liu K, Liu R, Wang L, Yang Z, Jiang H (2016) Electrochim. Acta
15. Zheng L, Wang C, Dong Y, Bian H, Hung TF, Lu J, Li YY (2015) Appl Surf Sci 362:399
16. Gonzalez-moragas L, Yu S, Murillo-cremaes N, Laromaine A, Roig A (2015) Chem Eng J 281:87
17. Zheng Y, Li Z, Xu J, Wang T (2016) Nano Energy 20:94
18. Krzysztof Wasinski GL, Walkowiak M, Połrolniczak P (2015) J Power Sources 293:42
19. Shanmugavani A, Selvan RK (2014) RSC Adv 4:27022
20. Pawar SJ, Patil SM, Chithra M, Sahoo SC, Patil PB (2020) AIP Conf Proc 030162
21. Xin Y, Dong X, Peng Z, Li J, Min Y (2014) Mater Lett 123:229
22. Jundale VA, Patil DA, Chorage GY, Yadav AA (2020) Mater Today Proc
23. Kennaz H, Harat A, Guellati O, Momodu DY, Barzegar F (2018) J Solid State Electrochem 22:835
24. He P, Yang K, Wang W, Dong F, Du L, Deng Y (2013) Russ J Electrochem 49:405
25. Xiong P, Huang H, Wang X (2014) J Power Sources 245:937
26. Cai W, Lai T, Dai W, Ye J (2014) J Power Sources 255:170
27. J-FL, Shin-Liang Kuo N-LW (2007) J Electrochem Soc 154:2
28. Wang B, Guo P, Bi H, Li Q, Zhang G, Wang R (2013) Int J Electrochem Sci 8:8966
29. Vignesh V, Subramani K, Sathish M, Navamathavan R (2018) Colloids Surfaces A 538:668
30. Wang R, Li Q, Cheng L, Li H, Wang B, Zhao XS, Guo P (2014) Colloids Surfaces A Physicochem Eng Asp 457:94
31. Nonaka LH, Almeida TSD, Aquino CB, Domingues H, Salvatierra RV, Souza VHR, Appl ACS (2020) Nano Mater 3:881
32. Kotutha I, Swatsitang E, Meewassana W, Maensiri S (2015) Jpn J Appl Phys 54
33. Vadiyar MM, Bhise SC, Patil SK, Kolekar SS (2016) ChemistrySelect 5:959
34. Vadiyar MM, Bhise C, Patil SK, Patil SA, Pawar DK, Ghule AV, Patil P, Kolekar SS (2015) RSC Adv 5:45935
35. Li L, Bi H, Shili G, He F, Gao P, Dai Y, Zhang X, Yang D (2017) Sci Rep 7:43116
36. Madagonda AVG, Vadiyar M, Kolekar SS, Chang J-Y, Ye Z (2017) ACS Appl Mater Interfaces 9:26016
37. KSG, AVG, Vadiyar MM, Bhise SC, Patil SK, Kolekar SS, Shelke AR, Deshpande NG, Chang J-Y (2015) Chem Commun 52:2557
38. Raut SS, Sankapal BR (2016) Electrochim Acta
39. Vadiyar MM, Kolekar SS, Deshpande NG (2016) Ionics (Kiel). 23:741
40. KSG, AVG, Vadiyar MM, Bhise SC, Kolekar SS, Chang J-Y (2016) J Mater Chem A 4:3504
41. Zhu M, Zhang X, Zhou Y, Zhuo C, Huang J, Li S (2015) RSC Adv 5:39270
42. Askari MMB, Salarizadeh P, Di Seifi A, Ramezan zadeh MH, Bartolomeo (2021) J Alloys Compd 860:158497
43. Anwar S, Muthu KS, Ganesh V, Lakshminarasimhan N, Soc JE, A-a P, Anwar S, Muthu KS, Ganesh V, Lakshminarasimhan N (2011) J Electrochem Soc 158:2
44. Kumar TYTN, Kumar A, Huang GM, Wu WW (2018) Appl Surf Sci 433:1100

45. Senthilkumar B, Kalai R, Vinothbabu P, Perelshtein I, Gedanken A (2011) Mater Chem Phys 130:285
46. Ghasemi A, Kheirmand M, Heli H (2019) Russ J Electrochem 55:341
47. Kumar N, Kumar A, Chandrasekaran S, Tseng TY (2018) J Clean Energy Technol 6:1
48. Venkatachalam V, Jayavel R, Conf AIP (2015) Proc 1665:2
49. Soam A, Kumar R, Sahoo K, Mahender C, Kumar B (2019) ChemistrySelect 4:9952
50. Wang Z, Zhang X, Li Y, Hao Z (2013) J Mater Chem A 1:6393
51. Senthilkumar B, Sankar KV, Sanjeeviraja C, Selvan RK (2013) J Alloys Compd 553:350
52. Yu Z, Chen L, Yu S (2014) J. Mater Chem A 2:10889
53. Muhammad Sufyan Javed CH, Zhang C, Chen L, Xi Y (2016) J Mater Chem A 4:8851
54. Fu M, Chen W, Zhu X, Liu Q (2018) J Power Sources 396:41
55. Wang W, Hao Q, Lei W, Xia X, Wang X (2014) J Power Sources 269:250

Chapter 11
Ferrite Nanoparticles for Antimicrobial Applications

Nishat Bhatia, Asha Kumari, Kashama Sharma, and Rahul Sharma

1 Introduction

The primary constituents of ferrites, Fe_2O_3 and FeO, which can be partially modified through other transition metal oxides, are chemical compounds with ferrimagnetic properties which are synthesized as powders or ceramic bodies [1]. Iron oxides mixed with metal elements like manganese (Mn), barium (Ba), nickel (Ni), zinc (Zn), cobalt (Co), and copper (Cu) result in the extraordinary ceramic substance known as ferrites [2–8]. Iron is the primary elements in the composition of ferrites, a magnetic material with ferromagnetic ordering. Pure phases of iron, which are found in nature in the form of iron oxide, include magnetite (Fe_3O_4), hematite (Fe_2O_3), iron oxide beta phase, maghemite, etc. These substances have different colors, trivalent oxidation states, and poor solubility. Due to their natural magnetism, ferrites are gaining more attention [9]. Magnetite (Fe_3O_4), which includes both Fe^{2+} and Fe^{3+} ions, is the most significant ferrite [10]. The family of magnetic nanoparticles known as ferrites consists mostly of derivatives of various metal oxides, including hematite and magnetite. Ferrites have a wide range of applications for both indoor and outdoor use due to their properties of electricity and magnetism and accessibility of synthesis. To be termed ferrite, the chemical formula must include at least one iron (III). Ferrites, such as MFe_2O_4, are common examples, and most of them have superparamagnetic (SPM) properties at diameters of less than or equal to 20 nm [11, 12]. Depending on their affinity for both places, the distributions of each metal cation over both sites vary. The stabilizing energy, the required ionic radii, the size of the interstices, the types of synthesis used, and the circumstances in situ at the moment of synthesis all influence

N. Bhatia · A. Kumari · K. Sharma · R. Sharma (✉)
Department of Chemistry, Career Point University, Bhoranj (Tikker—Kharwarian), MDR 35, Hamirpur, Himachal Pradesh 176041, India
e-mail: rahul.che@cpuh.edu.in

Centre for Nano-Science and Technology, Career Point University, Hamirpur, Himachal Pradesh 176041, India

P. Sharma et al. (eds.), *Engineered Ferrites and Their Applications*, Materials Horizons: From Nature to Nanomaterials, https://doi.org/10.1007/978-981-99-2583-4_11

this [13–16]. The chemical and physical properties of ferrite NPs are greatly influenced by the type and distribution of metal ions at the tetrahedral and octahedral sites [3, 17–19]. For example, the type and arrangement of cations at the spiral structure's tetrahedral and octahedral locations substantially relate to the magnetic properties of ferrite NPs. Since the net magnetization moment of ferrite NPs varies between both the two locations [20, 21]. Ferrite NPs with virtually equal size and composition may have different saturation magnetization (Ms) values due to variances in cation distribution between the two sites. Based on the kinds of cation distribution at both places, three types of spinel structures are known: normal, inverse, and mixed spinel types. Due to chemical stability, biocompatibility, affordable price compared to other metal NPs like silver NPs (i.e., gold standard anti-bacterial NPs), and special ferromagnetic properties, iron oxide-based NPs, particularly spinel ferrites, have recently emerged as popular candidates for emerging biomedical applications [21]. Current chapter describes the applications of magnetic nanoparticles as antimicrobial agent.

2 Synthesis Methods of Ferrite NPs

Due to the relevance of ferrite NPs in technology, their synthesis is one of the most attractive study topics. Identifying the most effective synthesis methods for producing high-quality ferrite NPs in terms of purification, structure, size, size distribution, consistency, and morphology [22]. There have been a few different synthesis techniques published recently for the production of ferrite NPs, but there is still no one universal way for the formulation of ferrite NPs. There are basically two methods of synthesis of ferrites. Conventional powder processing scheme and non-conventional powder processing schemes are shown in Fig. 1.

These synthesis methods may be divided into two categories: "top-down" and "bottom-up." The first four synthesis methods are the most commonly used for the "bottom-up" option. Co-precipitation, thermal degradation, hydrothermal, solvothermal, sol–gel, flame spray pyrolysis, ultrasonication, chemical vapor deposition, microwave-assisted, nanoemulsion, and polyol processes are among those used. On the other hand, mechanical grinding and pulsed laser ablation are the most often used "top-down" synthesis methods. Modified polyol, sonochemical method, and microwave irradiation are three novel synthesis procedures that have been employed more often in the present day to create a variety of ferrite NPs. These synthesis procedures are superior to previously mentioned synthesis methods in several ways, including faster reaction times, softer reaction conditions, greater yields, increased selectivity, and clean reactions. Various methods of ferrite NPs synthesis are.

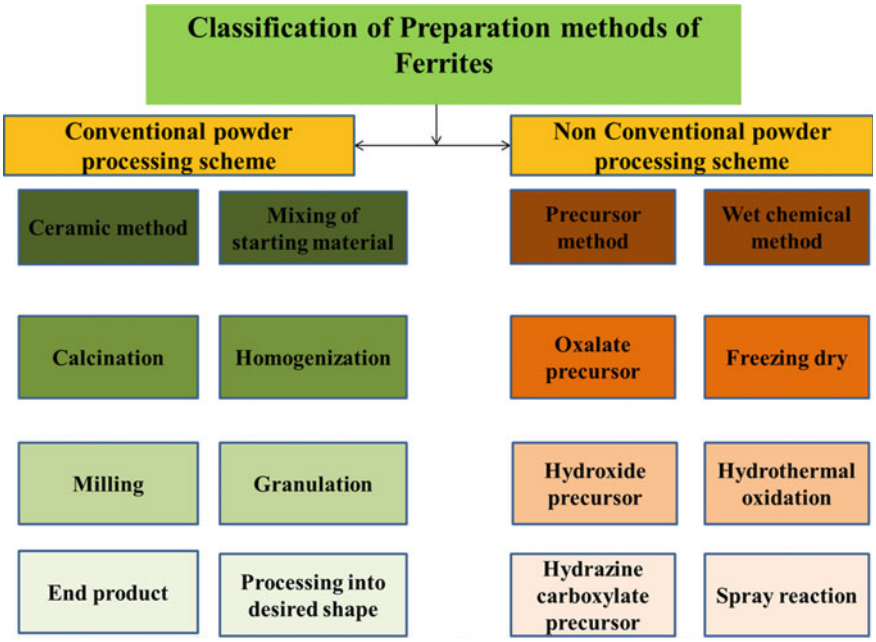

Fig. 1 Conventional powder processing scheme and non-conventional powder processing scheme

2.1 Green Ferrite Nanoparticle Synthesis

Green synthesis methods have been utilized to generate ferrite nanoparticles from biological sources such as plants, fungi, algae, and bacteria.

2.1.1 Plant Extract Mediated Green Synthesis of Ferrite Nanoparticles

Plant-based synthesis of ferrite nanoparticles is getting too much attention because of their less toxicity and durability, and the process of their formulation is also simple and cost-effective. Various plants are included in Table 1 whose ferrite-based nanomaterials have been synthesized.

2.1.2 Microbial Synthesis of Ferrite Nanoparticles

According to modern trends, microbial-based formulation of various ferrites (Fig. 2) is gaining lots of interest among researchers. Zinc doped cobalt ferrite nanoparticles made with *Lactobacillus delbrueckii* as a synthetic agent. In photocatalytic, optoelectronic, and pharmaceutical applications, the produced ferrite nanoparticles showed antimicrobial activity [32]. Cobalt ferrite ($CoFe_2O_4$) using *Saccharomyces*

Table 1 Green fabrication of different ferrite nanoparticles using plant extracts

S.No.	Name of the plant	Particle size (nm)	Shape	Reference
1	*Aloe barbadensis*	34	Spinel	[23]
2	*Aloe vera*	20	Agglomerated cubic	[24]
3	*Asparagus*	48	Spinel	[23]
4	*Coffeaarabica*	9.72	Cubic spinel	[25]
5	*Hibiscusrosa Sinensis*	39	Single phase cubic	[26]
6	*Limonia acidissima*	12	Spherical	[27]
7	*Ocimum sanctum*	21	Single phase cubic spinel	[28]
8	*Okra extract*	49	Spherical	[29]
9	Tragacanth gum	20	Cubic spinel	[30]
10	*Zingiber officinale*	46	Spinel	[31]

cerevisiae (yeast) revealed particle size of 7.23 nm. Anal K. Jha has reported the creation of cobalt ferrite nanoparticles in *S. cerevisiae* [33].

2.1.3 Co-precipitation Method

The co-precipitation technique involves the base-assisted precipitating of metal from a salt substrate as hydroxide in a solution [35–38]. For the synthesis procedure to produce high-quality ferrite NPs, the pH must be carefully adjusted and controlled. Ammonium or sodium hydroxide solutions are typically used to modify the pH of the solution. Under inert conditions, the solution then needs to be forcefully mixed or agitated in the absence as well as in the presence of heat. There have been several published research projects that used the co-precipitation approach to create ferrite NPs [39–41].

2.1.4 Hydrothermal Method

Hydrothermal synthesis is the most often utilized method for creating nanomaterials. It essentially employs a solution-reaction technique. Nanomaterials may be generated at a range of temperatures via hydrothermal synthesis, including very high temperatures and room temperature. One of the most promising synthesis techniques for the mass manufacturing of ferrite NPs is the hydrothermal approach. By choosing the right solvent combination and adjusting variables like temperature, pressure, and reaction time, it is feasible to create high-quality NPs with controlled size and size dispersion [42].

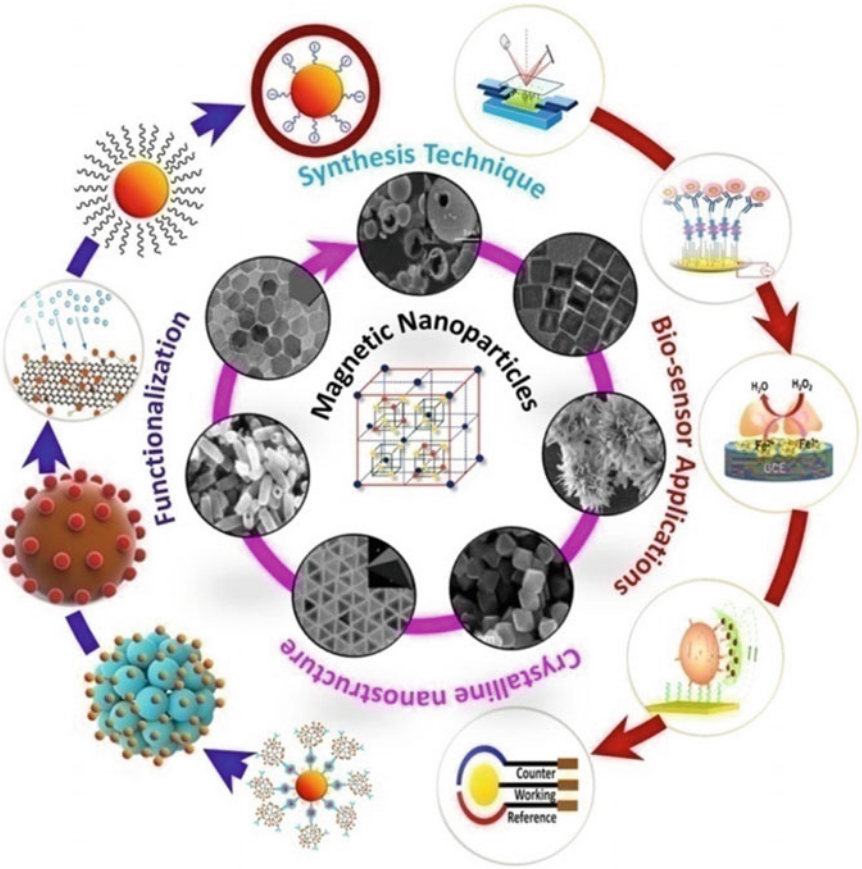

Fig. 2 Microbial synthesis and applications of Ferrites (Adapted and reprinted from Tripathy et al. [34]) (Licence Number 5432420494039)

2.1.5 Sol–Gel Method

The low temperature, cheap cost, and lack of specific equipment required for the sol–gel synthesis process are only a few of its benefits. Sol–gel processes may be used to create Ferrite NPs with a narrow size distribution and controllable form, where the reaction temperature ranges from 25 to 20 °C. The sol–gel approach is particularly appealing because of these benefits and how easily Ferrite NPs can be synthesized with it. Another advantage of this popular synthesis process is the flexibility to modify the composition, microstructure, purification, and shape of the NPs by altering factors such as sol percentage, stirring rate, and temperature [43]. The initial commercial uses of the sol–gel technique include the synthesis of ferrite NPs as well as films and coatings. The sol–gel method first commercial applications were the production of Ferrite NPs, and also films and coatings [44]. The main issue

of the process is that reaction byproduct contamination causes a lack of purity in the ferrite NPs produced, necessitating post-treatment to obtain pure ferrite NPs.

2.1.6 Electrochemical Method

Co-precipitation is identical to the electrochemical synthesis approach; the difference is that the ion carriers are produced by the scarification of anode electrodes throughout the oxidation reaction [45]. The excellent purity of the product and control over particle size are two advantages of electrochemical synthesis over conventional synthesis processes. Purity and particle size can be achieved by varying the current or regulating the spacing between the electrodes [44]. In general, electrochemical synthesis is a viable option for producing the majority of ferrite NPs. These techniques have been used to synthesize ferrite NPs such as $CoFe_2O_4$, $NiFe_2O_4$, and c-Fe_2O_3 [46, 47].

2.1.7 Microwave Assisted

Microwave synthesis has been employed to generate nanoparticles because it combines the advantages of speed and homogeneous heating of the precursor materials. When used in conjunction with a well-established synthesis technique, microwave-assisted synthesis aligns the material's dipoles in an external field through excitation caused by microwave electromagnetic radiations [48]. Compared to co-precipitation, hydrothermal, or thermal decomposition techniques, the microwave-assisted synthesis process frequently allows for the large-scale synthesis of Ferrite NPs with a low yield.

2.1.8 Microemulsion Method

In the manufacture of microemulsion, the thermodynamically stable isotropic dissemination of two relatively immiscible liquids sustained by surfactant molecules is commonly used. *N*-hexane has been mentioned as an oil phase, polyoxyethylene ethers as a non-ionic surfactant, and *n*-butanol as a co-surfactant [49].

One of the primary advantages of the microemulsion synthesis technique is the capacity to manufacture various Ferrite NPs by varying the kind of surfactant, co-surfactant, oil–water ratio, and process conditions [50, 51].

2.1.9 Solvothermal Method

The solvothermal synthesis technique is often helpful when it comes to creating ferrite NPs with enhanced physical and chemical characteristics that are suitable to both industrial and biomedical fields. Solvothermal synthesis is used for the

scalable generation of ferrite NPs with regulated size and form in addition to its simplicity in terms of reaction. As in the solvothermal synthesis technique, aqueous or non-aqueous solutions may be used to generate NPs with precise control over size distribution, morphology, and crystalline phases. These physical characteristics may be altered by modifying particular experimental parameters such as reaction temperature, reaction time, solvent, surfactant, and precursors.

The solvothermal synthesis method has been used to create a variety of ferrite NPs and their corresponding composites, including MWCNT/$CoFe_2O_4$ [52], Co_3O_4 [53], Fe_3O_4 [54], $CoFe_2O_4$ without the use of a template, NPs with such an ultra-low dielectric constant of 3.21 at 1 MHz [55], single crystalline α-Fe_2O_3 with varied morphologies [56], and Fe_3O_4.

2.1.10 Thermal Decomposition

One of the easiest techniques for synthesizing ferrite NPs is the thermal decomposition process [57]. The utilization of high or low temperature depends on the kind of precursor materials. In general, the technique may be used to create high-quality crystalline ferrite NPs on a huge scale (40 g for each synthesis) with size- and shape-controlled output [52, 58].

2.1.11 Mechanical Milling

NPs are typically prepared mechanically by milling in high-energy shakers, planetary ball mills, or glass mills. The process exemplifies a "top-down" approach to the creation of ferrite NPs. This method's greatest benefit is its ability to scale up to huge amounts of materials for a variety of applications, but its biggest disadvantage is the contamination of NPs during milling [54]. Mechanical milling has been used to synthesize a variety of ferrite NPs, including $CoFe_2O_4$ [59], $CuFe_2O_4$, and $NiFe_2O_4$.The milling approach is a straightforward and affordable way to create Ferrite NPs.

3 Types of Ferrites Used for Antimicrobial Properties

Ferrites magnetic properties are due to the interaction of metallic ions in certain positions relative to oxygen ions in the crystalline structure of iron oxides.

3.1 Spinel Ferrites

Ferrites with the chemical formulas MFe_2O_4 and $MeFe_{12}O_{19}$ with hexagonal crystal shapes are widely used. Me stands for Ba^{2+}, Sr^{2+}, etc., while M denotes a current divalent metal ion (such as Mn, Fe, Co, Ni, Cu, or Zn) with an ionic radius of roughly 0.6–1. Spinel ferrites are capable of combining two or more ions, which is referred to as a solid solution of two ferrites [60]. Eight molecules of MFe_2O_4 are found in the smallest spinel lattice cell, which has cubic symmetry, where comparatively massive oxygen ions form an FCC lattice.

Tetrahedral and octahedral interstitial sites as shown in Fig. 3, which are surrounded by four and six oxygen ions, respectively, are both present in a cubic close-packed structure.

Only 8 and 16 of the 64 tetrahedral and 32 octahedral sites (referred to as A and B sites, respectively) in this cubic unit cell are occupied by metal ions. One of the three metal ions in MFe_2O_4 occupies a tetrahedral position, whereas the other two occupy an octahedral site. In a typical spinel, the trivalent Fe ion occupies the octahedral (B) site, whereas the divalent M ion occupied the tetrahedral (A) site. Trivalent Fe ions occupy the other B site, the A site, and the divalent M ions occupy one of the B sites in an inverted spinel structure. The ions in the A sites of a spinel ferrite are antiparallel to those in the B sites, and the metal ions are isolated from the oxygen ions by these ions. There is a magnetization as a result of the two sub-lattices in the majority of ferrites having distinct numbers and kinds of ions.

Given that both ions in $MnFe_2O_4$ have five uncompensated spins and that the net magnetic moment is five spin per molecule. Bragg and Nishikawa were the first to identify the structure of SFs as they were found to exist for $MgAl_2O_4$ in 1915. The

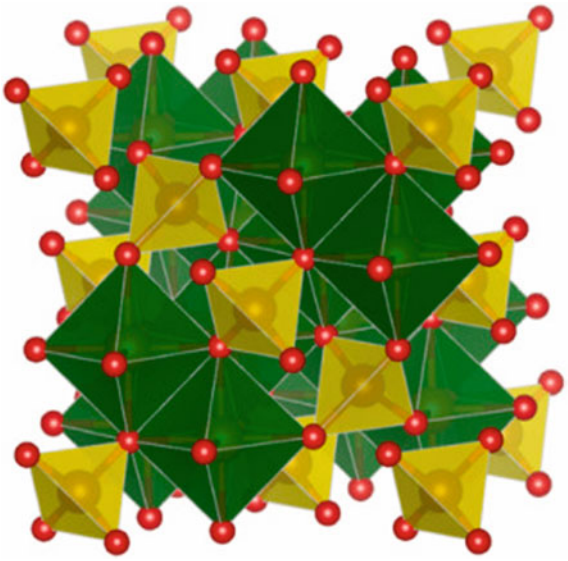

Fig. 3 The spinel ferrites [61] (Adapted and reprinted from Soufi et al. [62])

typical structural formula of a spinel ferrite is MFe_2O_4 where M is a divalent metal ion such as iron, cobalt, nickel, manganese, magnesium, copper, or a combination of these ions. The spinel structure belongs to the Fd3m space group [62]. The face-centered cubic (FCC) unit cell of spinel ferrite has eight $M_8Fe_{16}O_{32}$ formula units [15]. In a ferrite unit cell, there are 96 interstices (64 tetrahedral and 32 octahedral) between the densely packed oxygen atoms [63]. The cations only occupy 8 tetrahedral and 16 octahedral sites. Spinel ferrites were classified into three categories based on the cation distribution at the tetrahedral (A) and octahedral (B) sites. This classification is determined by the degree of inversion, x, which is commonly used to characterize the cationic disorder and is defined as the proportion of M^{2+} ions occupying octahedral positions [64].

Jesudoss, S. K. et al., reported the antibacterial efficacy of spinel magnetic $Mn_{1-x}Ni_xFe_2O_4$ nanoparticles was tested against two gram-positive organisms (*Staphylococcus aureus* and *Bacillus subtilis*) and two ram-negative organisms (*Pseudomonas aeruginosa* and *Escherichia coli*). Results of antibacterial activity in this study are equivalent to those obtained with streptomycin, an antibiotic [65].

3.2 Hexagonal Ferrites

Hexagonal ferrites, such as $BaFe_{12}O_{19}$, are examples of magnetoplumbite structures that have a complicated hexagonal unit cell. In the unit cell of the hexagonal structure, the twelve Fe^{3+} ions are distributed as follows: nine ions are located in the octahedral sites (with six O_2 neighbors closest to them), two ions are located in the tetrahedral sites (with four O_2 neighbors closest to them), and one ion is located in the hexagonal site (with five O_2 neighbors closest to it). These materials are good candidates for permanent magnets because they have a strong uni-axial magnetic direction [66]. Here are six different names for hexagonal ferrites:

3.2.1 The M Ferrites

BaM, $BaFe_{12}O_{19}$, has been around for a long; its melting temperature of 1390 °C was determined in 1936. It was not until Philips studied and magnetically described the form in the early 1950s that it was discovered to be isomorphism with hexagonal magnetoplumbite [67].

M-type ferrites NPs antimicrobial property were reported by Atacan et al., and silver nanoparticles were deposited on $CuFe_2O_4$ magnetic nanoparticles to increase antibacterial activity. All generated samples were more effective against gram-positive microorganisms (*S. aureus*) than gram-negative microorganisms (*E. coli*). By estimating the inhibition diameter of 250.1 mm in the synthesized materials, it was revealed that the $Ag/CuFe_2O_4$ exhibited a more powerful antibacterial ability against the *S. aureus* bacterium [68].

3.2.2 The W Ferrites

W ferrites have the formula $BaMe_2Fe_{16}O_{27}$, where Me is frequently a first-row transition metal or perhaps another divalent cation, and barium can be substituted by another group two metal. Fe_2W ($BaFe_2Fe_{16}O_{27}$) [69] was the very first W ferrite described; however, it was initially only synthesized as a combined phase with M and X ferrites. The hexagonal crystalline structure of single-phase Fe_2W was revealed to have a facile axis of magnetization all along the c-axis, but it had significantly better electrical conductivity than BaM due to the presence of Fe^{2+} ions. It's computed hardness in the *c*-axis is 5.5 GPa [70].

Sagayaraj et al., reported the antibacterial efficacy of W-type ferrite where the nanoparticles HFs/PVP (Polyvinylpyrrolidone) hybrid composites were tested against clinical gram-positive and gram-negative pathogens. W-type BHFs at higher concentrations (100 L) have been shown to be antibacterial agents [71].

According to the analysis, spinel ferrites, M-type ferrites, and W-type ferrites predominantly had the most antibacterial activity as compared to other forms of ferrites.

3.2.3 The X Ferrites

The X-type ferrites, given by the generic formula "$Ba_2Me_2Fe_{28}O_{46}$" (Me is a divalent cation), were initially suggested in 1952 which have mixed phases alongside M or W ferrites. The X-type hexaferrite is generally thought to be fascinating material because of its prospective uses as magnetic materials and microwave devices that must function at GHz frequencies [72]. X-type hexaferrite condones the substitution of various small and large cations due to the existence of three octahedral locations at the borders along S–S and R–S blocks, one octahedral and two tetrahedral locations in S block, or one trigonal bipyramidal as well as two octahedral locations in R block.

3.2.4 The Y Ferrites

The general formula for Y-type ferrites is Y ($Ba_2Me_2Fe_{12}O_{22}$). The Y ferrites were the first ferroxplana ferrites to be found, and it is now known that almost all Y ferrites have a preferred plane of magnetization perpendicular to the c-axis at room temperature [73]. The first two Y ferrites to be produced were Zn_2Y and Co_2Y, and their chemical formula is $Ba_2Me_2Fe_{12}O_{22}$, where Me is a tiny divalent cation. The density of Co_2Y is 5.40 gcm^3 and its molecular mass is 1410 g [69].

3.2.5 The Z Ferrites

The Z ferrites, which have the chemical formula $Ba_3Me_2Fe_{24}O_{41}$, were found concurrently with the ferroxplana Y ferrites [7]. Co_2Z has a maximum density of 5.35 g cm^3

and a molecular mass of = 2522 g. Except Co_2Z, which is linear at room temperature but has a complex magnetic anisotropy with at least four anisotropic states, all Z ferrites have a uniaxial anisotropy parallel to the *c*-axis.

3.2.6 The U Ferrites

Despite being found around the same time as the other hexagonal ferrites listed here, the U ferrites, $Ba_4Me_2Fe_{36}O_{60}$, were not thoroughly defined structurally or magnetically until recently. The densities of Co_2U and Zn_2U are estimated to be 5.44 g cm^3 and 5.31 g cm^3, respectively. They are all uniaxially anisotropic, except Co_2U, which has planar anisotropy at room temperature as well as a molecular mass of 3622 g [73].

Hexagonal ferrites find widespread use in medical equipment, microwave ovens, magnets, computers, power meters, circulators, resonance isolators, and other devices. Magnets are employed in a wide range of applications, including motors, generators, transformers, actuators and sensors, data storage, mobile communications, transportation, security, defense, aerospace, diagnostic devices, and electron beam focusing. Ferromagnetic metals and alloys, as well as ferrimagnetic ceramics, are the most often utilized magnetic materials. Hexagonal ferrites are by far the most often utilized ceramics [67].

3.3 The Garnet Ferrites

The garnet ferrites (Fig. 4) belong to a different family of ferrites and have the basic formula $3M_2O_{35}Fe_2O_3$ or two units of Me_3Fe_2 (FeO_{43}), where Me stands for the trivalent rare earth or a magnetic rare earth, such as ytterbium. Trivalent cations, such as rare earth and Fe^{3+}, occupy the tetrahedral, octahedral, or dodecahedral positions in the orthorhombic crystal structure of garnets. Because of the antiparallel interactions between both the tetrahedral and octahedral locations, the net magnetic moment is antiparallel to the rare earth ions on the dodecahedral locations. Ferrites are ferromagnetic ceramic materials that may be roughly divided into two groups: soft magnetic materials and hard magnetic materials. In the sense that ferromagnetism only manifests itself when a magnetic field is applied, the term "soft" denotes a transient state. Hard magnets, on the other hand, exhibit ferromagnetism in the absence of an outside field.

Mn–Zn ferrite, Ni–Zn ferrite, and other similar materials are examples of soft ferrites, whereas $BaFe_{12}O_{19}$ and $SrFe_{12}O_{19}$ are examples of hard ferrites. It is generally known that the chemical compositions, crystal structures, particle sizes, microstructures, and surface characteristics of ferrites affect their magnetic capabilities [75, 76].

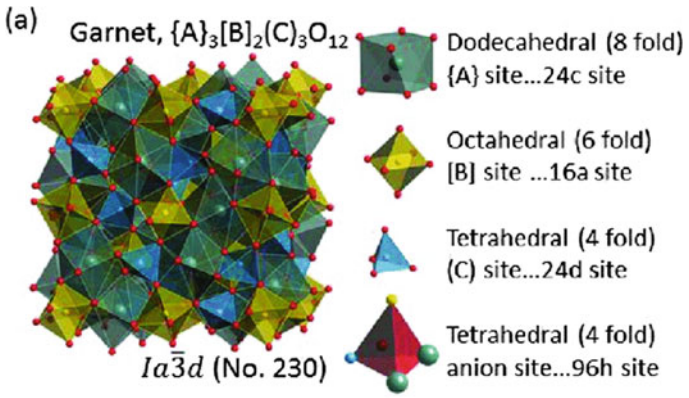

Fig. 4 Garnet Ferrites Adapted and reprinted from Ueda and Tanabe [74]

4 Factors Affecting Properties of Ferrite NPs (w.r.t. Antimicrobial Properties)

4.1 Preparation Method

Due to its ability to form microstructures with various microstructural parameters, including ion arrangement, crystallite size, lattice parameter, and lattice stresses, the preparation process can have an impact on the proportions of ferrites and further affect the antimicrobial properties. Ferrite nanoparticles may well be produced by several methods, ranging from physical operations using mechanical methods to chemical or biological processes involving multiple organic or inorganic substances and living creatures. Each approach has its own set of pros and downsides. However, as opposed to conventional procedures, biological approaches for the production of nanoparticles employ nontoxic and ecologically safe components along with green technology, making them more palatable and eco-friendlier. Metal-based ferrite nanoparticles have demonstrated efficacy against diseases mentioned as a priority in addition to their smaller size and selectivity for bacteria.

4.2 Precursor Compounds and pH

A substance that quickly transforms into a group of functional molecules is called a precursor. These compounds are accountable for alteration in the size and shape of ferrites. When using green technology to synthesize ferrite nanoparticles, pH is a significant component. The size and texture of the produced nanoparticle are influenced by the pH of the solution medium. As a result, changing the pH of the solution medium, the antimicrobial properties may be affected.

4.3 Temperature and Thermal Treatment

Thermal treatment of ferrites often leads to change in particle size distribution which further leads to alter in morphological properties. Temperature is another important component that affects the three main steps of ferrite nanoparticle synthesis. The physical process requires the highest temperature (> 350 °C), however, the chemical method requires a lesser temperature. The majority of the time, atmosphere temperatures or temperatures less than 100 °C are required for green technology-based ferrite nanoparticle production. The type of ferrite nanoparticle formed depends on the reaction medium's temperature.

4.4 Size and Shape

One of the key characteristics that control the physical stability and characteristics of S Ferrite NPs, including Ms, coercivity, and residual magnetizations, is their size and shape [74, 77]. The characteristics of nanoparticles are significantly influenced by particle size. For instance, it has been shown that when nanometer-sized ferrite nanoparticles become larger, their melting points fall. Because ferrite nanoparticles in all configurations contain comparable amounts of energy, changing their shape is simple. The nanoparticles form changes as a result of the typical energy type utilized during nanoparticle analysis. The chemical properties of nanoparticles created are substantially impacted by their energetic nature and shape.

4.5 Presence of Doping

The distribution of the cations between the tetrahedral and octahedral sites is altered by the doping of transition metal ions into ferrite structure, which results in varied magnetic characteristics. If literature is studied then various results shows good antimicrobial properties of doped materials against various pathogens as compared to undoped ferrite nanomaterials.

4.6 Proximity

Most of the time, qualities of isolated or solitary nanoparticles change when they come into touch with or are close to the surface of ferrite nanoparticles. Making more precise ferrite nanoparticles can take advantage of the nanoparticles

changing behavior w.r.t. antimicrobial properties. The proximity effect of nanoparticles has several ramifications, including those related to particle charging, substrate interactions, and magnetic characteristics.

5 Antimicrobial Applications

There are several biological applications for ferrite NPs, but illness diagnostics, cancer therapy, and medication administration and release are among the most widespread. SPM NPs with non-toxic properties, high magnetic susceptibility, high coercivity, and low Curie temperatures are ideal for a variety of biological applications. In particular, Ferrite NPs with these characteristics at room temperature are highly sought, and research on them is now focusing on finding solutions to several health issues. Early illness identification before they cause major harm and systematic medication distribution at the target site are two issues in biomedical fields that need quick attention.

The antimicrobial properties of ferrites are related to structural and chemical variations between gram-positive and gram-negative bacteria cell walls. The cation attraction by the protein in the bacterial cell wall, which results in the creation of insoluble metal proteinate and subsequent bacterial death, is credited with the antibacterial activity of ferrites. Many kinds of antimicrobial ferrites and nanoparticles carriers for antibiotic administration have been shown in vitro and in animal models to be beneficial in treating infectious infections, including antibiotic-resistant ones. High surface-to-volume ratios and nanoscale sizes of inorganic nanoparticles are their distinguishing features, which enhance their response to harmful bacteria [78]. The antimicrobial activity of 5.0 mg/mL (5000 ppm) metal-substituted cobalt ferrite nanoparticles toward *B. subtilis*, *S. aureus*, *E. coli*, *P. aeruginosa*, and *Candida albicans* is shown in Table 2. These findings demonstrate that ZCFO (5000 ppm) was the most potent and effective metal replacement in the cobalt ferrite nanoparticles against all pathogens chosen, followed by manganese ferrite nanoparticles. ZCFO demonstrated considerable antifungal activity against unicellular fungus and was more effective against gram-positive bacteria than gram-negative ones (*C. albicans*; 12 mm ZOI). There are several plausible explanations for how ZCFO ceramic nanoparticles work as an antimicrobial. According to some theories, ZCFO sticks to the membranes of microorganisms, lengthening their production time, lengthening the lag stage of their bacterial growth, and increasing cell division.

Because of their large surface area-to-volume ratio, these materials can give superior treatment than conventional pharmaceuticals, resulting in the development of novel mechanical, chemical, electrical, optical, magnetic, and electro-optical characteristics in comparison to their traditional counterparts. So, ferrites NPs have been proven to be intriguing in the battle against microorganisms.

In earlier reported $NiO.5ZnO.5Fe_2O_4$ ferrite NPs were produced. Using the agar diffusion technique, antimicrobial capabilities against G + bacteria (*S. aureus* and *Bacillus cereus*) and G − bacteria (*Vibrio cholerae*, *E. coli*, and *P. aeruginosa*) were

Table 2 Antibacterial and antifungal activities of irradiated and non-irradiated zinc cobalt ferrite (ZCFO) nanoparticles against selected pathogenic microbes in terms of zone of inhibition (ZOI) (in mm)

Pathogens	ZOI of irradiated ZCFO nanoparticles				ZOI of standard antibiotics[A]
	Control	50.0 kGy	100.0 kGy	150.0 kGy	
Bacillus subtillis ATCC 6633	$13.0^{ab} \pm 0.76376$	$12.0^{b} \pm 0.28868$	$13.0^{b} \pm 0.28868$	$15.0^{a} \pm 1.60728$	$13.0^{b} \pm 0.76376$
S. aureus ATCC 29213	$14.0^{b} \pm 0.76376$	$12.0^{b} \pm 0.50000$	$13.0^{ab} \pm 0.50000$	$16.0^{a} \pm 0.76376$	$15.0^{b} \pm 1.00000$
E. coli ATCC 25922	$11.0^{b} \pm 0.76376$	$11.0^{b} \pm 0.28868$	$12.0^{a} \pm 0.28868$	$14.0^{b} \pm 0.28868$	$11.0^{a} \pm 0.57735$
P. aeruginosa ATCC 27853	$11.0^{a} \pm 0.28868$	$12.0^{b} \pm 0.28868$	$12.0^{a} \pm 0.28868$	$15.0^{a} \pm 0.28868$	N/A
C. albicans ATCC 10231	$13.0^{b} \pm 0.50000$	$13.0^{c} \pm 0.50000$	$14.0^{c} \pm 0.57735$	$15.0^{a} \pm 0.28868$	N/A
Least significant difference	1.33333	0.83333	0.83333	0.50000	2.83333

Adapted and reprinted from Ashour et al. [79] Values are means ± SD (n = 3). Data within the groups are analyzed using one-way analysis of variance (ANOVA) followed by Duncan's multiple range test (DMRT), with the labels, a, b, c, d as the Duncan letters. The selected standard antibiotics are AMC (Amoxicillin/Clavulanic acid; 20/10 g/mL) as antibacterial standard and NS 100 (Nystatin; 100 g/mL) as antifungal standard

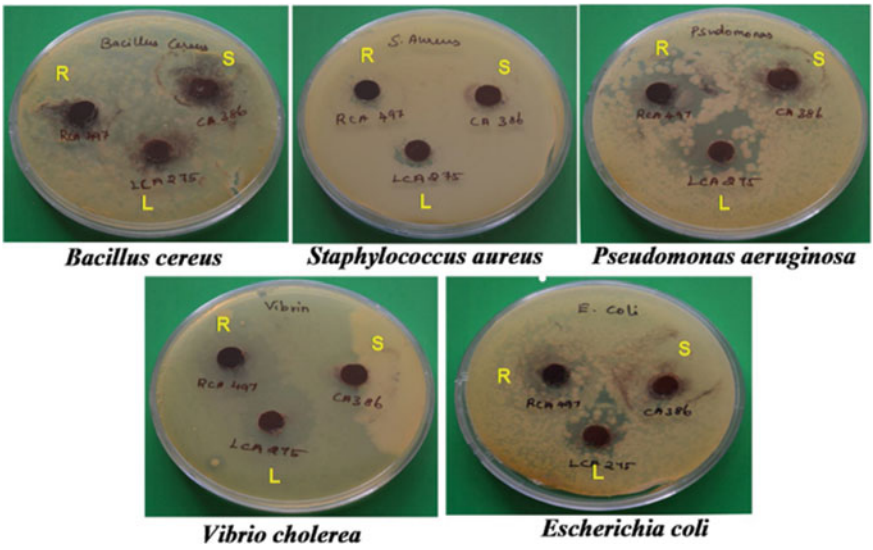

Fig. 5 Antibacterial activity of NiO · 5ZnO · $5Fe_2O_4$. Reprinted with the permission of Elsevier (License Number—5437680355906) Lakshmanan et al. [80]

investigated (Fig. 5). When compared to the fuel order to identify factors and fuel-rich ratios, the produced NPs with the fuel lean ratio demonstrate good antibacterial action against *P. aeruginosa* [80].

In another study, as shown in Fig. 6, zinc cobalt ferrite (ZCFO) NPs were result to be a new antibacterial agent against *Klebsiella pneumoniae* (28.0 mm ZOI) and the multidrug-resistant bacterium *Enterococcus faecalis* (27.0 mm ZOI). ZCFO NPs can thus be employed as candidate resources in industrial, medicinal, and biological applications [53].

Naik et al. in 2019 reported that Agar well-diffusion technique has remarkable antibacterial potential against harmful bacterial strains (*S. aureus*, *E. coli*, *Pseudomonas desmolyticum*, and *Klebsiella aerogenes*). Figure 7 demonstrates the zone of inhibition of $ZnFe_2O_4$ nanoparticles at different concentrations (50, 100, and 150 g/L) in comparison to the positive control (Ciprofloxacin). $ZnFe_2O_4$ nanoparticles have strong antibacterial action against *S. aureus*, *E. coli*, and *P. desmolyticum*, whereas *K. aerogenes* has moderate activity over *E. coli* and *S. aureus.*

The antibacterial efficacy of produced $CoFe_2O_4$ and Zn-doped $CoFe_2O_4$ NPs against gram-negative (*Salmonella typhi*) and gram-positive (*S. aureus*) bacterial strains was investigated using agar well diffusion. In this study, Naik and co-workers reported that nanoparticles concentration is adjusted between 25, 50, and 100 g/mL. Figures 8 shows that the nanoparticles created have strong antibacterial activity against the detected pathogens when compared to the traditional medication (Cifolac). The antibacterial efficacy of Zn-doped $CoFe_2O_4$ NPs against *S. typhi*

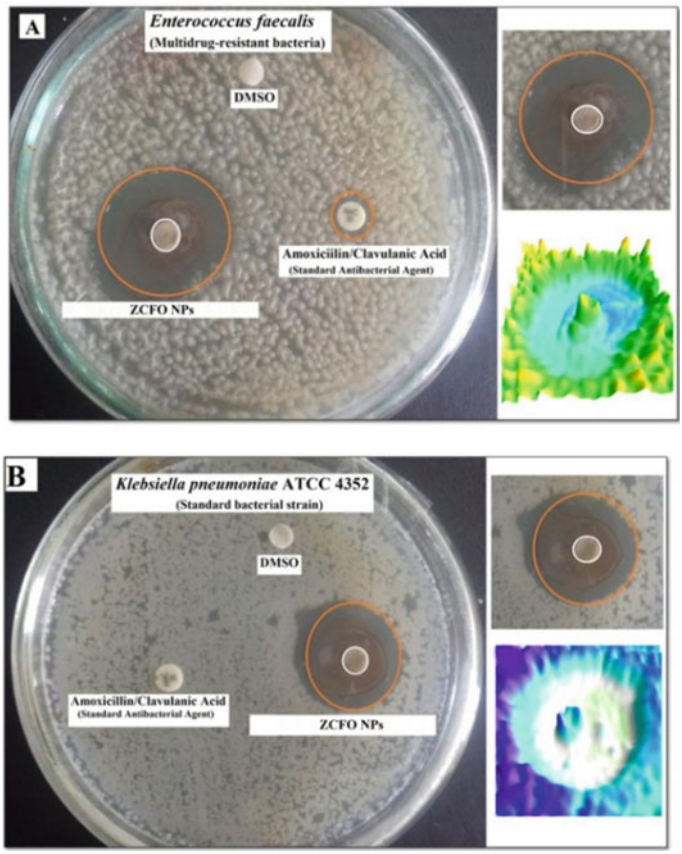

Fig. 6 Antibacterial activity of zinc cobalt ferrites. Reprinted with the permission of Elsevier (License Number—5437690262779) Maksoud et al. [53]

(22 mm) at a concentration of 100 g/mL was superior to that of gram-positive *S. aureus*.

The antibacterial potential of cobalt ferrite nanoparticles (5.0 mg/mL; 5000 ppm) against *B. subtilis*, *S. aureus*, *E. coli*, *P. aeruginosa*, and *C. albicans* is shown in Fig. 9. When compared to other metals replaced in cobalt ferrite nanoparticles, the results show that ZCFO (5000 ppm) was the most powerful and efficient against all diseases tested, followed by manganese ferrite nanoparticles. ZCFO worked better against gram-positive bacteria than gram-negative bacteria.

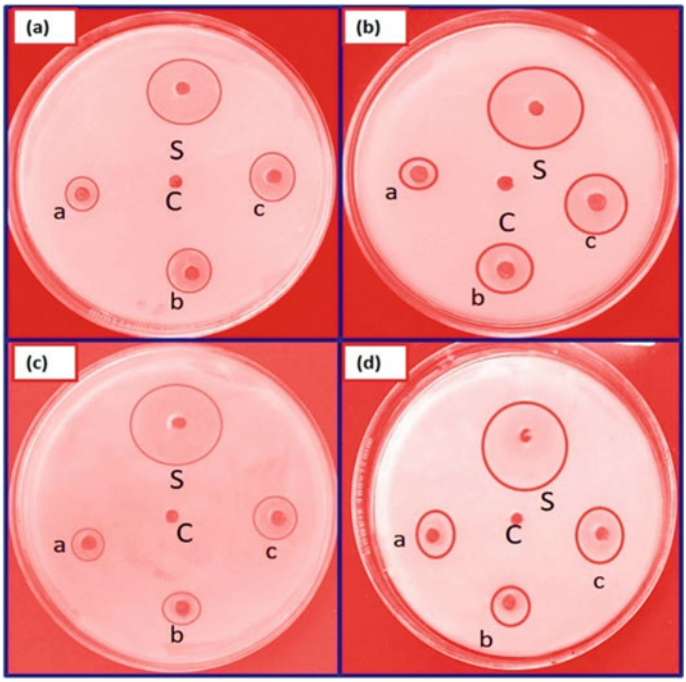

Fig. 7 **a** *Staphylococcus aureus*, **b** *Escherichia coli*, **c** *Pseudomonas desmolyticum* and **d** *Klebsiella aerogenes* (S = standard antibiotic; C = control; a, b and c are the different concentration of nanoparticles: 50, 100, and 150 μg/μL). Reprinted with the permission of Elsevier (License Number—5434071306856) Naik et al. [79]

5.1 Mechanism of Antimicrobial Action of Ferrites Nanoparticles

The comprehension of its method of action is a crucial component in the construction of a more effective antibacterial system. This requires two distinct steps: the first is how the system will react to physical and chemical changes in environments that involve aggregation, dissolution, Redox photo-reactions, release of adsorbed silver species, adsorption or desorption of ions, molecular species, or polymers, or interaction with other nanoparticles or surfaces, all of which can affect the speciation of Ferrites, change the metal's availability, and affect the amount of metal ferrites that is available. Figure 10 demonstrates the cell-based antimicrobial mechanism of Ferrite nanomaterials.

This effect is dependent on the organism under consideration, as well as synthetic factors (ligands type, shape, size, washing steps, dispersion, assessment methods for the bacterial strain used, growth inhibition due to toxicity criterion or complete elimination, nature of the test to assess it, presence of light or oxygen, medium composition, and so on [84]).

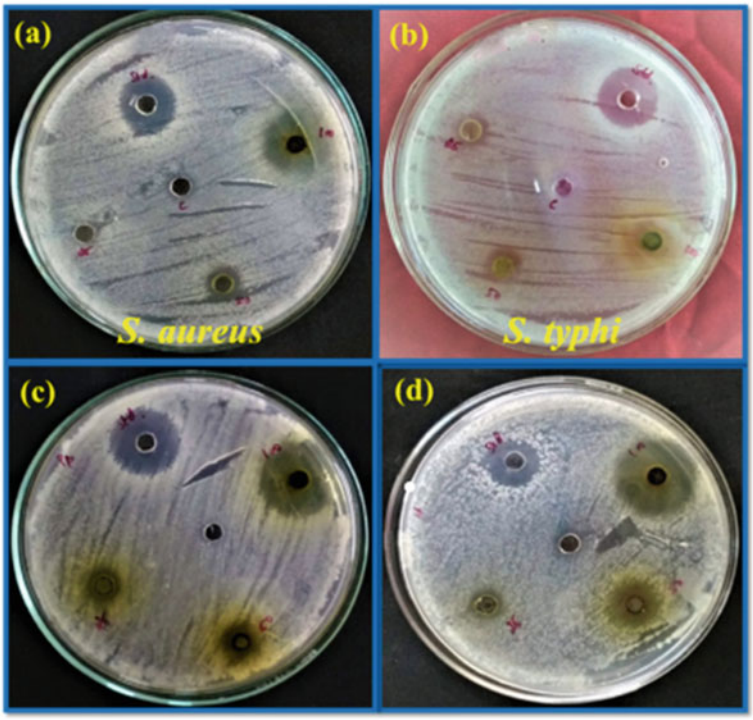

Fig. 8 Antibacterial activities of pure $CoFe_2O_4$ and Zn-doped $CoFe_2O_4$ NPs. Reprinted with the permission of Elsevier (License Number—5434100251305) Naik et al. [81]

6 Toxicity of Ferrites

The more pertinent query is: How harmful are ferrite nanomaterials at the conceivable amounts at which they may be used? Although practically everything can be poisonous at a high enough dose, The type of base material, size, shape, and coatings will all have a unique impact on any harmful consequences that ferrite nanomaterials may have. However, proper methodologies and data interpretation must be used together with evaluation of assumptions in order to identify and comprehend the harmful effects of nanomaterials. Different research teams employed various cell lines, culture settings, and incubation durations in their toxicity investigations of ferrite nanoparticles. When an external magnetic field is introduced, pure metals (Fe, Co, and Ni) are easily removed and have the highest modification. In contrast, they are very susceptible to oxidation and poisonous, making them of limited use in biological applications [85]. Iron oxide nanoparticles, for instance, are an extensively researched magnetic material for use in biological applications, and their biocompatibility is well proven, despite the fact that their associated ferrites are less harmful [86].

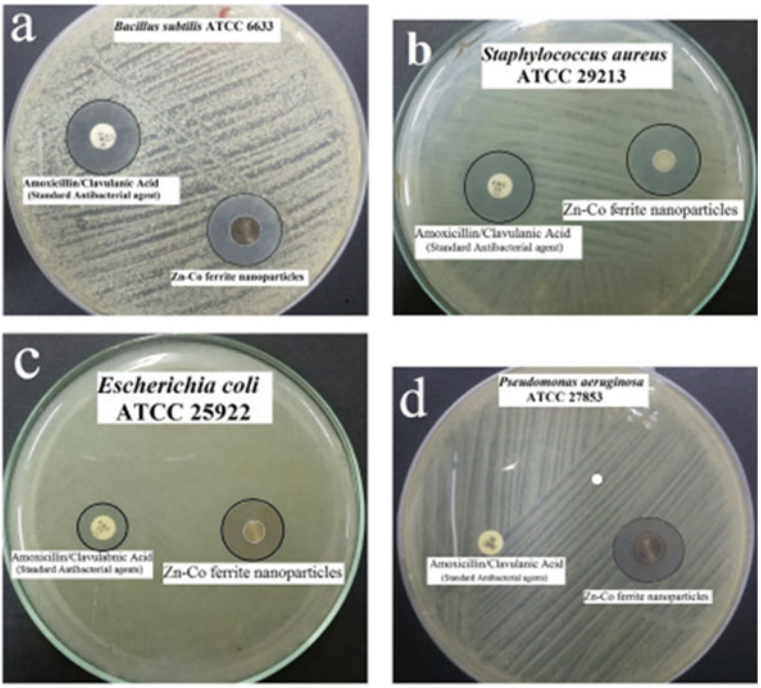

Fig. 9 Antibacterial activity of illuminated zinc cobalt ferrite nanoparticles (150 kGy) against **a** *Bacillus subtilis*, **b** *Staphylococcus aureus*, **c** *Escherichia coli*, **d** *Pseudomonas aeruginosa.* Reprinted with the permission of Elsevier (License Number—5434110409813) Ashour et al. [82]

Because toxicity is dependent on ferrite NP composition and matching size, it is frequently linked to the same characteristics that make them valuable. The spinel ferrite NPs have the ability to cause cytotoxicity in many body areas by inducing reactive oxygen species in the cell [87]. It has been speculated that the production of reactive oxygen species may be the cause of $CuFe_2O_4$'s potential toxicity to human cell line models.

Another study used in vitro cell culture models to investigate the hazard of $ZnFe_2O_4$ NPs on A549, skin epithelial (A431), and liver (HepG2) cells. According to the literature study, only the toxicity of Fe_3O_4 NPs to humans is known with certainty about the toxicity of routinely employed Ferrite NPs. However, reports of spinel ferrite NPs' toxicity to bacteria have been made. Even the mechanism of spinel ferrite NPs toxicity to bacteria is yet unknown, and the biocompatibility varies according to the numerous previously described parameters [87].

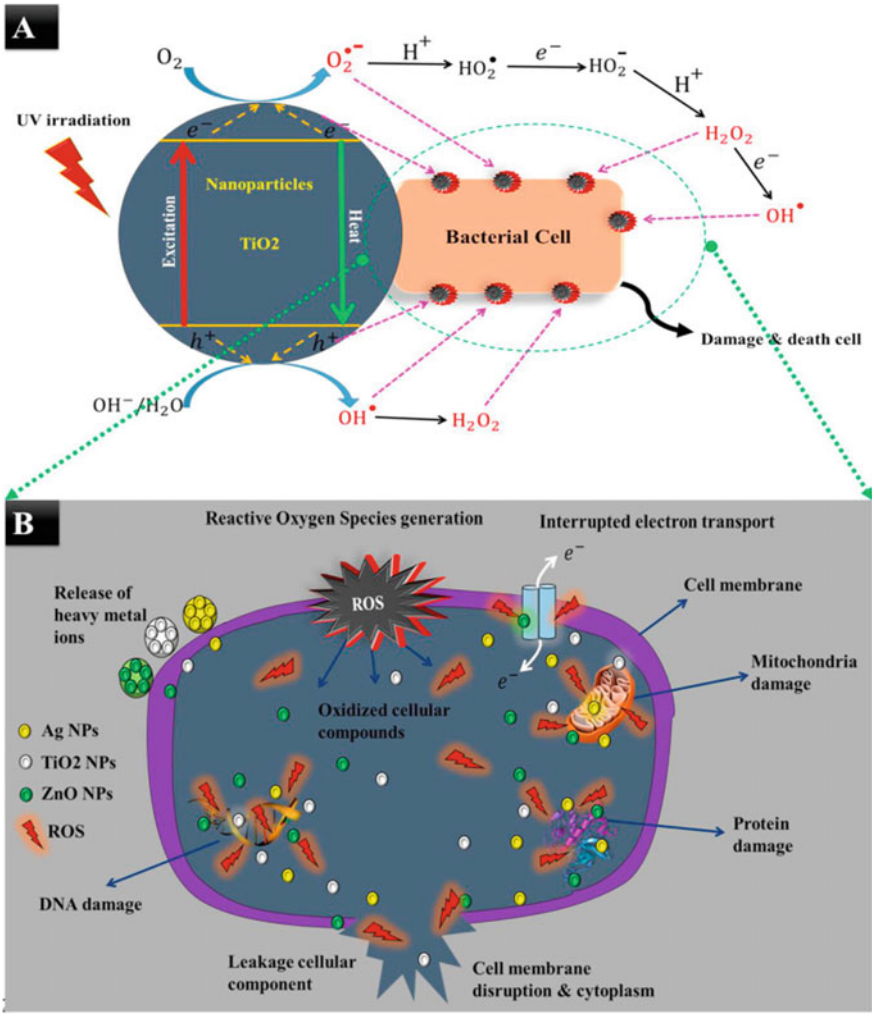

Fig. 10 Cell-based antimicrobial mechanism ferrites (Adapted and reprinted from Khezerlou et al. [83])

7 Gaps in Knowledge and Research Requirements

No one denies that ferrite manufacturing will continue to expand year after year, even in the future, as will the advancement of electronic technology, as stated at the opening. Ferrites will have consistent and expanded development in science and technology, and their industries will continue to prosper in the future, provided ferrites-interested researchers and engineers study more thoroughly at the future features of ferrites and commit themselves to issues of significant importance. There don't seem

to be any compelling basic research challenges that need to be resolved right now in the fields of ferrites that haven't already been solved for the most part. As a result, the majority of scholars who have investigated the fundamental science of ferrites are currently working on different topics. The creation of a novel, high-performance production method for thin and thick ferrite films is now a top priority since it will allow for more reliable mass production of films. Higher quality and more ferrite chip inductors will be produced as a consequence of the creation of a production method for ferrite films. The recent expansion of the ferrite sectors has indeed been ascribed to the improvement of manufacturing techniques and equipment, and the high efficiency of ferrite products is directly tied to their superior performance.

8 Conclusions

Ferrites-based synthesis of nanomaterials and characterization is one of the active study fields nowadays. The performance of ferrite NPs is improved by using effective synthesis techniques that enable them to resist the circumstances for which they are created. Therefore, finding simple synthesis techniques that produce ferrite NPs with the necessary size, shape, and characteristics requires sophisticated technology. Regardless of the availability of numerous synthesis strategies, present approaches must be developed in order to create purified ferrite NPs with the desired properties and amounts.

However, there are relatively few publications in peer-reviewed articles on the amounts of ferrite NPs synthesized. It is highly remarkable to provide data on the amounts of synthesized NPs in articles in order to motivate studies that aim to increase both the quality and the numbers. One crucial area that needs further focus is the usage of ferrite NPs in electronic materials as sensors and biosensors. Recent research has revealed that doped ferrites with transition metals or rare earth metals resulted in the formation of numerous distinct ferrite NPs with novel properties. The ability of doped Fe_3O_4 with Ni, Co, Mn or Zn to create new and improved Ferrite NPs has been extensively shown by study. Researchers are still working to completely utilize the doping of ferrite with rare earth metals, but progress has been achieved and outcomes are soon to be anticipated. Currently, the methods for characterizing synthesized ferrite NPs are nearly perfect and widely used in labs; nonetheless, given the widespread use of ferrite NPs for various purposes, it is possible to anticipate a growth in the amount of environmental contamination caused by these substances. Thus, novel apparatus and processes for characterization of diverse types of ferrite NPs are necessary in order to achieve higher sensitivity, resolving power, and much more accurate and consistent analytical results. Additionally, a portable gadget is very necessary to keep track of their environmental concentration. In general, ferrite NPs are very useful for electromagnetic interference shielding, energy storage, and sensors and biosensors. In reality, the synthesis of ferrite NPs in sufficient quantities with the appropriate size, shape, purity, and functionality will continue to be a focus of future study. Although we are still a long way from having the quality of synthesized

ferrite NPs and relevant devices deemed necessary for the detection and recognition of a disease or any biological substituent's. The incorporation of ferrite NPs into advanced materials or devices demonstrated potential characteristics for detection, identification, and rehabilitation of health conditions.

Acknowledgements Authors would like to thank Editor, book cover designer, or other assistance with the production.

Conflict of Interest The authors in the present study declare no conflict of interest.

References

1. Mohallem NDS, Silva JB, Nascimento GLT, Guimarães VL (2012) Study of multifunctional nanocomposites formed by cobalt ferrite dispersed in a silica matrix prepared by sol-gel process. Nanocomposites-new trends and developments
2. Spaldin NA, Cheong SW, Ramesh R (2010) Multiferroics: past, present, and future. Phys Today 63(10):38–43
3. Manikandan A, Yogasundari M, Thanrasu K, Dinesh A, Raja KK, Slimani Y, Jaganathan SK, Srinivasan R, Baykal A (2020) Structural, morphological and optical properties of multifunctional magnetic-luminescent ZnO@ Fe_3O_4 nanocomposite. Physica E 124:114291
4. Hou C, Yu H, Zhang Q, Li Y, Wang H (2010) Preparation and magnetic property analysis of monodisperse Co–Zn ferrite nanospheres. J Alloy Compd 491(1–2):431–435
5. Manikandan A, Vijaya JJ, Kennedy LJ (2013) Structural, optical and magnetic properties of porous α-Fe_2O_3 nanostructures prepared by rapid combustion method. J Nanosci Nanotechnol 13(4):2986–2992
6. Tatarchuk TR, Bououdina M, Paliychuk ND, Yaremiy IP, Moklyak VV (2017) Structural characterization and anti-structuremodelling of cobalt-substituted zinc ferrites. J Alloy Compd 694:777–791
7. Deraz NM, Alarifi A (2012) Structural, morphological and magnetic properties of nanocrystalline zinc substituted cobalt ferrite system. J Anal Appl Pyrol 94:41–47
8. Umapathy V, Manikandan A, Antony SA, Ramu P, Neeraja P (2015) Structure, morphology and opto-magnetic properties of Bi2MoO6 nano-photocatalyst synthesized by sol–gel method. Trans Nonferrous Metals Soc China 25(10):3271–3278
9. Hemingway BS (1990) Thermodynamic properties for bunsenite, NiO, magnetite, Fe_3O_4, and hematite, Fe_2O_3, with comments on selected oxygen buffer reactions. Am Miner 75(7–8):781–790
10. Torruella P, Ruiz-Caridad A, Walls M, Roca AG, López-Ortega A, Blanco-Portals J, López-Conesa L, Nogués J, Peiró F, Estrade S (2018) Atomic-scale determination of cation inversion in spinel-based oxide nanoparticles. Nano Lett 18(9):5854–5861
11. Mathew DS, Juang RS (2007) An overview of the structure and magnetism of spinel ferrite nanoparticles and their synthesis in microemulsions. Chem Eng J 129(1–3):51–65
12. Yadav RS, Havlica J, Masilko J, Kalina L, Wasserbauer J, Hajdúchová M, Enev V, Kuřitka I, Kožáková Z (2016) Impact of Nd3+ in $CoFe_2O_4$ spinel ferrite nanoparticles on cation distribution, structural and magnetic properties. J Magn Magn Mater 399:109–117
13. Marinca TF, Chicinaş I, Isnard O, Pop V, Popa F (2011) Synthesis, structural and magnetic characterization of nanocrystalline nickel ferrite—$NiFe_2O_4$ obtained by reactive milling. J Alloy Compd 509(30):7931–7936
14. Zaki HM, Al-Heniti SH, Hashhash A (2016) Effect of Al3+ ion addition on the magnetic properties of cobalt ferrite at moderate and low temperatures. J Magn Magn Mater 401:1027–1032

15. Reddy DHK, Yun YS (2016) Spinel ferrite magnetic adsorbents: alternative future materials for water purification? Coord Chem Rev 315:90–111
16. Henderson CMB, Charnock JM, Plant DA (2007) Cation occupancies in Mg Co, Ni, Zn, Al ferrite spinels: a multi-element EXAFS study. J Phys Condens Matter 19(7):076214
17. Cullity BD, Graham CD (2009) Introduction to magnetic materials. Wiley, New Jersey
18. Gaudon M, Pailhé N, Wattiaux A, Demourgues A (2009) Structural defects in AFe_2O_4 (A = Zn, Mg) spinels. Mater Res Bull 44(3):479–484
19. Kuanr BK, Mishra SR, Wang L, DelConte D, Neupane D, Veerakumar V, Celinski Z (2016) Frequency and field dependent dynamic properties of $CoFe_2-$ $xAlxO_4$ ferrite nanoparticles. Mater Res Bull 76:22–27
20. Lee N, Yoo D, Ling D, Cho MH, Hyeon T, Cheon J (2015) Iron oxide based nanoparticles for multimodal imaging and magnetoresponsive therapy. Chem Rev 115(19):10637–10689
21. Sharifi I, Shokrollahi H, Amiri S (2012) Ferrite-based magnetic nanofluids used in hyperthermia applications. J Magn Magn Mater 324(6):903–915
22. Akbarzadeh A, Samiei M, Davaran S (2012) Magnetic nanoparticles: preparation, physical properties, and applications in biomedicine. Nanoscale Res Lett 7(1):1–13
23. Pandit VA, Repe GR, Bhamre JD, Chaudhari ND (2020) A review on green synthesis and characterization technique for ferrite nanoparticles and their applications. In: Journal of physics: conference series, vol 1644, No 1. IOP Publishing, p 012009
24. Laokul P, Amornkitbamrung V, Seraphin S, Maensiri S (2011) Characterization and magnetic properties of nanocrystalline $CuFe_2O_4$, $NiFe_2O_4$, $ZnFe_2O_4$ powders prepared by the Aloe vera extract solution. Curr Appl Phys 11(1):101–108
25. Amiri M, Salavati-Niasari M, Pardakhty A, Ahmadi M, Akbari A (2017) Caffeine: a novel green precursor for synthesis of magnetic $CoFe_2O_4$ nanoparticles and pH-sensitive magnetic alginate beads for drug delivery. Mater Sci Eng C 76:1085–1093
26. Kombaiah K, Vijaya JJ, Kennedy LJ, Bououdina M (2016) Studies on the microwave assisted and conventional combustion synthesis of Hibiscus rosa-sinensis plant extract based $ZnFe_2O_4$ nanoparticles and their optical and magnetic properties. Ceram Int 42(2):2741–2749
27. Patil BN, Taranath TC (2016) Limonia acidissima L. leaf mediated synthesis of zinc oxide nanoparticles: a potent tool against *Mycobacterium tuberculosis*. Int J Mycobacteriol 5(2):197–204
28. Mahajana P, Sharma A, Kaur B, Goyal N, Gautama S, Adv Funct Mater Lab 76:1085–1093
29. Kombaiah K, Vijaya JJ, Kennedy LJ, Bououdina M, Ramalingam RJ, Al-Lohedan HA (2018) Okra extract-assisted green synthesis of $CoFe_2O_4$ nanoparticles and their optical, magnetic, and antimicrobial properties. Mater Chem Phys 204:410–419
30. Sorbiun M, Shayegan Mehr E, Ramazani A, Taghavi Fardood S (2018) Green synthesis of zinc oxide and copper oxide nanoparticles using aqueous extract of oak fruit hull (jaft) and comparing their photocatalytic degradation of basic violet 3. Int J Environ Res 12(1):29–37
31. Barkat F, Afzal M, Khan BS, Saeed A, Bashir M, Mukhtar A, Mehmood T, Wu K (2022) Formation mechanism and lattice parameter investigation for copper-substituted cobalt ferrites from *Zingiber officinale* and *Elettaria cardamom* seed extracts using biogenic route. Materials 15(13):4374
32. Naik MM, Naik HS, Nagaraju G, Vinuth M, Vinu K, Rashmi SK (2018) Effect of aluminium doping on structural, optical, photocatalytic and antibacterial activity on nickel ferrite nanoparticles by sol–gel auto-combustion method. J Mater Sci Mater Electron 29(23):20395–20414
33. Jha AK, Prasad K (2012) Biological synthesis of cobalt ferrite nanoparticles. Nanotechnol Dev 2(1):e9–e9
34. Tripathy A, Nine MJ, Silva FS (2021) Biosensing platform on ferrite magnetic nanoparticles: synthesis, functionalization, mechanism and applications. Adv Coll Interface Sci 290:102380
35. Li H, Qin L, Feng Y, Hu L, Zhou C (2015) Preparation and characterization of highly water-soluble magnetic Fe_3O_4 nanoparticles via surface double-layered self-assembly method of sodium alpha-olefin sulfonate. J Magn Magn Mater 384:213–218
36. Xing Y, Jin YY, Si JC, Peng ML, Wang XF, Chen C, Cui YL (2015) Controllable synthesis and characterization of Fe_3O_4/Au composite nanoparticles. J Magn Magn Mater 380:150–156

37. Drbohlavova J, Hrdy R, Adam V, Kizek R, Schneeweiss O, Hubalek J (2009) Preparation and properties of various magnetic nanoparticles. Sensors 9(4):2352–2362
38. Jain TK, Morales MA, Sahoo SK, Leslie-Pelecky DL, Labhasetwar V (2005) Iron oxide nanoparticles for sustained delivery of anticancer agents. Mol Pharm 2(3):194–205
39. Thakur S, Rai R, Sharma S (2015) Structural characterization and magnetic study of $NiFe_xO_4$ synthesized by co-precipitation method. Mater Lett 139:368–372
40. Zi Z, Sun Y, Zhu X, Yang Z, Dai J, Song W (2009) Synthesis and magnetic properties of $CoFe_2O_4$ ferrite nanoparticles. J Mag Magn Mater 321(9):1251–1255
41. Ma J, Wang T, Duan X, Lian J, Liu Z, Zheng W (2011) Ionothermal synthesis of aggregated α-Fe_2O_3 nanoplates and their magnetic properties. Nanoscale 3(10):4372–4375
42. Masthoff IC, Kraken M, Mauch D, Menzel D, Munevar JA, Baggio Saitovitch E, Litterst FJ, Garnweitner G (2014) Study of the growth process of magnetic nanoparticles obtained via the non-aqueous sol–gel method. J Mater Sci 49(14):4705–4714
43. Tang NJ, Zhong W, Jiang HY, Wu XL, Liu W, Du YW (2004) Nanostructured magnetite (Fe_3O_4) thin films prepared by sol–gel method. J Magn Magn Mater 282:92–95
44. Mazario E, Morales MP, Galindo R, Herrasti P, Menendez N (2012) Influence of the temperature in the electrochemical synthesis of cobalt ferrites nanoparticles. J Alloy Compd 536:S222–S225
45. Bashir AKH, Furqan CM, Bharuth-Ram K, Kaviyarasu K, Tchokonté MBT, Maaza M (2019) Structural, optical and Mössbauer investigation on the biosynthesized α-Fe_2O_3: study on different precursors. Physica E 111:152–157
46. Galindo R, Mazario E, Gutiérrez S, Morales MP, Herrasti P (2012) Electrochemical synthesis of $NiFe_2O_4$ nanoparticles: characterization and their catalytic applications. J Alloy Compd 536:S241–S244
47. Mondal AK, Chen S, Su D, Kretschmer K, Liu H, Wang G (2015) Microwave synthesis of α-Fe_2O_3 nanoparticles and their lithium storage properties: a comparative study. J Alloy Compd 648:732–739
48. Foroughi F, Hassanzadeh-Tabrizi SA, Amighian J, Saffar-Teluri A (2015) A designed magnetic $CoFe_2O_4$–hydroxyapatite core–shell nanocomposite for Zn (II) removal with high efficiency. Ceram Int 41(5):6844–6850
49. Hasany S, Abdurahman N, Sunarti A, Jose R (2013) Magnetic iron oxide nanoparticles: chemical synthesis and applications review. Curr Nanosci 9(5):561–575
50. Langevin D (1992) Micelles and microemulsions. Annu Rev Phys Chem 43(1):341–369
51. Wu H, Liu G, Wang X, Zhang J, Chen Y, Shi J, Yang H, Hu H, Yang S (2011) Solvothermal synthesis of cobalt ferrite nanoparticles loaded on multiwalled carbon nanotubes for magnetic resonance imaging and drug delivery. Acta Biomater 7(9):3496–3504
52. Park J, An K, Hwang Y, Park JG, Noh HJ, Kim JY, Park JH, Hwang NM, Hyeon T (2004) Ultra-large-scale syntheses of monodisperse nanocrystals. Nat Mater 3(12):891–895
53. Maksoud MA, El-Sayyad GS, Ashour AH, El-Batal AI, Abd-Elmonem MS, Hendawy HA, Abdel-Khalek EK, Labib S, Abdeltwab E, El-Okr MM (2018) Synthesis and characterization of metals-substituted cobalt ferrite [Mx Co (1–x) Fe_2O_4; (M= Zn, Cu and Mn; x= 0 and 0.5)] nanoparticles as antimicrobial agents and sensors for Anagrelide determination in biological samples. Mater Sci Eng C 92:644–656
54. Fantechi E, Innocenti C, Albino M, Lottini E, Sangregorio C (2015) Influence of cobalt doping on the hyperthermic efficiency of magnetite nanoparticles. J Magn Magn Mater 380:365–371
55. Kefeni KK, Msagati TA, Mamba BB (2017) Ferrite nanoparticles: synthesis, characterisation and applications in electronic device. Mater Sci Eng B 215:37–55
56. Ameer S, Gul IH, Mujahid M (2015) Ultra low permittivity/loss $CoFe_2O_4$ and $CoFe_2O_4$–rGO nanohybrids by novel 1-hexanol assisted solvothermal process. J Alloy Compd 642:78–82
57. Tao B, Zhang Q, Liu Z, Geng B (2012) Cooperative effect of pH value and anions on single-crystalline hexagonal and circular α-Fe_2O_3 nanorings. Mater Chem Phys 136(2–3):604–612
58. Byun M, Wang J, Lin Z (2009) Massively ordered microstructures composed of magnetic nanoparticles. J Phys Condens Matter 21(26):264014
59. Zhang Z, Yao G, Zhang X, Ma J, Lin H (2015) Synthesis and characterization of nickel ferrite nanoparticles via planetary ball milling assisted solid-state reaction. Ceram Int 41(3):4523–4530

60. Manova E, Kunev B, Paneva D, Mitov I, Petrov L, Estournès C, D'Orléan C, Rehspringer JL, Kurmoo M (2004) Mechano-synthesis, characterization, and magnetic properties of nanoparticles of cobalt ferrite, $CoFe_2O_4$. Chem Mater 16(26):5689–5696
61. Ziemniak SE, Hanson M (2002) Corrosion behavior of 304 stainless steel in high temperature, hydrogenated water. Corros Sci 44(10):2209–2230
62. Soufi A, Hajjaoui H, Elmoubarki R, ABdennouri, M., Qourzal, S. and Barka, N., (2021) Spinel ferrites nanoparticles: synthesis methods and application in heterogeneous Fenton oxidation of organic pollutants—a review. Appl Surface Sci Adv 6:100145
63. Amiri M, Eskandari K, Salavati-Niasari M (2019) Magnetically retrievable ferrite nanoparticles in the catalysis application. Adv Coll Interface Sci 271:101982
64. Sivakumar P, Ramesh R, Ramanand A, Ponnusamy S, Muthamizhchelvan C (2011) Synthesis and characterization of nickel ferrite magnetic nanoparticles. Mater Res Bull 46(12):2208–2211
65. Jesudoss SK, Vijaya JJ, Kennedy LJ, Rajan PI, Al-Lohedan HA, Ramalingam RJ, Kaviyarasu K, Bououdina M (2016) Studies on the efficient dual performance of $Mn_{1-x}NixFe_2O_4$ spinel nanoparticles in photodegradation and antibacterial activity. J Photochem Photobiol, B 165:121–132
66. Granone LI, Ulpe AC, Robben L, Klimke S, Jahns M, Renz F, Gesing TM, Bredow T, Dillert R, Bahnemann DW (2018) Effect of the degree of inversion on optical properties of spinel $ZnFe_2O_4$. Phys Chem Chem Phys 20(44):28267–28278
67. Pullar RC (2012) Hexagonal ferrites: a review of the synthesis, properties and applications of hexaferrite ceramics. Prog Mater Sci 57(7):1191–1334
68. Atacan K, Özacar M, Özacar M (2018) Investigation of antibacterial properties of novel papain immobilized on tannic acid modified $Ag/CuFe_2O_4$ magnetic nanoparticles. Int J Biol Macromol 109:720–731
69. Li Z, Gao F (2011) Chemical bond and hardness of M-, W-type hexagonal barium ferrites. Can J Chem 89(5):573–576
70. Tran N, Kim DH, Lee BW (2018) Influence of fabrication conditions on the structural and the magnetic properties of co-doped $BaFe_{12}O_{19}$ hexaferrites. J Korean Phys Soc 72(6):731–736
71. Sagayaraj R, Dhineshkumar T, Prakash A, Aravazhi S, Chandrasekaran G, Jayarajan D, Sebastian S (2020) Fabrication, microstructure, morphological and magnetic properties of W-type ferrite by co-precipitation method: antibacterial activity. Chem Phys Lett 759:137944
72. Lodhi MY, Khan MA, Akhtar MN, Warsi MF, Mahmood A, Ramay SM (2018) Role of Nd-Ni on structural, spectral and dielectric properties of strontium-barium based nano-sized X-type ferrites. Ceram Int 44(3):2968–2975
73. Cao HB, Zhao ZY, Lee M, Choi ES, McGuire MA, Sales BC, Zhou HD, Yan JQ, Mandrus DG (2015) High pressure floating zone growth and structural properties of ferrimagnetic quantum paraelectric $BaFe_{12}O_{19}$. APL Mater 3(6):062512
74. Ueda J, Tanabe S (2019) Review of luminescent properties of Ce3+-doped garnet phosphors: new insight into the effect of crystal and electronic structure. Optical Mater X 1:100018
75. Kerecman AJ, Tauber A, AuCoin TR, Savage RO (1968) Magnetic properties of $Ba_4Zn_2Fe_{36}O_{60}$ single crystals. J Appl Phys 39(2):726–727
76. Smit, J. and Wijn, H.P.J., 1959. Ferrites, Philips technical library. Eindhoven, The Netherlands, 278.
77. McLyman CWT (2004) Transformer and inductor design handbook. CRC Press
78. Smit J (1959) Ferrites. Philips Technical Laboratory, pp 278–280
79. Ashour AH, El-Batal AI, Maksoud MA, El-Sayyad GS, Labib SH, Abdeltwab E, El-Okr MM (2018) Antimicrobial activity of metal-substituted cobalt ferrite nanoparticles synthesized by sol–gel technique. Particuology 40:141–151
80. Lakshmanan A, Surendran P, Priya SS, Balakrishnan K, Geetha P, Rameshkumar P, Hegde TA, Vinitha G, Kannan K (2020) Investigations on structural, optical, dielectric, electronic polarizability, Z-scan and antibacterial properties of $Ni/Zn/Fe_2O_4$ nanoparticles fabricated by microwave-assisted combustion method. J Photochem Photobiol A 402:112794
81. Naik MM, Naik HB, Nagaraju G, Vinuth M, Naika HR, and Vinu K (2019). Green synthesis of zinc ferrite nanoparticles in Limonia acidissima juice: characterization and their application as photocatalytic and antibacterial activities. Microchem J, 146:1227-1235

82. Naik MM, Naik HB, Nagaraju G, Vinuth M, Vinu K, Viswanath R (2019) Green synthesis of zinc doped cobalt ferrite nanoparticles: structural, optical, photocatalytic and antibacterial studies. Nano-Structures Nano-Objects 19:100322
83. Khezerlou A, Alizadeh-Sani M, Azizi-Lalabadi M, Ehsani A (2018) Nanoparticles and their antimicrobial properties against pathogens including bacteria, fungi, parasites and viruses. Microb Pathog 123:505–526
84. Misra SK, Dybowska A, Berhanu D, Luoma SN, Valsami-Jones E (2012) The complexity of nanoparticle dissolution and its importance in nanotoxicological studies. Sci Total Environ 438:225–232
85. Karimi Z, Karimi L, Shokrollahi H (2013) Nano-magnetic particles used in biomedicine: core and coating materials. Mater Sci Eng C 33(5):2465–2475
86. Qu X, Brame J, Li Q, Alvarez PJ (2013) Nanotechnology for a safe and sustainable water supply: enabling integrated water treatment and reuse. Acc Chem Res 46(3):834–843
87. Ahamed M, Akhtar MJ, Alhadlaq HA, Khan MM, Alrokayan SA (2015) Comparative cytotoxic response of nickel ferrite nanoparticles in human liver HepG2 and breast MFC-7 cancer cells. Chemosphere 135:278–288

Chapter 12
Ferrite Nanoparticles for Corrosion Protection Applications

Nisha Sharma

1 Introduction

Deterioration of materials because of contact with their environment is a frequent issue. Research into developing an environmentally friendly way to preserve metallic substrates is advancing because of the current restriction on the use of hazardous substances. The greatest concern in the world is corrosion since it is a costly phenomenon that results in irreparable material loss or destruction. The cost of corrosion is comparable to about 4% of the GDP, or one-fifth of the global steel output produced to make up for corrosion-related losses [1–3]. Corrosion is an electrochemical phenomenon that results in the deterioration of metals by transferring charge from one chemical species to another. Corrosion is influenced by many environmental variables, such as temperature, pH fluctuations, humidity, gases, salts, contaminants, and the kinds of electrolyte species that are present on the metal surface [4, 5]. One of the main issues has been the corrosion that metals experience when exposed to an acidic or salty environment. Acid pickling, which eliminates impurities from alloys made of iron, copper, and aluminium by utilising powerful acids like HCl, HF, H_2SO_4, H_3PO_4, and HNO_3, frequently has corrosion as a side consequence. X-80 steel is recognised as an accessible resource when planning and building lengthy pipelines and tanks for submerged or underground applications because to its tolerance towards frequent exposure to acidic and saline conditions. Extreme environments, like those that are acidic or salty, render X-80 steel more prone to corrosion, which limits its viable applications for a very long time [6]. Significant losses in the oil business are also a result of corrosion processes [7].

The costs associated with repairing or replacing corroded materials can be significantly decreased or even eliminated with appropriate and effective anticorrosion

N. Sharma (✉)
Department of Physical Sciences, Sant Baba Bhag Singh University, Jalandhar, Punjab 144030, India
e-mail: nishi.hpu@gmail.com

P. Sharma et al. (eds.), *Engineered Ferrites and Their Applications*, Materials Horizons: From Nature to Nanomaterials, https://doi.org/10.1007/978-981-99-2583-4_12

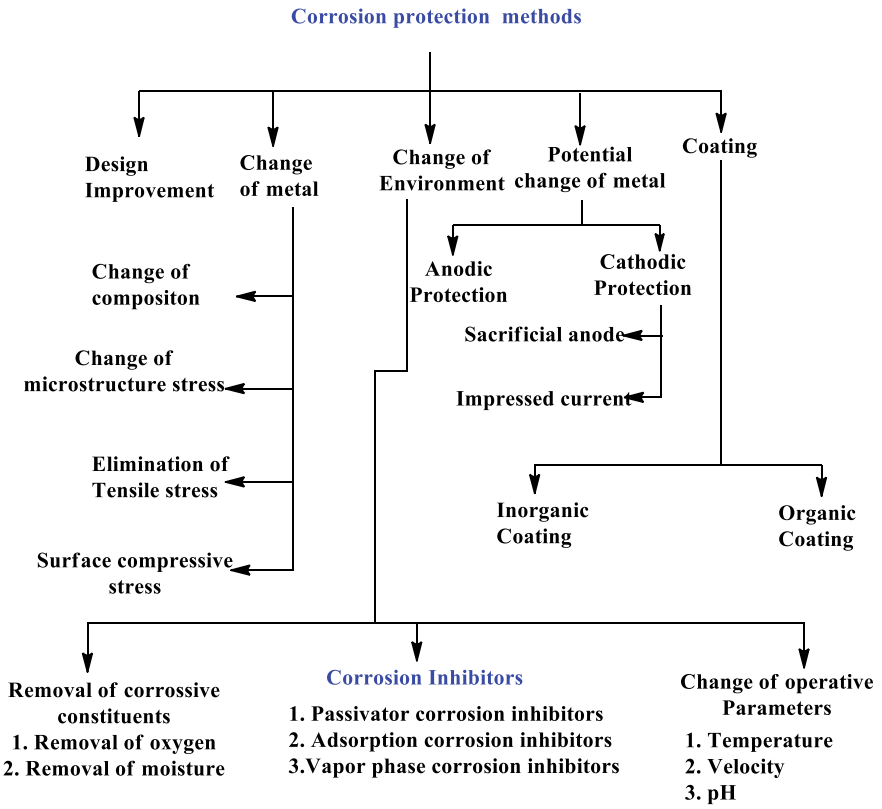

Fig. 1 Different corrosion protection methods

treatment [8]. The rate of corrosion can be slowed down by a variety of techniques, including coating the metal surface, modifying the surroundings, adding corrosion inhibitors, and modifying pH and potential through cathodic or anodic reaction [9]. In literature, there are various possible methods of corrosion protection (Fig. 1). Among the many strategies used to prevent corrosion, utilising a corrosion inhibitor is one of the easiest and most useful approaches.

2 Corrosion Inhibitor

Corrosion inhibitors are chemical substances that can be added to gases or liquids to slow down the corrosion of specific materials, mainly metals. The application of a coating to the metal's surface, acting as a passivation layer and blocking access to the metal's surface, would be one approach for inhibiting corrosion. To stop corrosion, the corrosion inhibitor creates a thin layer of adsorbed film on the metal's surface. This

layer isolates the metal from its surroundings and stops corrosion [10]. Inhibitors are widely used to inhibit corrosion on metal surface. By creating a coating that resembles a shield on the metal surface, such inhibitors aid in slowing down corrosion. Due of their low cost and simplicity of usage, corrosion inhibitors are extremely important. The prevention of metal corrosion is frequently caused by interactions between free electrons of the inhibitor and vacant orbitals of the metals, which result in the formation of metal protective surface complexes. These protective layers reduce the process of metal deterioration by suppressing either the cathodic, the anodic, or both processes [6].

3 Types of Corrosion Inhibitor

Based on how they resist corrosion on the metal, corrosion inhibitors can be divided into four broad categories. These kinds include: Cathodic, anodic, volatile corrosion inhibitors, and mixed inhibitors.

- **Cathodic inhibitors** reduce the cathodic reaction's speed or can selectively precipitate on the metal's cathodic regions to stop eroded elements from transferring to the metal surface. Examples of cathodic inhibitors include the ions sulphite and bisulphite, which can combine with oxygen to create sulphates. Redox reactions that nickel catalyses are another illustration of cathodic inhibitors.
- **Anodic inhibitors** coat the metal's surface with a thin protective oxide layer. This reaction causes a significant anodic shift, which transforms the metallic surface into a passivation region. The metal corrosion is lessened because to this passivation area. Chromate, nitrite, orthophosphate, and molybdate are a few examples of anodic inhibitors.
- **Volatile Corrosion Inhibitors** are mainly used to stop corrosion in **c**ondenser tubes in boilers. They may also be referred to as vapour phase inhibitors (VPIs). The pH of the outside atmosphere is changed by VPIs to a less acidic level to control corrosion. Common VPIs include the chemicals such as morpholine and hydrazine, which are used to prevent boiler condenser pipe corrosion.
- **Mixed corrosion inhibitors** also create a film on the metal's surface. Both cationic and anionic processes are reduced by them. This is accomplished by creating a precipitate on the metal's surface. Silicates and phosphates, which are employed as water softeners to prevent water from rusting, are examples of mixed inhibitors.

Corrosion has traditionally been controlled or reduced using organic, inorganic, and mixed materials inhibitors [7]. Numerous studies have been done on the application of various organic and inorganic/metallic nanoparticles with possible anticorrosion behaviour in the literature [11]. (i) Compounds having heterocyclic aromatic rings containing polar elements, such as nitrogen, oxygen, and sulphide, have a lone pair of electrons that interact chemically with the surface of the metal and make up a significant group of organic corrosion inhibitors for copper and its alloys. Using this method, a hydrophobic protective layer that prevents corrosion sites can be absorbed.

(ii) Amino acids have also been studied in literature as corrosion inhibitors in acidic settings [12–16]. There is a great need for suitable alternatives because inorganic and organic inhibitors are extensively employed in the metal industry but are very expensive and hazardous to both individuals and the environment [17]. (iii) Because of the risk to the environment and public health that traditional anticorrosive pigments containing lead or hexavalent chromium (VI) (zinc chromate) pose, they are currently prohibited from use. However, the demand for effective active anticorrosive pigments persists [18].

Since nanotechnology has impacted every part of our lives today, utilising nanomaterials as inhibitors has grown in popularity due to its remarkable qualities. Nano materials are effective corrosion inhibitors because they have several benefits, including a high level of inhibition, cheap cost, minimal toxicity, and ease of production [7]. The greater surface-to-volume ratio of nanoparticles and their additives compared to their traditional macroscopic counterparts makes them effective corrosion inhibitors [17, 19]. Nanocompounds slow down the rate of corrosion and stop surface reactions by obstructing the active sites on the metal surface. Additionally, they provide thermal stability, optical characteristics, endurance, hardness, straightness, and endurance [20]. Scientists and professionals have long been interested in finding safer anticorrosive pigments to replace those that contain hazardous chromium. Attempts to employ complex metal oxides as pigments that can prevent steel corrosion have emerged as one of the most promising directions for this search in recent years [21]. The solution to this requirement could be non-toxic ferrites. The primary focus of the current work is the utilisation of nanoparticles based on ferrite as corrosion inhibitors.

4 Ferrite Nanoparticles

Nanoferrites are significant magnetic compounds that exhibit exceptional magnetic and electrical characteristics as well as high levels of chemical and thermal stability. These nanomaterials have a wide range of uses. The configuration of ferrite's tetrahedral and octahedral position modifies its general qualities, including its magnetic property, thermal conductivity, electrical conductivity, and resistivity [7]. Ferrites have grown in significance and importance over the past few decades because of their numerous uses in communication, electronics, magnetic recording, biotechnology, biomedical sciences, and microwave absorption-based devices, mostly due to their superparamagnetic capabilities [22]. Over the past ten years, there has been a lot of interest in nanostructured ferrites since these materials' structural, surface reactivity, magnetic, electrical, and other properties are all considerably influenced by the nanostructured phase. Nanoferrites' anticorrosion properties have not yet been fully investigated, making this a novel industrial use for ferrites that must be addressed to offer fresh options for corrosive prevention.

5 Anticorrosion Properties of Ferrite Nanoparticles

Numerous ferrites have recently been described as pigments that prevent corrosion [6]. Recent studies have concentrated their efforts on screening and evaluating nanoferrite-based anticorrosion compounds as more suitable substitutes to replace the problems chromate-based pigments. The potential for using ferrites to prevent corrosion has been demonstrated. These materials are strong, have a low calcination temperature, superior mechanical and tensile strength, are environmentally benign, and have a variety of other features [23]. As potential eco-friendly pigments, Grigoriev has carefully examined anticorrosion capabilities, inhibition mechanisms, preparation methods, novel types of ferrite pigments, and ferrite-based multifunctional coatings based on various ferrites [23]. In the presence of ferrites, there is a noticeable reduction in corrosion rate. How well lesser quantities of inhibitors perform as a pigment filler in various polymeric matrixes could serve as a starting point for the development of corrosion-resistant protective coatings [6]. The cationic soaps that are created as a result of the reaction between the ferrite pigments and the binder not only strengthens it mechanically but also makes it less permeable to dangerous organisms. Ferrites with calcium, magnesium, and zinc cations have also been evaluated as additive for cationic soap. Hybrid coatings that include organically modified silicate and zinc nickel ferrites also show improved anticorrosion behaviour for aluminium alloy. The denser arrangement of organically modified silicate via nickel-zinc ferrites is thought to have contributed to the coatings' better performance. Furthermore, Miszczyk and Darowicki investigated the using atomic force microscopy, cathodic and anodic regions were made on steel surfaces, and the effects of extracts of micronized nickel and zinc ferrite in distilled water were studied [10]. Chaudhry et al. investigated nano-nickel ferrites as an anticorrosion pigment for API 5L X-80 line pipe steel. Using 1 M H_2SO_4 and 3.5% NaCl, nanoferrites were isolated, and their defence mechanisms against corrosion are outlined. The effects of nanoferrite concentration and metal immersion period on the electrochemical properties of X-80 line pipe steel have been examined [6]. Al–Cr co-doped magnesium ferrite and pure magnesium ferrite have been evaluated for their anticorrosion behaviour by Ahmed et al. These mixed derivatives were made using a polymeric citrate route combustion technique with urea as an aid. Using electrochemical impedance spectroscopy, corrosion protection performance of a thin coating in acidic conditions on carbon steel has been assessed. Results showed that nanoparticles formed a monolayer on the surface of the steel, effectively shielding it from oxidation. It improved the pathway that iron oxide is formed when water and oxygen combine with iron. Cr doped Mg ferrite demonstrated the maximum anticorrosion efficiency with a charge transfer resistance of 27 k. 0.025 g/L of nanoferrite dose for 2 h immersion duration provide improved corrosion resistance. To prevent surface damage in harsh environmental conditions, steel alloy samples are coated with ferrites to prevent corrosion [24].

The synthesis, characterisation, and corrosion characteristics of zinc and cobalt ferrites as a function of time have been examined by Rather. $ZnFe_2O_4$ and $CoFe_2O_4$

nanoparticles were created using a thermal treatment approach using poly(vinyl pyrrolidone) as a stabilizing agent to stabilise the particles and inhibit any aggregation. Zinc ferrite provides corrosion resistance since there become unavailability of metals for the redox pair reaction. While the passivation layer that has built up over time provides cobalt-ferrite corrosion protection [25].

By using electrochemical techniques, Herme et al. examined the anticorrosion behaviour of strontium hexaferrite coating on steel samples in the presence of chloride ions. Strontium hexaferrite coatings with and without Nd–Co dopants have been created and tested in a NaCl solution for up to 45 days. At various immersion times, time variations in the corrosion potential and polarisation resistance measures have also been assessed. All of the tested ferrite coatings showed strong defence and corrosion resistance, which gradually increases with the time of submerging the coated sample in chloride solution. Even after 48 h of immersion in NaCl 0.5 M, the samples coated in doped ferrite showed the greatest resistance to the severe environment [26]. Fe_2O_3 and ZnO in a molar ratio of 1:1 when calcinated at 1200 °C, results in formation of zinc-ferrite pigment. Such pigment compositions have been given additional functionalization using linseed oil. In some paint compositions, the produced pigment was used. The developed paint films' corrosion resistance, physicochemical, and mechanical characteristics were examined. Zinc ferrite being the basic pigment composition used in anticorrosive paints and also added to organic coating mixture which cannot saponify resulting in formation of highly corrosion-resistant coatings. In such coatings, corrosion protection behaviour increases with rise in pigment to binder ratio [27]. Wu et al. developed hybrid coatings from polyaniline fuctionalised NiZn ferrite and organically modified silicate through sol–gel fabrication method. These hybrid films were spin coated over an aluminium alloy to improve its corrosion resistance. The impacts of the NiZn ferrite: polyaniline composition on the anticorrosion behaviour, chain dynamics, and ferromagnetic behaviour of the coated samples have been evaluated. These hybrids exhibited super-paramagnetic behaviour as their magnetic characteristics, including zero coercivity at 45 K temperature. As compared to untreated aluminium alloy substrates, these hybrid coatings display extraordinary corrosion protection and barrier behaviour as obtained from potentio-dynamic and salt-spray analysis [28]. Another study evaluated an organic covering for anticorrosive behaviour after impregnating it with nanoferrite. Polyaniline-surface-modified pigments with a variety of chemical makes and particle morphologies were created as corrosion inhibitors for coatings. These pigments are based on ferrites with alkaline earth metals Mg, and Ca cations and with Zn cations. The oxidative polymerization of aniline was then used to coat the primary particles' surfaces, thus functionalizing them with electrically conductive polymer. Alkyl resin with a solvent base was used to create the model coating compositions to test the corrosion behaviour. In the chosen alkyd resin, the presence of polyaniline is more effective at preventing corrosion than spinel-type pigments alone [29]. Zinc ferrites and polyaniline hybrid conductive paint pigments have also been examined as electroactive and anticorrosion paints. By analysing the linseed oil consumption, specific conductivity, and density of the tested pigments, these hybrid conductive particles could be added for paint compositions as anticorrosion component. These coated particles sustain in harsh environment

thus having high chemical stability. These zinc ferrite/polyaniline particles have the potential to be used as both an electroactive paint [30]. Al-Rubaiey and colleagues have studied anti-corrosion capabilities of zinc and nickel ferrite nanomaterials on carbon steel in Iraqi bentonite mud as a source of the corrosion. It has been observed that ferrites function as effective corrosion inhibitors of carbon steel under the specified circumstances. After being calcined at 600 °C, these zinc and nickel ferrites were discovered to be effective corrosion inhibitors. These nanoferrites achieved up to 35% reduction of corrosion rate [7]. In recent study, Al-Rubaiey et al. have investigated nickel and zinc nano-ferrite materials like nickel ferrities ($NiFe_2O_4$), zinc ferrities ($ZnFe_2O_4$), and Zn-Ni doped ferities ($Zn_{0.6}Ni_{0.4}Fe_2O_4$) as prospective inhibitors to lessen the corrosion of carbon steel in an oil environment. The anti-corrosion capabilities of carbon steel in Iraqi oil media have been assessed. It has been discovered that nano-nickel and nano-zinc ferrites could function as a powerful corrosion inhibitor for the metal carbon steel. When utilising Zn–Ni doped ferities ($Zn_{0.6}Ni_{0.4}Fe_2O_4$) in an environment where crude oil is corrosive, an average reduction in the corrosion rate of around 38% has been realised [31]. Miszczyk et al. have studied NiZn ferrites as pigment additive for protective coatings. A ceramic approach has been used to create NiZn ferrites ($Ni_xZn(1x)Fe_2O_4$) with varied amounts of $x = 0, 0.2, 0.4, 0.6, 0.8$, and 1.0. Electrochemical experiments employing methods like polarisation curves, linear polarisation, and electrochemical impedance spectroscopy (EIS) as well as immersion tests in ferrite extracts have all been used to assess the protective effect of ferrites. These NiZn ferrite-based pigments can be employed in coatings to act as both an electromagnetic interference problem-protecting substance and an active anticorrosion pigment [10]. By employing zinc as a lamellar-shaped core and zinc oxide to cover it, Benda et al. have generated a new anticorrosion pigment. This pigment, with the specified formula $Me_xZn_{1-x}Fe_2O_4/Zn$ and $Me_xZn_{1-x}Fe_2O_4$ (where Me = Ca, Mg), is created during the calcination of zinc. The so-called "barrier effect" of this anticorrosion pigment is a result of its form. This core–shell pigment's key advantage is that it combines barrier defence, active anticorrosion defence (typical for ferrite), and chemical defence supplied by partially oxidised zinc core [32]. It was found that solvent-borne epoxy resins worked best with the needle-shaped zinc ferrite $ZnFe_2O_4$ (–FeO · OH) that was made from goethite. $ZnFe_2O_4$ ($FeO \cdot Fe_2O_3$) synthesised from magnetite, has demonstrated strong anticorrosion performance in the case of water-borne epoxy resins. Paints made with styrene-acrylate usually have lower complex anticorrosion effectiveness scores. The most efficient one, however, is zinc ferrite $ZnFe_2O_4$ (lam-Fe_2O_3) produced from specularite. All anticorrosion pigments made with a zinc ferrite structure, it can be said, are ideal choices for use in epoxy water-borne and solvent-borne binders [33]. A number of ferrite spinel nanopigments have been created by Javidparvar et al. using a surfactant-assisted solvothermal technique and further functionalized using 3-amino propyl trimethoxy silane (APTMS). Electrochemical impedance spectroscopy and a salt spray test were used to examine the inhibitory capabilities of the spinel nanopigments after being incorporated into epoxy coatings. The APTMS-modified $ZnFe_2O_4$ nanopigment improved the barrier behaviour and inhibitive potential of the epoxy coating

as compared to Fe_3O_4 nanopigment, [34]. It has been established that organic coatings containing zinc ferrites can shield metal substrates, most frequently low-carbon steel, by acting as an inhibitor. A functionalized organic covering has been created by Nechvlová and Kalendová to shield metal surfaces. To assess their synergistic effect, the anticorrosion behaviour of conductive polymers with zinc ferrite incorporation has been examined. For a better understanding of the efficiency of the zinc ferrite component, the organic coatings were created using hematite and specularite at pigment concentrations of 5, 10, 20, and 25 wt%. Since conductive polymers are made up of a system of conjugated double bonds, they naturally possess the ability to transport a charge along the chain, which gives them their own electrical conductivity in organic coatings. One hypothesis is that the iron substrate (ferrite component) and the charge from the chain work together to produce electrons that resulting in the formation of passivation products on the surface. According to experimental findings, ferritic pigments' corrosion resistance to a sulphur oxide-containing industrial atmosphere is significantly increased when they are homogenised with conductive polymers. Nanoferrites' spherical shape improved corrosion in the cut, and their lamellar particle structure prevented blisters from forming on the surface of the paint film. Since the conductive polymer filled the spaces between the ferritic pigment particles, it was possible to determine the distribution of the particles in the paint layer based on their size. With the help of the topcoat's barrier action, this had the effect of preventing the corrosive medium from reaching the substrate metal and provided a synergistic anticorrosion protective effect [35]. In epoxy-based paints, Ahmed Nivin et al. have created a brand-new ferrite/kaolin core–shell pigment anticorrosion formulation and compared its effectiveness as compared to original ferrites. The new pigments are based on precipitating kaolin (core), a widely accessible and economical material which constitutes up to 80–90%, and shell of different ferrites which constitutes up to 10–20% composition of the entire pigment. These pigments demonstrate better corrosion prevention abilities since they integrate the traits of both their core and shell counterparts. The pigments are also touted as being just as effective at protecting steel substrates as original ferrites while being just as inexpensive and environmentally benign. Physico-mechanical characteristics and corrosion behaviour of dry films have been evaluated using accelerated laboratory analysis in 3.5% brine for 28 days. These ferrite/kaolin core–shell pigments' represents identical anticorrosion behaviour as depicted for ferrite pigments. These pigments can be used as fillers and reinforcing agents in other polymer composites, such as rubber and plastic. These environmentally friendly pigments, ferrite and ferrite/kaolin are also cost-effective [36]. Using a co-precipitation technique, Andrzej Miszczyk has created nanoscale NiZn ferrites, of chemical formula $Ni_xZn(1x)Fe_2O_4$. The ability of these nano-sized ferrites to suppress corrosion has been examined on carbon steel samples. The results were compared to prior information collected for ceramic ferrites of micron size. Nano-sized ferrites have been made at calcining temperatures about 600 °C, which is in comparison to the micro-sized ferrites made by the traditional ceramic solid-state reaction, which require a temperature of 1200 °C. Nanoparticles exhibit more advantageous anticorrosion characteristics on steel. These nanoscale ferrites have also been studied as microwave absorbers, with the microwave reflectance of the

coating being evaluated between 6.5 and 15 GHz. Contrary to micro-ferrite-filled coating, nanoferrite-filled coating displayed a greater minimum reflection frequency. Nanoferrites exhibit stronger anti-corrosion inhibitory characteristics as validated through various electrochemical experiments. These NiZn ferrites have also been discovered to be appropriate for use in the reduction of EMI as microwave shielding and absorption materials. They might be an acceptable and affordable addition to contemporary multifunctional coatings because of their anti-corrosion qualities [18]. To create polymer films and further assess their anti-corrosion effects on API 5L X-80 carbon steel, Chaudhary et al. created a novel organic coating impregnated with nano nickel-zinc ferrite. Organic coatings with anti-corrosion capabilities can benefit from the synergistic effects of adding inorganic oxide, which improve physical and/or chemical properties. Corrosion behaviour have been evaluated by treating the sample in 3.5% NaCl for 216. The surface that had corroded was examined using optical microscopy, field emission scanning electron microscopy, and X-ray diffraction methods. Improvements in the steel's anti-corrosion capabilities were seen when nickel zinc ferrite was included into the polymeric covering. The mechanism for corrosion protection was thought to be the leaching and precipitation of metallic ions on the damaged surface, which lowered corrosion activity [37]. Paints with mixed metal oxide-based pigments have been examined for their anticorrosion qualities by Andrea Kalendová et al. The high-temperature solid-phase technique has been used to create various spinels of cation combinations, such as Ti–Zn–Mg or Fe–Zn–Mg, with layers of ZnO and MgO. Investigations have been made into the anticorrosion and physico-mechanical characteristics of various paint films comprising nanoferrite and alkyl resin containing soy oil. The pigments based on ferrite showed the best anticorrosion effectiveness. With higher Zn levels in the pigments, the anticorrosion effectiveness was shown to rise [38].

6 Possible Anticorrosion Mechanisms Adopted by Nanoferrites

There are numerous theories about how ferrites prevent corrosion. Depending on their composition, mode of interaction, method of manufacturing, etc., various nanoferrites take on distinct modes of operation. The primary mechanisms used by nanoferrites are barrier generation and neutralisation and passivation. According to published research, the most widely recognised and suggested mechanism for ferrite's anticorrosive behaviour is based on the formation of non-soluble compounds [39] and passivation of the metal's surface [10, 27, 40–42]. Nanoferrites precipitate on the metal's surface and slow down the electrochemical reaction that results in the mobility of ionic and non-ionic species [43]. According to Kinnari et al., "the observed inhibitive activity is owing to the adsorption of magnetic nanoparticles on the steel surface, providing a barrier between the metal and the harsh environment" is one of their proposed mechanisms [7]. The anticorrosion activity of ferrite spinel pigments is

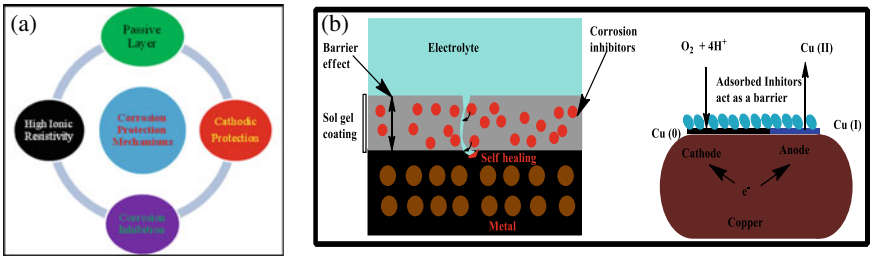

Fig. 2 Type of anticorrosion mechanism (**a**) plausible anticorrosion mechanisms adopted by nanoferrites (**b**)

based on the formation of zinc or calcium soaps through interaction with a suitable binder [44]. Since the aqueous extracts of spinel pigments have a pH of 9.8, they neutralise the acid binders and change the pH to a range that does not encourage corrosion. As a result, spinel pigments also exhibit neutralising capabilities. Spinel pigments can also be utilised to replace existing harmful anticorrosion pigments because they are medically safe [45]. The paint film's mechanical characteristics are enhanced as a result, while its permeability to the harsh environment is decreased. If the corrosive substances are changed into a state that doesn't harm the metal, the spinel-type pigment exhibits both a barrier effect and a neutralisation effect [46]. Plausible anticorrosion mechanism adopted by nanoferrites is depicted in Fig. 2.

In active–passive areas, ferric salts and nitrates promote metal passivity. The extract method can be used to analyse the inhibitory action of ferrites on metal substrates. In this procedure, the pigments are dissolved in corrosive solution to produce pigment ions, and the substrate metal is submerged in the solution to test for anticorrosion features like passive layer development [6]. Such nanoferrite-based pigments prevent cathodic reaction and have strong anticorrosive properties. In addition, they can serve as a suppressor for microwaves [10].

7 Factors Affecting Anticorrosion Behaviour of Ferrite Nanoparticles

According to published reports, because of their potent electromagnetic properties, tolerable saturation magnetization, and good chemical stability, zinc ferrites and nickel zinc ferrite are particularly appealing additives for corrosion protection. Nanoferrites are soft magnetic materials due to their low hysteresis and high permeability [43]. Nanoferrites' anticorrosion behaviour is influenced by several elements. For ferrites to increase their anticorrosion characteristics, their morphology and chemical composition are critical [47]. Compared to a straightforward epoxy resin coating, the inclusion of strontium hexaferrite improves the steel's protection against corrosion

[24]. It was established that ferrites doped with Nd–Co had higher corrosion protection and resistance to harsh environments than ferrites that are unaltered. These paints that have been modified to contain hexaferrite can be used on exposed surfaces to shield against radiation and provide strong corrosion protection. Ferrites can be used as anticorrosion pigments in spinal-based inorganic pigments because they maintain their effectiveness even when exposed to high temperatures and harsh environments. When a concentrated NaCl solution was utilised as the corrosive agent, the coatings continued to offer protection, and the currents increased by an order of magnitude while remaining consistent despite changes in immersion time [26].

8 Future Scope of Nanoferrites

Although only a few studies on nanoferrites' anticorrosion uses have been done, there is still plenty of room for functionalizing and modifying new such spinals for corrosive inhibition as well as materials/additives for more safer technologies. These materials could be used in the near future for various applications like aerospace research, defence research, as well as deep sea oil refining and transportation as they are stable at greater temperatures as well as in severe circumstances.

9 Conclusion

Although technological development and advancements have improved quality of life, they have also had certain unfavourable repercussions. One of the worst effects on metallic surfaces is corrosion. Corrosion deteriorates the material's physical and chemical properties, causes serious flaws in the machinery, and ultimately serves as the primary cause of numerous accidents and deaths. The primary remedy for this entails a variety of chemical and electrochemical processes, as well as coating for the exposed metallic surfaces; however, these remedies are similarly transient in nature.

In recent years, nanotechnology has become a leading source of information for a variety of issues because to the creation of complex nanomaterials. The main characteristics of nanoscale materials include increased surface area, improved chemical reactivity, and mobility. New nanomaterials called ferrite nanoparticles have a high surface-to-volume ratio and exhibit superparamagnetic behaviour. Diverse researchers' main areas of study in recent years have included the potential anticorrosion behaviour of ferrite-based nanoparticles. Nanoparticles may be anticorrosive through a variety of ways. According to the foregone study, nanoferrites have proven to be good additives for anticorrosion applications, and there is still much need for research into the precise mechanism and important features of materials that are changed by the addition of nanoferrites.

References

1. Umoren SA, Solomon MM (2014) Recent developments on the use of polymers as corrosion inhibitors: a review. Open Mater Sci 8(1):39–54. https://doi.org/10.2174/1874088X01408010039
2. Weber J (1983) Current corrosion protection problems. Mater Des 4(2):723–727. https://doi.org/10.1016/0261-3069(83)90137-1
3. Valença DP, Alves KGB, de Melo CP, Bouchonneau N (2015) Study of the efficiency of polypyrrole/ZnO nanocomposites as additives in anticorrosion coatings. Mater Res 18(2):273–278. https://doi.org/10.1590/1516-1439.371614
4. Okonkwo PC, Abdul Shakoor AMA, Mohamed (2015) Environmental factors affecting corrosion of pipeline steel: a review. Int J Mech Prod Eng Res Dev 5(5):57–70
5. Dwivedi D, Lepková K, Becker T (2017) Carbon steel corrosion: a review of key surface properties and characterization methods. RSC Adv 7(8):4580–4610. https://doi.org/10.1039/C6RA25094G
6. Chaudhry AU, Mittal V, Mishra B (2015) Nano nickel ferrite ($NiFe_2O_4$) as anti-corrosion pigment for API 5L X-80 steel: an electrochemical study in acidic and saline media. Dyes Pigm 118:18–26. https://doi.org/10.1016/j.dyepig.2015.02.023
7. Al-Rubaiey NA, Kadhim FS, Ati AA (2017) Nano ferrites as corrosion inhibitors for carbon steel in local Iraqi bentonite mud. Eng Tech J 35(8):849–855. https://doi.org/10.30684/etj.35.8A.11
8. Ebrahimi G, Rezaei F, Neshati J (2017) Investigation on corrosion protection mechanism of polyaniline nanoparticles doped with phosphoric acid by scanning Kelvin probe and other electrochemical methods. J Taiwan Inst Chem Eng 70:427–436. https://doi.org/10.1016/j.jtice.2016.11.007
9. Fotovvati B, Namdari N, Dehghanghadikolaei A (2019) On coating techniques for surface protection: a review. J Manuf Mater Pro 3(1):28. https://doi.org/10.3390/jmmp3010028
10. Miszczyk A, Darowicki AK (2011) Study of anticorrosion and microwave absorption properties of NiZn ferrite pigments. Anti-Corr Meth Mat 58(1):13–21. https://doi.org/10.1108/00035591111097657N24
11. Jain P, Patidar B, Bhawsar J (2020) Potential of nanoparticles as a corrosion inhibitor: a review. J Bio Tribo-Corr 6:43. https://doi.org/10.1007/s40735-020-00335-0
12. Sisso O, Dor S, Eliyahu D, Sabatani E, Eliaz N (2020) Corrosion inhibition of copper in ferric chloride solutions with organic inhibitors. npj Mat Deg 4:38. https://doi.org/10.1038/s41529-020-00139-0
13. Geuli O, Mandler D (2018) The synergistic effect of benzotriazole and trimethylsiloxysilicate towards corrosion protection of printed Cu-based electronics. Corr Sci 143:329–336. https://doi.org/10.1016/j.corsci.2018.08.027
14. Rani BEA, Basu BBJ (2012) Green inhibitors for corrosion protection of metals and alloys: an overview. Int J Corros 12, Article 380217. https://doi.org/10.1155/2012/380217
15. Finšgar M, Milošev I (2010) Inhibition of copper corrosion by 1,2,3-benzotriazole: a review. Corros Sci 52(9):2737–2749. https://doi.org/10.1016/j.corsci.2010.05.002
16. Hluchan V, Wheeler BL, Hackerman N (1998) Amino acids as corrosion inhibitors in hydrochloric acid solutions. Mater Corros 39:512–517. https://doi.org/10.1002/maco.19880391106
17. Roduner E (2006) Size matters: why nanomaterials are different. Chem Soc Rev 35(7):583. https://doi.org/10.1039/b502142c
18. Miszczyk A (2020) Protective and suppressing electromagnetic interference properties of epoxy coatings containing nano-sized NiZn ferrites. Front Mater 7:183. https://doi.org/10.3389/fmats.2020.00183
19. Abdeen D, El Hachach M, Koc M, Atieh M (2019) A review on the corrosion behaviour of nanocoatings on metallic substrates. Mater 12(2). https://doi.org/10.3390/ma12020210

20. Rathish RJ, Dorothy R, Joany RM, Pandiarajan M, Rajendran S (2013) Corrosion resistance of nanoparticle-incorporated nano coatings. Eur Chem Bull 2(12):965–970. https://doi.org/10.17628/ECB.2013.2.965-970
21. Ziganshina M, Kulikova D, Stepin S, Mendelson V (2021) Synthesis by the calcining method and investigation of metal manganites' anticorrosive properties. In: Materials science proceedings of the 10th international advances in applied physics and materials science congress & exhibition. https://doi.org/10.1063/5.0058179
22. Hazra S, Ghosh NN (2014) Preparation of nanoferrites and their applications. J Nanosci Nanotech 14(2):1983–2000. https://doi.org/10.1166/jnn.2014.8745
23. Grigoriev DO, Vakhitov T, Stepin SN (2016) Ferrites as non-toxic pigments for eco-friendly corrosion protection coatings, chap. 3. In: Biobased and environmental benign coatings by MA Salem, Scrivener Publishing, Hoboken, NJ, Wiley. https://doi.org/10.1002/9781119185055.ch3
24. Ahmed S, Ahmad I, Ahmad Z, Jalil A, Ashiq MN, Shafique A (2021) Fabrication and corrosion inhibition behavior of hierarchical Al-Cr co-doped magnesium ferrites nanomaterial for steel. Sur Coat Tech 405:126687. https://doi.org/10.1016/j.surfcoat.2020.126687
25. Rather SU (2017) Corrosion study of ferrites prepared by hydrothermal method. Bulg Chem Comm 49(2):444–448
26. Herme CA, Cicileo GP, Bercoff PG, Jacobo SE (2015) Corrosion of steel alloys with ferrite coating. Int Congress Sci Tech Metall Mat SAM—CONAMET 2014. Procedia Mat Sci 9:150–155. https://doi.org/10.1016/j.mspro.2015.04.019
27. Abu Ayana YM, El-Sawy SM, Salah SH (1997) Zinc-ferrite pigment for corrosion protection. Anti-Corr Meth Mat 44(6):381–388. https://doi.org/10.1108/00035599710367681
28. Wu KH, Chao CM, Liu CH, Chang TC (2007) Characterization and corrosion resistance of organically modified silicate–NiZn ferrite/polyaniline hybrid coatings on aluminum alloys. Corr Sci 49(7):3001–3014. https://doi.org/10.1016/j.corsci.2007.02.008
29. Brodinová J, Stejskal J, Kalendová A (2007) Investigation of ferrites properties with polyaniline layer in anticorrosive coatings. J Phy Chem Sol 68(5–6):1091–1095. https://doi.org/10.1016/j.jpcs.2006.11.018
30. Munteanu L, Munteanu A, Sedlacik M, Kutalkova E, Kohl M, Kalendova A (2022) Zinc ferrite/polyaniline composite particles: pigment applicable as electro-active paint. J Indust Eng Chem 115:440–448. https://doi.org/10.1016/j.jiec.2022.08.030
31. Al-Rubaiey NN, Albrazanjy MG, Kadhim WA, Mohammed HD, Rahim MHA (2021) The potential of using $Zn_{0.6}Ni_{0.4}Fe_2O_4$ nanoparticles as corrosion inhibitor for carbon steel in oil environment. Mater Sci Forum 1021:335–343. https://doi.org/10.4028/www.scientific.net/MSF.1021.335
32. Benda P, Kalendová A (2013) Anticorrosion properties of pigments based on ferrite coated zinc particles. Phy Pro 44:185–194. https://doi.org/10.1016/j.phpro.2013.04.023
33. Ulbrich M, Kalendová A (2013) Properties of organic coatings with nonisometric ferrite particles. Phys Pro 44:247–255. https://doi.org/10.1016/j.phpro.2013.04.030
34. Javidparvar AA, Ramezanzadeh B, Ghasemi E (2016) Effect of various spinel ferrite nanopigments modified by amino propyl trimethoxy silane on the corrosion inhibition properties of the epoxy nanocomposites. Corr 72(6):761–774. https://doi.org/10.5006/2021
35. Nechvílová K, Kalendová A (2018) Influencing the anticorrosion efficiency of pigments based on zinc ferrite by conductive polymers. Koroze a ochranamateriálu 62(3):83–86. https://doi.org/10.1515/kom-2018-0012
36. Ahmed Nivin M, El-Gawad A, Walaa M, SouavaEglal R (2016) Study on the corrosion protection performance of new ferrite/kaolin core-shell pigments in epoxy-based paints. Anticorr Meth Mat 63(1):36–46. https://doi.org/10.1108/ACMM-12-2014-1475
37. Chaudhry AU, Mittal V, Hashmi MI, Mishra B (2017) Evaluation of $Ni_{0.5}Zn_{0.5}Fe_2O_4$ nanoparticles as anti-corrosion pigment in organic coatings for carbon steel. Anti-Corr Meth Mat 64(6):644–653. https://doi.org/10.1108/ACMM-10-2016-1725
38. Kalendova A, Vesely D, Kohl M (2014) Synthesis of Me_2TiO_4 and $MeFe_2O_4$ spinels and their use in organic alkyd resin-based anticorrosion coatings. Corros Rev 32:51–72. https://doi.org/10.1515/corrrev-2013-0050

39. Palmer DA, Anovitz LM (2009) Solubility of zinc silicate and zinc ferrite in aqueous solution to high temperatures. J Sol Chem 38:869–892. https://doi.org/10.1007/s10953-009-9418-z
40. Havlík J, Kalendová A, Veselý D (2007) Electrochemical, chemical and barrier action of zinc dust/anticorrosive pigments containing coatings. J Phys Chem Solids 68(5–6):1101–1105. https://doi.org/10.1016/j.jpcs.2006.11.016
41. Yongsheng H, Fuchun L, Enhou H (2012) Inhibitive behavior and mechanism of a ferrite inhibition pigment in epoxy paints. J Electrochem Soc 159:C403–C410. https://doi.org/10.1149/2.049209jes
42. Deya C, Blustein G, del Amo B, Romagnoli R (2010) Evaluation of eco-friendly anticorrosive pigments for paints in service conditions. Prog Org Coat 69:1–6. https://doi.org/10.1016/j.porgcoat.2010.03.011
43. Karthick R, Venkatesh R (2015) On the nature of ferrite nanoparticles. Int J Res App Sci Eng Tech (IJRASET) 3(IV)
44. Sharma N, Sharma S (2021) Anticorrosive coating of polymer composites: a review. Mat Today Proc 44(6):4498–4502. https://doi.org/10.1016/j.matpr.2020.10.726
45. Kurian M, Nair DS (2016) Effect of preparation conditions on nickel zinc ferrite nanoparticles: a comparison between sol-gel auto combustion and co-precipitation methods. J Saudi Chem Soc 20:S517–S522. https://doi.org/10.1108/ACMM-12-2014-1475
46. Kalendová A (2000) Alkalising and neutralising effects of anticorrosive pigments containing Zn, Mg, Ca, and Sr cations. Prog Org Coat 38:199–206. https://doi.org/10.1016/S0300-9440(00)00103-X
47. Kalendová A, Rysánek P, Nechvílová K (2015) Investigation of the anticorrosion efficiency of ferrites $Mg_{1-x}Zn_xFe_2O_4$ with different particle morphology and chemical composition in epoxy-ester resin-based coatings. Prog Org Coat 86:147–163. https://doi.org/10.1016/j.porgcoat.2015.05.009

Chapter 13
Biomedical Applications of Ferrites

Akshay Sharma, Ramesh C. Thakur, and Renuka Sharma

Abbreviations

AFM	Atomic Force Microscopy
AIDs	Acquired Immuno Deficiency syndrome
IONPs	Iron Oxide Nanoparticles
MFNPs	Magnetic Ferrite Nanoparticles
MHT	Magnetic Hyperthermia
MRI	Magnetic resonance imaging
NPs	Nanoparticles
PET	Positron Emission Tomography

1 Introduction

Ferrite, a kind of ceramic, is predominantly made of iron (III) oxide with minute quantities of one or more other metallic elements (Fe_2O_3, rust) [1]. Its chemical formula is M (Fe_xO_y), where M stands for any metal that forms divalent connections. Figure 1 displays the unit cell of a spinel structure. They are ferrimagnetic, which means that they can be magnetized or drawn to a magnet, and are electrically nonconductive, making them one of the few substances with these two properties [2]. Ferrites have advantages over other types of magnetic materials like high resistivity, wide frequency range, low cost, a wide range of materials, economical assembly, and time and temperature stability [3].

A. Sharma · R. C. Thakur (✉) · R. Sharma
Department of Chemistry, Himachal Pradesh University, Summer Hill, Shimla, Himachal Pradesh 171005, India
e-mail: drthakurchem@gmail.com

P. Sharma et al. (eds.), *Engineered Ferrites and Their Applications*, Materials Horizons: From Nature to Nanomaterials, https://doi.org/10.1007/978-981-99-2583-4_13

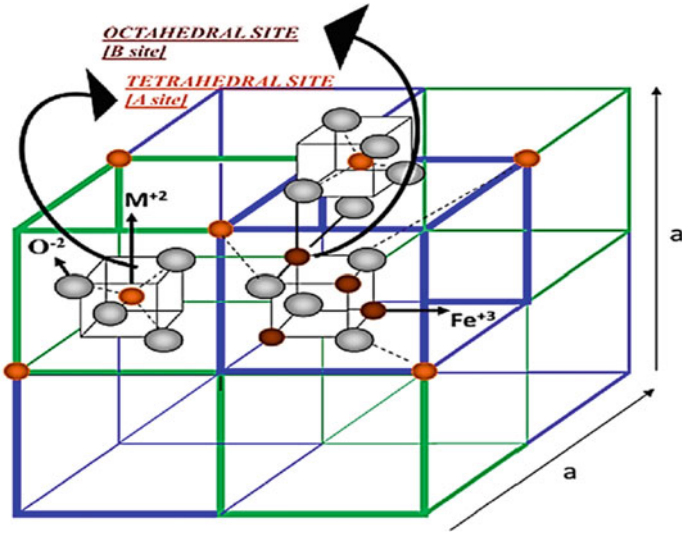

Fig. 1 Crystal structure of a cubic ferrite, Reprinted from Publication "Ferrite Materials: Nano to Spintronics Regime", vol. 23, R. K. Kotnala and J. Shah Copyright (2015), with permission from Elsevier [4]

Ferrites can be categorized into two families considering their magnetic coercivity, or resistance to demagnetization. Because of their high coercivity, hard ferrites are difficult to demagnetize. They are employed in the manufacturing of magnets, which are utilized in components for tiny electric motors, loudspeakers, and refrigerator magnets, among other things. Low coercivity is a property of soft ferrites. They are employed in the electronics industry to produce ferrite cores for inductors, transformers, and various microwave components. Orthoferrites, garnet, spinel, and magnetoplumbite are the four crystal forms that can form from ferrites [5]. In Table 1, several ferrites have been categorized.

Ancient people's first naturally occurring ferrite was Magnetite (Fe_3O_4), also known as a loadstone, and has been applied to the treatment of widespread illnesses. Due to their uses in a variety of fields, particularly the biomedical fields where their improved magnetic characteristics enable a range of imaging diagnoses and therapy, ferrites in particular are different metal oxide nanoparticles that have garnered a lot of interest recently. There are several additional types of ferrites that have been developed and suggested for use in various applications, but cobalt, nickel, and zinc ferrite due to their strong magnetic anisotropy and biocompatibility, has the potential to be employed in biomedical applications [6–12]. Such magnetic ferrite nanoparticles' (MFNPs) most enticing feature in medicinal applications is that they may carry out numerous tasks initiated by an undetectable, tissue-penetrating magnetic field because magnetic fields can't penetrate organic tissues [13, 14]. Natural magnetotactic bacteria, for instance, in their cells build a permanent dipole using a chain

Table 1 Classification of ferrites

Ferrites	Crystal structure	Composition and examples
Spinel	Cubic	$M^{2+}Fe_2{}^{3+}O_4$ where M^{2+} can be any ion like Ni^{2+}, Zn^{2+}, Mn^{2+}, Cu^{2+}, Mg^{2+} ions, or their combination
Orthoferrites	Orthorhombic perovskite	$AFe_{12}O_{19}$ M-type $A_2M_2Fe_{16}O_{27}$ Y-type $A_4M_2Fe_{36}O_{60}$ U-type where M^{2+} can be ions like Fe^{2+}, Ni^{2+}, Mg^{2+} ions, or their combination
Hexaferrite	Hexagonal magnetoplumbite	$R^{3+}Fe^{3+}O_3$ Where R^{3+} can be ions like Gd^{3+}, Sm^{3+}, Lu^{3+}, Y^{3+}, Nd^{3+}
Garnet	Cubic	$R^{3+}Fe_5{}^{3+}O_{12}$ Where R can be ions like Y^{3+}, Gd^{3+}

of IONPs, which enables them to move to their preferred habitats by the detection of the earth's magnetic field [15]. Numerous fascinating in vivo biomedical applications are made possible by the remarkable magneto-responsive characteristics of MFNPs. These include the use of imaging for non-invasive disease detection [16], hyperthermia disease treatment [17], magnetically powered nanorobots [18], magnetic activation of ion channels for cell signaling [19], control over the function and fate of individual cells [20, 21], and more. Cancer is recognized as one of the most difficult difficulties confronted by medical researchers. The use of magnetic nanoparticles (NPs) is intended to both enhance therapy efficacy and track the development of advanced metastatic cancer [22]. The ability of magnetic NPs to functionally bind with various species, including chemotherapeutic agents, nucleic acids, antibodies, and radio nuclides, is used in drug delivery procedures [23]. Additionally, their work in the field of theragnostic therapy is seen as a blend of research and treatment. Applications of spinel ferrites that have recently attracted a lot of attention include the treatment of tumor cells with magnetic hyperthermia and contrast MRI of human body parts. Compared to conventional approaches, the utilization of thermotherapy and radiology-based diagnosis and treatment for diseases with a chronic carcinogenic origin has several advantages. Maintaining high magnetism is difficult since it declines when size is shrunk to the nanoscale, so engineering and intrinsic magnetic properties of these nanoferrites are critical, with the appropriate synthesis method playing a critical role. In the following sections of this chapter, we summarize comprehensively the magneto-responsive mechanism and the crucial magnetic properties of MFNPs that might affect the effectiveness of the applications, and other innovative biomedical ferrite applications and discuss the prospects and challenges of this field.

2 Hyperthermia

Hyperthermia, or a mild rise in temperature to about 40 degrees Celsius, may cause cancer cells to die and improve the effects of radiation and chemotherapy. However, due to its failure to effectively and locally heat malignant cells, it was unable to reach its full potential as a clinically important therapeutic approach. The majority of current research focuses on the effectiveness and effects of magnetic hyperthermia as a possible therapeutic intervention for cancer [24]. By targeting cancer cells that collect in tumors using magnetic nanoparticles administered intravenously, changing the magnetic field is then employed to raise the nanoparticles' temperature, which is present in the tumor tissue. This focused technique enables the local warming up of cancer cells while preventing damage to nearby healthy tissue, thereby improving the efficacy and safety of hyperthermia. Magnetite nanoparticles are the materials that are most frequently utilized to treat brain gliomas in mice, and after three cycles of treatment, tumor size decreased from 30,376 to 2683 mm^3. Unusual FM vortex-domain nanoring (FVIOs) has recently been developed with extraordinarily high SAR up to 3050 W/g, a factor of magnitude larger than the clinically employed SPM IONPs. In the in vivo investigation, it was demonstrated that using FVIOs to deliver effective anti-tumor magnetic thermotherapy at low doses (0.3 mg/cm^3 of tumor tissue) was possible (as shown in Fig. 2). Magnetic nanoparticles can be administered intravenously, intra arterially, intracavitarially, or intratumorally to the tumor. Because the majority of the nanoparticles will be eliminated by the body, oral administration is not an option.

Magneto Thermodynamic (MTD) therapy (Fig. 2) was suggested as a comparable treatment. By combining magnetic heating of IONPs with its immunological action associated with the generation of active oxygen, this suggested MTD treatment solved the drawbacks of conventional magnetic hyperthermia and efficiently inhibited tumor development. Magnetic particles are localized in the tumor through intra-tumoral and intra-cavitary injection, which can effectively heat primary tumors. Intravenous administration is the most adaptable delivery route for a variety of oncological disorders, even though the aforementioned methods of administration are suitable for some situations. The buildup of tumor nanoparticles depends in part on the effect of increased permeability and retention when magnetic iron oxide particles are given in this manner. This phenomenon describes how nanoparticles have the propensity to collect primarily in tumors because of the permeability of their vasculature and inadequate lymphatic drainage. Target ligands, such as peptides, aptamers, and ligands of certain receptors found on the surface of tumor cells, might increase the absorption of nanoparticles by cancerous cells. When a magnetic field is alternately present, their predominant concentration in malignant neoplasms causes targeted local heating of tumors while protecting nearby normal tissues. Dextran-coated magnetic nanoparticles were used in recent research to cure dangerous glioblastomas in Fisher rats [26]. The researchers also noted a statistically significant difference between the monitoring and treatment groups' mean survival rates ($p < 0.01$) [27]. The development of precipitates also increased when the temperature rose up to 47 °C inside the tumor,

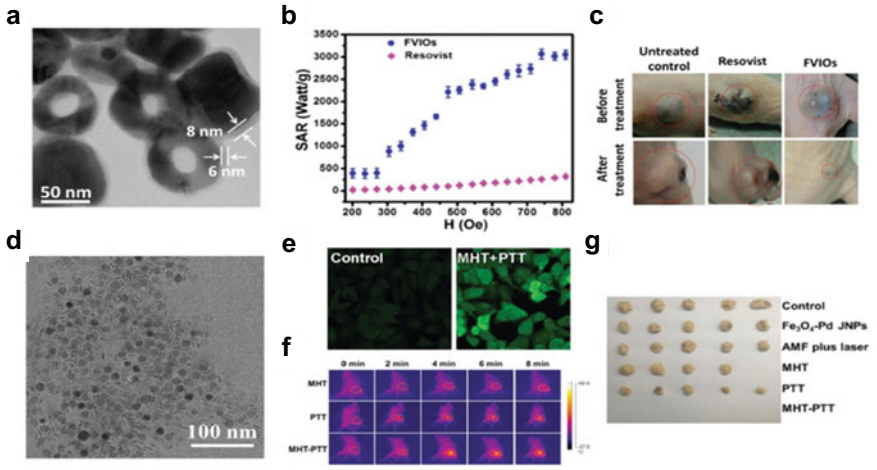

Fig. 2 **a** TEM picture of FVIOs, **b** FVIOs and Resovist's SAR, **c** hyperthermia for Resovist and FVIOs, respectively Fe_3O_4-Pd NPs are shown in (**d**) by TEM. **e** Images of 4T1 cells taken under the following various treatments. Using DCFH-DA, ROS production was observed (green). Fe_3O_4-Pd NPs exposed to AMF, 4T1 tumor-bearing mice were thermally imaged (**f**). **g** Digital images of tumor tissues after they had various treatments. Reprinted from Publication "Enhancing the magnetic responsiveness of ferrite nanoparticles for cutting-edge biomedical applications", Wang et al. (2020) Materials Today Advances, Volume 8, with permission from Elsevier [25]

indicating that the animal's survival rate increased by 4.5 times, from 15.4 (6.3) to 39.7 (3.5) days. A recently developed biocompatible Fe_3O_4-Pd NPs may concurrently generate more ROS and much higher magnetic photo heating efficiency. The anticancer experiment demonstrated that the tumor was entirely eradicated on Day 18 and that 4T1 orthotopic breast cancers were totally inhibited (as shown in Fig. 2). Additionally, few studies demonstrate the use of iron oxide and iron-based magnetic NPs for the treatment of melanoma in vivo. After receiving magnetic NPs treatment, tumor weight dropped from 1.6 to 0.75 (control) mg in a statistically significant ($p <$ 0.1) manner. In a new finding for the magnetic characterization, thermal characteristics, and cytotoxicity of Fe_3O_4, $CoFe_2O_4$, $MgFe_2O_4$, and $NiFe_2O_4$ nanoparticles, the Fe_3O_4 nanoparticles displayed a high-temperature increase and good biocompatibility [28]. These nanoparticles are therefore appropriate for hyperthermia treatment. Despite the positive outcomes of magnetic hyperthermia preclinical experiments, there are still many issues to be resolved. This includes establishing the best ranges for magnetic field intensity and frequency, relating those ranges to the length of the course of treatment, assessing the toxicity of magnetic nanoparticles (including how much of that toxicity depends on the presence of particular ligands that facilitate the accumulation of magnetic particles in tumor cells), and figuring out the best concentration for the organ in question.

3 MRI and Cancer Diagnosis

Because early detection is connected with a better prognosis with any sort of therapy, there are several motivations to create technology that can detect cancer in its early stages [29]. Due to the availability of curative therapy, first-stage cancer discovery is often linked with a 5-year survival rate of more than 90% of patients. Cancer may currently be found using several medical tests, including blood, urine, or imaging methods [30]. Conventional imaging methods often identify cancer after it has already developed to a size of a few millimeters (e.g., MRI) or centimeters (e.g., PET) and contain more than a million cells [31]. To address this drawback, molecular imaging has recently been proposed. Recent advancements in molecular cell biology, imaging, and nanotechnology made it feasible to create this novel imaging modality. While magnetic resonance imaging (MRI), which offers the high-quality resolution in comparison to other employed techniques and is very minimally invasive, is of particular interest, molecular imaging applies to a variety of imaging methods such as computed tomography, ultrasound, and positron emission tomography (PET). Unfortunately, because of its limited specificity, MRI has not been used to its full potential for the detection of cancer. However, the unique features of superparamagnetic nanoparticles (NPs), which may be used to be identified with MRI in fewer quantities and cell markers, can be used to overcome the lack of MRI specificity. When super (paramagnetic) nanoparticles are introduced into a magnetic field, they disrupt the field and speed up the water proton relaxation process, allowing for MRI detection. Due to their distinct magnetic properties and smaller sizes, which however are comparable to the biological molecules, such as enzymes, and receptors, nanoparticles, which are typically smaller than 100 nm, have been used in medicine to enable diagnostic, therapeutic, and combined diagnostic and therapeutic procedures [30, 32].

Nanoparticles with potential medicinal uses for MRI are made of a variety of substances, including metals (cobalt, gold, and silver) and metal oxides (Fe_3O_4, TiO_2, and SiO_2). The smallest and tiniest superparamagnetic iron oxide particles are the most prevalent and the first to be used in MRI nanoparticles (SPIO and USPIO). Considering that they were employed for the clinical identification of localized liver and spleen lesions using MRI since 1987, magnetic iron oxide particles have been used in medicine. As a result of the liver's iron overload brought on by the hepatobiliary system's selective activity, applications of iron-based nanoparticles increased MRI sensitivity. Biologists, pharmacologists, physicists, doctors, and the pharmaceutical sector have lately used nanoparticles. For the therapy, roughly 20 clinically authorized nanomedicines are employed. Examples include the cobalt-based drug Doxil, which is made up of nanoparticles with a polyethylene glycol covering and is used to treat Kaposi's sarcoma linked to AIDS as well as refractory ovarian cancer. Breast cancer is treated with Abraxane, a cobalt-containing albumin-bound form of paclitaxel with an average particle size of 130 nm.

3.1 Contrast Agents

Contrast enhancers are often utilized in MRI images, which are classified based on relaxation times T1 or T2 [33]. The MRI signal is likely to have been enhanced by the MFNPs' dipole–dipole interaction with the surrounding water molecules, which decreased the longitudinal (T1) or transverse (T2) relaxation durations of the nearby water protons. Utilizing relaxivity, the MR contrast agent's ability to contrast is evaluated (r1 or r2). Based on theoretical considerations, it is well acknowledged that relaxation enhancement of contrast agents follows both inner- and outer-sphere routes. The inner-sphere proton must be relaxed by a direct interaction between water molecules and paramagnetic ions. However, coherent proton spin dephasing and outer-sphere proton relaxation are related. The contrast agent's relaxivity is thus determined by the sum of the inner-sphere and outer-sphere contributions [34–40]. The outer-sphere contribution frequently predominates the T2 relaxation augmentation for MFNPs. The relaxation contributions of the outer-sphere and inner-sphere proton are both significant for the enhancement of T1 relaxation, as shown by the fact that the contribution from the inner-sphere mechanism cannot be disregarded when the nanoparticles are smaller than 5 nm [41]. T2, the relaxation times can be impacted by superparamagnetic NPs, and such contrast agents with increased magnetic susceptibility and relaxivity have been obtained and reported in the literature. Additionally, T1-T2 switchable MRI may be accomplished by designing MFNPs as a flexible platform for dual modal T1-T2 contrast agents (Fig. 3).

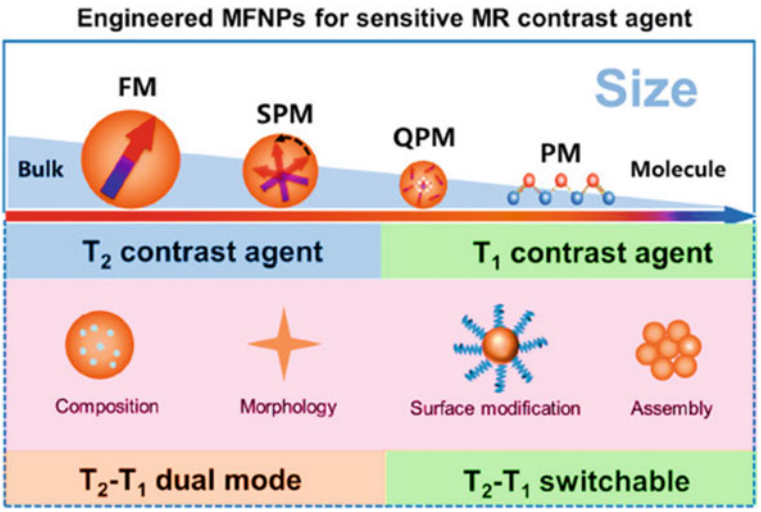

Fig. 3 Diagrammatic representation of the engineering considerations while modifying the relaxivities of MFNPs. Reprinted from Publication "Enhancing the magnetic responsiveness of ferrite nanoparticles for cutting-edge biomedical applications", Wang et al. (2020) Materials Today Advances, Volume 8, with permission from Elsevier [25]

Additionally, these NPs have been widely employed for the marking and monitoring of individual cells as well as imaging cell clusters and tissues [42]. For all-purpose targeted imaging, a number of non-specific superparamagnetic contrast agents are acceptable [43]. These can also be employed for targeted medication administration to help their aggregation in cancer areas and enhance MRI resolution. To target hepatocellular carcinoma specifically, anti-glypican antibodies and anti-fetoprotein can be utilized as the outer shell [44]. Despite the lack of particular biomarkers, contrast agents made of superparamagnetic NPs can provide higher contrast with a small amount [45]. Superparamagnetic contrast chemicals have been crucial for tissue imaging and diagnostics. The potential of MRI as a trustworthy, non-invasive imaging and early cancer detection technique will grow as a result of a future research study using tailored contrast agents [46].

4 Drug Delivery

Due to their versatility in modifying their properties for various biological applications, spinel ferrite nanoparticles have attracted a lot of interest as a drug delivery system when used in conjunction with an external magnetic field [47–50]. A "magic bullet" that would solely kill sick tissue was proposed around a century ago [51]. The use of microencapsulated medication particles has been around since the 1950s [52]. Since then, there have been a significant number of papers in this biological field. The literature now accessible contains several studies and research papers concerning nanoparticles made of silica, gold, polymers, and other materials [53–55]. Since a variety of nanoparticles may be employed, it is clear that magnetism isn't a requirement when building a drug delivery nanosystem. However, there has been a lot of interest in using magnetic ferrite nanoparticles for drug delivery in recent years [12]. The conventional drug delivery approach results in whole-body toxicity and decreased therapeutic effectiveness by distributing drugs to cells and tissues in non-specific ways and causing metabolic instability [7]. Another impressive property of spinel ferrite nanoparticles is their capacity to deliver harmful drugs to cells by encasing them within the polymer matrix [56, 57]. With the use of an external magnetic field, spinel ferrite nanoparticles may readily travel to the target tumor location and help offer successful therapeutic treatment of cancer cells by avoiding normal cells [58]. They can also carry medications and circulate without spilling. Multifunctional nanoparticles, which include semiconductors (for cell imaging), anticancer medicines, and spinel ferrite nanoparticles, are excellent for cancer treatment. It has been established that $CoFe_2O_4$ nanoparticles with lauric acid caps might be employed as a potential drug delivery system with the pH-sensitive release [59]. Due to increased permeability and retention (EPR) caused by the nano-sizes of NPs, in tumor tissues, there is a tendency for passive accumulation [60]. This passive targeting takes use of the damaged vasculature, the micro tumor environment's varying pH and temperature levels, and the lymphatic drainage system's poor function, as well as the altered vasculature that increases the EPR effect in cancer cells. According

to a study, manganese ferrite nanoparticles coated in chitosan and PEG effectively encapsulated methotrexate, whereas $Mg_{0.5}Co_{0.5}Fe_2O_4$ nanoparticles functionalized with chitosan enhanced 5-FU distribution in in vitro MCF-7 cells. Under acidic circumstances, a drug release that is pH-sensitive was triggered in both trials. Under various pH settings, identical stimuli-responsive drug delivery employing $ZnFe_2O_4$ and $Ag^+Zn^+Fe_2O_4$ NPs was shown.

It was also determined that $Zn^+Mg^+Fe_2O_4$ NPs with high drug-loading capacities and predictable drug releases were used for drug delivery. Furthermore, 90.6 to 95% of the medication is released steadily over 24 h at a pH of 7.4 was observed in Gd^{3+} ion-doped $CoFe_2O_4$ NPs for MRI contrast enhancement and tailored drug delivery. These studies demonstrate that $CoFe_2O_4$ NPs can be combined with a variety of other nanocarrier substances, including liposomes, polymers, hydrogels, and silica, improving critical elements for drug delivery applications to be successful, it is essential to have precise targeting, accelerated and sustained drug release, and enhanced half-life. In a different work, co-precipitation was used to create bismuth-doped Ni-ferrites ($NiFe^{2+}Bi^+O_4$) NPs, which were suggested as being effective for locating magnetic carriers. Additionally, adding biocompatible materials to the top or bottom of spinel ferrite nanoparticles may aid to increase their stability and lessen their toxicity in cells. Spinel ferrite nanoparticles must not retain any magnetization after the external magnetic field has been removed in order to be employed for magnetically driven medication delivery. Additionally, they can maintain colloidal stability and avoid aggregation as a result, consequently, they might be utilized in biological applications. One of the hypothesized causes of the agglomeration of spinel ferrite nanoparticles is a magnetic attraction between the particles [61].

Protein-based therapies and nucleic acid biopolymers are predicated in great part on effective cellular absorptions. It is crucial to employ magnetic NPs as vectors given the focus on expensive production methods, concerns about viral safety, and the need to avoid using non-viral vectors. The accumulation and precipitation of nucleic-based treatments are also helped by the manipulation of external magnetic fields for superparamagnetic NPs, which numerous studies have demonstrated dramatically lowers in vitro gene manifestation rates [62].

5 Biosensors

Recently, sensors created using nanostructured materials offer several benefits over sensors made with traditional materials in terms of sensitivity and specificity. Nanostructured materials exhibit unique qualities and present a special type of quick and affordable sensing detection. Magnetic oxides, such as nanoferrites, have been more widely used among these materials for the last 20 years as noble detecting materials in the manufacturing, medical, and ecological detection sectors. Energy storage technologies (batteries and supercapacitors), transformer cores, sensors, microwave applications, and medicinal applications, nanoferrite materials have found successful use in all the above-mentioned devices. Recently it has also been found that spinel

ferrites nanoparticles have shown immense potential, specifically in electrochemical sensors, gas sensors, and biosensors [63]. It is the composition, microstructure, environmental factors, synthesis methods and distribution of cations and anions between the tetrahedral and octahedral positions of the crystal lattice which decide the electrical characteristics of nanoferrites.

Biosensors consist of the biological element and transducer, which make use of an associated physical change, as the main component. The associated physical change could be caused by various changes, for example calorimetric biosensors make use of amount of heat produced by the reaction, potentiometric sensors make use of the charge distribution, potentiometric biosensors make use of changing electrical potential, amperometric biosensors make use of the movement of electrons generated in a redox reaction, antigen–antibody reactions' detection and amplification is the main principle of immuno biosensors and the optical biosensors make use of amount of light generated during the reaction [64]. There are numerous treatments of different varieties which utilize non-invasive biosensors, decrease the level of environmental pollution, screening of different illnesses, keep track of general health care, various veterinary and agricultural applications, and industrial processing and tracking. Screening and tracking of various environmental pollutants are done by making use of various biosensors that combine immunosensors, aptasensors, genosensors, and enzymatic biosensors. The suitable recognition components of these biosensors are antibodies, aptamers, nucleic acids, and enzymes. In the past few years, the sensing performance of $CoFe_2O_4$, $NiFe_2O_4$, $ZnFe_2O_4$, $MnFe_2O_4$, and mixed ferrites has been explored as a high sensing material for the biotic sensors in many industries [65]. Future trends in sensor development that are projected to have an impact on biosensor action mostly relate to immobilization techniques, nanomaterials, miniaturization, and the design of multisensory systems.

6 Brain Stimulation

The magneto-thermo-genetics approach (magneto genetics) is a technique that uses MFNPs to stimulate the brain under AMF based on the magneto thermal effect [66]. The benefits of magneto genetics include cell type specificity, improved geographical and temporal precision, and a lack of need to tether animals to an energy source when compared to second-generation techniques (electrodes and chemicals) and conventional techniques (electrodes and chemicals) (ultrasound and optogenetics). Because of this magneto genetics to trigger the TRPV1 has garnered a lot of interest (316 K), a transient receptor potential vanilloid 1 that is heat-sensitive [67]. For instance, it was seen that heating $MnFe_2O_4$ NPs may activate the TRPV1 channel. Increased intracellular calcium concentration, primary hippocampus neuron action potentials, and retraction movements in C. Elegans worms under partial anesthesia were the effects of this. To control the production of insulin in mice, Fe_3O_4 Anti-His antibody-coated nanoparticles may use an extracellular approach to target the TRPV1 channel with His 6-epitope tag, remotely trigger the generation and release

of proinsulin and activate TRPV1. The identical study group then developed a modified chloride-permeable TRPV1, and they achieved neural inhibition utilizing the same heat stimulation that reduced eating in response to blood sugar levels. Fe_3O_4 remotely activates TRPV1 and elicits excitement in the targeted ventral tegmental region in vivo. Recently, it was proven that capsaicin receptor TRPV1 which is heat-sensitive, activation by magnetic nanoparticles can cause minimally invasive and distant neuronal stimulation. Mice's ventral tegmental area is stimulated using wireless magneto thermal technology, exciting the targeted brain region, excitatory input-receiving structures, and neuronal subpopulations [68]. The release of tiny molecules (agonists or inhibitors) from thermally sensitive lipid vesicles might be triggered by the heat generated by MFNPs and used to them genetically activates designed receptors [62]. A crucial and innovative technique for brain stimulation is the chemogenetic regulation of specific neural circuits utilizing MFNPs in order to study brain processes and neurological disorders [25].

7 Magnetically Powered Nanorobots

In order to diagnose and cure illnesses in intricate biological contexts, MFNPs may be combined into nanorobots of various forms and propelled magnetically thereafter [69, 70]. As an illustration, effectively controlled and in the vitreous body of the eye, we accomplish effective cluster movement by fabricating nanorobots in the form of propellers wrapped in a lubricating nanoliquid layer [71]. A magnetic soft robot with a rectangular sheet form was created [18] using silicone elastomer-encased, hard magnetic neodymium-iron-boron micro particles. This robot can alter its shape and perform a variety of tasks, including crawling, rolling, walking, leaping, and swimming, by gradually altering the external magnetic field. It was able to discharge the payload that was attached to the robot as well as do other practical duties like grasping an object and moving it to a certain area. A technique for encoding numerous shape deformation instructions into micromachining by programming a nonmagnetic array of single-domain on a stretchable silicon nitride (Si_3N_4) substrate has recently been developed [72]. In the nanomagnets by delivering a certain magnetic field sequence with a sufficiently adjusted switching field, this operation was accomplished, which led to the precise shape alterations of the bespoke micro machines. A magnetic DNA hydrogel that is incredibly soft and elastic was used as the foundation for a DNA robot [73]. This DNA robot demonstrated shape-adaptive behavior and allowed magnetic mobility in constrained and unstructured environments. Future innovations in minimally invasive medicine are anticipated to come from magnetically propelled nanorobots.

8 Organ Resuscitation

The "standard approach" for thawing tiny quantities of frozen biological tissue is convective warming. Convective warming, on the other hand, will not be sufficiently uniform across the system when biological tissue volume grows, leading to the breakdown of cell structure as a result of water crystallization. Too far, convective warming of modest amounts, typically about 1 mL, is the only method that can successfully rewarm tissues that have been vitrified in VS55 [74]. In order to limit thermal mechanical stress and the initiation of fractures as well as to stop the crystallization of the rewarming phase, successful rewarming needs both uniform and quick rates. Cryopreserved biomaterials' thawing process may be made better by using MFNPs with rapid and uniform heat production under AMF.

Having an 80 mL maximum capacity for the preservation solution, few researchers [75] reported successfully thawing the heart valves and blood arteries of big by coating IONPs with silicon dioxide. Without producing ice crystals, the tissue may be evenly heated at a roughly constant pace. The NPs were removed from the tissue after it had entirely melted in order to leave behind a largely pure and functional tissue. The tissue restored using this nanoheating technique was essentially equivalent to the normal tissue, as was proven in the comparison test trial at the cellular level. This finding demonstrated that the tissue was not damaged by the nanoheating technology, in contrast to other tissues retrieved using conventional heating techniques that showed varying degrees of destruction.

9 Conclusion and Future Perspective

Ferrites have drawn a lot of interest in the past ten years because of their elemental makeup, which makes them biocompatible and biodegradable. Magnetic nanoparticles are particularly appealing, especially for applications in the biomedical field. Recently, however, research has focused on alternatives such as spinel ferrites, a kind of magnetic nanomaterial that can increase magnetic qualities like coercivity and anisotropy without sacrificing the benefits of iron oxide nanoparticles themselves. Cancer gene therapy, drug release, biosensors, nanorobots, and cancer diagnostics are some of the major biological uses of SFNPs. All of these biological applications are made possible by nanoferrites' outstanding characteristics and adjustable magnetic behavior.

Further study is necessary to synthesize significant amounts of ferrites for medicinal use at a reasonable cost. When employing different nanoferrites for biomedical applications, stability and biocompatibility are the main issues that need to be taken into consideration to increase effectiveness. Additionally, the use of ferrites in several biological fields appears to be crucial, but before commercialization or widespread use, it is vital to take into account and thoroughly examine the danger and toxicity of specific ferrites. Therefore, the appropriate measures should be adopted in order

to prevent unanticipated repercussions and contribute to sustainable uses in many biological application areas. Generally speaking, the incorporation of ferrites into innovative materials or devices demonstrates potential properties for the identification, and remediation of health concerns, while there is still a long way to go to achieve the quality of synthesized ferrites and applicable technologies required for sickness detection and identification.

References

1. Carter MG, Barry C, Norton (2007) Complex crystal and glass structures. In: Ceramic materials: science and engineering. Springer, p 215
2. Spaldin NA (2010) Magnetic materials fundamentals and applications, 2nd edn. Cambridge University Press, p 120
3. Srivastava R, Yadav BC (2012) Ferrite materials: introduction, synthesis techniques, and applications as sensors. Int J Green Nanotechnol Biomed 4:141
4. Kotnala RK, Shah J (2015) Ferrite materials: nano to spintronics regime, vol 23. Elsevier
5. Parker G (2001) Encyclopedia of materials: science and technology. In: Guide-wave optical communications: materials. Elsevier, pp 3703–3707 (n.d.)
6. Lu Y et al (2017) Iron oxide nanoclusters for T1 magnetic resonance imaging of non-human primates article. Nat Biomed Eng 1:637
7. Lee N, Yoo D, Ling D, Cho MH, Hyeon T, Cheon J (2015) Iron oxide based nanoparticles for multimodal imaging and magnetoresponsive therapy. Chem Rev 115:10637
8. Lee JH, Jang JT, Choi JS, Moon SH, Noh SH, Kim JW, Kim JG, Kim IS, Park KI, Cheon J (2011) Exchange-coupled magnetic nanoparticles for efficient heat induction. Nat Nanotechnol 6:418
9. Lee JH et al (2007) Artificially engineered magnetic nanoparticles for ultra-sensitive molecular imaging. Nat Med 13:95
10. Du K, Zhu Y, Xu H, Yang X (2011) Multifunctional magnetic nanoparticles: synthesis modification and biomedical applications. Progress Chem 23:2287
11. Fan K, Cao C, Pan Y, Lu D, Yang D, Feng J, Song L, Liang M, Yan X (2012) Magnetoferritin nanoparticles for targeting and visualizing tumour tissues. Nat Nanotechnol 7:459
12. Veiseh O, Gunn JW, Zhang M (2010) Design and fabrication of magnetic nanoparticles for targeted drug delivery and imaging. Adv Drug Deliv Rev 62:284
13. Riedinger A, Guardia P, Curcio A, Garcia MA, Cingolani R, Manna L, Pellegrino T (2013) Subnanometer local temperature probing and remotely controlled drug release based on Azo-functionalized iron oxide nanoparticles. Nano Lett 13:2399
14. Kalambur VS, Han B, Hammer BE, Shield TW, Bischof JC (2005) In vitro characterization of movement, heating and visualization of magnetic nanoparticles for biomedical applications. Nanotechnology 16:1221
15. Shih-Bin RC, Joseph lK (1989) Magnetofossills the magnetization of sediments, and the evolution of the magnetite biomineralisation. Annu Rev Earth Planet Sci 17:169
16. Shin TH, Choi Y, Kim S, Cheon J (2015) Recent advances in magnetic nanoparticle-based multi-modal imaging. Chem Soc Rev 44:4501
17. Jang JT et al (2018) Giant magnetic heat induction of magnesium-doped γ-Fe_2O_3 superparamagnetic nanoparticles for completely killing tumors. Adv Mater 30:1
18. Hu W, Lum GZ, Mastrangeli M, Sitti M (2018) Small-scale soft-bodied robot with multimodal locomotion. Nature 554:81
19. Huang H, Delikanli S, Zeng H, Ferkey DM, Pralle A (2010) Remote control of ion channels and neurons through magnetic-field heating of nanoparticles. Nat Nanotechnol 5:602

20. Kang H, Jung HJ, Wong DSH, Kim SK, Lin S, Chan KF, Zhang L, Li G, Dravid VP, Bian L (2018) Remote control of heterodimeric magnetic nanoswitch regulates the adhesion and differentiation of stem cells. J Am Chem Soc 140:5909
21. Wu C, Shen Y, Chen M, Wang K, Li Y, Cheng Y (2018) Recent advances in magnetic-nanomaterial-based mechanotransduction for cell fate regulation. Adv Mater 30:1
22. Srinivasan SY, Paknikar KM, Bodas D, Gajbhiye V (2018) Applications of cobalt ferrite nanoparticles in biomedical nanotechnology. Nanomedicine 13:1221
23. Rana S, Gallo A, Srivastava RS, Misra RDK (2007) On the suitability of nanocrystalline ferrites as a magnetic carrier for drug delivery: functionalization, conjugation and drug release kinetics. Acta Biomater 3:233
24. Balivada S et al. (2010) A/C magnetic hyperthermia of melanoma mediated by iron(0)/iron oxide core/shell magnetic nanoparticles: a mouse study. BMC Cancer 10
25. Wang Y et al (2020) Engineering ferrite nanoparticles with enhanced magnetic response for advanced biomedical applications. Mater Today Adv 8
26. Jordan TB, Seen AJ, Jacobsen GE (2006) Levoglucosan as an atmospheric tracer for woodsmoke. Atmos Environ 40:5316
27. Shinkai M, Yanase M, Suzuki M, Honda H, Wakabayashi T, Yoshida J, Kobayashi T (1999) Intracellular hyperthermia for cancer using magnetite cationic liposomes. J Magn Magn Mater 194:176
28. Tomitaka A, Jeun M, Bae S, Takemura Y (2011) Evaluation of magnetic and thermal properties of ferrite nanoparticles for biomedical applications. J Magn 16:164
29. Lanzalaco S, Armelin E (2017) A review on recent progresses in biomedical applications. Gels 3:16
30. Weissleder R (1979) Molecular imaging in cancer. Science 312:1168
31. Sharma I, Garg E (2022) A review on recent progresses in biomedical applications. Int J Basic Appl Sci 11:16
32. Kelkar SS, Reineke TM (2011) Theranostics: combining imaging and therapy. Bioconjug Chem 22:1879
33. Xing G, Yuan H, He R, Gao X, Jing L, Zhao F, Chai Z, Zhao Y (2008) The strong MRI relaxivity of paramagnetic nanoparticles. J Phys Chem B 112:6288
34. Lauffer RB (1987) Paramagnetic metal complexes as water proton relaxation agents for NMR imaging: theory and design. Chem Rev 87:901
35. Zeng J, Jing L, Hou Y, Jiao M, Qiao R, Jia Q, Liu C, Fang F, Lei H, Gao M (2014) Anchoring group effects of surface ligands on magnetic properties of Fe_3O_4 nanoparticles: towards high performance MRI contrast agents. Adv Mater 26:2694
36. Lee N, Hyeon T (2012) Designed synthesis of uniformly sized iron oxide nanoparticles for efficient magnetic resonance imaging contrast agents. Chem Soc Rev 41:2575
37. Ni D, Bu W, Ehlerding EB, Cai W, Shi J (2017) Engineering of inorganic nanoparticles as magnetic resonance imaging contrast agents. Chem Soc Rev 46:7438
38. Zhou Z, Yang L, Gao J, Chen X (2019) Structure-relaxivity relationships of magnetic nanoparticles for magnetic resonance imaging. Adv Mater 31:1
39. Wu L, Mendoza-Garcia A, Li Q, Sun S (2016) Organic phase syntheses of magnetic nanoparticles and their applications. Chem Rev 116:10473
40. Penfield JG, Reilly RF (2007) What nephrologists need to know about gadolinium. Nat Clin Pract Nephrol 3:654
41. Zhang H et al (2017) Ultrasmall ferrite nanoparticles synthesized via dynamic simultaneous thermal decomposition for high-performance and multifunctional T1 magnetic resonance imaging contrast agent. ACS Nano 11:3614
42. Nitin N, LaConte LEW, Zurkiya O, Hu X, Bao G (2004) Functionalization and peptide-based delivery of magnetic nanoparticles as an intracellular MRI contrast agent. J Biol Inorg Chem 9:706
43. Tan BK, Adya R, Randeva HS (2010) Omentin: a novel link between inflammation, diabesity, and cardiovascular disease. Trends Cardiovasc Med 20:143

44. Ghasemian Z, Shahbazi-Gahrouei D, Manouchehri S (2015) Cobalt zinc ferrite nanoparticles as a potential magnetic resonance imaging agent: an in vitro study. Avicenna J Med Biotechnol 7:64
45. Bakhtiary Z, Saei AA, Hajipour MJ, Raoufi M, Vermesh O, Mahmoudi M (2016) Targeted superparamagnetic iron oxide nanoparticles for early detection of cancer: possibilities and challenges. Nanomedicine 12:287
46. Wang Y-XJ (2011) Superparamagnetic iron oxide based MRI contrast agents: current status of clinical application. Quant Imaging Med Surg 1:35
47. Mody Vv, Cox A, Shah S, Singh A, Bevins W, Parihar H (2014) Magnetic nanoparticle drug delivery systems for targeting tumor. Appl Nanosci (Switzerland) 4:385
48. Estelrich J, Escribano E, Queralt J, Busquets MA (2015) Iron oxide nanoparticles for magnetically-guided and magnetically-responsive drug delivery. Int J Mol Sci 16:8070
49. Hauser AK, Wydra RJ, Stocke NA, Anderson KW, Hilt JZ (2015) Magnetic nanoparticles and nanocomposites for remote controlled therapies, vol 219. Elsevier B.V.
50. Guo H, Chen W, Sun X, Liu YN, Li J, Wang J (2015) Theranostic magnetoliposomes coated by carboxymethyl dextran with controlled release by low-frequency alternating magnetic field. Carbohydr Polym 118:209
51. Chan DCF, Kirpotin DB, Bunn PA Jr (1993) Synthesis and evaluation of colloidal magnetic iron oxides for the site-specific radiofrequency-induced hyperthermia of cancer. J Magn Magn Mater 122:374
52. Jordan A, Wust P, Fählin H, John W, Hinz A, Felix R (1993) Inductive heating of ferrimagnetic particles and magnetic fluids: physical evaluation of their potential for hyperthermia. Int J Hyperth 9:51
53. Jordan A, Scholz R, Wust P, Fähling H, Felix R (1999) Magnetic fluid hyperthermia (MFH): cancer treatment with AC magnetic field induced excitation of biocompatible superparamagnetic nanoparticles. J Magn Magn Mater 201:413
54. Jordan A et al (2001) Presentation of a new magnetic field therapy system for the treatment of human solid tumors with magnetic fluid hyperthermia. J Magn Magn Mater 225:118
55. Kawai N, Ito A, Nakahara Y, Futakuchi M, Shirai T, Honda H, Kobayashi T, Kohri K (2005) Anticancer effect of hyperthermia on prostate cancer mediated by magnetite cationic liposomes and immune-response induction in transplanted syngeneic rats. Prostate 64:373
56. Mattingly SJ, Otoole MG, James KT, Clark GJ, Nantz MH (2015) Magnetic nanoparticle-supported lipid bilayers for drug delivery. Langmuir 31:3326
57. Ding Y, Shen SZ, Sun H, Sun K, Liu F, Qi Y, Yan J (2015) Design and construction of polymerized-chitosan coated Fe_3O_4 magnetic nanoparticles and its application for hydrophobic drug delivery. Mater Sci Eng C 48:487
58. Bahrami B, Hojjat-Farsangi M, Mohammadi H, Anvari E, Ghalamfarsa G, Yousefi M, Jadidi-Niaragh F (2017) Nanoparticles and targeted drug delivery in cancer therapy. Immunol Lett 190:64
59. Nanoparticles LCO (2018) One-pot synthesis and surface modification of, 2
60. Maeda H (2001) The enhanced permeability and retention (EPR) effect in tumor vasculature: the key role of tumor-selective macromolecular drug targeting. Adv Enzyme Regul 41:189
61. Karimi Z, Mohammadifar Y, Shokrollahi H, Asl SK, Yousefi G, Karimi L (2014) Magnetic and structural properties of nano sized dy-doped cobalt ferrite synthesized by Co-precipitation. J Magn Magn Mater 361:150
62. Kim D, Yu MK, Lee TS, Park JJ, Jeong YY, Jon S (2011) Amphiphilic polymer-coated hybrid nanoparticles as CT/MRI dual contrast agents. Nanotechnology 22
63. Shobana MK (2021) Nanoferrites in biosensors—a review. Mater Sci Eng B Solid State Mater Adv Technol 272:115344
64. Kumbhar VS, Jagadale AD, Shinde NM, Lokhande CD (2012) Chemical synthesis of spinel cobalt ferrite ($CoFe_2O_4$) nano-flakes for supercapacitor application. Appl Surf Sci 259:39
65. Tsay CY, Chiu YC, Lei CM (2018) Hydrothermally synthesized Mg-based spinel nanoferrites: phase formation and study on magnetic features and microwave characteristics. Materials 11
66. Nimpf S, Keays DA (2017) Is magnetogenetics the new optogenetics? EMBO J 36:1643

67. Sauer U et al (2012) Radio-wave heating of iron oxide. Science 336:604
68. Chen R, Romero G, Christiansen MG, Mohr A, Anikeeva P (2015) Wireless magnetothermal deep brain stimulation. Science 347:1477
69. Lum GZ, Ye Z, Dong X, Marvi H, Erin O, Hu W, Sitti M (2016) Shape-programmable magnetic soft matter. Proc Natl Acad Sci U S A 113:E6007
70. Li J, de Ávila BEF, Gao W, Zhang L, Wang J (2017) Nm delivery surgery, sensing, detox. Sci Robot 2:1
71. Wu Z et al (2018) A swarm of slippery micropropellers penetrates the vitreous body of the eye. Sci Adv 4:1
72. Cui J, Huang TY, Luo Z, Testa P, Gu H, Chen XZ, Nelson BJ, Heyderman LJ (2019) Nanomagnetic encoding of shape-morphing micromachines. Nature 575:164
73. Tang J, Yao C, Gu Z, Jung S, Luo D, Yang D (2020) Super-soft and super-elastic DNA robot with magnetically driven navigational locomotion for cell delivery in confined space. Angew Chem 132:6
74. Kakwere H, Leal MP, Materia ME, Curcio A, Guardia P, Niculaes D, Marotta R, Falqui A, Pellegrino T (2015) Functionalization of strongly interacting magnetic nanocubes with (thermo)responsive coating and their application in hyperthermia and heat-triggered drug delivery. ACS Appl Mater Interfaces 7:10132
75. Etheridge ML, Xu Y, Rott L, Choi J, Glasmacher B, Bischof JC (2014) RF heating of magnetic nanoparticles improves the thawing of cryopreserved biomaterials. Technology (Singap World Sci) 02:229